THE OPTIMAL PLACEMENT OF GEOGRID REINFORCEMENT IN LANDFILL CLAY LINERS

by

David Hercules Marx

Submitted in partial fulfillment of the requirements for the degree
Master of Engineering (Geotechnical Engineering)

in the

Department of Civil Engineering
Faculty of Engineering, Built Environment and Information Technology

UNIVERSITY OF PRETORIA

April 2017

OPSOMMING

DIE OPTIMALE PLASING VAN GEOROOSTER VERSTERKING IN DIE KLEIVOERINGS VAN STORTINGSTERREINE

deur

David Hercules Marx

Studieleier(s):	S.W. Jacobsz
Departement:	Siviele Ingenieurswese
Universiteit:	Universiteit van Pretoria
Graad:	Magister in Ingenieurswese (Geotegniese ingenieurswese)
Sleutelwoorde:	Georooster, stortingsterreinvoering, optimale versterking, kraak meganika, klei, eindige element analise, sentrifuge modellering.

Volgehoude bevolkingsgroei in Suid-Afrika plaas bestaande rommelstortingsfasiliteite onder druk. ’n Tekort aan grond geskik vir die bou van stortingsterreine moedig die soektog na alternatiewe oplossings soos abba-stortingsterreine aan. Hierdie metode behels ’n splinternuwe stortingsterrein wat bo-op bestaande rommel gebou word. Versakking van die bestaande rommel kan egter veroorsaak dat krake vorm in die nuwe stortingsterrein se kleivoering wat daarop lê.

Vorige navorsing het die vorming van krake in die kleivoerings al welgeslaagd verhoed deur van georoosters as versterking gebruik te maak. Die huidige studie het op daardie navorsing gebou deur die optimale versterkings strategie (OVS) te bepaal vir so ’n kleivoering wat vervorm onder versakking van die onderliggende rommel. Die OVS definieer beide die optimale versterkings posisie in ’n kleivoering, en die styfheid van die georooster wat in daardie posisie geplaas moet word, gegewe ’n sekere totale versterkingskoste.

Eerstens was daar ondersoek ingestel na die kraakgedrag van onversterkte kleivoerings. Vierpunt-buigtoetse van kleibalkies was hiervoor gebruik. Die krake het oor drie fases gevorm: eerstens was daar lineêre gedrag tot en met mikro-krake gevorm het. Dit is gevolg deur nie-lineêre gedrag wat gelei

het tot makro-krake. Sodra die makro-krake gevorm het, is die maksimum las bereik wat die klei kon ondersteun.

Na afloop van die balkbuigtoetse was eindige element analises in ABAQUS uitgevoer om die gedrag van versterkte kleivoerings wat bo-op versakkende afval lê te ondersoek. Die spanning toegepas op die oppervlak van die kleivoerings, die dikte van die kleivoerings en die versakkingstrogwydte, -vorm en -diepte was gevarieer om die effek daarvan op die gedrag van die kleivoerings te ondersoek.

Na aanleiding van die resultate van die numeriese analise is ’n reeks sentrifuge toetse van kleivoerings wat aan versakking onderwerp word uitgevoer. ’n Onversterkte kleivoering, kleivoerings versterk in die boonste en onderste kwarte, en een versterk in beide die boonste en onderste kwart was getoets. Die gedrag van die verskillende kleivoerings was vergelyk deur die oppervlaktekrake op te meet met ’n laserskandeerder. Verder is die vervorming van die kleivoerings bepaal vanaf die verplasing van die grondpartikels tussen opeenvolgende digitale foto’s. Na aanleiding van hierdie resultate word dit aanbeveel dat die beskikbare georooster versterking opgedeel moet word tussen die boonste en onderste kwart van die kleivoerings ten einde optimale gedrag te verseker indien versakking sou plaasvind.

SUMMARY

THE OPTIMAL PLACEMENT OF GEOGRID REINFORCEMENT IN LANDFILL CLAY LINERS

by

David Hercules Marx

Supervisor(s):	S.W. Jacobsz
Department:	Civil Engineering
University:	University of Pretoria
Degree:	Master of Engineering (Geotechnical Engineering)
Keywords:	Geogrid, landfill liner, optimal reinforcement, fracture mechanics, clay, finite element analyses, centrifuge modelling.

Continued population growth is placing strain on the waste disposal facilities available in South Africa. However, limited air space suitable for landfilling drives the need for alternative solutions such as piggyback landfills to expand the waste disposal capacity. This method entails building a new, fully lined, landfill on top of existing waste. However, the old underlying waste is prone settlement that can result in the cracking of new landfill clay liner.

Geogrid reinforcement have been successfully used in clay liners to mitigate cracking induced by waste settlement. This research focused on investigating of the optimal reinforcement strategy (ORS) of such a liner subject to settlement . The ORS entails the optimal position for geogrid reinforcement in a liner, and the stiffness to be used at that position, given a total reinforcement cost.

Firstly, the fracture behaviour of unreinforced clay liners was investigated by means of four point bending tests on clay beams. It was found that the fracture of this clay occurred in three stages: linear behaviour, followed by non-linear behaviour when micro-cracks forms and finally macro-cracks that opened once the peak load was reached.

Thereafter, the behaviour of geogrid-reinforced clay liners, subjected to differential settlement, was investigated with finite element analyses in ABAQUS. A number of key factors were varied and the resulting change in behaviour of the liners was observed. These were: the overburden stress applied, clay liner thickness, magnitude of central settlement and the width and shape of the settlement trough developing in the underlying waste body.

Based on the numerical results, a series of plane-strain centrifuge tests of reinforced clay liners subject to differential settlement were designed. An unreinforced liner, a liner reinforced at the bottom quarter, a liner reinforced at the top quarter and a liner reinforced at both the bottom and top quarters were tested. Laser scanner scans of the surface and strains calculated from digital image velocimetry results were used to compare the behaviour of the liners. Based on these results it is recommended that for optimal performance the available reinforcement should be divided between the top and bottom quarters of the liner to mitigate the effect of settlement.

DECLARTAION

I, the undersigned hereby declare that:

- I understand what plagiarism is and I am aware of the University's policy in this regard;
- The work contained in this thesis is my own original work;
- I did not refer to work of current or previous students, lecture notes, handbooks or any other study material without proper referencing;
- Where other people's work has been used this has been properly acknowledged and referenced;
- I have not allowed anyone to copy any part of my thesis;
- I have not previously in its entirety or in part submitted this thesis at any university for a degree.

Signature of student:

Name of student: David Hercules Marx

Student number: u11035707

Date: 2017/05/06

ACKNOWLEDGEMENTS

Even though I might have written this thesis, it would not have come to life without the help and support of a number of people. I would like to thank the following people:

1. Prof. Jacobsz, my supervisor, for his insight, guidance and the wonderful opportunities he created for me.
2. My family David, René and Douw Marx, and wife Rykie Marx for their understanding, patience and support.
3. Prof Kearsley for her help during my centrifuge modelling and valuable discussions on fracture mechanics.
4. Prof Heymann for his insights on laboratory testing.
5. The laboratory technitions: Mr Scholtz, Mr Mostert, Mr Van Staden, Mr Botha, Mr Jansen and Mr Nkadimeng for their help and humor.
6. Tiago Gaspar and Rick Van Doorne who tackled this challenge with me, as well as Phia Smit, Louis Geldenhuys, Ridwaan Fakir and the rest of our the postgraduate group.
7. The Geosynthetics Interest Group of South Africa (GIGSA) for the funding they provided for this research, as well as the funding to attend the 6th European Geosynthetics Congress in Ljubljana, Slovenia.
8. The financial assistance of the Deutscher Akademischer Austausch Dienst (DAAD) and the National Research Foundation (NRF) towards this research is hereby acknowledged. Opinions expressed and conclusions arrived at, are those of the author and are not necessarily to be attributed to the NRF.
9. Dr M Elshafie for inviting me to visit the University of Cambridge's Schofield Centre, the ISSMGE for helping to fund the visit and Talia da Silva for hosting me and sharing her knowledge on centrifuge modelling, reinforcement and clays.
10. Jones and Wagener Environmental and Consulting Engineers for allowing me to pursue master studies.
11. The Department of Electrical, Electronic and Computer Engineering of the University of Pretoria for creating the bulk of this LaTeX template.

TABLE OF CONTENTS

LIST OF FIGURES

LIST OF TABLES

CHAPTER 1 INTRODUCTION

> *One of the greatest social and political challenges that the world, as a whole, faces today and well into the 21st century is the proper disposal of waste products and the prevention of the waste components from entering the environment* - Koutsourais et al. (1991).

1.1 BACKGROUND TO THE STUDY

In 2012 South Africans produced over 53 000 tons of municipal solid waste (MSW) per day. By 2025 waste production is expected to have grown to over 72 000 tons per day, an increase of more than 35%. Global waste generation is expected to grow with almost 70% by 2025 as result of the current rise in urbanisation (Hoornweg & Bhada-Tata, 2012).

By far the most preferable solution to the alarming growth in waste production is to apply Integrated Waste Management, i.e. to reduce and reuse the waste generated. Nonetheless, these practices are not always feasible and the Best Practical Environmental option could be to dispose the waste at a landfill (DWAF, 1998). Worldwide 52% of all refuse is disposed of in landfills and dumps (Hoornweg & Bhada-Tata, 2012). However, as the availability of suitable greenfield sites for new landfills decreases, alternative solutions have to be investigated. One such solution is the re-use of old, decommissioned landfill sites.

In South Africa several landfills and dump sites were constructed before the publication of the *Minimum Requirements for Waste Disposal by Landfill* by the Department of Water Affairs and Forestry in 1998. These Minimum Requirements dictated the minimum acceptable waste disposal practices for landfills. Lining landfills with clay to protect the subsoil and ground water became mandatory. The liner designs were later superseded by the *National Norms and Standards for Disposal of Waste to Landfill* (DEA,

2013). These Norms and Standards require that a clay liner (or equivalent) should separate the waste from the soil below for all types of waste except construction rubble and spoils.

A number of old landfill sites in South Africa do not comply to the new legislation. Before these old landfills can be reused, a new lining system has to be built on top of the existing waste. This concept is known as a piggyback landfill and is illustrated in Figure 1.1. Building a complex liner system on top of an existing landfill has a number of challenges. General municipal solid waste consists of a highly heterogeneous combination of materials with potential for differential and local settlement throughout the waste body (e.g. El-Fadel & Khoury, 2000). Despite its ductility, a clay liner founded on waste will eventually fissure and crack as the underlying waste settles. Consequently, crack growth in the clay has to be stunted before it becomes critical. Should the cracks reach a critical size, the permeability of the liner will locally increase to a level where its ability to protect the groundwater will be compromised.

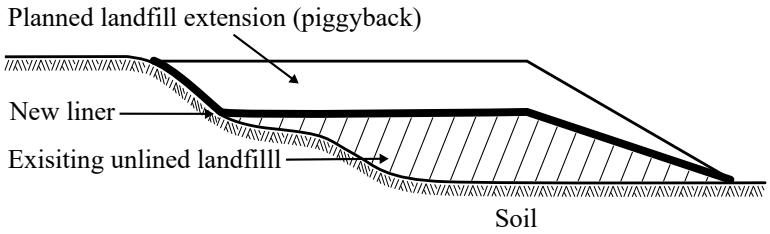

Figure 1.1: The layout of a typical piggyback landfill.

One approach to protect the clay liner from the settlement of the underlying waste is to reinforce it with a geosynthetic such as a geogrid. The geogrid both increases the stiffness of the system, decreasing its deflection, and inhibits excessive crack growth. Geogrid reinforcing of clay liners has been investigated by a number of authors such as Viswanadham & Jessberger (2005) and Rajesh & Viswanadham (2009). However, limited research has been done to determine the optimal position for reinforcement in the clay liners. Finding the optimal position for geogrid reinforcement inside a clay liner was the focus of this study.

1.2 OBJECTIVES OF THE STUDY

The objective of this study was threefold:

1. To gain a better understanding of the behaviour of clay beams in fracture.

2. To investigate the influence of the position of geogrid reinforcement on the performance of clay liners subject to settlement.
3. To develop recommendations regarding the optimal position for geogrid reinforcement in a clay liner subject to local and differential settlement.

1.3 SCOPE OF THE STUDY

In this study geogrid reinforced clay liners subject to differential settlement was investigated. Bending beam tests, numerical analyses and centrifuge modelling were conducted as discussed in Section 1.4.

The scope of this study was focussed to the following:

1. This study was limited to the modelling of a single clay liner. The behaviour of a complete liner system consisting of geomembranes, drainage layers, etc. was not studied.
2. This study was limited to investigating horizontal liners. Slopes were not modelled.
3. The model clay liners for the centrifuge tests were constructed from consolidated, pure kaolin clay and no other materials were considered.
4. The centrifuge modelling was limited to investigating the influence of a single type of geogrid reinforcement on integrity of clay liners. Only the position of reinforcement was varied. The effect varying the geogrid stiffness and the type of geosynthetic reinforcement on the integrity of the liner was not considered.
5. The long term effect of voids below the clay liners was not considered. Creep of the clay liner and geogrids was ignored.
6. The integrity, or performance, of the clay liners was quantified in terms of strain measurements. The actual hydraulic conductivity of the clay liners in response to the imposed strains was not tested.

1.4 METHODOLOGY

This study consisted of a literature review, finite element analysis and physical modelling. Firstly, the behaviour of clay in fracture, the properties of geogrids and the behaviour of geogrid reinforced clay liners were investigated from literature. The literature review was followed by four-point bending tests

on clay beams. The four-point bending beam test is a common flexural test that was used to investigate the behaviour of the clay beams during flexural fracture. These bending beams are considered to be representative of the model clay liners later used in the centrifuge tests. However, before the centrifuge tests were conducted, the problem was modelled using finite element (FE) analyses. The results of the FE analyses was used to optimise the position of reinforcement in the model liner to give insight into variables that are fundamental to the behaviour of a geogrid reinforced clay liner. Based on the results of the FE analyses a centrifuge test was designed to further study the behaviour of a reinforced liner subject to differential settlement. Five centrifuge tests were done modelling both reinforced and unreinforced liners. Finally, the results of the bending beam tests, FE analyses and centrifuge modelling were aggregated to formulate recommendations on the optimal reinforcement positions for clay liners subject to differential settlement.

1.5 ORGANISATION OF THE THESIS

The thesis is structured as follows:

Chapter 1: The current chapter, an introduction to the thesis.

Chapter 2: A review of the literature available on the topic.

Chapter 3: The methodology, results and analysis of the bending beam tests.

Chapter 4: The finite element model, optimisation techniques implemented and the corresponding optimal positions for geogrid reinforcement.

Chapter 5: The methodology, results and analysis of the bending centrifuge tests.

Chapter 6: The conclusions of the study and recommendations for further study.

References.

Appendix A: Constructs used to calculate the c_v values from the oedometer results.

Appendix B: Details of the penetrometer testing.

Appendix C: Additional calculations to interpret the results of the double reinforced liner.

Appendix D: Scaling of the strain fields.

Appendix E: Additional strain fields for the centrifuge tests.

Appendix F: Additional histograms of strain distribution for the centrifuge tests.

CHAPTER 2 LITERATURE REVIEW

This chapter explores the current understanding of geogrid reinforced landfill liners subject to differential settlement. The literature review commences with a brief overview of landfill design (Section 2.1). Subsequently, in Section 2.2 the settlement of municipal solid waste (MSW) is discussed. The settlement of the MSW can result in fracture of the clay liner. Consequently, the investigation of the fracture behaviour of clay liners is investigated through full scale tests, elements tests and centrifuge tests (Section 2.3).

To reduce the cracking of the clay liners geogrid reinforcing can be used. In Section 2.4 the principle of geogrid reinforcement is briefly discussed. Amongst others, the factors influencing the bond between clay and a geogrid is explored. A number of authors investigated reinforced clay liners in the geotechnical centrifuge as discussed in Section 2.5.1. Some of these authors developed numerical models of the centrifuge tests as discussed in Section 2.5.3. Finally, the limited research available on optimal geogrid placement is discussed in Section 2.6.

2.1 LANDFILL DESIGN

The purpose of a landfill is to store waste material in such a manner that no harm befalls the environment. Air, water and soil pollution are all possible consequences of improper waste storage. To prevent the pollution a barrier is usually erected between the waste in the landfill and the surrounding environment (Jessberger & Klos, 1992). A typical landfill consists of four key components: 1) an impermeable layer (barrier), 2) a drainage layer, 3) an interface layer between the drainage and the waste and 4) a cover over the waste after the landfill has been completed (Viswanadham & Mahesh, 2002). The first three components forms part of the liner system. Two typical examples of lining systems is shown in Figure 2.1. Figure 2.1a shows the lining system required by South African legislation (DEA, 2013)

for a landfill used for the disposal of general waste, including MSW. In Figure 2.1b the lining system required for the disposal of hazardous waste is shown (Class A landfill).

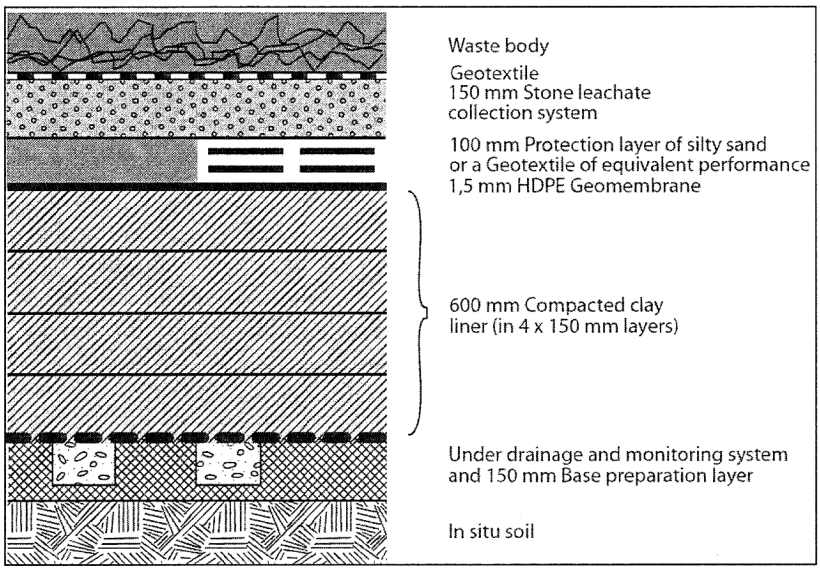

(a)

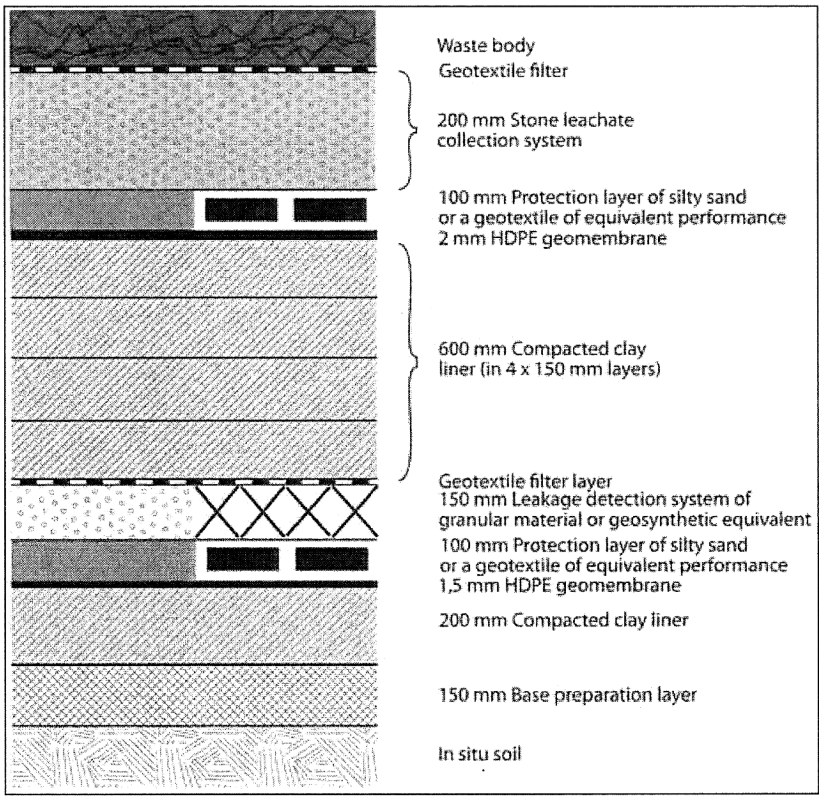

(b)

Figure 2.1: Typical liner designs for a) Class B landfill, b) Class A landfill (DEA, 2013).

Of significance for the current study is that a 600 mm clay liner (or equivalent geosynthetic clay liner)

is required for both of the liners designs shown. The final capping liners also require a similar layer of clay. It is this clay liner that cracks when the underlying soil (or waste in the case of a piggyback landfill) settles.

In a piggyback landfill the lining system shown in Figure 2.1 is constructed on a foundation of old, decomposing waste (the decommissioned landfill). A number of authors have presented their design experiences for this problem (Leung & Law, 1994; Richardson & Allen Marr, 1996; Stulgis et al., 1996; Badu-Tweneboah et al., 2009). These designs address both the ultimate limit state (ULS) and serviceability limit state (SLS) failures of the landfill. At ULS complete failure of the landfill will occur, such as a slope collapse. After an SLS failure the landfill would still be stable but will not be able to fulfil its intended function, e.g. fracture and leaking of the lining system (Jones & Dixon, 2005). Various factors might cause a SLS failure: dessication cracking, frost, chemical attack by the leachate and of special importance in piggyback landfills, distortion of the liner due to differential settlement of the underlying waste (Jessberger & Stone, 1991).

2.2 SETTLEMENT OF MUNICIPAL SOLID WASTE

Municipal solid waste (MSW), commonly known as rubbish or refuse, is a broad term encompassing all discard generated by households. MSW is distinct from hazardous waste, garden waste, packaging, tyres and building waste. A number of studies has investigated the engineering strength properties of MSW (**Zekkos2005**; Kavazanjian et al., 1995; Jones & Dixon, 2005). Of greater interest to the current study is the deformation characteristics of MSW and the associated settlement that occurs.

As with most MSW properties, the deformation characteristics of MSW is highly variable and time dependent. Immediately after placement, primary settlement due to mechanical compression of the waste occurs. This is followed by secondary settlement and physical creep as the waste degrades (Charles, 1991; Stulgis et al., 1996). From the results of a number of earlier studies Richardson & Allen Marr (1996) found that primary compression of the waste occurred during the first 8 weeks after placement. During this period the compression coefficient ranged from 0.1 to 0.4 as defined below. After eight weeks, the secondary settlement commenced and the compression coefficient ranged from 0.01 to 0.02. The compression coefficient (C_c) appears to depend on the magnitude of the applied load

(McDougall & Pyrah, 2001) and is analogous to that found in soil mechanics :

$$C_C = \frac{\Delta H/H}{\log(P_2/P_1)} \tag{2.1}$$

where H is the thickness of the compressible material and P the applied stress.

Similarly, Edgers et al. (1992) found a high initial rate of settlement for MSW during the first 14 weeks after placement. Thereafter, the settlement rate decreased as secondary settlement commenced. However, as the secondary compression occurs over a significantly longer period the magnitude of settlement is much greater. The total settlement of the liner can be anywhere between 25 - 50% of the landfill's height (Edgers et al., 1992; Ling et al., 1998). A summary of the settlement of 24 landfills over a period of approximately 19 years is shown in Figure 2.2.

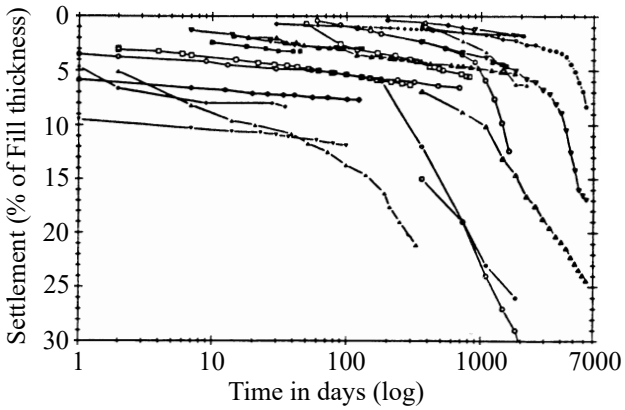

Figure 2.2: Landfill settlement over time as a percentage of initial thickness (Edgers et al., 1992).

The primary and secondary compression of the waste could result in differential settlement of the landfill body over time. Localised settlement can also occur in a landfill due to the sudden collapse of large objects (Chen et al., 2009). The "rusted refrigerator assumption" is conventionally used to estimate the size of such localized subsidence. It is assumed that, should an old refrigerator in the landfill suddenly collapse, a void of 1.8 m in diameter will form (Carroll & Chouery-Curtis, 1991; Stulgis et al., 1996). These two mechanisms, localized subsidence and differential settlement, as well as temperature fluctuation in the liner and shrinkage of the clay, result in the distortion and fracture of clay liners (Fang, 1994; Liang et al., 1994). The present study will focus only on the effects of settlement.

2.3 FRACTURE BEHAVIOUR OF CLAY

Firstly, an overview of fracture mechanics is given in Section 2.3.1. This is followed by a discussion of a full scale bursting test of a clay liner by Gourc et al. (2010) in Section 2.3.2. In Section 2.3.3 the results of a number of element tests conducted on clay beams are presented. Finally, in Section 2.3.4 the behaviour of unreinforced clay liners subject to differential settlement in a centrifuge is discussed.

2.3.1 An overview of fracture mechanics

The fracture behaviour of a clay liner subject to settlement can be understood by considering its potential energy. Similar to a ball that rolls to the bottom of a hill, the potential energy stored in a clay beam will always tend to the lowest possible state. Only once it reaches this state will it be in equilibrium. Most materials are riddled with defects or micro-cracks. As the liner settles, bending stress will be generated in the clay. Once the stress in the clay is large enough, the micro-cracks will grow to macro-cracks, releasing strain energy and reducing the potential energy of the material. Consequently, cracks in linear elastic materials grow spontaneously, without any external input, once the tensile strength is reached. However, in a ductile material such as clay, crack growth does not occur spontaneously. In ductile materials a number of energy sinks are present that absorbs the energy released during fracture, retarding crack growth (Hallett & Newson, 2001).

The first breakthrough in the understanding of fracture mechanics was in a paper by Griffith (1920). This paper forms the basis of linear elastic fracture mechanics (LEFM). Even though clay is an elasto-plastic material, the simplicity of LEFM makes it ideal to understand the basic principles of fracture (Fang, 1994).

The Griffith (1920) theory of rupture can be explained as follows. Assume a tensile load is applied to a body of material containing some defects or micro-cracks. In over-consolidated clays these micro-cracks can be present due to a number of different processes such as swelling (Vallejo, 1994). As the body extends under the applied load, potential energy is stored in the form of elastic strain (similar to a spring that is stretched). Once the load reaches a critical value the micro-cracks grow into macro-cracks, forming two new crack surfaces. For the surfaces to form, the cohesive force between the particles on either side of the crack has to be broken. In a clay this cohesive force could be due to

both the electrical charge on the plates and matric suction. Furthermore, as the macro-crack opens, the crack tips displaces, releasing strain energy and lowering the potential energy of the system. Thus, the crack both has an energy sink that absorbs energy (the forming of the surfaces) and an energy source that drives its growth (the strain relaxation and applied load). Consequently, the cracks will continue to grow until all the stored strain energy is released.

The energy associated with a crack in a block of elastic material is shown in Figure 2.3 as a function of crack length. Line O-A illustrates the increase in potential energy as the crack surface area grows with crack length. The decrease in energy as strain is relaxed is represented by line O-C. The sum of the two is line O-B, the net energy of the crack. If the micro-cracks in the block is of length a_i and they grow with δa, the potential energy of the system will increase. Consequently, spontaneous crack growth will not occur if the micro-cracks are of length a_i as the block will always tend towards the lowest possible state of energy. However, if the crack in the block is of length a_c and it grows with δa, the potential energy of the system will decrease. Since further crack growth will continue to reduce the potential energy of the system, the crack will grow until the block is broken apart Griffith (1920). This critical crack length from where spontaneous crack growth will occur is a function of the applied stress and can be calculated as:

$$a_c = \frac{2E\gamma}{\pi\sigma^2} \tag{2.2}$$

where a_c is the critical crack length, E the Young's Modulus of the material, γ the surface energy and σ the applied stress.

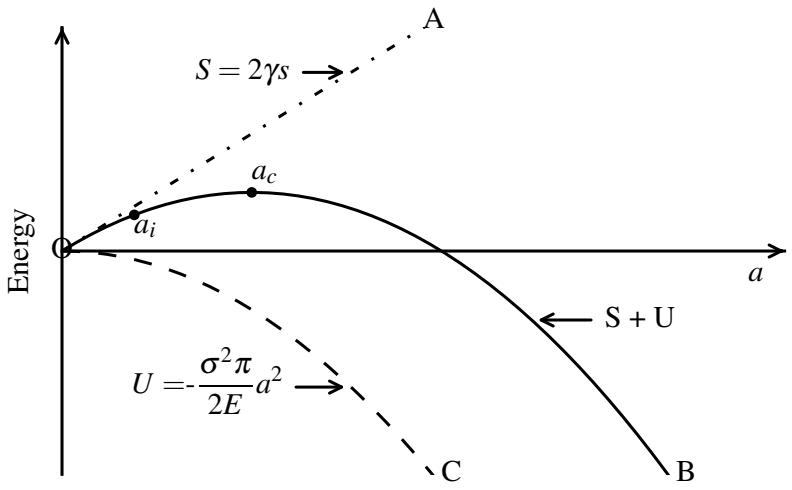

Figure 2.3: The energy balance for crack growth in a linear elastic material (after Roylance (2001)).

To summarise, say a micro-crack of length a_j is present in a body of material. The stress applied to the body can be increased until $a_j = a_c = \frac{2E\gamma}{\pi\sigma^2}$. Once the critical crack length (a_c) equals the size of the micro-cracks (a_j), a macro-crack will form and start to propagate spontaneously (as it decreases the potential energy of the system) until the material failed. This would be a typical brittle failure. This brittle, spontaneous failure only occurs in linear elastic materials.

In any other material the fracture process is slightly more involved. Figure 2.4 shows zones of linear elastic behaviour (E), plastic behaviour (P) and the fracture process or micro-crack zone (M) around a crack in a linear elastic material, elasto-plastic material and quasi-brittle material. In the fracture process zone the material progressively weakens while micro-cracks forms until it is weak enough for micro-cracks to aggregate into the macro-crack (Karihaloo, 1995). Turner & Kolednik (1994) divided this process into two stages. During the first stage plastic deformation and damage occurs, preparing the material for the second stage. In the second stage the macro-crack open up, driven by the release in strain energy. Both the plastic deformation and micro-crack growth acts as additional energy sinks not found in linear elastic material. The behaviour of overconsolidated clay falls between the plastic and the quasi-brittle material.

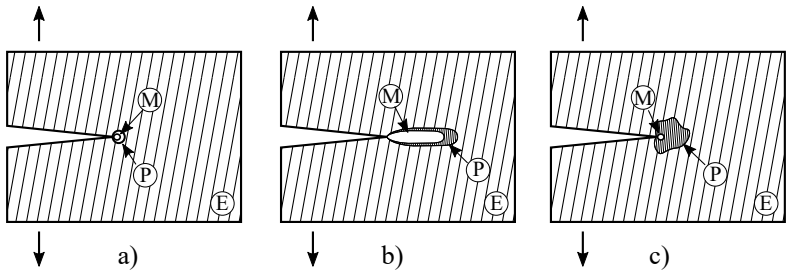

Figure 2.4: Fracture in a) an elastic material b) a quasi-brittle material c) a ductile material. *E* indicates an elastic zone, *P* a plastic zone and *M* a zone of micro-cracks (after Karihaloo, 1995).

Another energy sink additional to those in Griffith's model is friction between the two surfaces of the crack. All the cracks discussed to this stage were so-called Mode I cracks (Figure 2.5a). In Figure 2.5b & c two other types of cracks, Mode II (sliding or shearing) and Mode III (tearing), are shown. Due to the friction between the surfaces pure Mode II and Mode III cracks cannot propagate continuously, only under mixed mode fracture (Mode I & II or Mode I & III) will the cracks propagate (Karihaloo, 1995).

These additional energy sinks (plastic deformation, micro-crack growth and friction) are the reason why cracks in a ductile material, such as clay, do not spontaneously grow as predicted by the Griffith

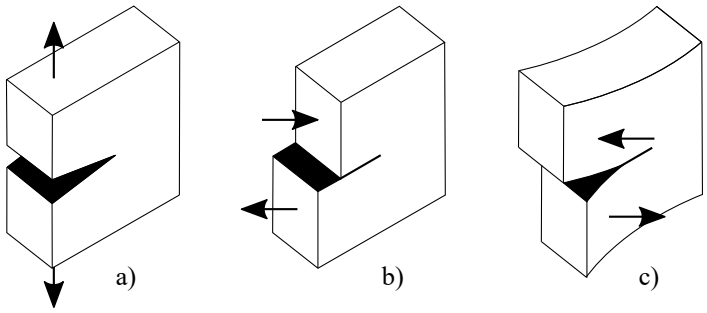

Figure 2.5: Different modes of cracks: a) Mode I crack (tensile), b) Mode II crack (sliding/shear) and c) Mode III crack (tearing) (after Karihaloo, 1995).

theory for elastic materials. For a Griffith material spontaneous crack growth occurs once the energy supplied by the source equals that absorbed by the sink. In a clay, due to the plastic deformation and micro-cracks, energy has to be continuously added to the material for crack growth, i.e. the work done on the material has to increase (Hallett & Newson, 2001). Consequently, clay liners do not suddenly fail catastrophically.

The emergence of the micro-crack growth can be identified from the load-deflection curve of the material. In Figure 2.6 a typical load-deflection curve of a material in tension is shown. From O to A the behaviour is linear. Once micro-cracking damages the material (A) it supports a smaller load increment for a given displacement increment (i.e. it becomes non-linear). When the curve reaches its peak (B) the macro-cracks opens (Turner & Kolednie, 1994; Karihaloo, 1995). If the material is elastic-plastic (Figure 2.4c) the load will remain constant as the deflection increases (B-C). For a quasi-brittle material (Figure 2.4b) the load will drop and finally plateau (B-D).

The cracks, both micro and macro, reduces the hydraulic conductivity of the liner, compromising its ability to perform its intended function (Liang et al., 1994). The macro-cracks decrease the drainage path length of the clay, while the micro-cracks increases the permeability. For a saturated, cracked clay there is a direct relationship between the permeability and the void ratio of the soil on a micro-mechanical level (Fredlund et al., 2010):

$$k = \frac{2}{fA^2} \cdot \frac{e^3}{1+e} \tag{2.3}$$

where k is the permeability (m/s) at a reference temperature of 20°C, f the angularity of the particles, A the specific surface area of the grains (mm^2/mm^3) and e the void ratio. Thus, a small increase in void ratio, say due to the forming of micro-cracks, will result in a significant increase in permeability.

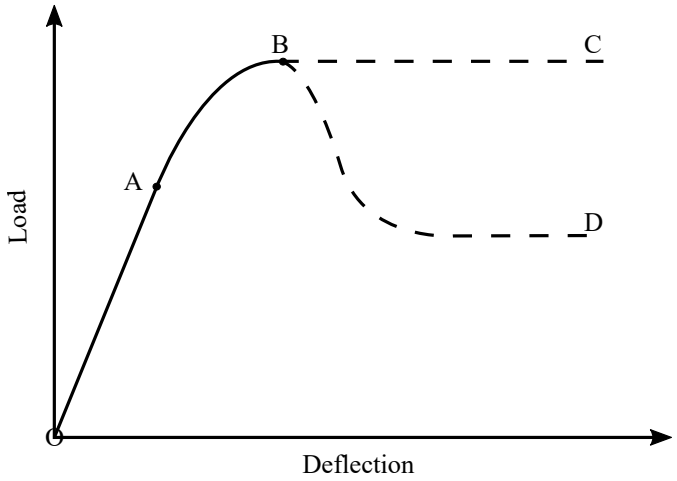

Figure 2.6: Typical tensile load-deflection curve of a material that cracks. B-C is an elastic-plastic material while B-D is a quasi-brittle material.

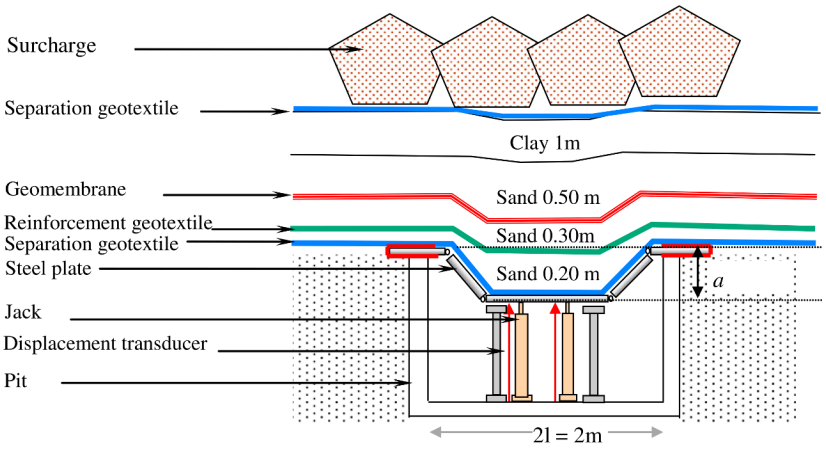

Figure 2.7: Model setup for full scale field bursting tests (Gourc et al., 2010).

2.3.2 Full scale fracture tests

A method to study the fracture behaviour of clay liners is full scale bursting tests. Gourc et al. (2010) conducted a series of such tests. A compacted clay liner was placed on top of a sand layer spread over hinged steel plates, supported by a series of four hydraulic jacks placed inside a 2x2 m concrete pit (Figure 2.7). As the jacks pushed upwards, the clay bent, simulating a burst of the liner. It was in effect a large scale, inverted, bending beam test. Three of these full scale test were done: two for a barrier of thickness 0.7 m and moisture content $(w) = OMC + 2\%$ and one for a thickness of 0.8 m and $w = OMC + 3.5\%$.

In the first and second tests a number of macro-cracks formed at the centre of the liner (see Figure 2.8a). For the third test, at a higher moisture content, only one macro-crack formed (see Figure 2.8b). These results would suggest that at lower moisture contents the clay is brittle, while at higher moisture contents the failure is ductile. The higher plasticity of the wetter clay allowed it to flow during bending, rather than simply cracking.

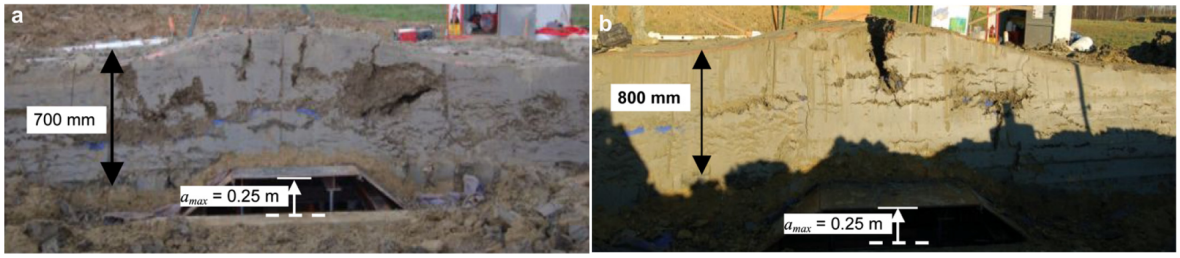

(a) **(b)**

Figure 2.8: Tensile cracks observed in full scale bursting tests of clay liners: a) $d = 0.7$ m & $w = OMC + 2\%$ and b) $d = 0.8$ m & $w = OMC + 3.5\%$ (Gourc et al., 2010).

2.3.3 Element tests of clay fracture behaviour

Full scale fracture tests of clay liners are expensive and the results are more prone to scatter. Consequently, several authors reverted to element testing and centrifuge modelling to investigate the fracture behaviour of clay liners. In this section, the results of a number of element tests are presented.

Numerous studies on the fracture mechanics of concrete has shown that the size of the specimen has a significant influence on the observed fracture behaviour. Small specimens tend to behave ductile while large samples of the same material failed in a more brittle manner (Karihaloo, 1995). There are a number of similarities between concrete and soil: a) both are strong in compression, b) both are weak in tension and c) the liquid bridge model for suction in soil (Kim & Sture, 2008) shares a number of similarities with the model used to calculate the strength of two cemented soil grains (Mitchell & Soga, 2005). Furthermore, the difference in behaviour between large and small concrete samples lies in the stress distribution through the sample and not the stress-strain relationship (Karihaloo, 1995). Consequently, it can be assumed that the fracture behaviour of small clay beams will not be fully representative of that of clay liners, similar to concrete. However, these element tests are some of the only means available to investigate the fracture behaviour.

The direct tensile test is fundamentally the most representative of the tensile behaviour of a soil (Ajaz & Parry, 1975). However, the direct tensile test is temperamental with samples prone to failing at the clamps due to stress concentrations. Consequently, a number of authors used bending beam tests to study the fracture behaviour of clays (Ajaz & Parry, 1975; Thusyanthan et al., 2007; Plé et al., 2012). Even though the four point bending test is not a direct tensile test, it is representative of a clay liner in field conditions where direct tension is rare. Furthermore, the bending beams of Ajaz & Parry (1975), Thusyanthan et al. (2007) and Plé et al. (2012) all showed distinct Mode I (pure tension) fractures in the centre of the beam. Thusyanthan et al. (2007) found that only at high effective stresses did the failure become a mixed Mode I and Mode II fracture. Thus, the bending beam test can give an accurate portrayal of the tensile behaviour of the clay.

In Figure 2.9 a simple schematic of the four-point bending test on a clay beam is shown. The lengths b and c can either be equidistant (Thusyanthan et al., 2007; Plé et al., 2012) or a can be half the distance of c (Ajaz & Parry, 1975). As there are some boundary effects associated with the loading bars, it might be preferable to keep them further apart and thus use the equidistant arrangement. The stress at failure for a setup where $b = c$ can be calculated as:

$$\sigma_t = \frac{Pl}{bd^2} \tag{2.4}$$

where b is the width of the beam.

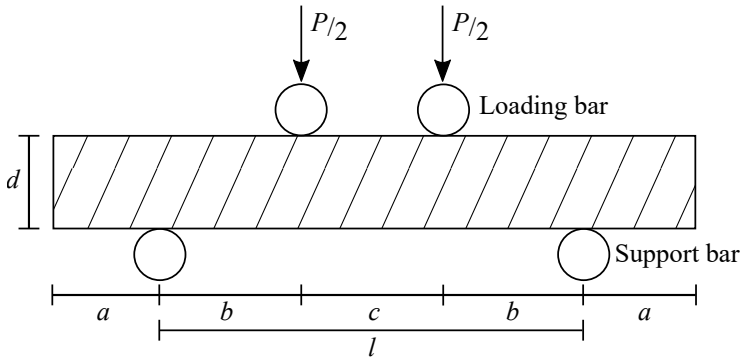

Figure 2.9: Typical setup for a four point bending beam test.

The loading rates and sample size for the bending beam tests by Ajaz & Parry (1975), Thusyanthan et al. (2007) and Plé et al. (2012) are summarised in Table 2.1. In Table 2.2 the tensile strain at fracture for a number of different bending, direct and full scale bursting tests is summarized. Ajaz & Parry (1975) found that bending beam tests reported a higher tensile strain at failure when compared to

equivalent direct tension tests. This difference could be due to the clamps of for direct tensile tests inducing strain concentrations on the samples.

Table 2.1: Geometry and loading rate of some bending beam tests conducted on clay.

Test	Loading method	Sample size[i] [mm]
Ajaz & Parry (1975)	Manual load control	$228.6 \times 51 \times 51$
Thusyanthan et al. (2007)	Load control: 19.6 N every 3 min Displacement control: 0.23 mm/min	$240 \times 80 \times 80$
Plé et al. (2012)	Displacement control: 0.2 mm/min	$300 \times 100 \times 100$

[i] The longest dimension shown is equal to l, the distance between the support bars.

Table 2.2: A summary of the strain at fracture initiation for a number of element and full scale fracture tests of clay.

Test	Clay type[2]	Moisture content [%]	Dry density [kN/m^3]	Strain at fracture[%]
Ajaz & Parry (1975)*	Gault clay	19.4 - 30.37	13.1 - 14.1	0.08 - 0.31
Ajaz & Parry (1975)+	Gault clay	22.2 - 31.5	13.6 - 14.4	0.56 - 1.7
Edelmann et al. (1996)o	-	-	-	0.2 - 1.3[1]
Thusyanthan et al. (2007)+	K: 100%	-[4]	-	~0.57[4]
Gourc et al. (2010)o	K: 50%, I: 40%, C: 10%	19 - 20.5	17.2 - 17.3	1.5 - 2.5 [5]
Plé et al. (2012)+	K: 50%, I: 40%, C: 10%	14.5 - 19	17.0 - 17.6	0.1 - 0.5

* Direct tension tests; + Bending beam tests; o Full scale bursting tests.
[1] C_K: Kaolin, C_I: Illite, C_C: Chlorite. [2] Values from Gourc et al. (2010).
[3] The suction in the beams was varied. [4] From $\varepsilon_{crack} = 14 s_i^{'-0.5}$ where $s_i^{'}$ is the initial effective consolidation pressure, $s_i^{'}$ = 600 kPa and was used to calculate and approximate lower bound.
[5] Maximum local strain.

Gravimetric moisture contents for some the tests found in literature are presented in Table 2.2. However, the degree of saturation of the samples would have been a more insightful measure. As a number of authors dried the samples out, or mixed it to the correct moisture content, there is reason the believe that not all the results in Table 2.2 are for fully saturated samples. Consequently, the tensile behaviour would have been governed by matric suction and the results should be viewed in the context of the field of unsaturated soil mechanics.

The unsaturated behaviour could be the cause of the discrepancy in behaviour reported by some authors. Plé et al. (2012) reported that in clay close to saturation the compaction energy did not have an influence on the tensile strength of the soil. However, for the direct tensile tests by Tang et al. (2014) sample density made a significant difference as expected (Rogowski, 1964; Kim & Hwang, 2003; Kim & Sture, 2008).

2.3.4 Centrifuge tests of unreinforced clay beams

As an alternative to the element tests discussed in the previous section a number of authors investigated the fracture behaviour of unreinforced clay liners with centrifuge modelling (Section 2.3.3). Viswanadham & Rajesh (2009) found good agreement between the strain at fracture as measured in the centrifuge and those from flexural tests conducted on compacted clay beams. Centrifuge modelling entails building a scale model of a prototype (full scale) problem and artificially increasing the gravitational acceleration of the scale model. By increasing the acceleration the stress in the scale model can be raised until it matches the stress expected in the prototype. Consequently, the failure mechanisms observed in the scale model is assumed to represent those found in the prototype. A more detailed explanation of centrifuge modelling can be found in Section 5.1.

In Table 2.3 a number of centrifuge tests of unreinforced clay liners subject to differential settlement are summarised. In the remainder of this section, each of the tests are discussed. The symbols used in Table 2.3, as well as the remainder of the report, are defined in Figure 2.10.

Jessberger & Stone (1991) modelled subsidence below a simple clay liner with and without overburden pressure. Two different liners were constructed: 1) a pure kaolin liner and 2) a "fine/coarse" mixture of sand, silica flour and bentonite. The pure kaolin liner was prepared to 95% of the Proctor compaction density by consolidating it to 630 kPa. This compaction specification was assumed to be typical for compacted clay liners.

The "fine/coarse" mixture was scaled to have a grading parallel to the typical clay used in prototype liners. Two different preparation methods were used for the these liners. Firstly the clay was prepared at optimum moisture content (OMC) and loaded with a 100 kPa pressure for three days. As an alternative the dry material was vibro-compacted in four layers and saturated afterwards. The preparation technique did not appear to have a significant influence on the behaviour of the liner.

The completed model liners were placed on a sacrificial sand layer spread over a trap door. A piston supported the trapdoor. As the piston was lowered, the sand settled and the liner on top distorted. The permeability of the liners was measured and the cracks were monitored with digital images.

Table 2.3: Summary of a number of centrifuge tests conducted on unreinforced clay liners subject to subsidence.

Author	Acceleration [g]	Liner thickness (d) [m] [i]	Prototype length (L) [m]	Trough length ($2l$) [m]	Displacement mechanism	Material [ii]	Surcharge (σ_v) [kPa]	Variables considered
Jessberger & Stone (1991)	50	1.75, 2, 2.25	32.9	4.36*	Piston lowering flaps	C_K: 100% and S_C: 64%, F: 22%, C_B: 14%	0, ~40	Liner material, thickness and overburden pressure
Viswanadham & Mahesh (2002)	150	1.5, 2.25, 3, 3.75	18	7.5	Dissolving of salt	C_K: 100%	20, 30, 40, 80	Consistency index, Liner thickness, Overburden pressure
Viswanadham & Rajesh (2009)	40	0.6, 1.2	28.8	~16	Piston lowering flaps	S: 20%, C_K: 80%	12.5, 25	Liner thickness, overburden pressure
Gourc et al. (2010)	12.5	0.7	9.375	4.5	Piston extending flaps	S: 20%, M: 34%, C: 46%	0	Validation test
Richards & Powrie (2011) [ii]	40	0.6	22 [iii]	11[ii]	Piston lowering	S_F: 70%, S_C: 10%, C_B: 20%	~26.49	Discontinuity type, geometry, thickness of fill below the liner

[i] All dimensions are in prototype scale [ii] C_K: Clay (Kaolin) C_B: Clay (Bentonite) F: Silica Flour M: Silt S_C: Coarse sand S_F: Fine sand
[iii] Only half of the settlement trough was modelled.

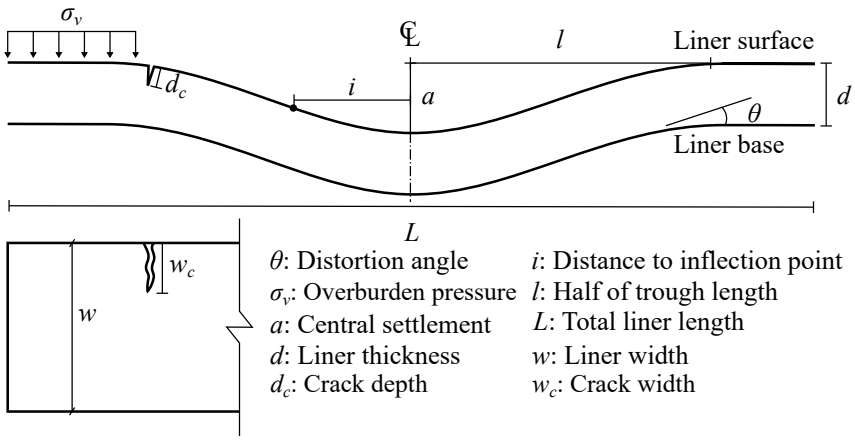

Figure 2.10: Standard symbols used to describe the geometry of clay liners subject to settlement.

Significant tensile cracks opened where the unreinforced liner hogged in the absence of any overburden pressure (see Figure 2.11a). At a distortion angle of 16 ° (refer toFigure 2.10) the cracks extended all the way through the kaolin liner, despite the liner thickness. However, a preliminary study did find that the distortion at which these cracks initiated differed with liner thickness (Jessberger et al., 1989). The cracking pattern observed agrees with the failure mechanisms visible in the full scale tests of Gourc et al. (2010).

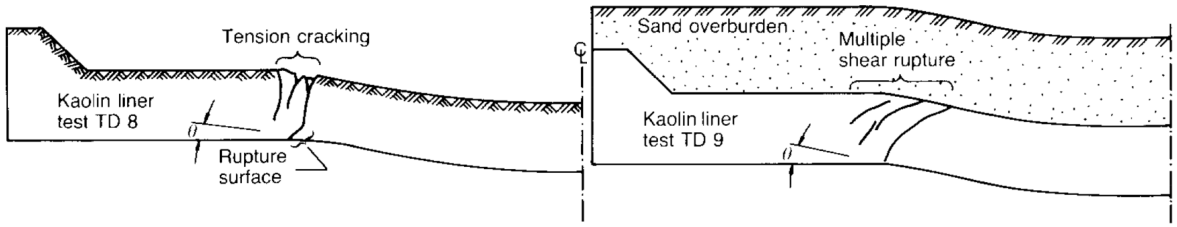

Figure 2.11: Crack types observed in kaolin liners subject to differential settlement a) with overburden pressure and b) without overburden pressure (Jessberger & Stone, 1991).

When overburden pressure was applied to the kaolin liners, no tensile cracking occurred. Consider Figure 2.12 where the clay liner is assumed to behave similar to an elastic beam. As the liner without overburden distorts, tensile (negative) stress is generated by the bending moment (σ_B) at the surface . However, if overburden pressure (σ_O) is applied, the net stress in the liner remains positive. Before the liner can bend sufficiently for the stress to become tensile, stress localisation occurs and shear ruptures form. These curved shear ruptures are illustrated in Figure 2.11b.

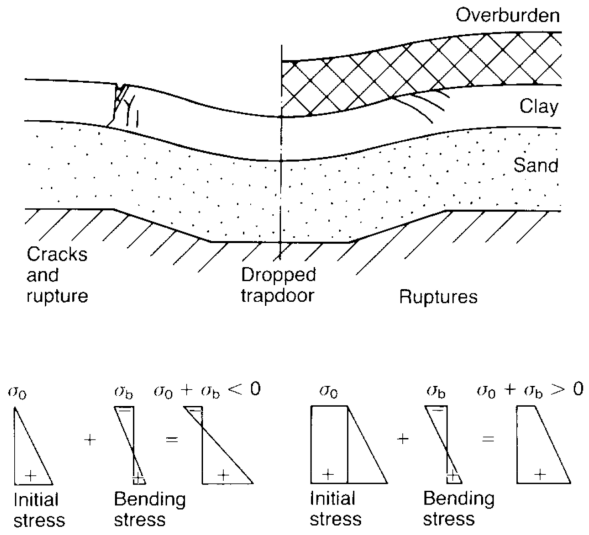

Figure 2.12: Elastic strain distribution in a clay liner with and without overburden pressure (Jessberger & Stone, 1991).

The shear ruptures observed are not simple Mode I, II or III cracks (Figure 2.5), but a progressive failure due to a number of Mode II discontinuities. This process is illustrated in Figure 2.13. Firstly (Stage i), so-called Riedel slip discontinuities develop at an angle $\phi/2$ to the applied shear force. After a while, thrust discontinuities form at an angle of 0 to $\phi/2$ to the shear force (Stage ii). Finally, in Stage iii, the Riedel and thrust discontinuities aggregate and form a continuous shear surface or rupture (Vallejo, 1994).

A theoretical calculation by Richards & Powrie (2011) showed that such a shear rupture (assuming an increase of void ratio from 0.5 to 0.8) would increase the permeability in that region five fold (Equation 2.3 predicts a 3.5 times increase). However, a change in permeability from $1 \cdot 10^{-9}$ m/s to $5 \cdot 10^{-9}$ m/s would have only a small effect in practice. Likewise, the permeability measurements by Jessberger & Stone (1991) found that these shear ruptures had no significant effect.

It was mentioned earlier that Jessberger & Stone (1991) also constructed model liners from sand, silica flour and bentonite. These liners were found to be more resilient against cracking than the pure kaolin liners. The exact mechanism for this behaviour is not clear. However, it was postulated that the mixture was more ductile due to the clay flowing around the sand particles. In a similar manner the wetter, more ductile liner by Gourc et al. (2010) cracked significantly less (Figure 2.8b).

Viswanadham & Mahesh (2002) modelled a similar problem to Jessberger & Stone (1991) at a higher

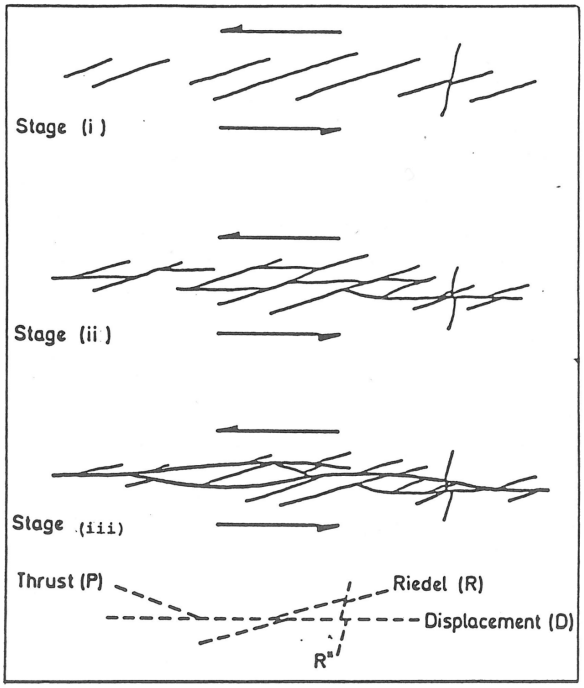

Figure 2.13: Progressive formation of a shear surface (Vallejo, 1994).

acceleration in a smaller centrifuge. Subsidence was induced by dissolving salt in a compartment below the liner. The clay liner was prevented from completely collapsing into the cavity by a metal stopper. The influence of overburden pressure, liner thickness and consistency (I_c) of the clay were investigated.

As with the experiments of Jessberger & Stone (1991), it was found that an increase in overburden pressure suppressed the occurrence of tensile cracks in the liner. Figure 2.14 illustrates how both the final crack width (w_c) and depth (d_c) decreased with an increase in overburden pressure. The fracture pattern also changed from wide continuous cracks to a scattering of short discrete ruptures. At high overburden pressure (40 kPa and greater) net tensile stress in the liner is not possible and shear rupturing takes place (as observed by Jessberger & Stone (1991)).

Viswanadham & Mahesh (2002) also varied the prototype thickness of the liners between 1.5 m and 3.75 m. As the thickness increased, both crack depth and width followed suit (see Figure 2.15). Interestingly, crack size normalised by liner thickness (d_c/d,w_c/d) decreased with an increase in liner thickness. Thus, as the thickness of the liner increased, the relative area of the liner that had cracked decreased.

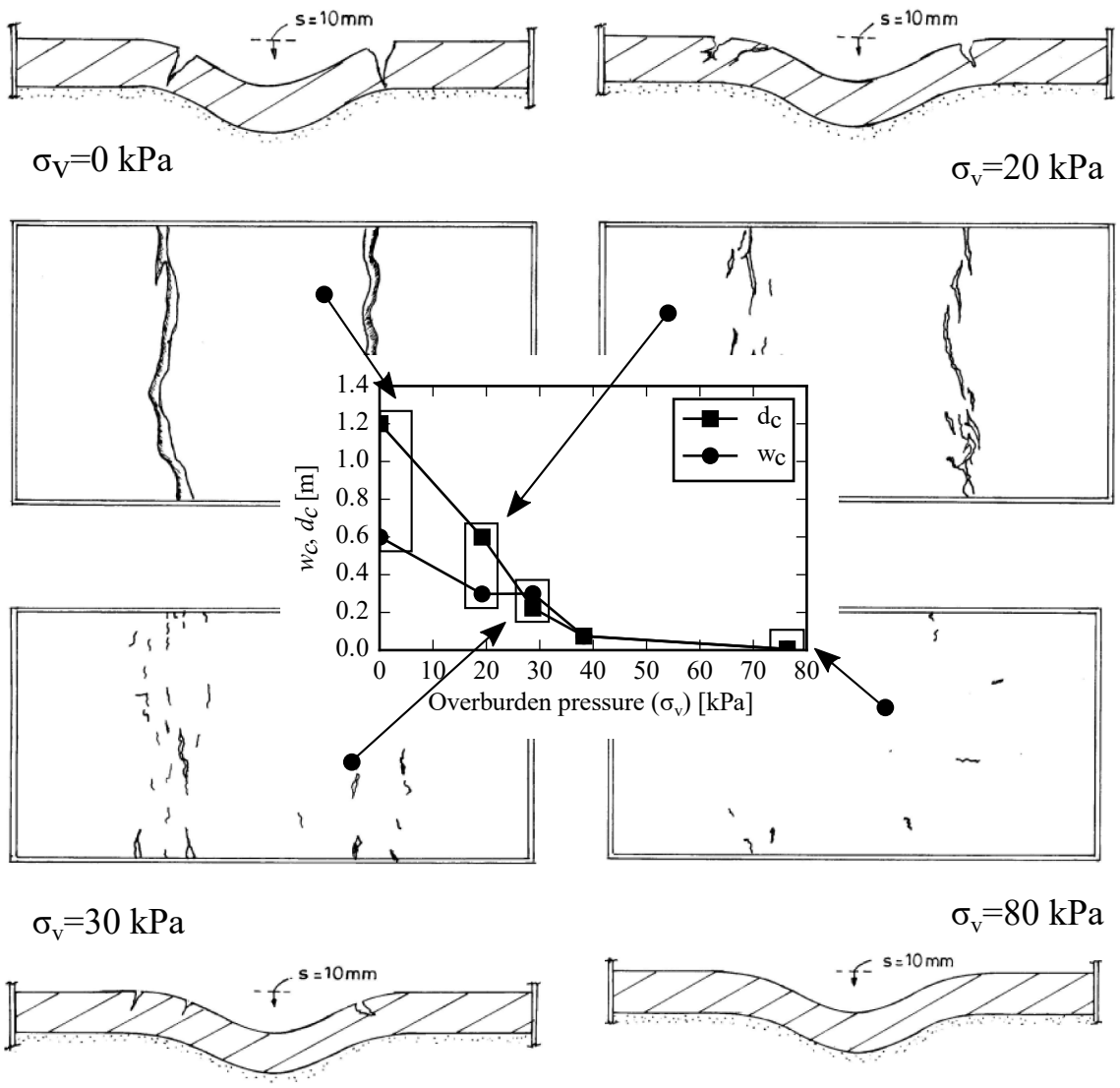

Figure 2.14: Effect of overburden pressure (σ_O) on crack width (w_c) and depth (d_c), for a 1.5 m thick liner (adapted from Viswanadham & Mahesh (2002)).

The effect of liner thickness on the fracture behaviour can be explained by the definition for strain in a bending liner (Viswanadham, 1996):

$$\varepsilon_{of}(x) = \varepsilon_{\Delta l}(x) + R_{of}\kappa(x)d, \qquad \kappa \approx \frac{d^2 s}{dx^2} \tag{2.5}$$

where ε_{of} is the strain in the outer fibre of the liner, $\varepsilon_{\Delta l}$ is the strain due to elongation, R_{of} the so-called neutral layer coefficient, d the thickness of the clay liner and κ is the curvature of the liner. Therefore, greater strain occurs at the surface of thicker liners due the increased distance from the neutral axis. This results in larger cracks.

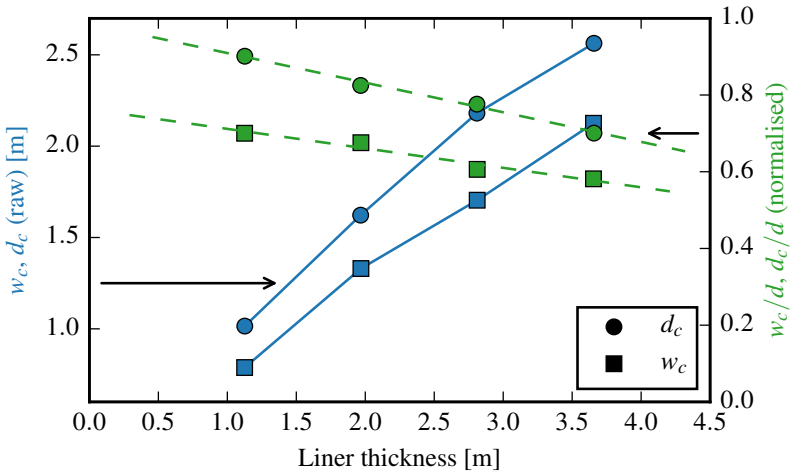

Figure 2.15: Effect of liner thickness on crack width (w_c) and depth (d_c), for a 1.5 m thick liner (adapted from Viswanadham & Mahesh (2002)).

Finally, similar to Jessberger & Stone (1991) and Gourc et al. (2010), Viswanadham & Mahesh (2002) also found that as the moisture content of the liner decreased, the tensile strength of the liner increased. However, the liner became more brittle, resulting in deep wide cracks.

Viswanadham & Rajesh (2009) modelled a similar experiment to Viswanadham & Mahesh (2002) in a slightly larger centrifuge. As with Jessberger & Stone (1991), a hydraulic piston was used to induce differential settlement. Both the influence of liner thickness and overburden pressure on the liners' performance was investigated. *Digital Image Analysis* was used to track the settlement trough and strain in the liner. The infiltration rate through the liner was also measured. As expected, the thickest liner with the highest overburden pressure maintained its integrity (measured in terms of infiltration rate) up to the greatest distortion. Interestingly, the applied overburden pressure was not high enough to completely suppress tensile cracks and induce shear ruptures. The liner still cracked in tension from the top through to the base for all three tests.

Gourc et al. (2010) conducted centrifuge modelling in parallel with the full scale bursting tests discussed in Section 2.3.2. The model configuration was similar to that of Viswanadham & Rajesh (2009). However, rather than moving the piston downwards to induce a settlement trough, it was moved upwards to burst the clay. The burst in the centrifuge was 4.5 m wide (prototype scale), compared to the width of 2 m in the field. Furthermore, the liner used in the centrifuge model was 0.1 m thinner than the comparable full scale model, the moisture content differed by 0.5% and a different type of

clay was used. Nonetheless, since the same distortion level was applied in the centrifuge and the field, the results were presumed to be comparable. The distortion level is defined as the settlement at the trough centre over the trough half width: a/l (see Figure 2.10).

The strain at crack initiation, as well as final crack depth, was in reasonable agreement with the comparable full scale test. The authors concluded that the scaling relationships used to design the centrifuge tests are valid. Furthermore, it was concluded that centrifuge modelling can be used as a valid substitution to full scale tests.

Richards & Powrie (2011) investigated the influence of settlement trough shape on the failure of a clay liner founded on sacrificial sand. In Figure 2.16 the two trough shapes, step and a slope discontinuities, that were modelled are shown. The step discontinuity modelled a rather severe localised subsidence near the liners base, while the slope discontinuity modelled a deeper subsidence that results in a smoother settlement trough. The influence of subsidence on a sloped liner was also investigated. However, liners at a slope falls outside the scope of the present study.

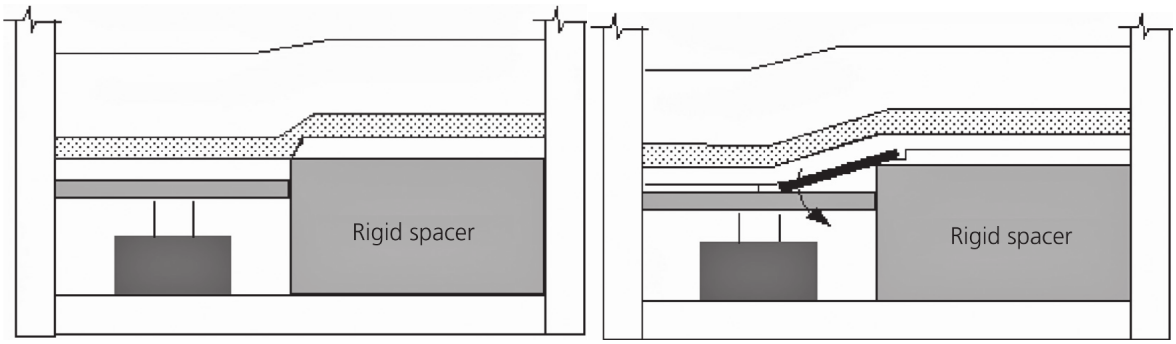

Figure 2.16: Step discontinuity a) and slope discontinuity b) modelled by Richards & Powrie (2011).

As expected, the severe discontinuity (step) resulted in failure at a significantly lower central displacement than for the slope discontinuity. Even at a central displacement of 2 m the slope discontinuity did not fail.

Further modelling varied the depth of the granular layer under the flat liner. As the thickness of the granular layer increased, the settlement through became more smooth and higher central settlement was required for failure. Interestingly, the behaviour of the liners differed even though the distortion

level (a/l) was the same. This would suggest that the distortion level alone is not an adequate measure to compare settlement troughs.

The tests with a step discontinuity were characterised by the liner necking before finally breaking (see Figure 2.17). This behaviour suggests a plastic, rather than brittle elastic material. However, the samples with the lower moisture content failed in a more brittle manner as the photographs in Figure 2.17 shows.

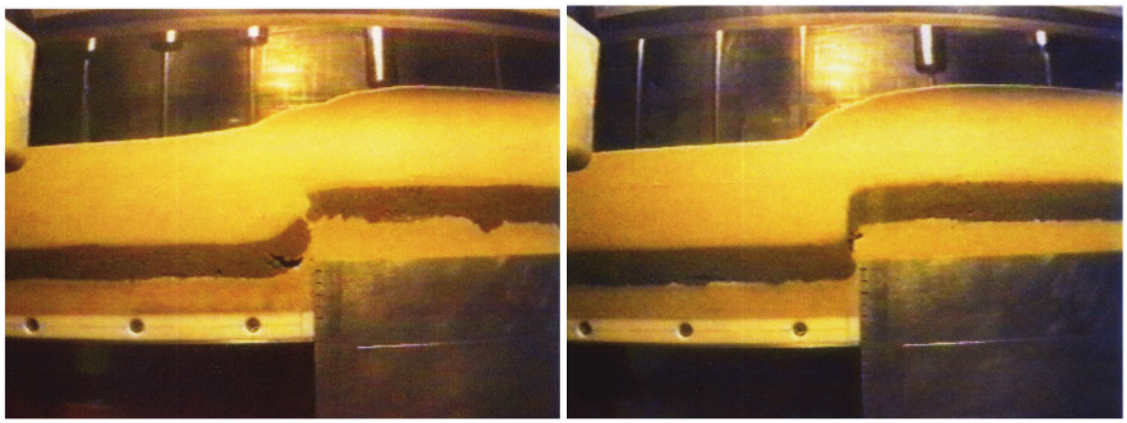

(a) **(b)**

Figure 2.17: Two examples of liners failing in necking a) $w = 24.3\%$ and b) $w = 25.3\%$ (Richards & Powrie, 2011).

2.3.5 A summary of unreinforced centrifuge tests on clay liners

The centrifuge models of the unreinforced clay liners discussed in the previous section all share the four components illustrated in Figure 2.18:

1. Overburden pressure applied (most models).
2. A clay liner.
3. Sacrificial sand layer(s) immediately below the clay liner to reduce shear concentrations in the liner.
4. A mechanism to induce settlement of the centre of the liner.

From the results of the tests the following failure mechanisms can be identified in clay liners subjected to subsidence: a) tension cracking, b) shear ruptures, c) shear failure and d) necking and tension fracture

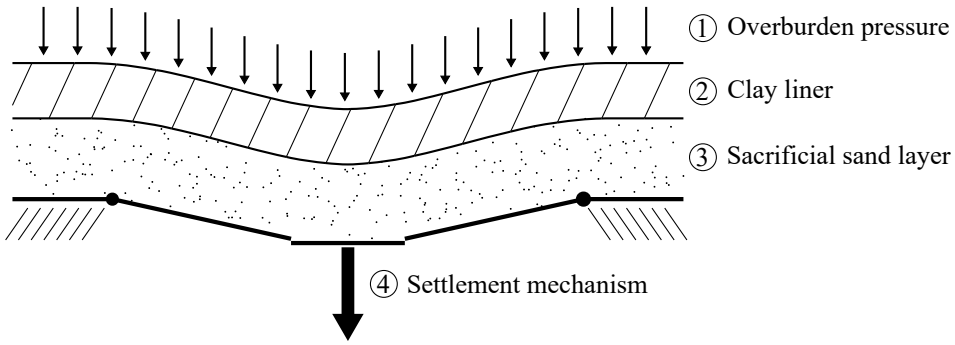

Figure 2.18: Typical features of centrifuge models used to study the influence of subsidence on clay liners: 1) overburden, 2) clay, 3) sacrificial sand and 4) mechanism to induce settlement.

of the liner. These failure mechanisms are illustrated in Figure 2.19. The third failure mechanism (c) is only postulated and has not been observed in the work discussed earlier.

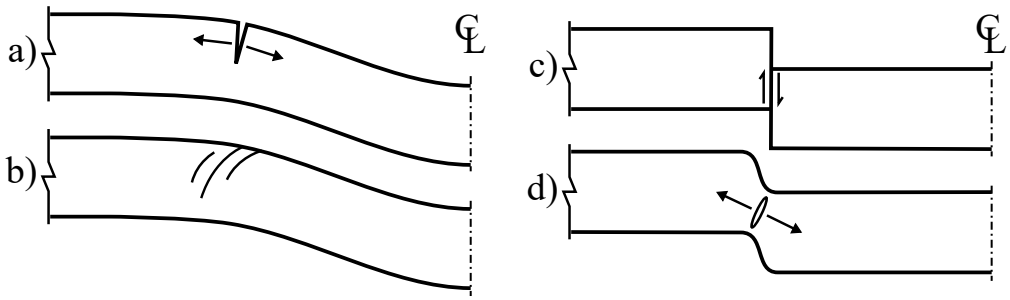

Figure 2.19: Failure mechanisms observed in clay liners subject to local subsidence.

Viswanadham & Jessberger (2005) provided a summary of the factors that influence the failure of these clay liners:

1. Overburden pressure.
2. Shear strength of the material.
3. Stiffness of the clay (both in compression and tension).
4. Tensile strength of the clay.
5. Thickness of the clay.

From the other studies the following factors can be added:

6. Shape of the settlement trough.
7. Moisture content of the liner.

2.4 GEOGRID REINFORCEMENT

Reinforcement can be used to reduce the cracking of the clay liners as the underlying waste settles. One solution is to reinforce the clay liners with geogrids. A geogrid is defined by the International Geosynthetics Society as: *A planar, polymeric structure consisting of a regular open network of integrally connected tensile elements, which may be linked by extrusion, bonding or interlacing, whose openings are larger than the constituents, used civil engineering applications (primarily for reinforcement applications)* (IGS, 2009). Two typical geogrids are illustrated in Figure 2.20.

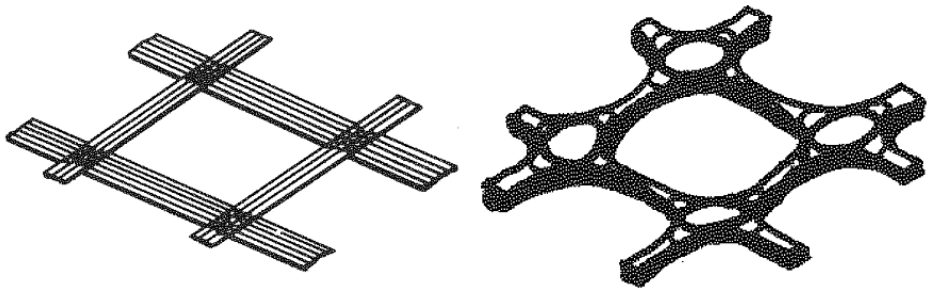

(a) **(b)**

Figure 2.20: Two typical types of geogrids: a) welded strips and b) punched and drawn (Viswanadham, 1996).

Geogrids can be manufactured from numerous types of polymers such as polyester, polyethylene and polypropylene. Once the polymer has been selected a sheet of the polymer can be punched and drawn to form the geogrid. Alternatively, strands of the polymer can be placed in a grid pattern and friction bonded or welded together. Each of the different materials and manufacturing processes result in geogrids with different physical and mechanical properties. Arguably, the four most significant physical and mechanical properties of a geogrid are:

1. Durability
2. Strength
3. Stiffness
4. Bond.

The durability of geogrids will not be considered in this literature review as the long term behaviour of landfill liners falls outside the scope of this study. Furthermore, the breaking strain of most geogrids is far above the fracture strain of compacted clay. Consequently, even if the strain in the clay was fully

compatible with that in the geogrid, the clay will crack long before the geogrid reaches its failure strain. Thus, the ultimate tensile strength of a geogrid is not relevant for this study.

The two remaining key properties of a geogrid relevant to this study are stiffness and bond. Without the higher tensile stiffness of the geogrid relative to the clay, there would be no reinforcing effect. The geogrid stiffness is usually defined as the secant stiffness modulus (J_{sec}, force per elongation).

The reinforcing effect of the geogrid is the result of two distinct mechanisms. Firstly, the geogrid increases the stiffness of the system, resulting in lower deflection for a given load. As the liner deflects less, the strain, and thus the cracking of the clay, is reduced. In Figure 2.21a a section of a clay liner and a transformed section of a geogrid reinforced liner are shown. The moment of inertia of the reinforced liner is higher than that of the unreinforced clay and thus the reinforced liner will settle less[1]. Less settlement implies lower deformation, thus less strain and cracking.

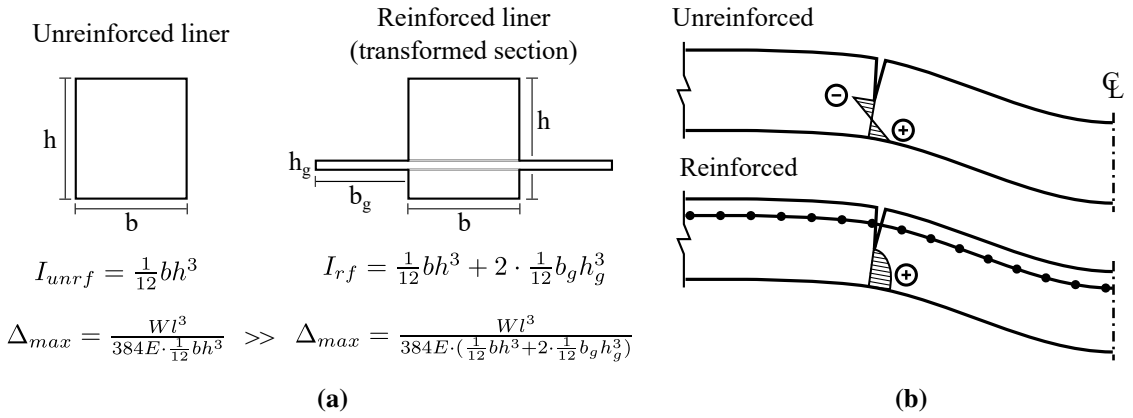

Figure 2.21: Mechanisms of geogrid reinforcement: a) increase in stiffness of the system and b) change in stress distribution at crack tip.

Even if there is no bond between the geogrid and the clay, load will still be transferred from the clay above the geogrid to the geogrid. Consequently, the clay above the geogrid will settle less than when unreinforced. This principle is the basis for most geogrid reinforced liner designs. The geogrid is placed below the clay liner and is assumed to span over a void as a tensioned membrane (Giroud, 1981; Giroud et al., 1990). By considering the arching of the waste, the stress applied to the geogrid can be calculated. Subsequently, the strain and deflection of the geogrid can be determined. As the geogrid is embedded in the clay liner, it is assumed that the strains are compatible. A geogrid is selected to be

[1]The settlement was calculated by assuming that a liner spanning over a void is equivalent to a beam subject to a distributed load, with no rotation nor movement allowed at the ends.

strong enough to bear the applied load and stiff enough to limit the strain in the clay below its fracture strain. Thus, it firstly represents a serviceability limit state design and secondly an ultimate limit state design (refer to Section 2.1).

Secondly, if the geogrid is sufficiently bonded to the clay, it will change the stress distribution at the crack tip. In Figure 2.21b the stress distribution at the tip of a crack in an unreinforced beam is shown. The neutral axis of the liner lies in the centre of the intact part of the beam. Consequently, the stress at the tip of the crack is tensile. As there is a tensile load and a pre-existing crack, all the components required for crack growth are available (discussed in Section 2.3.1). However, in the reinforced liner the neutral axis moves upwards and the tensile stress is carried by the geogrid. Consequently, the intact part of the clay is in compression and crack growth will not occur.

This second mechanism of geogrid reinforcement depends strongly on the bond between the geogrid and the clay. As bond plays a significant role in the behaviour of a geogrid, it has to be properly understood before a model geogrid for centrifuge tests can be selected.

2.4.1 Geogrid - clay interaction

The bond of the geogrid is a broad term encompassing a number of different mechanisms. These mechanisms governing the interaction between soil and geogrids manifests as: 1) direct shear over the reinforcement and 2) pull-out failure (Jewell et al., 1984). For both of these two mechanisms a representative test was developed, i.e. the direct shear test and the pull-out test.

The pull-out test is used to measure the anchorage strength of a geogrid. The geogrid is placed in the centre of a body of soil confined in all planes. One of the horizontal faces of the box has a gap through which the geogrid is pulled. This face is usually lubricated to create a frictionless surface. A number of different configurations can be used to reduce the boundary effects at the face where the geogrid is pulled out from. Additional to the boundary effects, size effects can also influence the results of the test (Palmeira, 2009). Finally, stress can also be applied to the top of the sample.

The anchorage resistance of a geogrid measured in a pull-out test has two components: 1) soil-geogrid interface friction and 2) bearing capacity of the transverse members. The pull-out resistance dropped

with more than 50% when Teixeira (2003) did pull-out tests without transverse members. Similarly, Chang et al. (1977) found that bearing resistance contributed more to anchorage strength than shear resistance.

The shear resistance of geogrid is usually measured in a large direct shear box. The bottom half of the shear box is filled with soil and a geogrid is fixed over it. Thereafter the other half is filled and placed on top of the geogrid. Normal stress is applied to the top half of the box while the box is sheared. The test is best used to determine interface shear strength of a geosynthetic, but it does have some limitations: 1) interface shear stiffness cannot be measured, 2) boundary effects may influence the results and 3) inclined reinforcement is problematic to test (Palmeira, 2009).

An alternative to the direct shear test is the ramp test. In a ramp test a series of geosynthetic and soil layers are placed on top of a hinged platform that is gradually lifted. As the platform lifts the shear force on the interface between the layers increase. Multiple layers of geosynthetics can be tested. This test suited for measuring interface shear at low confining stresses.

Bergado et al. (1993) defined a so-called bond coefficient (interface efficiency or coefficient of interaction) to quantify the effect of the geogrid on the shear strength of the soil at the interface. The bond coefficient is defined as:

$$c_b = \frac{\text{soil-reinforcement resistance}}{\text{soil-soil resistance}} \tag{2.6}$$

That is the ratio between the shear strength of the geogrid-soil interface to the shear strength of the soil-soil interface in a direct shear test. In cohesive soils it would be:

$$c_b = \frac{c_r + \sigma_n \tan \phi_r}{c_s + \sigma_n \tan \phi_n} \tag{2.7}$$

where the subscript r refers to the geosynthetic reinforced soil and s to the unreinforced soil, thus the ratio in shear strengths.

In the remainder of this section some literature on the interaction between geogrids and cohesive soils are discussed with a focus on direct shear tests.

Koutsourais et al. (1991) did an extensive series of direct shear box tests to determine the interface parameters of a number of materials found in landfill linings. The interface friction of a geonet,

geotextiles, geomembranes and a geogrid was measured in sand, kaolin and fly ash. The geogrid (Nicoln Matrex 90) was classified as flexible with large apertures.

The direct shear tests were done for a range of different normal stresses. After the sample was sheared for a given normal stress, the normal stress was increased and the same sample sheared again (multi-stage shear box tests).

In Table 2.4 the bond coefficient is shown for the various normal stresses applied. As shear strength is related to normal stress ($\tau = c' + \sigma_n \tan\phi$), the interface properties would be expected to vary with the normal stress. However, from this set of results it appears that the bond coefficient is independent of the normal stress applied. Nonetheless, the constant results could be an artefact of the multi-stage test procedure. After the first shearing stage, a failure plane has been created. Subsequent tests would simply have slipped along this plane. Consequently, the same bond coefficient would have been measured. It can, however, be assumed that the bond coefficient at higher normal stress would have been at least 0.8 or more.

Table 2.4: Ratio of geogrid-clay interface strength to clay shear strength (Koutsourais et al., 1991).

Normal stress [kPa]	Bond coefficient(c_b)
20	0.80
35	0.80
48	0.80
62	0.81

Bergado et al. (1993) conducted large scale pull-out test and direct shear tests on steel grids, bamboo grids and polymer geogrids in weathered Bangkok clay. The clay was compacted to 95% of Proctor density, dry of optimum. It was reported to have a friction angle of 35.9° and c' = 57 kPa from undrained unconsolidated triaxial tests. The relatively high friction angle could be viable for a soil of a plasticity index of 10.02% (Mesri & Abel-Ghaffar, 1993). The c' value, however, would be high for any type of soil. Nonetheless, c' values of similar magnitude have been reported (inconsistently) for this clay in literature (see the summary by Surarak et al. (2012)). However, the friction angle and c' measured with undrained shear box tests were 11.3°and 21.9 kPa. The significant difference to the triaxial results was attributed to the strain-softening behaviour of Bangkok clay. Whether the shear-box test sufficiently prevents the dissipation of excess pore pressure to qualify as an undrained test is an open question.

As with Koutsourais et al. (1991), multi-stage tests were conducted for both the pull-out and shear tests. After 25 mm of displacement the test was stopped for two hours. Thereafter, the normal stress was increased and the test resumed for another 25 mm. Again the question arises if these test remained undrained and whether the material sufficiently recovered during the two hours. Residual slip planes might still have been present.

Bergado et al. (1993) found that as the stiffness of the materials increased (geogrid→ metal strands→bamboo) the load mobilised for a given displacement increased. For both the steel grids and geogrids the pull-out capacity appeared to be insensitive to the normal stress. As shear resistance is related to normal stress, this insensitivity could indicate that the majority of the pull-out resistance was bearing resistance against the transverse members. However, similar to the tests of Koutsourais et al. (1991) this insensitivity could be an artefact of the multi-stage shear tests.

The shear resistance increased with normal stress as expected. For the range of overburden pressures investigated, the bond coefficient was equal or greater than unity. A bond coefficient greater than unity suggests that the geogrid increased the shear strength of the soil. However, as the authors rightly suggested, in practice the soil will fail where it is the weakest. Accordingly, an upper-bound of unity exists for the bond coefficient. The bond coefficient, of course, depends on which of the soil shear strength parameters were used for calculation (Equation 2.6). Should the undrained triaxial shear strength parameters be used, the bond coefficient would be lower than 0.4. However, the strength parameters from the shear box test are more relevant for the calculation of the bond coefficient as the reinforced tests were all done in direct shear.

Abu-Farsakh et al. (2007) did direct shear tests on, amongst others, three clays of different plasticities (6%, 25%, 49%) and three different geogrids. A large shear-box apparatus was used. For each of the normal stresses investigated a new sample was prepared. The properties of the geogrids and the results of the direct shear tests, for each of the clays, at a number of normal stresses, are summarised in Table 2.5.

The bond coefficient was found to be relatively insensitive to the plasticity of the clay, yet appears to increase with geogrid stiffness. However, rather than attributing the increase in bond coefficient to the stiffness, Abu-Farsakh et al. (2007) credited it to the raw materials. The polypropylene geogrid performed worse than the polyester. The study also found that the interface properties of the geogrid

Table 2.5: Bond coefficient as a function of normal stress for three different geogrids for clays with different plasticities (Abu-Farsakh et al., 2007).

Geogrid	Aperture size	Stiffness	Normal stress	Bond coefficient for different clays		
	[mm]	[kN/m]	[kPa]	PI = 6%	PI = 25%	PI = 49%
Tensar BX-6100 (Polypropylene)	30.2 x 36.5	180	25	0.70	0.66	0.77
			50	0.71	0.69	0.70
			75	0.71	0.71	0.66
Mirafi BasXgrid 11 (Polyester)	25.4 x 25.4	268	25	0.70	0.97	0.73
			50	0.70	1.02	0.80
			75	0.69	1.05	0.84
Mirafi Miragrid 8XT (Polyester)	22.0 x 22.0	736	25	0.86	0.79	0.86
			50	0.89	0.83	0.83
			75	0.90	0.86	0.81

worsened as the moulding moisture content of the soil increased. This could either be due to the lower suction or the generation of excess pore water pressure. Increasing the dry density of the clays improved the interface strength. In conclusion the authors recommended compacting the soil to 95% of maximum dry density at OMC + 2%.

2.5 SUMMARY OF GEOGRID-CLAY INTERACTION

The bond coefficient between a geogrid and clay, representative of the shear efficiency, appears to be in the order of 0.8. Thus, from the preceding discussion it is apparent that the inclusion of the geogrid creates a weakened shear plane in the clay. The extent of this weakness is the function of a number of factors related to the interaction properties of the geogrid. From the preceding discussion and the work of Alfaro et al. (1995) the following properties that influence the bond (interface behaviour) of a geogrid can be identified:

1. Transverse member properties.
2. Aperture size.
3. Skin friction.
4. Stiffness of the geogrid relative to the surrounding soil.

The transverse members primarily influences the interlock capacity and bearing resistance of the geogrid. Depending on the spacing between the members, interference effects could arise. Dyer (1985) conducted photo-elastic pull-out tests of geogrids embedded in crushed glass particles. Figures 2.22a

and b illustrate how the strain distribution surrounding the transverse members changes as the spacing decreases. A continuum finite element model by Dias (2003) modelled a similar interference effect to Dyer (1985) (Palmeira, 2009). As clay can be assumed to be a continuum, the implication is that this interference effect could occur in clays as well.

The size of the transverse members, however, does not influence the pull-out capacity of geogrids when the ratio between member size and average particle diameter was greater than 12 (Palmeira & Milligan, 1989). Thus, for clays the pull-out strength will be independent of the transverse member size. The shape of the transverse member could, however, change the bearing resistance of the transverse member and, in turn, the pull-out capacity.

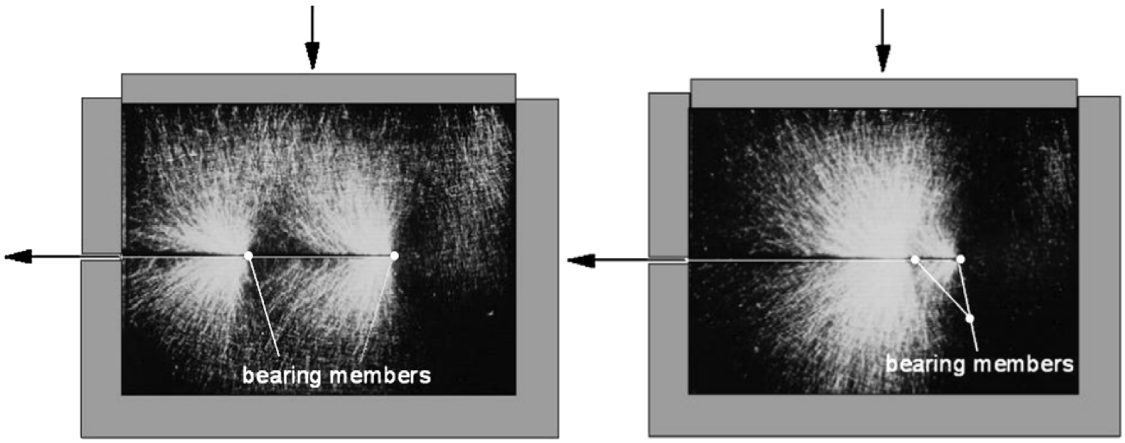

Figure 2.22: Interference effects in geogrids for: a) further spaced and b) closely spaced transverse members (Dyer (1985) from Palmeira (2009)).

The Aperture size is commonly quantified by the percentage open area of the geogrid. It defines the area of soil above the geogrid that is in contact with soil below the geogrid. The greater this area, the closer the shear resistance will be to soil-soil shear. Koutsourais et al. (1991) mentioned that in sand the interface behaviour of geogrids with large apertures approached soil-to-soil frictional behaviour. The aperture size is also representative of the transverse member spacing.

The Skin friction of a geogrid is of great importance for shear failure. The lower the skin friction of the geogrid is in comparison with the soil, the lower the bond coefficient will be.

The Geogrid stiffness appears to be more significant for pull-out tests than shear tests. A stiffer grid will have less slack after installation. Accordingly, for higher geogrid stiffnesses more load was mobilised at a given displacement. For direct shear tests a slight improvement in bond coefficient can be observed for geogrids of greater stiffness.

These four properties, i.e. transverse members, aperture size, skin friction and stiffness should all be considered when selecting a model geogrid for centrifuge testing and when doing finite element modelling of geogrid reinforced soil.

2.5.1 Centrifuge tests of geogrid reinforced clay liners

A number of authors studied the effect of geogrid reinforcing on clay liners subject to differential settlement in the geotechnical centrifuge. In Section 2.3.4 a brief summary of the geotechnical centrifuge technique was presented and a further discussion can be found in Chapter 5. A summary of a number of the centrifuge studies of reinforced clay liners found in literature is given in Table 2.6

Viswanadham & Jessberger (2005) were some of the first authors to model geogrid reinforced clay liners in a geotechnical centrifuge. A model reinforced clay liner was placed on top of two sacrificial layers of sand, separated from a trapdoor by a thick geotextile. The trapdoor had a hinged flaps at each edge and was supported by a piston. As with the unreinforced tests of Viswanadham & Rajesh (2009) and Gourc et al. (2010), the piston was lowered to induce distortion on the clay liner. Both settlement of, and flow of water through, the liner were measured.

The liner itself was constructed by one-dimensionally consolidating a kaolin slurry inside a centrifuge strong box to 1250 kPa. After consolidation the load was released and the clay was allowed to swell. For the reinforced tests the clay was consolidated in two stages. The bottom clay was consolidated first. Subsequently, the model geogrid was placed on top of the bottom layer and the second clay layer was consolidated on top of it. The scaling laws applicable to geogrids are discussed in Section 5.2.2.2.

The centrifuge tests lasted conducted for a period of 9 to 10 hours each. After every 5 min of settlement (at a prototype rate of 50 mm/min) the piston was stopped for 30 min. During this period, equivalent

Table 2.6: Summary of some centrifuge tests conducted on reinforced clay liners subject to subsidence.

Author	Artificial acceleration [g]	Liner/cap thickness [m] [i]	Prototype width [m]	Trough width [m]	Displacement mechanism	Material [ii]	Surcharge [kPa]	Variables considered	Geogrid secant stiffness [kN/m]
Viswanadham & Jessberger (2005) [iii]	50	1.25	42.4	20	Piston lowering flaps	C_K: 100%	0	Geogrid stiffness	500, 3500, 5750
Viswanadham & Muthukumaran (2007)	40	1.2, 1.6, 2	28.8	~16	Piston lowering flaps	C_K: 80%, S: 20%	0	Liner thickness	3800
Rajesh & Viswanadham (2009)	40	0.6, 1.2	28.8	~16	Screwjack lowering flaps	C_K: 80%, S: 20%	12.5, 25	Liner thickness and Overburden pressure	3608
Rajesh & Viswanadham (2011)	40	0.6, 1.2	28.8	~16	Screwjack lowering flaps	C_K: 80%, S: 20%	25	Liner thickness and geogrid stiffness	232, 3600
Rajesh & Viswanadham (2012b)	40	0.6, 1.2	28.8	~16	Screwjack lowering flaps	C_K: 80% , S: 20%	0, 25	Liner thickness, geogrid stiffness, overburden pressure	232, 3600

[i] All dimensions are in prototype scale [ii] C_K: Clay (Kaolin) S: Sand [iii] From Viswanadham (1996).

to 54 days of prototype consolidation time, the seepage through the liner, as well as the deflected shape, were measured. The process was repeated up to a final central settlement of 1.25 m (prototype scale).

In Figure 2.23 the cracks observed in unreinforced and reinforced liners, for a central settlement of 1.25 m, are shown. All stiffnesses (J) and dimensions are in prototype scale. Similar to the results of Section 2.3.4, two deep continuous cracks formed where the unreinforced liner hogged. No cracks were observed where the liner sagged. The authors suggested that this lack of cracks where the liner sagged could be the result of a) friction below the liner or b) increased vertical stress at the base.

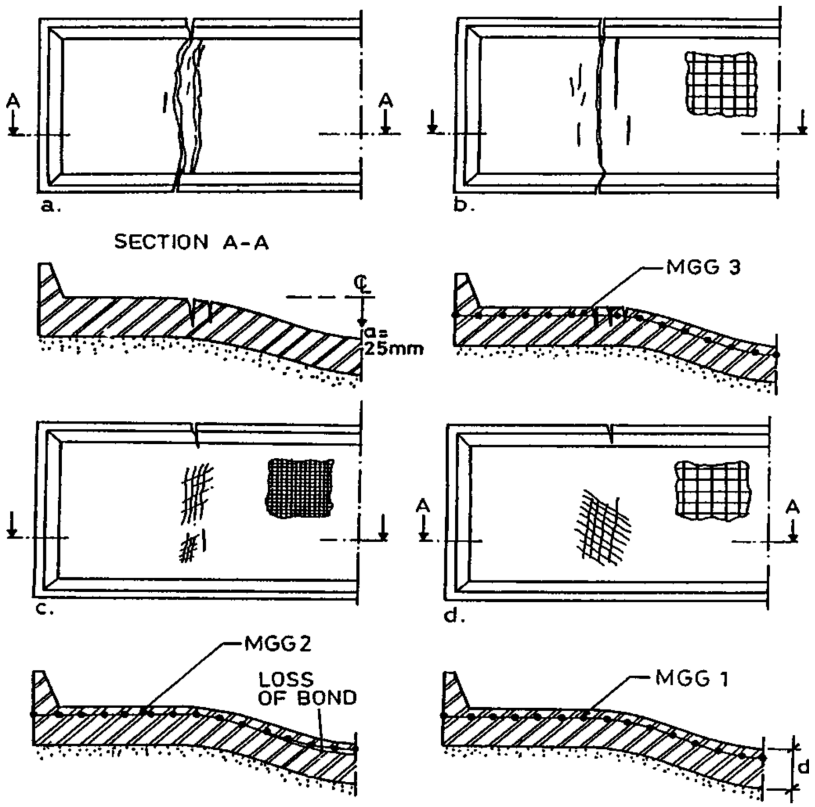

Figure 2.23: Cracks observed in a) a unreinforced liner and reinforced liners: b) J = 500 kN/m, c) J = 5750 kN/m and d) J = 3500 kN/m, for a central settlement of 1.25 m (Viswanadham & Jessberger, 2005).

To compare the fracture of the liners Viswanadham & Jessberger (2005) normalised the width of the cracks (w_c) by its spacing (a_c) and plotted this ratio against central settlement (a). For the unreinforced liner (Δ_1) the ratio varied between 0.16 - 0.32 (Figure 2.24). On the contrary, for the reinforced liner the ratio varied only between 0.025 - 0.065 (Δ_2). Thus, for the reinforced liner the cracks were not only smaller (lower w_c/a_c values), but also more homogeneous (smaller range).

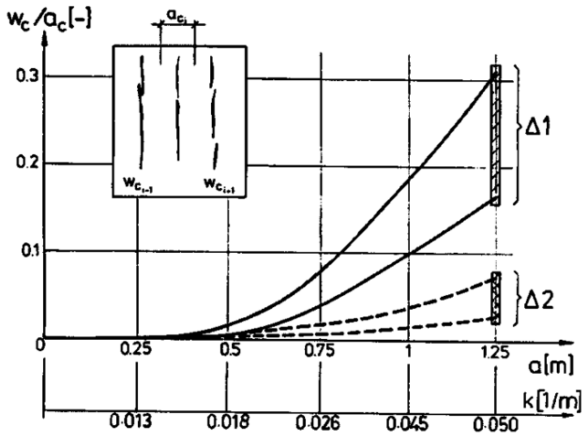

Figure 2.24: Crack width (w_c) normalised by crack spacing (a_c) as a function of central settlement (a) (or curvature (κ)) for an unreinforced liner (Δ_1) and a reinforced liner (Δ_2) (Viswanadham & Jessberger, 2005).

In Figure 2.23b to d it can be observed how the crack volume decrease as the stiffness of the geogrid increase. However, for the geogrid with the greatest stiffness, the underlying clay body eventually separated from the geogrid (Figure 2.23c). As the reinforced liner deformed, the geogrid eventually started to strain. After even more displacement occurred, the geogrid spanned and a void formed below it. If the cohesive force between the clay on either side of the geogrid is lower than the self-weight of the clay below the geogrid, the liner will separate from the geogrid (as observed). Thus, two factors dictate the potential for separation: a) geogrid stiffness and b) the cohesive force between the clay above and below the geogrid. This cohesive force is the product of the cohesive stress in the clay and the area it acts on, i.e. the aperture size. The specific geogrid that separated was both stiffer and had a lower percentage open area than the others.

While the liners distorted, the flow through it was measured. The results of three of the liners are presented in Figure 2.25. For both the unreinforced liner and the liner with J = 3500 kN/m there was flow at the start of the test. As there was no distortion, it is assumed that water seeped through at the boundaries. At a central settlement of ≈0.5 m (full scale) a catastrophic failure of the unreinforced liner occurred. Both the reinforced liners failed as well, with the stiffer liner failing to a lesser extent and at greater central settlement.

Viswanadham & Jessberger (2005) glued discrete markers to every fifth transverse rib of the geogrid. By measuring the movement of the markers between successive photographs, the strain in the geogrid was calculated. In Figure 2.26 the geogrid strain (ε_g) and the strain of the clay at the interface (ε_{sg})

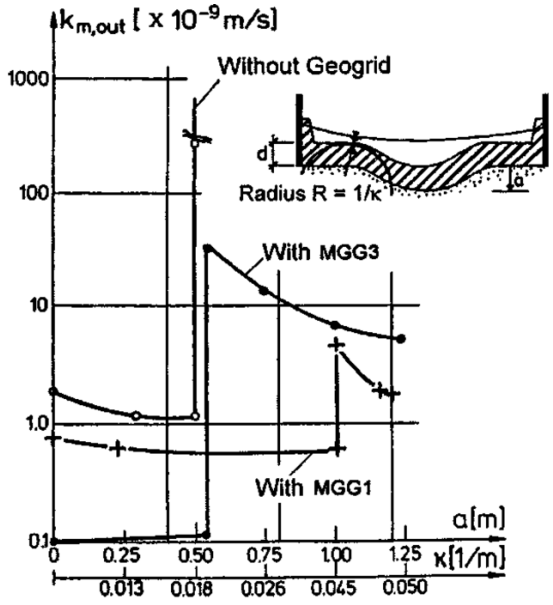

Figure 2.25: Variation of liner permeability with central settlement for both unreinforced and reinforced liners (MGG3: J = 500 kN/m, MGG1: J = 3500 kN/m) (Viswanadham & Jessberger, 2005).

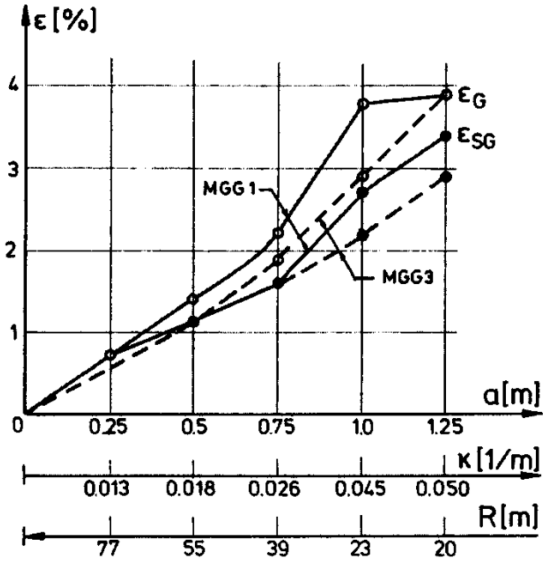

Figure 2.26: Geogrid strain (ε_g) and soil strain at the geogrid interface (ε_{sg}) as a function of central settlement (a) for two reinforced liners reinforced liners (MGG3: J = 500 kN/m, MGG1: J = 3500 kN/m)(Viswanadham & Jessberger, 2005).

are shown for two of the geogrids. After some central displacement, the strain in the geogrid deviated from that in the clay, indicating a loss of compatibility. At this central settlement, a major increase in flow through the liner occurred (Figure 2.25) and the liner failed. Thus, once compatibility was lost, the liner failed. From there onwards the majority of the load was carried by the geogrid and it strained to a higher magnitude than the clay. From Figure 2.26 it can also be seen that the greater the difference in stiffness between the clay and geogrid, the earlier the loss of compatibility occurred.

Viswanadham & Jessberger (2005) concluded that, for effective geogrid reinforcement, the following is required:

1. Soil-geogrid compatibility (related to bond).
2. Adequate geogrid stiffness.

The bond is a function of 1) soil-geogrid friction, 2) stiffness of the geogrid relative to the surrounding soil and 3) the interlock between the soil in the geogrid. The effect of the interlock, in turn, depends on the relative deformation between the soil and the geogrid (Viswanadham, 1996).

Viswanadham (1996) is the parent study for the results used in the paper by Viswanadham & Jessberger (2005). Additional to the results presented in Viswanadham & Jessberger (2005), Viswanadham (1996) also investigated reinforcement at the base of a liner. The cracking pattern for a liner reinforced at the base with a geogrid with J = 3500 kN/m is illustrated in Figure 2.27. The liner cracked at a smaller central settlement than one reinforced with a similar geogrid at the top quarter (Figure 2.23d). As the hogging section of the clay liner was in compression at the depth of the geogrid, the tensile reinforcement has no effect. At the sagging section of the liner the friction provided by the sand suppressed the cracks and thus the geogrid did not appear to help. Only once the geogrid strains enough to span the void, will it improve the behaviour of the liner.

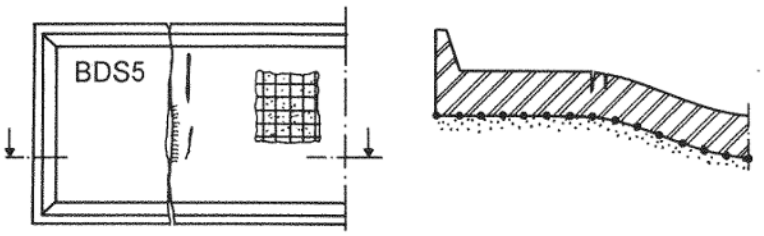

Figure 2.27: Cracking pattern observed in a liner reinforced at the bottom (J = 3500 kN/m) (Viswanadham, 1996).

The maximum outer fibre strains for the two liners discussed in the previous paragraph, as well as an unreinforced liner, are summarised in Table 2.7. All three liners were consolidated to 1250 kN/m. The moisture contents for the three liners were similar, as were the densities. After a central settlement of 0.75 m, the strains in the outer fibres of the three liners were equivalent for all practical purposes. This is expected as the strain at the periphery of the liner only depends on the distance from the neutral axis and the curvature of the liner (Equation 2.5). However, the fracture pattern and thus the hydraulic conductivity at that strain, differed considerably between the liners (compare Figures 2.23a, d, 2.27). The geogrid disrupted the strain concentrations and distributed the applied stress. Accordingly, a network of fine cracks developed, rather than the two deep cracks of the unreinforced liner (see Figure 2.23). Thus, the strain at the outer fibre alone is not indicative of the integrity of the liner.

Table 2.7: Maximum strain in the outer fibres of the liner for 0.75 m settlement (Viswanadham, 1996).

Model	Moisture content [%]	Dry unit weight [kN/m^3]	Outer fibre strain [%]
Unreinforced	35.3	14.5	2.3
Reinforced at the base [1]	36.3	14.2	2.2
Reinforced at the top quarter [i]	35.3	14.5	2.4

[i] Geogrid with stiffness 3500 kN/m

Viswanadham & Muthukumaran (2007) investigated the effect of liner thickness on the performance of geogrid reinforced clay liners subject to local subsidence. Both reinforced and unreinforced liners of three different thicknesses (1.2, 1.6 and 2 m) were tested. Each liner was prepared by compacting the clay wet of optimum moisture content in layers. The experimental setup was similar to Viswanadham & Jessberger (2005). Liner thickness was found to have two significant effects on the integrity of a reinforced liner:

1. The thicker liners distorted less before it started to crack. Thus, for the same central settlement a thicker liner strains more (as predicted by Equation 2.5).
2. The fraction of a thick (1.6 m) reinforced liner that cracked (20% of the total thickness) was lower than for a thinner (1.2 m) liner. This is similar to the behaviour of unreinforced liners discussed earlier (Section 2.3.4). The thickest reinforced liner did not seem to have any significant cracks at all.

Thus, a thicker liner cracks at lower distortion. However, the effect of the cracks in a thicker liner was less severe than in a thinner liner for the same central settlement. A comparison between unreinforced and reinforced liners of the same thickness also showed that the reinforced liners can withstand significantly higher distortion. The final difference between the reinforced and unreinforced liners lied in the strain distribution through the liner. In Figure 2.28 the strain along the surface of an reinforced and unreinforced liner is shown. The strain at the surface of the unreinforced liner peaked at three distinct locations. On the contrary, the reinforced liner had only a single, significantly lower peak. These strain distributions corresponds to the discrete deep cracks observed in unreinforced liners and multiple fine cracks in reinforced liners.

Rajesh & Viswanadham (2009) built on the work of Viswanadham & Muthukumaran (2007) by investigating the effect of both overburden pressure and liner thickness on the integrity of reinforced liners. Three reinforced liners and one unreinforced liner was tested in the centrifuge with a similar experimental setup to Viswanadham & Rajesh (2009). A screwjack connected to an electric motor was used instead of a hydraulic piston to lower the trapdoor and induce settlement. The clay was mixed at OMC+5% and compacted to the required density of 14.2 kN/m^3. The geogrid used had a stiffness of ~3608 kN/m and was embedded a quarter from the top of the liner. The overburden was applied either by free-standing water or saturated sand.

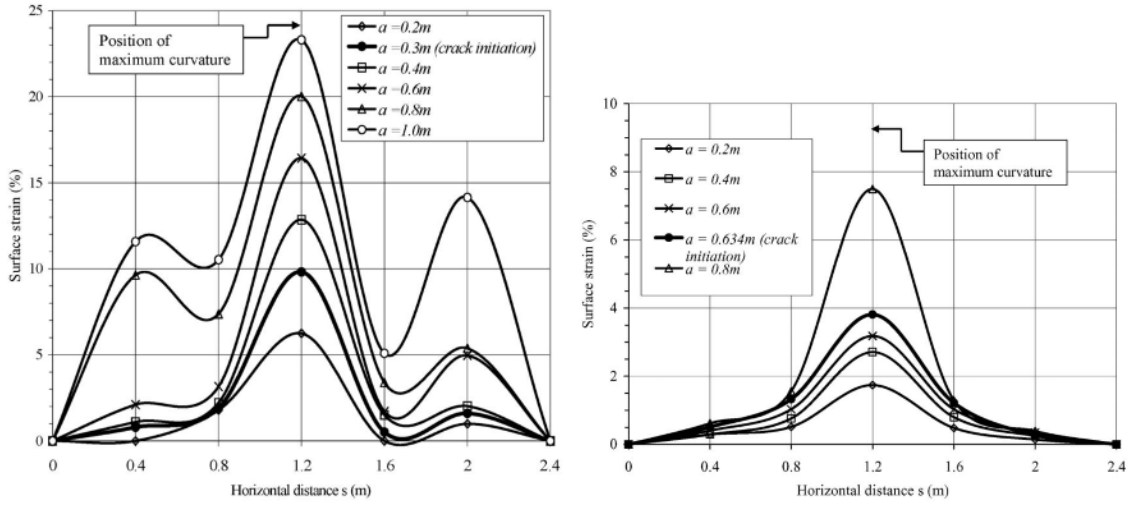

Figure 2.28: Strain along the surface of an unreinforced liner a) and a reinforced liner b) (Viswanadham & Muthukumaran, 2007).

The study found that increasing the overburden pressure suppressed crack formation (similar to the unreinforced liners). No cracks extended past the geogrids for a central settlement of 1 m. This could be due to the high compatibility between the geogrid and the clay liner.

Rajesh & Viswanadham (2011) modelled reinforced liners in the centrifuge for different overburden pressures and geogrid stiffness. Both an increase in stiffness and overburden pressure improved the performance of the liner.

Rajesh & Viswanadham (2012b) instrumented model geogrids with strain gauges (see Figure 2.29). The geogrids were embedded in model liners (0.6 m and 1.2 m thick at prototype scale) and tested in a centrifuge model similar to Rajesh & Viswanadham (2011). It was found that not only did a greater ultimate tensile load mobilise in the stiffer geogrid, but the stiffer geogrid deformed less before it became load bearing (compared to a less stiff geogrid).

2.5.2 Failure of reinforced clay liners

Giroud et al. (1990) identified the three different scenarios for design of reinforced clay liners shown in Figure 2.30. The first entails breaking of the geogrid and is not considered in this study (Figure 2.30a).

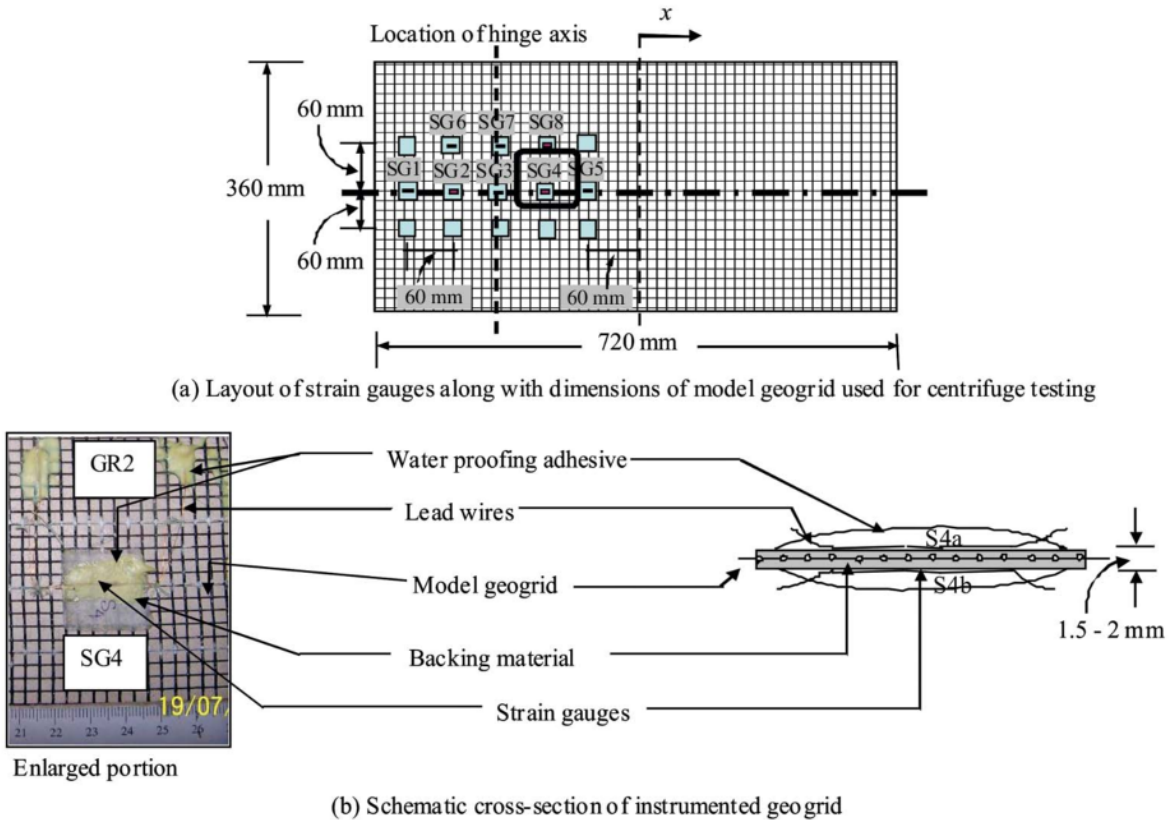

Figure 2.29: Strain gauge instrumentation of model geogrids: a) plan view of layout and b) photo of setup (Rajesh & Viswanadham, 2012b).

The second and third are linked to the stage of settlement of the liner. During the first stage a depression grows below the liner. The liner deflects but remains in contact with the bottom of the depression (Figure 2.30b). Consequently, only a portion of the load is supported by the geogrid while the remainder is transferred to the surface of the depression. As the depression continues to grow, the geogrid will eventually be too stiff to fully deflect and will span to form a void (Figure 2.30c). This is Stage 2 and is characterised by the geogrid supporting all of the applied load.

From the previous section a number of failure mechanisms can be identified for reinforced liners during Stage 1 settlement. These are similar to the ones identified by Palmeira (2009) in geogrid reinforced retaining walls. The mechanisms (illustrated in Figure. 2.31) are:

1. Shear of the geosynthetic-soil interface This failure occurs when bond is lost between the geogrid and the clay. The 500 kN/m liner of Viswanadham & Jessberger (2005) is illustrative of such a shear failure. This sliding failure is of special concern when using geosynthetics at an incline. Examples include covers of landfills and erosion protection on slopes (Palmeira, 2009). The

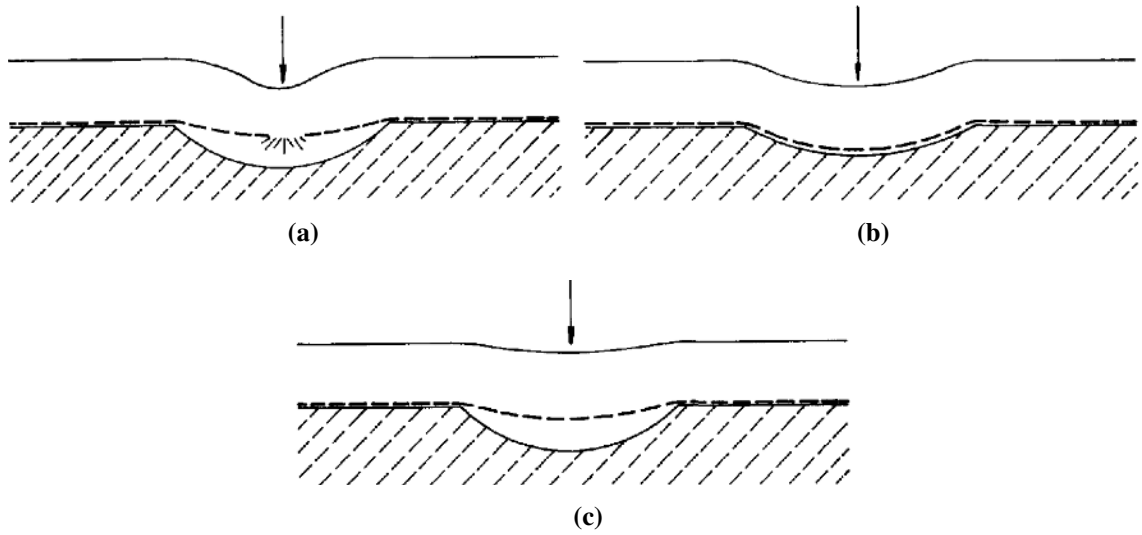

Figure 2.30: Three scenarios for design: a) Rupture of the geogrid, b) Stage 1 settlement and b) Stage 2 settlement (Giroud et al., 1990).

failure can be modelled with a direct shear test (Section 2.4.1).

2. Shear across the interface This failure has not been explicitly observed in the reinforced tests. However, it is assumed that under the correct conditions the shear ruptures observed by Jessberger & Stone (1991) (Figure 2.11b) will occur in the reinforced liners as well.

3. Lateral deformation of the geosynthetic-soil interface This failure can either be due lateral extension of the liner (e.g. the necking observed by Richards & Powrie (2011), Figure 2.17) or the result of excessive curvature (e.g. the tensile cracks observed by Jessberger & Stone (1991) and Viswanadham & Mahesh (2002), see Figures 2.11a & 2.14).

4. Pull-out of the geogrid These failures occur when a tensile load is applied to the geogrid and bond is lost on both surfaces. A pull-out test can be used to model these failures (Section 2.4.1).

An additional failure mechanism can be identified for a reinforced liner during Stage 2 settlement:

5. Vertical separation of the geosynthetic from the underlying soil This will occur when the cohesive strength of the clay at the interface is lower than the self weight of the clay. Consequently,

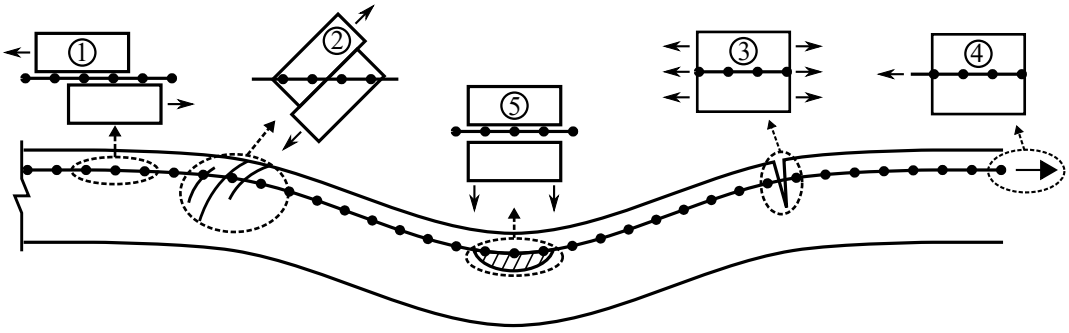

Figure 2.31: Failure mechanisms possible in a geogrid-reinforced clay liner.

the bottom clay tears off and falls down (see Figure 2.23 d).

Of the five failure mechanisms, the fourth, i.e. pull-out failure, is not applicable to the current study. The remainder can be grouped based on the preferential seepage paths created: the first set creates horizontal flow paths through the liner (mechanisms 1 and 5) and the second in vertical flow paths (mechanisms 2 and 3). These failure mechanisms can also occur as a combination as seen in the thicker clay liners of Viswanadham & Mahesh (2002) that failed both in shear (2.5.2) and tension (2.5.2) (Section 2.3.4).

2.5.3 Numerical modelling of reinforced clay liners

Accurate numerical modelling of geogrid reinforced clay liners is complex due to the non-linear materials and interaction between geogrid and clay. Gabr & Hunter (1994), Plé et al. (2012), Rajesh & Viswanadham (2012a) and Rajesh & Viswanadham (2015) are some authors who modelled clay liners (reinforced and unreinforced) subjected to settlement. As most of these studies aimed to replicate the results of physical modelling, the key findings of the results have already been presented in earlier sections. Of importance are the modelling techniques applied.

The compacted clay was modelled as an elasto-platic Mohr-Coulomb material by Plé et al. (2012), Rajesh & Viswanadham (2012a) and Rajesh & Viswanadham (2015). Additionally, Rajesh & Viswanadham (2015) added a tension cut-off to the material model. Gabr & Hunter (1994) modelled a sand layer subject to settlement and thus used a power-law for the stiffness of the soil. All authors used plane-strain elements.

To model the geogrid, Gabr & Hunter (1994), Rajesh & Viswanadham (2012a) and Rajesh & Viswanadham (2015) used bar elements with a linear-elastic material model. To model the interaction between the geogrid and the soil, Gabr & Hunter (1994) placed interface elements on either side of the geogrid. These interface elements had zero thickness and consisted of two springs, one in the vertical and one in the horizontal direction that linked the soil and geogrid. A hyberbolic material model was used to relate shear stress and shear strain in the interface elements. Rajesh & Viswanadham (2012a) and Rajesh & Viswanadham (2015) both used the zero-thickness interface elements of Plaxis (2002) and the strength at the interface was assumed to be 67% of that of the soil.

To model the void below the liner, Gabr & Hunter (1994) assumed the void to be in place below the liner when the analysis began (see Figure 2.32a). The load applied to the surface of the clay was incrementally increased to model deposition of waste. In contrast, Plé et al. (2012), Rajesh & Viswanadham (2012a) and Rajesh & Viswanadham (2015) all assumed that the void (or burst) gradually developed under the liner after the waste had been placed. Consequently, a displacement profile was applied directly to the clay liner (Plé et al., 2012). Similarly, Rajesh & Viswanadham (2012a) applied a displacement profile to sand elements that were connected to the clay elements as illustrated in Figure 2.32b.

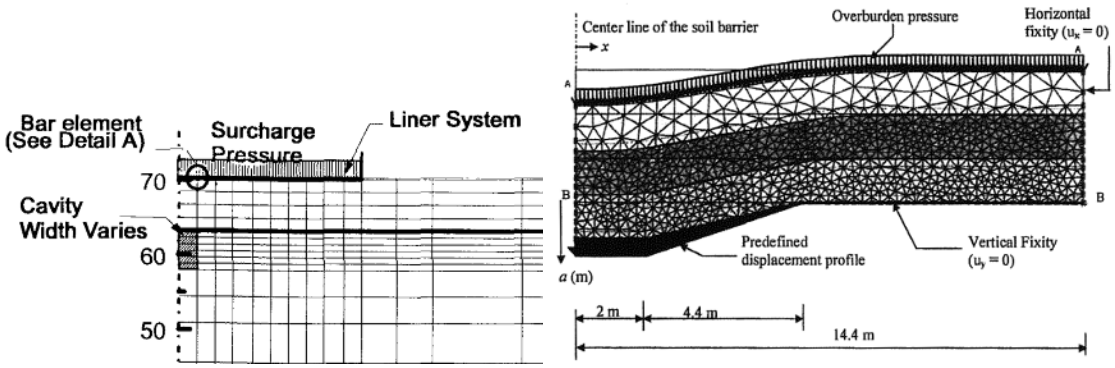

Figure 2.32: Modelling of the void below the liner: a) pre-existing void (Gabr & Hunter, 1994) and b) gradual development of the void (Rajesh & Viswanadham, 2012a).

2.6 OPTIMAL REINFORCEMENT OF CLAY LINERS

Although geogrid reinforcement of clay liners subject to differential settlement have been investigated extensively, limited research has been done into the optimal reinforcement position for a geogrid in

such a clay liner. The calculations by Giroud et al. (1990) for a reinforced soil layer assumes that the geogrid is placed at the bottom of the liner. Viswanadham (1996) recommended placing reinforcement at the top quarter of the liner after the results of centrifuge experiments.

A few other recommendations on optimal reinforcement positions in soil layers can be found in literature outside of landfill liners. Palmeira & Viana (2003) determined the optimum geogrid position in a sand layer using a ramp test. For these shear tests on sand, it was found that the optimum geogrid position occurred one third from the bottom of the liner. In a similar manner Kuo & Hsu (2003) found the optimal geogrid position in an asphalt overlay to be one third from the base of the road. Mishra et al. (2014) conducted triaxial tests and discrete element models of railway ballast reinforced horizontally with geogrids. They found that the maximum increase in shear strength was achieved when two geogrids were used, one at 2/5^{ths} from the top and one at 2/5^{ths} from the bottom.

2.7 SUMMARY

In this chapter, literature with regard to geogrid reinforcing of landfill clay liners subject to settlement was investigated. Firstly, a brief overview of landfill design and waste settlement was presented in Sections 2.1 and 2.2. In Section 2.3.1 it was shown that the fracture of clay is a two-stage process. As a clay beam is loaded, the load displacement behaviour is linear until micro-cracks starts to form. Once the micro-cracks forms, the behaviour becomes non-linear until a macro-cracks opens up and the load carried by the beam either plateaus or reduces. This fracture behaviour was investigated in literature by full-scale modelling (Section 2.3.2), element tests (Section 2.3.2) and centrifuge modelling (Section 2.3.4). In the centrifuge tests it was found that, notwithstanding the properties of the clay, the overburden pressure applied, thickness of the clay and settlement through shape all influenced the fracture behaviour of the liners.

Geogrids were identified as a viable reinforcement option to reduce the fracture of the clay. A geogrids mitigates the effect of settlement on the liner by increasing the stiffness of the system and changing the stress distribution at the mouth of the crack (Section 2.4). A number of geogrid properties that should be considered for numerical modelling and the selection of model geogrids for centrifuge tests were also identified (Section 2.5).

In Section 2.5.1 centrifuge tests of reinforced clay liners were explored. It was found that the addition of geogrids reduced the volume of cracks in the liner. Adequate stiffness compatibility and bond were required for optimal performance. Finite element modelling of geogrid reinforced clay liners (Section 2.5.3) modelled the clay with Mohr-Coulomb elastic-plastic plane strain elements, the geogrid as linear-elastic bar elements and the interaction with interface elements. Void growth was simulated by applying a displacement profile to the base of the liner. Finally, it was found that limited research has been done on optimal geogrid placement in a soil layer, and even less for clay liners subject to settlement.

Gourc et al. (2010) found that centrifuge modelling is a viable alternative for full scale tests of clay liners. Furthermore, Viswanadham & Rajesh (2009) found that bending beam tests approximates the behaviour of centrifuge test. Consequently, in the following section the fracture behaviour of clay liners are firstly explored using bending beam tests. Following the bending beam tests, the effect of reinforcement on the clay liners are investigated in Chapter 4 to determine the optimal reinforcement position. Finally, the insights gained from Chapters 3 and 4 are used to design and construct a centrifuge model of reinforced clay liners subject to differential settlement in Chapters 5.

CHAPTER 3 BENDING BEAM TESTS

Four point bending beam tests were done to obtain a preliminary grasp on the fracture behaviour of clay liners subject to differential settlement. As part of these tests, the tensile strength of the clay and the strain at fracture was calculated. Thirteen such tests were done. However, due to the inherent variability of tensile tests on clay, only five of the tests were used for further analysis.

Firstly, the properties of the kaolin clay that was used for the bending beam samples are presented. (Section 3.1). Subsequently, the methodology of the tests is discussed in Section 3.2. The discussion entails the test setup, preparation of the beams and the analysis techniques implemented. Finally, in Section 3.3 the results of the bending beam tests are presented. Both the tensile stress-deflection results and the distribution of strain in the beams are explored. These results are used to identify the occurrence of micro- and macro-cracks in the beams.

3.1 PROPERTIES OF THE KAOLIN CLAY USED

In practice compacted clay liners (CCLs) are constructed of local, natural clays containing clay minerals, sands and silts (Benson et al., 1994). Some centrifuge studies of landfill liners simulated these natural clays by mixing kaolin/bentonite with sand/silt (Jessberger & Stone, 1991; Rajesh & Viswanadham, 2009). For the present study the clay beams were prepared by one-dimensionally consolidating a washed kaolin slurry. Similar to Thusyanthan et al. (2007) and Richards & Powrie (2011) pure kaolin, rather than a mixture, was used for the beams to ensure repeatability of the model preparation. The clay mineral kaolin was used to allow for comparison to the results of similar studies found in literature (Sections 2.3.3-2.3.4).

A number of test were done to characterise the kaolin:

1. Specific gravity and particle size distribution (PSD) measured by trained personnel at the University of Pretoria laboratories.
2. Atterberg limits and the Proctor density curve measured by a commercial laboratory (Geostrada).
3. Oedometer tests by the author.

The methodology and results of these tests are discussed in the following subsections.

3.1.1 Basic properties

The kaolin clay powder used in this study has been water washed after it was mined in the Gujurat province of India. Serina Trading, the South African distributor, supplied the chemical composition of the clay as summarised in Table 3.1. The specific gravity of the kaolin was measured by an AccuPyc II 1340 Pycnometer as 2.6618. A Malvern Mastersizer 2000 particle size analyser was used to measure the particle size distribution (PSD) of the clay shown in Figure 3.1.

Table 3.1: Chemical composition of the kaolin clay used.

Compound	Percentage [%]
SiO_2	46.12
Al_2O_3	37.86
Minor oxides	1.75
Organic material	13.74

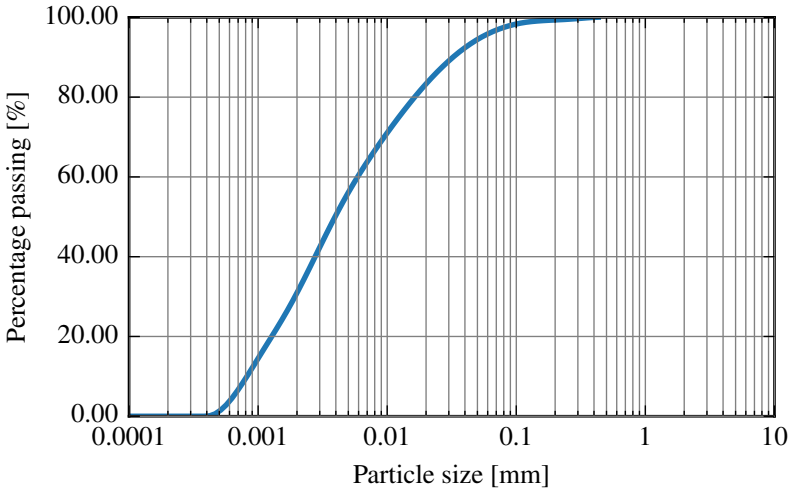

Figure 3.1: Particle size distribution of the kaolin clay.

As mentioned in the introduction to this section, the Atterburg limits of the kaolin were tested by Geostrada, a commercial South African soils laboratory. They measured the liquid limit (LL) as

37% and the plasticity index (PI) as 9%. This liquid limit is fairly low when it is considered that the liquid limits for the kaolin used for model liners in literature ranges between 42% and 61% (Schofield & Wroth, 1968; Koutsourais et al., 1991; Viswanadham, 1996; Viswanadham & Mahesh, 2002; Thusyanthan, 2005; Lehane et al., 2009). Furthermore, on the plasticity chart this kaolin plotted below the A-line in a region usually associated with silts (see Figure 3.2). However, this behaviour appears to be common for kaolin clays (Casagrande, 1932) and might be related to the relatively coarse particle size (only 31% of the powder is smaller than $2\mu m$, see Figure 3.1). Repeating the liquid limit test with three different operators consistently measured the LL as ≈9%.

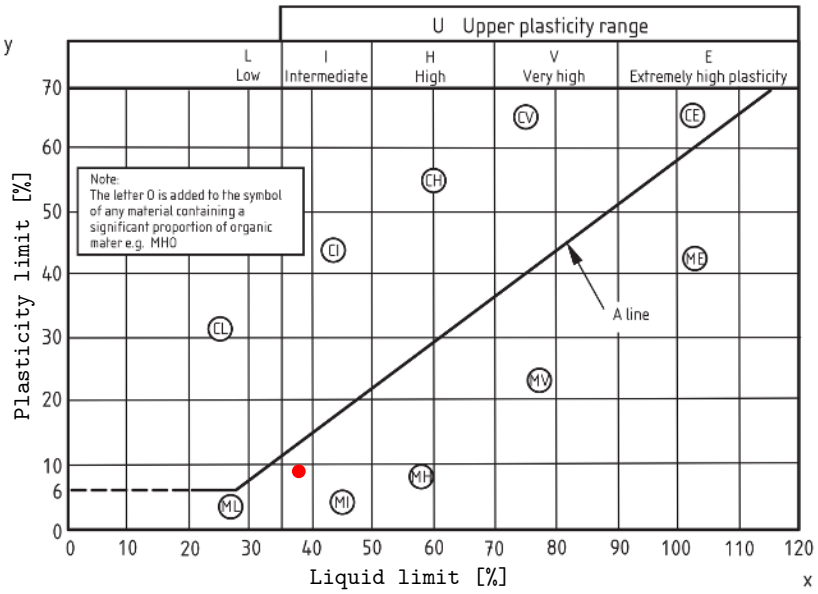

Figure 3.2: Kaolin used in the present study indicated on the BS5930:1999 plasticity chart (adapted from BS5930:1999).

Benson et al. (1999) summarised the permeability[1] of 85 landfill liners and the properties of the clays used. Viswanadham & Muthukumaran (2007) performed a regression analysis on these permeabilities and clays properties and found that for a clay to have a permeability of $1x10^{-9}$ m/s or less the requirements summarised in Table 3.2 has to be met. A maximum permeability of $1x10^{-7}$ m/s for landfill liners is recommended by Benson et al. (1994) and required by the *Minimum Requirements for Waste Disposal by Landfill* (DWAF, 1998) for a hazardous waste landfill. The *Minimum Requirements for Waste Disposal by Landfill* also stipulates a maximum Plasticity Index of 10 for a clay used in a compacted clay liner. The kaolin clay used in this study satisfies all of those requirements.

[1]For this study permeability (k) will be defined as per geotechnical convention: $k = q/(Ai)$ with A the cross sectional area, q the flow rate and i the hydraulic gradient (Knappett & Craig, 2012). The units for permeability is m/s.

Table 3.2: Clay requirements for a liner to have a permeability of $1x10^{-9}$ m/s or less.

Property	Minimum	Kaolin used in present study
Liquid limit [%]	20	37
Plasticity index [%]	7	9
Fines fraction (< 74 μm[i]) [%]	30	91.1
Clay fraction (< 2 μm[i]) [%]	15	29.7

[i] ASTM D653-14 (2014)

The Geostrada laboratories also performed a standard Proctor density test on the clay. The maximum dry density was found to be 1490 kg/m^3 at an optimum moisture content of 23.8 %. In Figure 3.3 this Proctor curve, as well as the 95% Proctor density wet of optimum is shown.

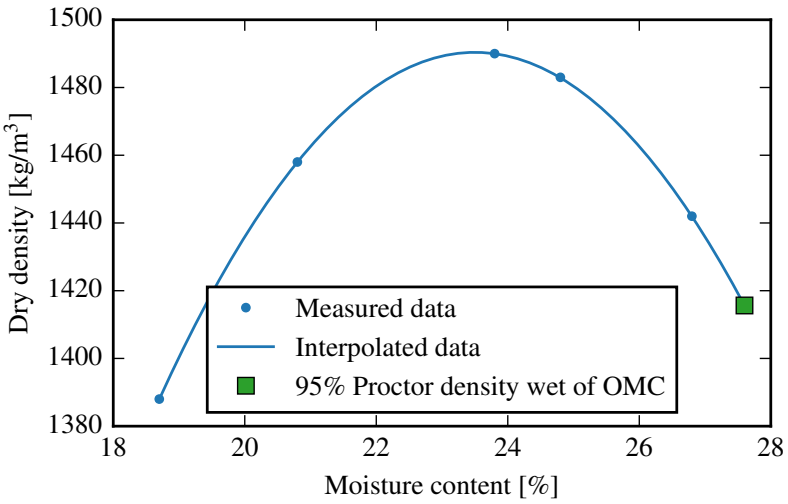

Figure 3.3: Standard Proctor density curve for the kaolin clay used in this study.

3.1.2 Oedometer tests

The beams used for the bending beams tests were cut from kaolin blocks consolidated to the required density (see Section 3.2.2). Accordingly, the relationship between consolidation pressure and density (or void ratio) was required. Oedometer tests were done to measure this relationship.

The oedometer samples were prepared similar to the bending beam samples (see Section 3.2.2) to ensure that the results are relevant. Consequently, a reconstituted slurry was tested in the oedometer. The kaolin slurry was prepared by high speed mixing equal parts of clay powder and distilled water by

mass (300 g each). After the slurry was thoroughly mixed, it was vibrated under vacuum to remove air bubbles. As the clay slurry is highly compressible, a standard oedometer ring would hold too little material for a representative sample. To increase the volume of material tested 75 mm diameter perspex cylinders of heights 73 mm and 75 mm were used to hold the samples. The cylinders were lubricated with petroleum jelly before it was filled with the clay slurry to reduce side friction.

The first load increment for the oedometer tests was the placement of the top porous disk. After a minimum of three hours, the load was doubled by adding small weights. This process was repeated until the load on the clay was equivalent to that of the oedometer top cap. Thereafter, the weights were replaced with the top cap and the standard oedometer test procedure was followed. A potentiometer was used to measure the settlement.

The void ratio and dry density of the kaolin as a function of the effective stress applied is shown in Figure 3.4. Swelling was measured only for the second oedometer test. The compression index (C_c) was -0.1954 and the swelling index (C_e) was -0.01318.

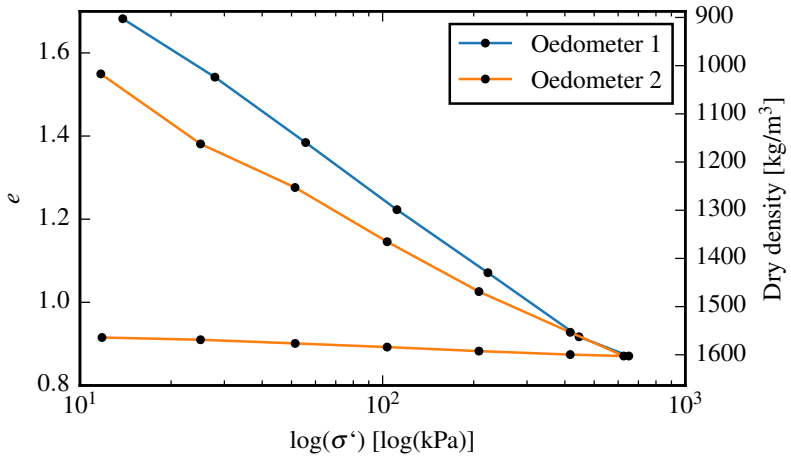

Figure 3.4: $e - \log p$ and dry density-$\log p$ curves for the kaolin clay.

Finally, the coefficient of consolidation (c_v) was also calculated from the oedometer tests. Taylor's method (also known as the root time method) was used to calculate t_{90}. The constructs used for the calculations are shown in Appendix A. The coefficient of consolidation of the kaolin is shown as a function of the consolidation stress in Figure 3.5 for oedometer test 2. As the consolidation pressure increases, the density of the sample increases and the permeability (and thus c_v) is expected to decrease. However, the opposite trend is seen in Figure 3.5. Similarly, Robinson & Allam (1998) found that for kaolin, consolidated from a remoulded kaolin slurry, c_v increased with consolidation pressure. A

possible explanation is that at higher consolidation pressures the clay plates are aligned, resulting in less torturous flow paths. At a consoldation pressure of 103.5 kPa, c_v is 2.64 m^2/y and at a consolidation pressure of 625.9 kPa, c_v is 8.78 m^2/y for this kaolin.

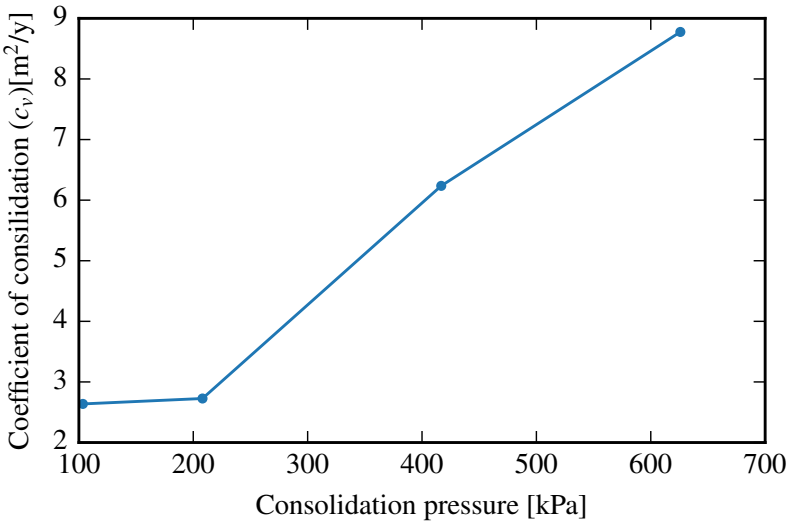

Figure 3.5: Coefficient of consolidation as a function of applied stress for the kaolin clay for oedometer test 2.

3.2 BENDING BEAM TEST METHODOLOGY

In principle, the four-point bending beam test consists of a clay beam supported with two rollers at the base and loaded with two more rollers at the top (see Figure 2.9). As the top two rollers move downwards, it applies a bending moment to the beam. If the top two rollers are spaced at thirds the maximum stress in the beam due to the bending moment can be calculated as:

$$\sigma = \frac{PL}{bd^2} \tag{3.1}$$

where σ is the maximum stress in the beam (both compression and tension), P the applied load, b the width of the beam and d the depth of the beam. As Equation 3.1 was derived for a linear elastic beam it assumes the same stress in tension (bottom) and compression (top) for the beam. Once tensile stress at the base of the beam exceeds the tensile strength of the beam it will crack at the base (where the maximum tensile stress occurs). Thus, the test can be used to study the fracture behaviour of clay beams and determine the tensile strength.

3.2.1 Test setup and procedure

The bending beam tests were done in a Lloyds 5 kN press fitted with a Lloyds LC 5kN (15643) load cell. The clay beams rested on two support bars of 16.1 mm diameter that were 98 mm apart shown in Figure 3.6. One of the two bottom supports can swivel out of plane. The beams were loaded at thirds with two more bars. These loading bars were connected to the Lloyds LC 5 kN (15643) load cell and can swivel in plane. The accuracy of the load cell was ±5% and the resolution 0.25 N.

The top bars were lowered at a rate of 3 mm/min to coincide with rate of central settlement used in the centrifuge tests (Chapter 5). The load applied was measured using the aforementioned load cell and the settlement by the press. Photos of the beams were captured at 6 s intervals with a Canon 100D camera equipped with a fixed 40 mm lens for subsequent digital image correlation analysis. After the tests were completed, moisture content samples were collected.

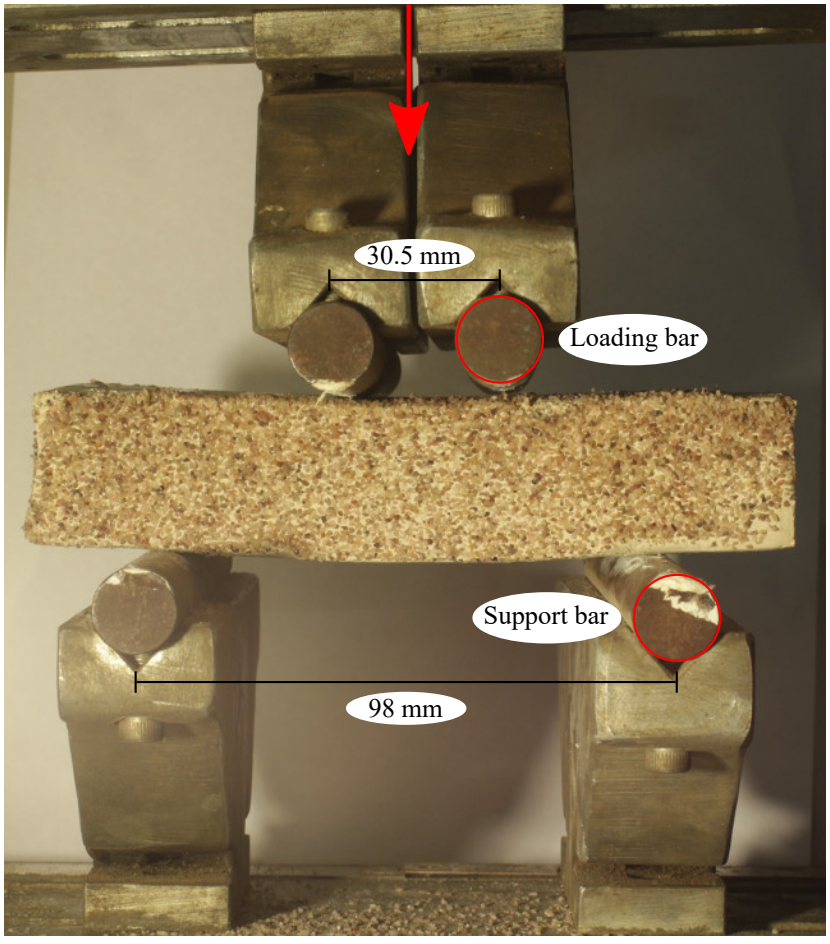

Figure 3.6: Four-point bending test layout.

3.2.2 Clay beam preparation

The clay beams tested had to be representative of landfill liners for the results of the study to be relevant. Consequently, the density of the beams should be equivalent to the 95% Proctor density of the clay (Jessberger & Stone, 1991). In the previous section it was mentioned that some authors constructed model landfill liners by compacting it in layers, similar to practice. The argument can be made that as successive layers are compacted on top of each other, some compaction energy is transferred downwards. This would result in a linear increase in the density of the liner that can not be achieved by one-dimensional consolidation. However, at 95% Proctor density, the density of the liner will be near the zero air-voids line and any additional compaction energy will have little influence. Consequently, the density of a compacted liner can be assumed to be constant through the profile. Furthermore, Jessberger & Stone (1991) found little difference in behaviour between a compacted model clay liner and a consolidated liner. In the following paragraphs the mixing, consolidation, swell and cutting of the clay beams used for the bending beam tests are discussed.

Mixing and pouring: The clay was mixed with a motorised mixer at a gravimetric moisture content of 100% for a minimum of 10 min to ensure that is a homogeneous mixture. Subsequently, a vacuum was applied for the final mixing stage to remove air bubbles.

After mixing, the slurry was poured into an oiled rectangular steel mould (710 mm x 155 mm in plan). The mould was oiled to minimise friction with the clay and to prevent rust. All clay that came into contact with the oil was removed after consolidation (see subsequent discussion on cutting). A photo of the partially disassembled mould, after consolidation, is shown in Figure 3.7. Spacers were placed between the base of the mould and the bottom of the side panels to create a drainage path below the clay. This cavity was filled with a thick non-woven geotextile to act a drainage layer. To prevent the geotextile from clogging, a layer of filter paper was placed on top of it.

After the slurry was poured to the required thickness, another layer of filter paper was placed on top of it. This was followed by a thick non-woven geosynthetic, perforated aluminium plates and finally a steel channel beam (with a number of drainage holes).

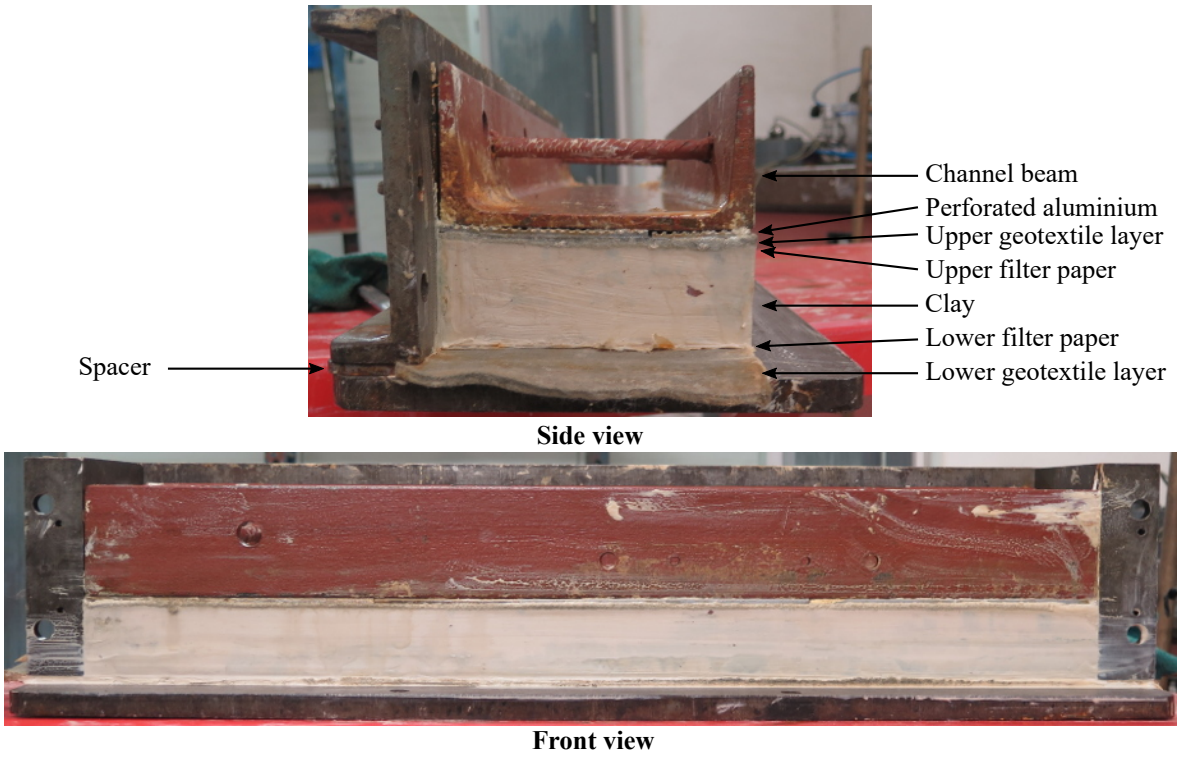

Figure 3.7: The partly disassembled mould used for consolidation of the model clay liners.

Consolidation: The clay-filled mould was placed in the consolidation press shown in Figure 3.8. The load was applied with a hydraulic piston that pressed onto a 10 ton load cell. From the load cell the force was transferred to a 40 mm thick solid steel section that distributed the applied load evenly over the channel beam.

The clay had to be consolidated to 95% of the Proctor maximum density of 1490 kg/m^3 (see Figure 3.3). This density of 1416 kg/m^3 is achieved under a consolidation pressure of 608 kPa (from Figure 3.4). Consequently, the clay was consolidated to 610 kPa. Similarly, Jessberger & Stone (1991) consolidated their liners to 630 kPa.

For the first loading increment the channel beam, as well as the solid steel section, was placed on top of the clay. After approximately three hours the load cell and two 10 kg weights were added to double the applied load. Thereafter, the load was raised to 12.5 kPa with the hydraulic piston whereafter it was doubled in every subsequent stage up to 610 kPa.

As the clay compressed, the piston rod extended. This increased the volume of the oil inside the

Figure 3.8: The press used for consolidation of the clay.

piston. The increase in volume resulted in a pressure drop, and thus the applied load reduced. To help alleviate this problem two heavy springs were placed below the mould. As the clay compressed the springs extended, pushing the mould upwards and keeping the load on the clay approximately constant. However, due to the fast rate of consolidation of the kaolin, even with the creep springs, the load did not remain completely constant and had to be adjusted every 15 minutes.

The time for 95% consolidation for a 50 mm clay slurry at a 103 kPa was 140 min (σ = 100 kPa) and for a 30 mm clay liner at 626 kPa is 15.2 min (σ = 600 kPa). The 15 min for clay consolidated to 626 kPa corresponds to the centrifuge tests where consolidation was found to take less than 15 min (see Section 5.2.5). After the load remained constant for more than 30 minutes, the clay was judged to have consolidated sufficiently for the next loading stage. The final load increment of 610 kPa was sustained for a full working day (8-10 hours).

Swell: After the clay was fully consolidated at 610 kPa, it was swelled in steps of approximately 100 kPa per hour back to 50 kPa. The clay remained at the final swell pressure of 50 kPa for a minimum of two hours to allow for the pore pressures to equilibrate.

Rust (2003) found that after swelling was completed, the undrained shear strength of a consolidated

kaolin clay block required a week to stabilise (see Figure 3.9). However, in this week the clay can age sufficiently for the structure to change significantly. Consider Figure 3.10 where compression characteristics are shown for a reconstituted natural clay. The-top most curve is for a standard oedometer test where the load is increased once a day. For the second curve the test was stopped at a consolidation pressure of 40 kPa for 12 weeks before it was continued. Once the test continued, it plotted above the conventional consolidation liner. The only viable explanation is that the structure of the clay changed during the 12 weeks (Burland, 1990).

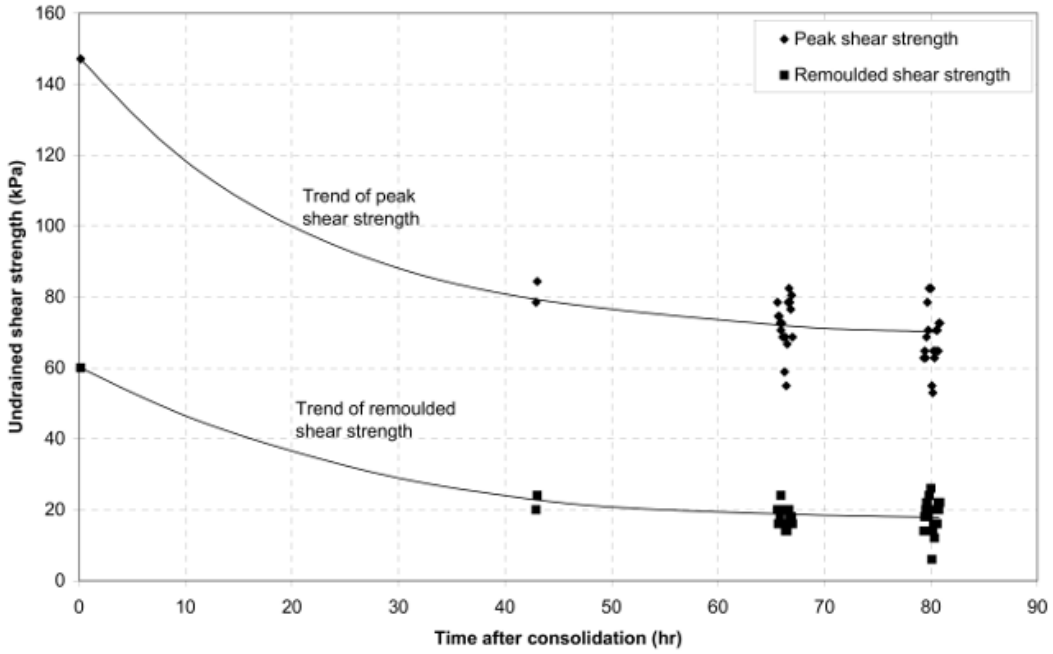

Figure 3.9: Change in undrained shear strength with time of a consolidated kaolin block (Rust, 2003).

Thus, there are disadvantages to either using the consolidated clay immediately after swelling or for allowing it to rest. Most triaxial and other element tests are conducted immediately after the consolidation or swelling stage is completed. Thus, for the sake of consistency the clay beams were tested immediately after the swelling was completed.

Cutting and preparation: Two hours after the final swelling stage the clay was removed from the consolidation press. Firstly, the clay was demoulded and the surface levelled using two wooden guides and a sharpened metal plate as shown in Figure 3.11. Thereafter, 13 beams between 27.9 mm and 29.4 mm thick, 50 mm wide and ≈150 mm long were cut from the block. Washed sand grains were added to the surface of the beam to provide texture to improve the digital image correlation analysis (Section 3.2.3.1).

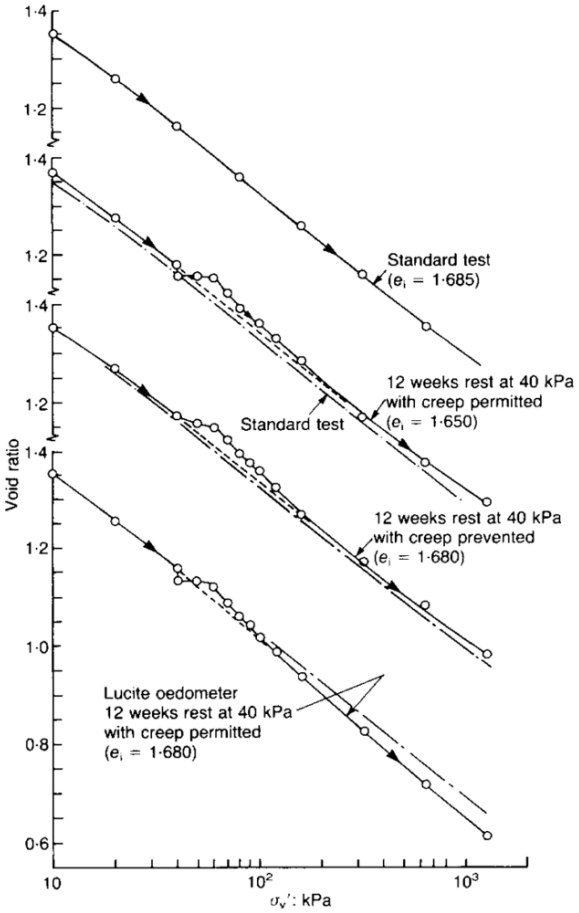

Figure 3.10: Change in compressive behaviour of a reconstituted natural clay with time (Leonards & Ramiah (1959) from Burland (1990)).

3.2.3 Analysis techniques

The strains in the beams during bending were measured using digital image correlation (DIC). This technique is discussed in the following subsection. The calibration of the DIC results, as well as the technique used to find the effective centre of the beams, are also discussed.

3.2.3.1 Digital image correlation

Soil movement in some geotechnical problems can be measured by taking a series of photos of the problem over time and comparing the relative movement between the images (frames). The technique is known as Digital Image Correlation (DIC) or in some geotechnical publications as Particle Image Velocimetry (PIV) (Stanier et al., 2015).

Figure 3.11: Trimming the consolidated clay liner to the required thickness.

Firstly, the technique isolates a patch in a reference image. Secondly, subsequent images are searched for the location of this patch to determine its relative displacement. The process is repeated for a number of patches spread over the image to generate a displacement field. An overview of the DIC method implemented by the GeoPIV-RG software (Stanier et al., 2015) is shown in Figure 3.12.

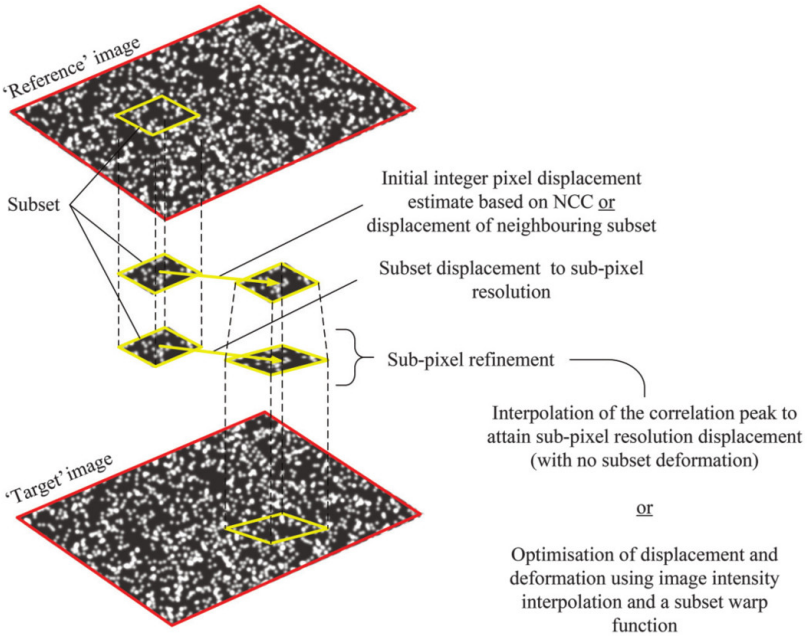

Figure 3.12: Overview of the DIC process to track the displacement of a patch from a reference image to the target image (Stanier et al., 2015).

The reference image can either be kept constant through the analysis (compare image 1→2, 1→3, 1→4, . . . , 1 → i), or it can be updated (compare image 1→2, 2→3, 3→4, . . . , i→ i+1). The first method, a leapfrog analysis, might suffer from loss of correlation as the soil deforms excessively. For the second type, a sequential analysis, "random walking errors" might occur. A "random walking error"

occurs when movement is measured while none has taken place (Stanier et al., 2015). Consequently, care has to be taken when choosing an updating scheme.

Two different DIC software packages were used for the analysis of the bending beams: GeoPIV-8 (White et al., 2003) and its successor, GeoPIV-RG (Stanier et al., 2015). The latter has a number of improvements over the former such as the ability to track deformed and rotated patches, improved resolution, improved precision, automated updating of the reference image and faster processing time. By first estimating the movement of a patch from the movement of the neighbouring patches, rather than searching through the whole image, the processing time of GeoPIV-RG is reduced. Consequently, the software requires regularly gridded patches as input. This makes it less suitable for tracking a row of patches.

For the analyses performed with GeoPIV-RG, the maximum permissible error ($\|\Delta\mathbf{p}\|_{max}$) was set to 10^{-5}. That is the difference allowed between the original patch and its match in the new image before the search terminates. The reference image was set to update only once a patch deformed or rotated so excessively that no match could be found in later images. This updating approach shares some of the problems of using a high leapfrog number in GeoPIV-8. However, it was required by the nature of the images analysed.

After the displacements were calculated, wild vectors and patches with poor correlation were filtered from the dataset. This left gaps in the displacement data. Consequently, linear interpolation was performed on the displacement field to generate a new regularly gridded dataset.

The output data of the DIC analyses was in image space (pixel coordinates). The calibration applied to convert the data from image space to object space (actual dimensions) is discussed next.

3.2.3.2 Calibration of the DIC results

Both software packages (GeoPIV-8 and GeoPIV-RG) have sophisticated calibration algorithms to compensate for lens distortion, refraction through a glass pane, irregular shaped pixels on the camera's sensor and alignment errors (White et al., 2003). However, considering that: 1) camera sensor technology has come a long way since the software was initially released, 2) there was no glass

between the camera and the beam and 3) the camera and lens combination took photos of very low distortion; only a single calibration factor was used for the bending beams. In Section 5.2.4.1 the distortion of the images will be discussed in more detail.

To calculate the calibration factors, the movement of the two loading bars were tracked with GeoPIV-8 and compared to the movement recorded by the loading press. The measured and calculated movements of the loading bars are shown in Figure 3.13 for Beam 12. For this beam the calibration factor was 0.08511 mm/px.

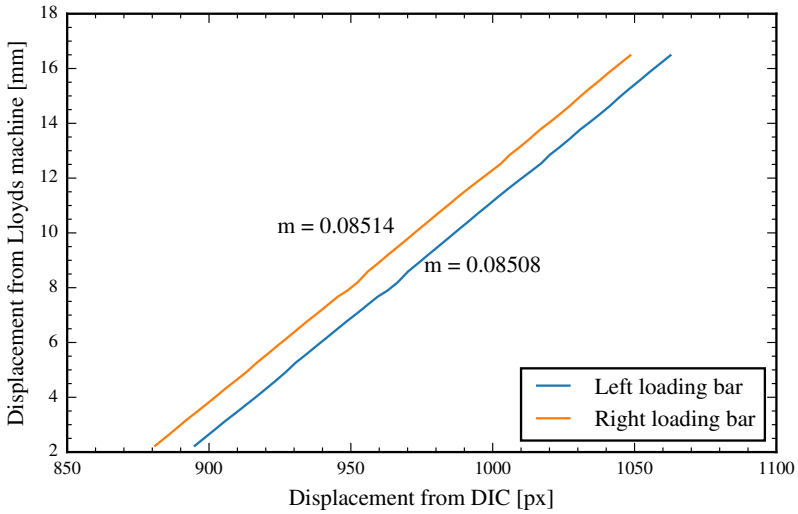

Figure 3.13: Calibration of the DIC results based on the movement of the loading bars.

3.2.3.3 Calculating the effective centre of the beams

The four point bending beam setup used had one loading bar and one support bar that could swivel out of plane. For a stiff material, such as concrete, this allows equal loads to be applied to the sample even when it was initially skew or uneven. For a softer material, such as clay, the loading bars do not level immediately. Consequently, an unequal load might have been applied to the sample. When combined with some inherent variability of clay, the effective centre of rotation of the beam is not necessarily equal to the geometric centre. Consequently, the effective centre of the beam had to be calculated before subsequent analyses could be done.

It was assumed that the minimum horizontal movement will occur at the effective centre of the beam. To determine this coordinate GeoPIV-RG analyses were done on the beams and square displacement

fields extracted (patch spacing of 12 pixels ≈ 1.02 mm). For each of the columns of patches in the square the horizontal movement was calculated relative to its original x-coordinate.

The intuitive way to compare the magnitude of horizontal movement of the patch columns would have been to compare the sum of the absolute value of the movements. However, as the absolute value function is non-smooth, this is problematic for optimisation and other numerical techniques. Consequently, the average of the square root of the sum of the square of the movements (differences) over all the frames was used for comparison:

$$\Delta_C = \frac{\sum_{j=2}^{m} \sqrt{\frac{\sum_{n}^{i=1} (x_i - x_1)^2}{n}}}{m} \tag{3.2}$$

where Δ_C is the horizontal movement indicator for the column of patches, m is the number of frames (photos) analysed and n the number of patches in the column.

This measure is similar to the equation used to calculate the root mean squared error (RMSE) of a data set. The function is smooth and significantly better behaved than the absolute value function. The final 10% of frames of each test were not used for this calculation as macro-crack opened in these frames and resulted in wild horizontal movement.

To find the exact location of minimum movement (that might fall between the tracked columns of patches) a parabola was fitted to 30 points around the perceived minimum and differentiated. In Figure 3.14 the horizontal movement indicator, the fitted parabola and the calculated effective centre of Beam 12 are shown. The average horizontal movement of the central column was 5.37 pixels, that is ≈ 0.458 mm. The process was repeated to find the effective beam centres for all five tests.

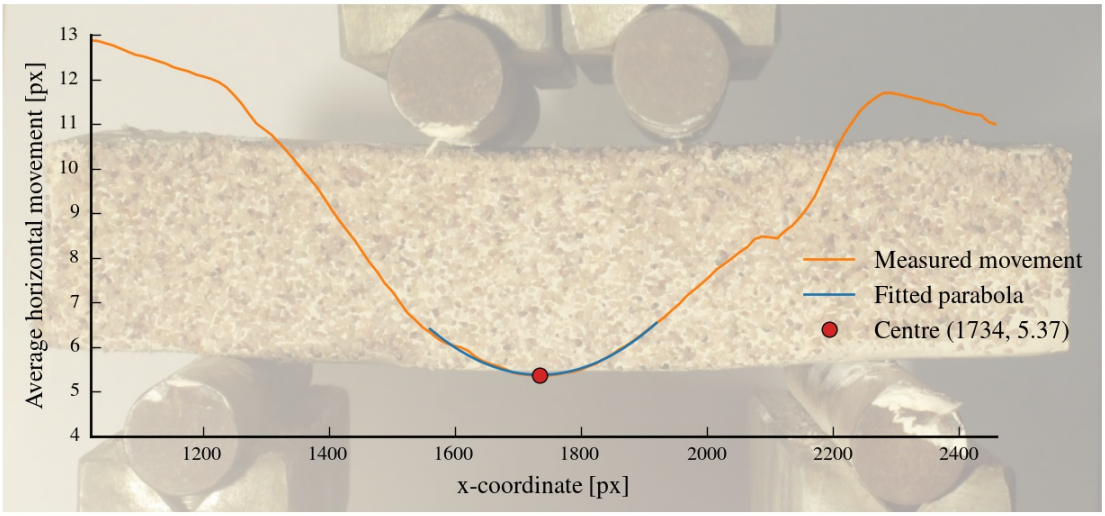

Figure 3.14: Horizontal movement of columns of patches tracked by DIC used to find the acting centre of Beam 12.

3.3 BENDING BEAM TEST RESULTS

In the following section the results of the bending beam tests is discussed. Firstly, graphs of maximum tensile stress in the beams are presented as a function of the deflection measured by the loading press. These stress-displacement results were manipulated (Section 3.3.1.1) before it was used to identify the locations of micro and macro-crack growth (Section 3.3.1.2).

Digital image correlation analysis of the beam allowed for the calculation of curvature with displacement (Section 3.3.2), linear strain at the peripheries (Section 3.3.3.1) and strain fields throughout the beam (Section 3.3.3.2). Finally, these results were used to identify the mobilisation of failure mechanisms in the beams (Section 3.3.4).

3.3.1 Tensile stress-displacement results

The tensile stress at the base of the beams as a function of deflection, for the five beams selected for further analysis (beams 8, 10-13), are shown in Figure 3.15. The deflection shown is that of the two loading bars, as measured by the loading press. The variation in beam thickness (27.9 mm to 29.4 mm) made a noticeable difference in the load-deflection behaviour measured. Consequently,

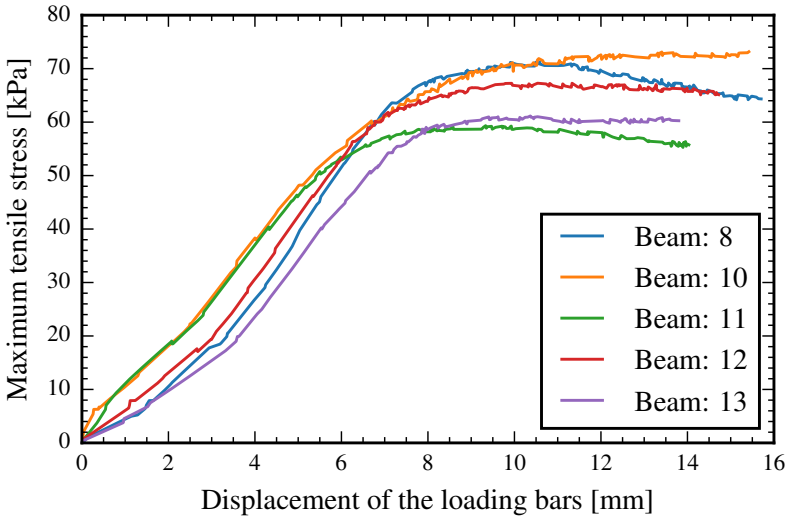

Figure 3.15: Raw tensile stress-deflection results of the bending beam tests.

the maximum tensile stress in the beam was rather calculated and plotted against deflection as it considers the thickness of the beam (see Equation 3.1). For this report the tensile stress measured will be shown as positive, contrary to geotechnical convention. This is done for the sake of clarity and to ensure the curves are comparable to the typical load-deflection curves found in fracture-mechanics literature.

3.3.1.1 Manipulation of the tensile stress-deflection results

The initial segments of the tensile stress-deflection behaviour of the beams were unexpectedly non-linear. This non-linearity is highlighted in Figure 3.16a for Beam 12. As linear behaviour is expected up until micro-fractures form (see Section 2.3.1), further investigation of the stress-deflection data was conducted.

Firstly, the displacement used for the stress-displacement plots was reconsidered. The displacement of a single patch of ≈ 3.4 x 3.4 mm at the effective centre of the beam was tracked using GeoPIV-8. The analysis was repeated for both a patch at the base and a patch at the top of the beams. There was little difference in movement at the top and bottom of the beam, reinforcing the validity of the technique used to find the effective centre.

Once the tensile stress at the base of the beams was plotted against this displacement, the initial

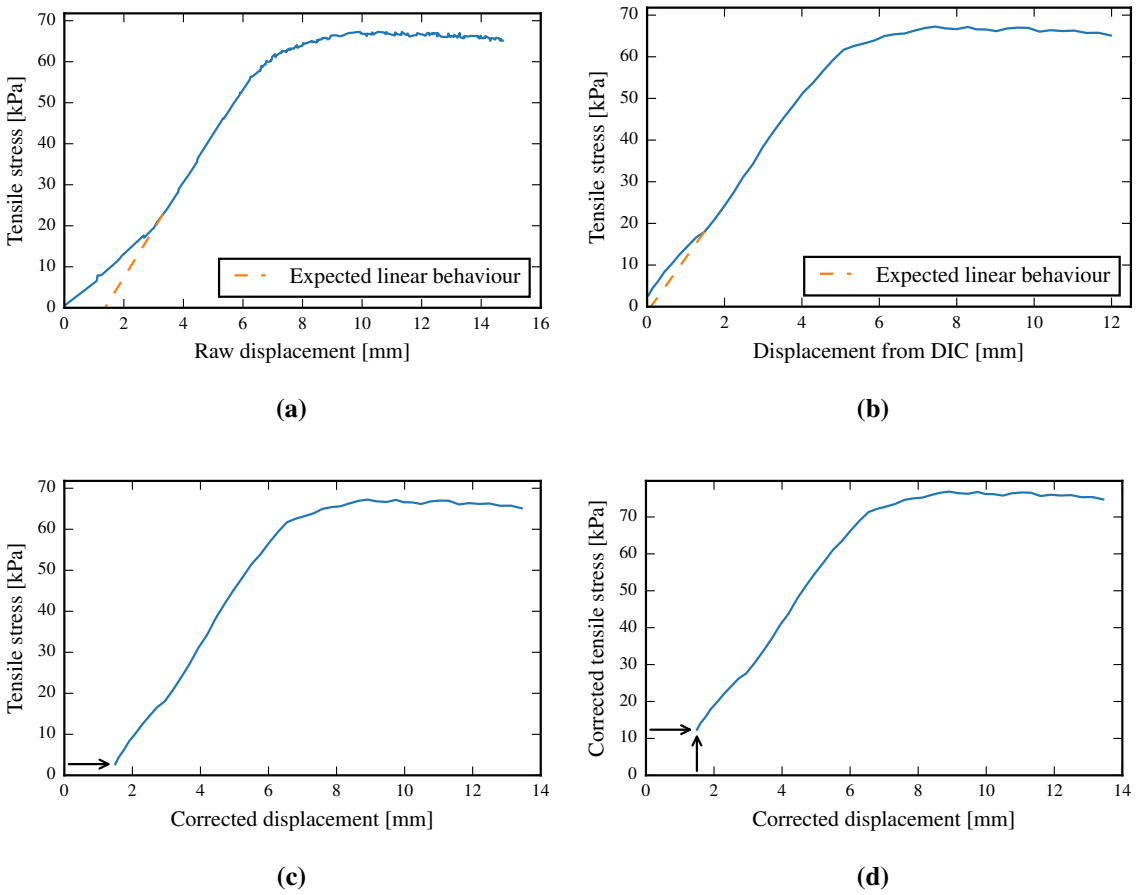

Figure 3.16: Load deflection curves of Beam 12: a) raw data from loading press, b) displacement from DIC analysis, c) displacement offset and d) load and displacement offset.

behaviour of the curve was significantly closer to the expected linear behaviour (Figure 3.16b). Thus, at the start of the tests the loading bars probably punched into the clay, resulting in the skewed displacement measurements from the loading press. Once the contact area between the clay and the loading bars had increased sufficiently, the expected linear behaviour was recorded by the loading press.

A further consideration for interpreting the stress-deflection curves is that the clay beams are soft enough to deflect under own weight. Consequently, the displacement was offset by this initial mid-span deflection (see Figure 3.16c).

Finally, the load (stress) applied also had to be adjusted for the self-weight of the beam. The equilibrium of the system was investigated with Figure 3.17. The reactions due to the self-weight of the beam

are R_C and R_D. To convert the distributed load of the self-weight to an equivalent point load offset, the reactions at the supports due the load offset (R_A and R_B) should equal R_C and R_D. Given an average moisture content for the five beams of 31% (see Table 3.3), and a G_s value of 2.661 g/cm^3 for kaolin, the unit weight of the beams at full saturation is calculated as 18.75 kN/m^3. For Beam 12 with dimensions 150 x 75 x 28.62 mm the reactions are $R_C = R_D = 3.01$ N $= R_A = R_B$, thus the offset is $P = 6.04$ N. From here onwards all stress-displacement plots are those of the corrected data as shown in Figure 3.16d.

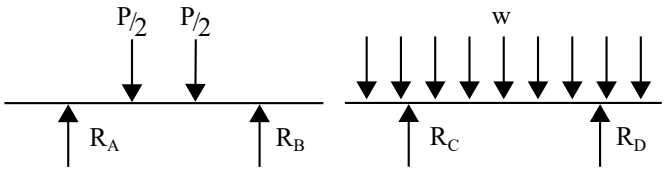

Figure 3.17: Free body diagrams used to calculate the load offset (P).

Table 3.3: Post-test moisture content of the five beams analysed.

Beam	Moisture content [%]
8	30.79
10	30.99
11	31.03
12	31.06
13	31.14

3.3.1.2 Identification of micro- and macro-crack growth

The tensile stress-deflection curves in Figure 3.18a are initially linear until micro-cracks form and plastic damage occurs at the crack tips. These micro-cracks grow until macro-cracks open and the tensile stress reaches it peak. Thus, the maximum load occurred when the system as a whole reached failure, and not at the first local failure. After the macro-cracks opened, the stress in the beams can either plateaus or drop (see Section 2.3.1). The stress plateau, rather than stress drop, observed for the current results represents the ductile behaviour expected of a) a clay and b) a small fracture specimen (see Section 2.3). The tests were terminated before total collapse of the sample occurred, as shear at the supports was thought to be skewing the load measurements towards the end of the tests.

In Figure 3.18a the occurrence of micro-cracks and the opening of macro-cracks are indicated with black dots. The occurrence of micro-cracks were assumed to coincide with a sharp change in slope.

Marco-cracks were judged to occur at the peak bending-stress. Incidentally, the two outliers observed were for Beam 10. This beam was significantly thinner than the others, reinforcing the principle that fracture behaviour is specimen size dependent (Section 2.3.1).

The five stress-deflection curves, as well as the displacements of crack growth, were averaged to obtain the stress-deflection curve in Figure 3.18b. This curve is taken as representative for these kaolin beams consolidated to 610 kPa.

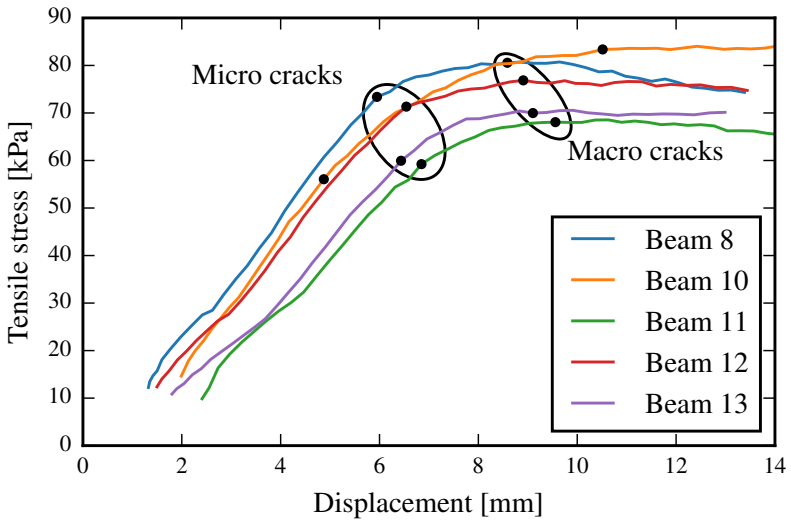

(a)

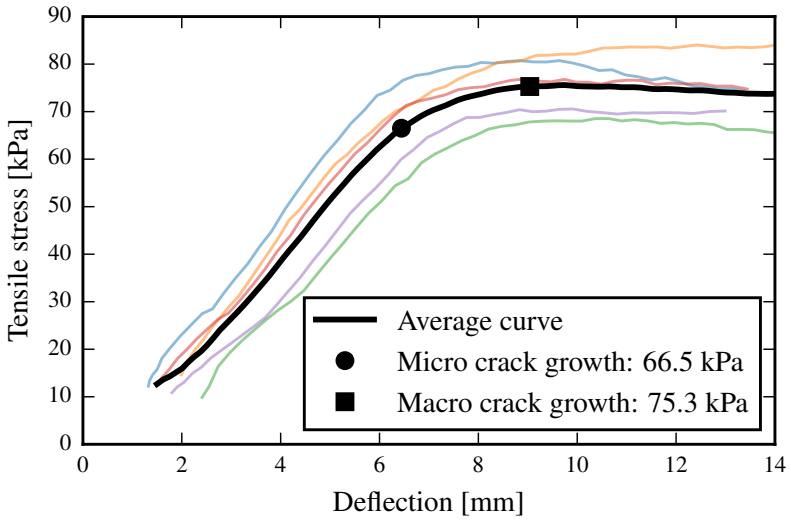

(b)

Figure 3.18: Stress-displacement curves for the five bending beam tests used: a) micro- and macro-crack growth indicated and b) average stress-deflection plot.

3.3.2 Radius of curvature

The DIC results allowed for the calculation of the radius of curvature of the beams during the bending beam tests. To calculate these radii at the base of the beams, a series of patches similar to those shown in Figure 3.19 were tracked for each beam. The GeoPIV-8 software was used. The leapfrog flag was set to 1, implying a sequential analysis. As there was large movements between frames, the risk of random walking errors was quite low.

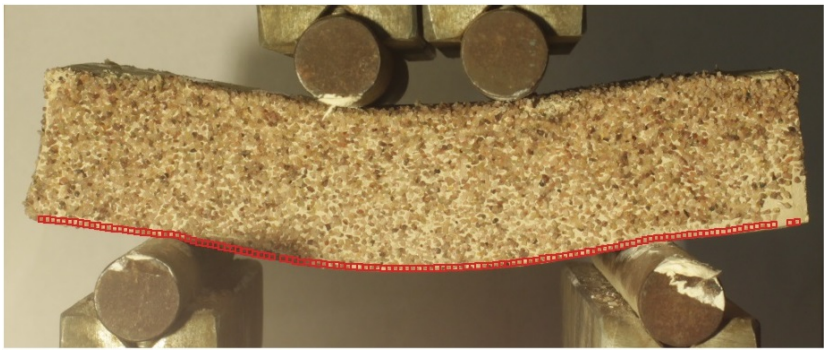

Figure 3.19: Tracking the edge of the beam using DIC.

If a small enough segment of the beam is considered, the beam can be assumed to approximate an arc and the radius of curvature is calculated as:

$$\rho = \frac{H}{2} + \frac{W^2}{8H} \tag{3.3}$$

where H and W is defined in Figure 3.20. Consequently, only three coordinates are required to calculate the curvature: A, B & C. Curve A-C-B was extracted from the DIC results over a width AB = 30.5 mm, with C at the acting centre of the beam. The distance of 30.5 mm was the separation between the two loading bars. The calculation was repeated for every image to generate the relationship between radius of curvature at the base of the beams and central displacement shown in Figure 3.21. The average radius of curvature-displacement curve, as well as micro and macro-crack growth are also shown.

3.3.3 Strain behaviour of the beams

The strains in the beams as the tests progresses were calculated from the displacement results of the DIC analyses. Patches with a diameter of 1.02 mm, spaced at 1.02 mm were used. Firstly, linear horizontal strain was calculated (Section 3.3.3.1) around the effective centre of the beams,

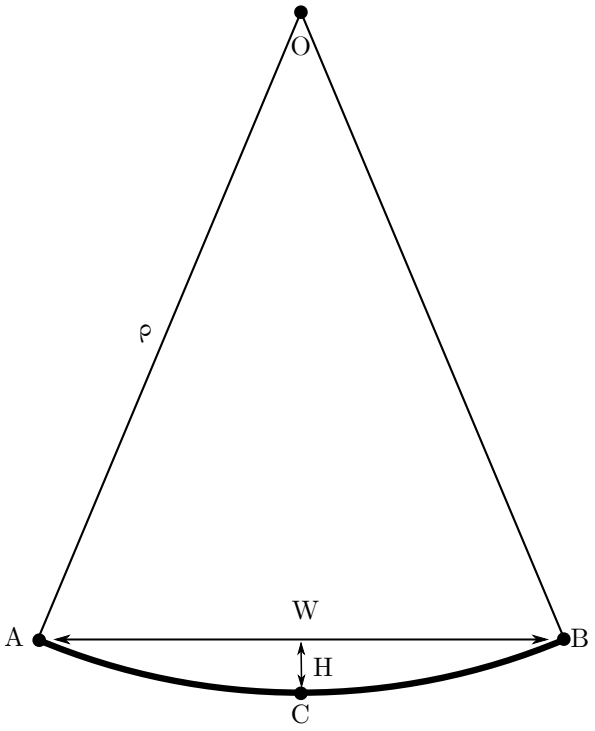

Figure 3.20: Construct used to calculate the radius of curvature (ρ) of the beams.

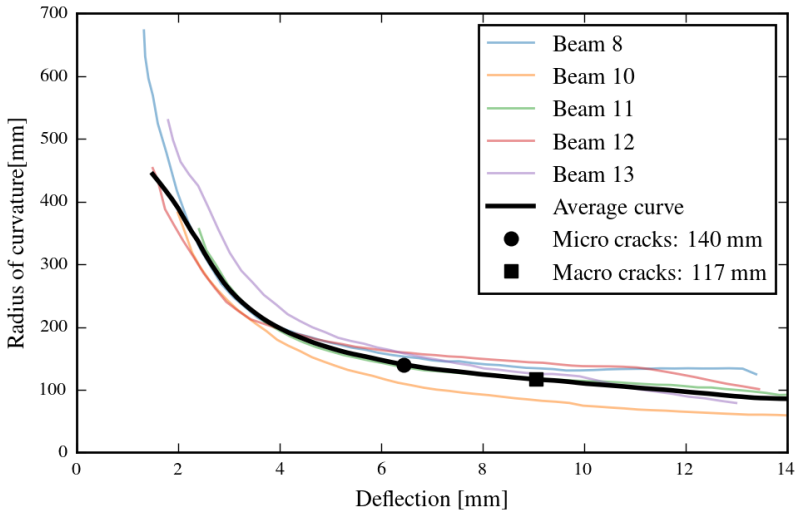

Figure 3.21: Radius of curvature at the bottom of the beams as a function of central displacement.

whereafter the GeoPIV-RG algorithm was used to calculate strain fields over the beam as a whole (Section 3.3.3.2)

3.3.3.1 Linear strain

The linear horizontal strain at the base of the beams were calculated from the patches shown in Figure 3.19, around the effective centre of the beam as (Gere & Timoshenka, 1991):

$$\varepsilon_H = \frac{\Delta l}{l_0} \tag{3.4}$$

where Δl is calculated from the movement of the patches and l_0 the gauge length.

As with the stress-displacement curves in Section 3.3.1.1, the deflection of the beam due to self-weight had to be taken into account. This initial deflection generated strain in the beam that was not measured by the DIC analyses. As the own-weight deflection is usually quite small, the initial deflection was assumed to be elastic. Consequently, the initial elastic strain due to own weight deflection could be estimated as:

$$\varepsilon_H = \kappa \cdot y \tag{3.5}$$

where κ is the curvature of the beam (the inverse of the radius of curvature (ρ) calculated in the previous section) and y the distance from the neutral axis to the periphery.

As clay is an elsto-plastic material, the behaviour of the beams did not remain elastic throughout the tests and the strain calculated was sensitive to the gauge length (l_0) used. The tensile strain at the periphery of Beam 12 calculated for a number of different gauge lengths is shown in Figure 3.22. Not only did the magnitude of strain differ with gauge length, but also the strain behaviour.

From the results in Figure 3.22 two representative gauge lengths were chosen for the subsequent analyses. The first of 3.05 mm represented the group of curves that had an steep initial increase in strain before it flattens out. As this gauge is relatively fine, it could be representative of the micro behaviour of the beam. The second group of curves represented the macro behaviour of the beam and had a slightly flatter initial increase before it steeply shot off and was represented by a gauge length of 15.23 mm. The gauge lengths corresponded to 1/10th and 1/2 of distance between the two loading bars. Thusyanthan et al. (2007) did not state the strain gauge length used for their bending beam tests, however, the behaviour appears similar to that of the longer strain gauge.

In addition to the results of Figure 3.22, the linear strain calculation was also applied to the displacement

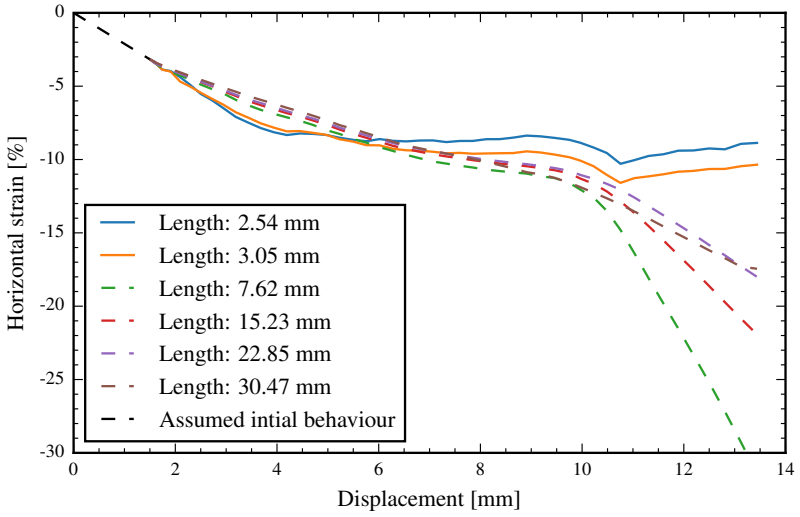

Figure 3.22: The effect of gauge length on the strain calculated for Beam 12.

fields from a standard GeoPIV-RG analysis. This allowed for the calculation of the horizontal strain distribution with depth. Two columns of patches were isolated to either side of the effective centre and the linear strain was calculated between them. This approach was also followed by Thusyanthan et al. (2007). As with all the strain results discussed before, these were offset with the relationship $\varepsilon_H = \kappa \cdot y$ to account for the initial deflection of the beam. In Figure 3.23 the strain distribution with depth is shown for Beam 12 for both the narrow and the wide gauge as the central displacement increased.

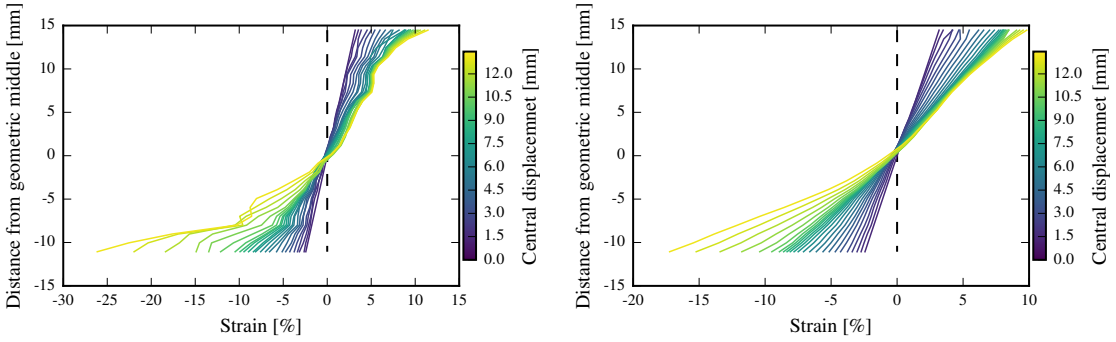

Figure 3.23: Linear strain with depth at the centre of Beam 12 at various central displacements: a) Gauge length = 3.05 mm, b) Gauge length = 15.23 mm.

Due to the presence of wild vectors some data was lost at the base of the beam. Initially the neutral axis is in the centre of the beam and the strain distributions changes linearly with depth, similar to

the findings of Thusyanthan et al. (2007). Once macro cracks forms the strain distribution becomes non-smooth for the small gauge length and non-linear for the longer gauge length as fracture (tension) or yield (compression occurred). The neutral axis also moves downwards as the beam yields in compression.

For further discussion of the linear horizontal strain only the strain at the peripheries of the beams are considered. In Figure 3.24 tensile stress-displacement and curves of horizontal strain at the periphery are shown for all five beams for a gauge length of 3.05 mm. A similar plot is shown in Figure 3.25 for a gauge length of 15.23 mm. For all plots the average curve, as well as the displacements of behaviour change (i.e. from linear to non-linear) are shown. As discussed in Section 3.3.1.2, the behaviour changes of the stress-displacement curve are judged to correspond to micro and macro-crack growth.

In the strain plots for the 3.05 mm gauge (Figure 3.24) the compressive behaviour changed from linear to non-linear at a consistent displacement for all tests. Similarly, the tensile behaviour plateaued at the same displacement. However, the magnitude of these displacements varied between compression, tension and micro-crack growth on the stress-deflection curve. The variation could be due to the slightly noisier data for the smaller gauge (compare Figure 3.23a and b). Furthermore, as macro-cracks opens the strain is expected to increase. However, after the change in behaviour the compressive strain plateaued and the tensile strain dropped for the small gauge.

Due to the nature of the bending beam test (two loading bars) there are two locations where the bending moment changes sharply and thus two cracks will eventually open (see Figure 3.28c, discussed later). The small gauge length fell between these cracks on the segment of clay that stopped straining once the cracks opened. Thus, the strain measured with the small gauge plateaued and decreased.

For the wider 15.23 mm gauge the strain behaviour in Figure 3.25 changed from linear to non-linear at different strains in tension and compression. The change in tensile strain aligned with the micro-crack growth identified from the stress-displacement curve, verifying that micro-crack growth occurred at this displacement. The change in compressive strain aligned with the macro-crack growth that usually coincides with plastic deformation. Both the change in compressive and tensile strain occurred at the same magnitude of strain, however, at different central settlements.

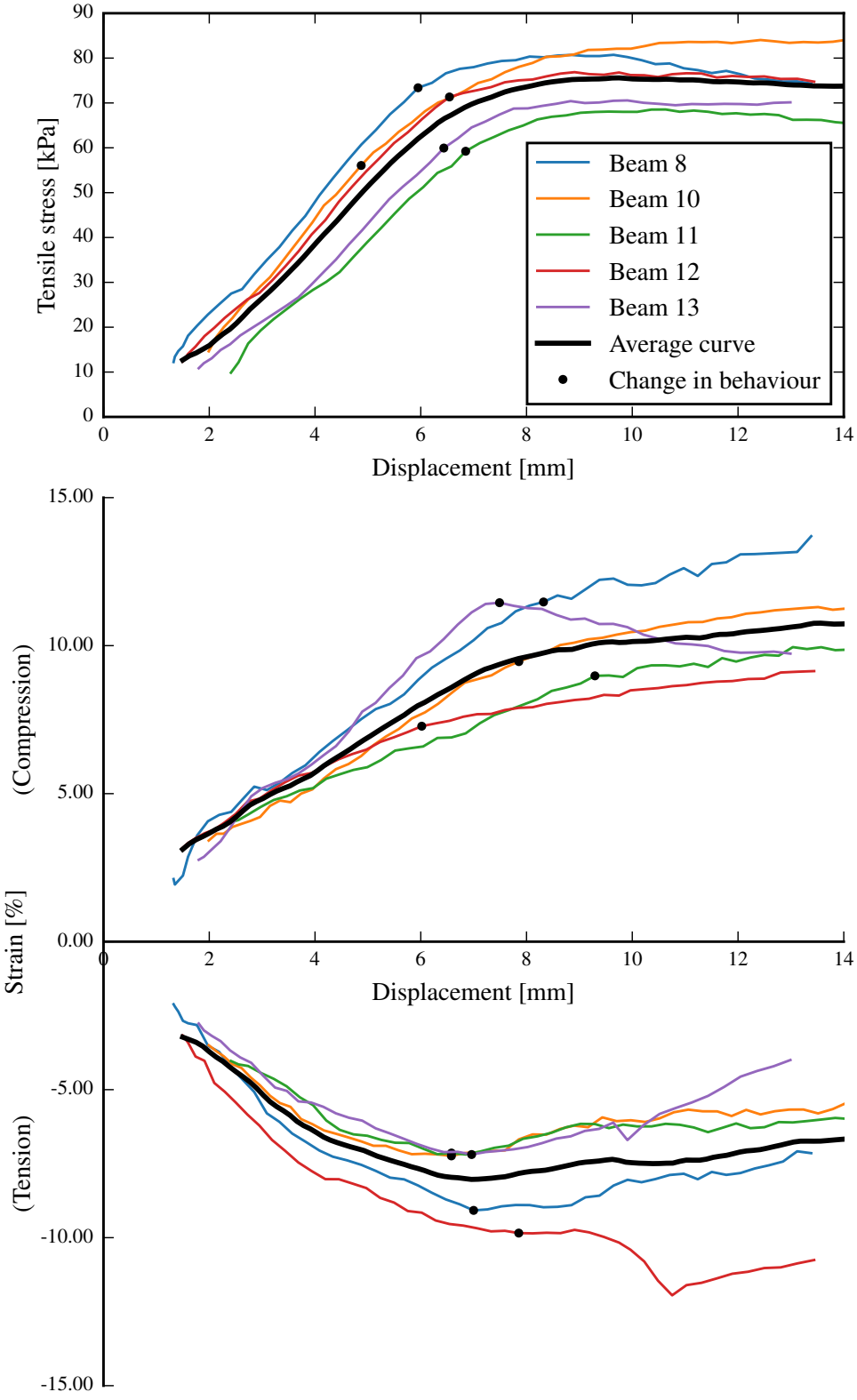

Figure 3.24: Stress-deflection and linear horizontal strain-deflection plots for five beams, strain calculated with a gauge length of 3.05 mm.

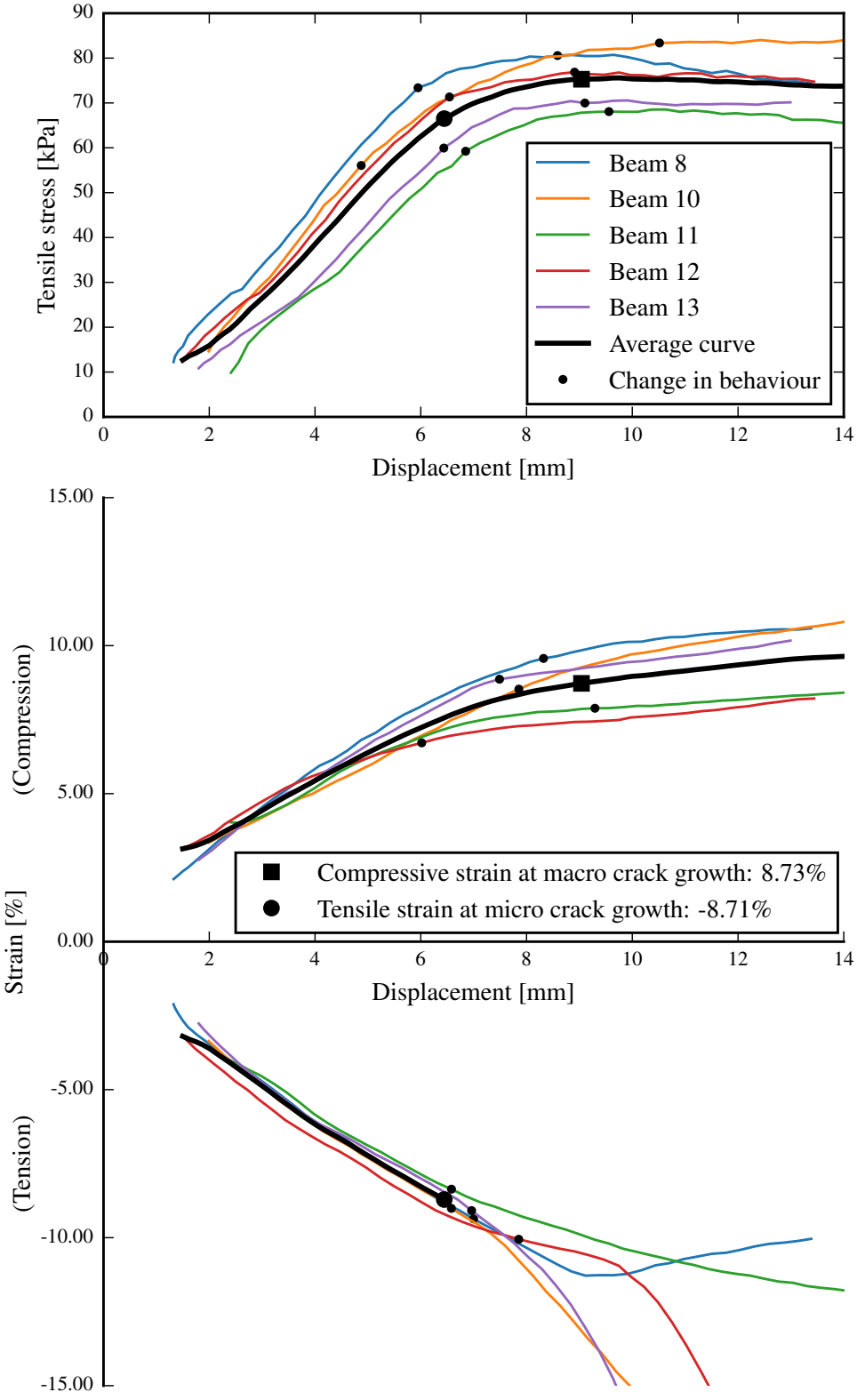

Figure 3.25: Stress-deflection and linear horizontal strain-deflection plots for five beams, strain calculated with a gauge length of 15.23 mm.

The tensile strain where micro-cracks occurred was -8.71% at a stress of 66.5 kPa for the average curve shown in Figure 3.25. Macro-cracks were judged to have opened at a stress of 75.3 kPa and a compressive strain of 8.73%. These strain values are significantly higher than those found in literature (see Table 2.2). The higher strain magnitudes could be due to the following four reasons:

1. Thusyanthan et al. (2007) found that the tensile strain at failure in a four point bending beam test of a clay increased with the consolidation pressure. The consolidation pressure of 610 kPa used for the current analysis is higher than that used for most of the tests in literature.
2. Thusyanthan et al. (2007) found that as the initial suction in the sample decreased the failure strain increased sharply. In Figure 3.26 the fracture strain of a clay beam is shown as a function of the initial effective stress (or suction in this case) in the beams. Since the beams for the present study were tested at fairly low suctions (no drying out was allowed) the higher strain measured is viable.
3. The strain magnitude measured is highly sensitive to the strain gauge length used. If a larger strain gauge was used, the strain measured at fracture would have been lower.
4. A smaller sample does not accurately capture the structure of the full scale material as it contains fewer fissures and fractures. For example, the undrained shear strength of clay has been shown to be highly dependent on the size of the sample tested (Clayton et al., 2016). Similarly, fracture behaviour has been shown to be specimen size dependent (Section 2.3.1). Consequently, the small clay beams tested would have failed at a higher strain than a full scale liner.

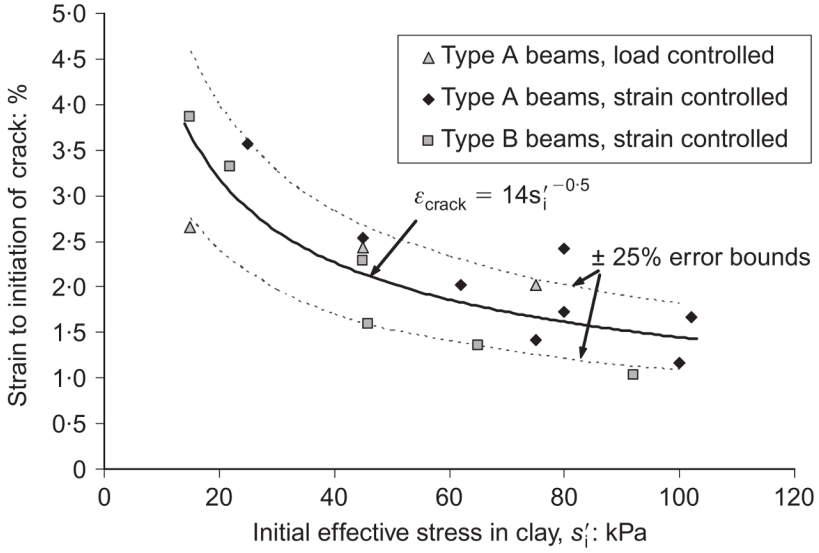

Figure 3.26: Relationship between failure strain and initial effective stress in the clay (equivalent to the suction) for test done by Thusyanthan et al. (2007).

3.3.3.2 Strain fields

The GeoPIV software includes an algorithm to calculate strain fields from the measured displacement fields. In Figure 3.27 strain fields of linear horizontal are shown for Beam 12. Figure 3.27a is from the linear part of the load-displacement curve, 3.27b at the origin of micro-crack formation and 3.27c at the origin of macro-crack formation (as identified from the load-deflection plots). The displacement that occurred from 3.27a to 3.27b at midspan is the same in magnitude as that from 3.27b to 3.27c. A similar series of strain fields is shown in Figure 3.28 for total shear strain. No adjustments were made to the strain fields for the initial deflection of the beam due to own weight.

In the horizontal strain fields shown in Figure 3.27 the strain in the centre of the beam varied linearly from top to bottom as expected. Two diagonal strain concentrations are also present, extending from the bottom supports inwards. These concentrations are more pronounced in the shear field plots in Figure 3.28 and appears to be initiate at the expected angle of 45°. From Figure 3.28b to Figure 3.28c macro-cracks opened and these strain concentrations changed from diagonal to curved. As the macro-cracks opened these concentrations became significantly more pronounced.

The strain fields in Figures 3.27 and 3.28 can be summarised as histograms of the fraction of the beam at a given strain. In Figure 3.29a the histogram for the horizontal strain fields shown in Figure 3.27 is presented. The histogram for the strain fields in Figure 3.28 is shown in Figure 3.29b. The size of the bins is 0.5% strain.

Initially, during linear stress-displacement behaviour in Figure 3.27a, a significant fraction of the beam was without any horizontal strain (see Figure 3.29a). Once micro-cracks occurred, the fraction of unstrained soil reduced significantly. From the occurrence of micro-cracks to the opening of macro-cracks the strained area of the beam did not increase that much. However, the average strain of the beam increased (represented by the area of the histogram in tension). Furthermore, a greater fraction of the beam is in tension than compression as the histograms are not symmetrical but skewed to the right. The fractions of strain shown in Figure 3.29a are slightly obscured by the two overhanging edges of the beams where no strain occurred.

In contrast to the histograms of horizontal strain, the histogram for the shear strain shown in Figure 3.29b is double peaked during linear behaviour. The first peak at zero shear strain is due

to the overhanging edges of the beam. The second peak, however, implies that a significant part of the beam is at approximately 3.4% strain. This peak possibly coincides with the strain concentrations present in Figure 3.28a. The peak in the distribution moved to the right when micro-cracks occurred (i.e. increasing in magnitude) while flattening out (i.e. less concentrated) until there was a more uniform distribution in shear strain when the macro-cracks opened. The lack of any peak (concentration) in the histogram when the macro-cracks opened indicates that the two strain concentrations now dominates the behaviour of the beam.

3.3.4 Mobilisation of failure mechanisms

From the strain fields shown in Figures 3.27 and 3.28 the evolving failure mechanisms can be identified. The development of the mechanisms were similar in all five beams. These steps, illustrated in Figure 3.30, are:

Bearing capacity failure (Figure 3.30a): Below the two loading bars the clay strains in shapes similar to the slip surfaces calculated by Stuart (1962) below two adjacent footings on cohesive soil. This bearing capacity failure of the clay below the loading bars resulted in the initial non-linear stress-displacement behaviour discussed in Section 3.3.1.1. The lack of symmetry of the strain could be due to the right-hand loading bar swivelling (Section 3.2.1) and making contact at the back of the sample first.

Shear compression failure (Figure 3.30b): In Figures 3.28a and b two diagonal strain concentrations runs from support bar to loading bar. Failure along these diagonals would be a typical shear-compression failure also found in concrete (Kong & Evans, 1987). The compression refers to crushing of the material below the loading bar.

Shear-tension failure (Figure 3.30c): As the displacement of the beam increased (Figures 3.27c and 3.28c) the strain concentrations at the support bars curved away from 45° towards the base of the beam. These strain concentrations eventually grew into a macro-crack as a shear-tension failure (Kong & Evans, 1987). Thusyanthan et al. (2007) predicted that these cracks will occur whenever the minor principle strain is in tension. From Figure 3.31 it can clearly be seen that this is the case for Beam 12.

Zero net-stress (Figure 3.30d): This mechanism is not a failure mechanism as such but the result of interplay between the shear, tensile and compressive stresses. In both Figures 3.27c and 3.28c a X-shaped area of low strain can be seen. In this area the shear and tensile and compressive stresses cancels out resulting in a region of zero net stress (and strain) (Case & Chilver, 1971).

3.4 SUMMARY OF THE BENDING BEAM TESTS

The bending beam tests has been successfully used as an initial investigation into the behaviour of unreinforced clay liners subject to differential settlement. Strain fields in the beams, generated from DIC results, have verified the use of the four-point bending test to study the tensile behaviour of clay. Not only were there significant tensile-shear strain concentrations once macro-cracks opened (Figure 3.27c), but the majority of the beam was also in tension (Figure 3.31).

The analyses highlighted the importance of choosing the correct gauge length for strain calculations in bending beam tests. Only for the wider gauge was both the tensile and compressive strain behaviour initially linear as expected. Furthermore, only for the wider gauge length did the rate of tensile strain increase after fracture, as expected.

The tensile stress-displacement curves were calculated in Section 3.3.1, as the load-displacement results were not comparable due to the variation in beam thickness. However, the tensile stress-displacement behaviour is equivalent to the load-displacement behaviour. Furthermore, as load-displacement is a more intuitive concept, the remainder of the report will refer to the load-displacement behaviour of the clay, rather than the tensile stress-displacement.

From the results of the bending beam tests it was found that clay in tension behaves in three distinct stages: 1) initial linear elastic load-displacement behaviour, 2) forming of micro-cracks and 3) opening of macro-cracks. A summary of these stages is presented in Table 3.4.

Table 3.4: Behaviour of clay in tension during the linear elastic stage, forming of micro-cracks and forming of macro-cracks.

Property	Linear elastic stage	Micro cracks forms	Macro cracks forms
Load-deflection curve	Linear	Changes from linear to non-linear	Peaks and then either plateaus or drops
Shear strain distribution in the beams	Shear strain concentrated and of low magnitude.	Shear strain less concentrated and at a higher magnitude	Gradual distribution of shear strain.
Change in horizontal strain distribution in the beams	N.A.	Significant increased in strained area.	Smaller increase in strained area corresponding to a smaller change in load.
Governing mechanism	45° shear strain concentrations.	45° shear strain concentrations.	Curving shear-tensile strain concentrations.
Failure type	N.A.	Local.	Global.

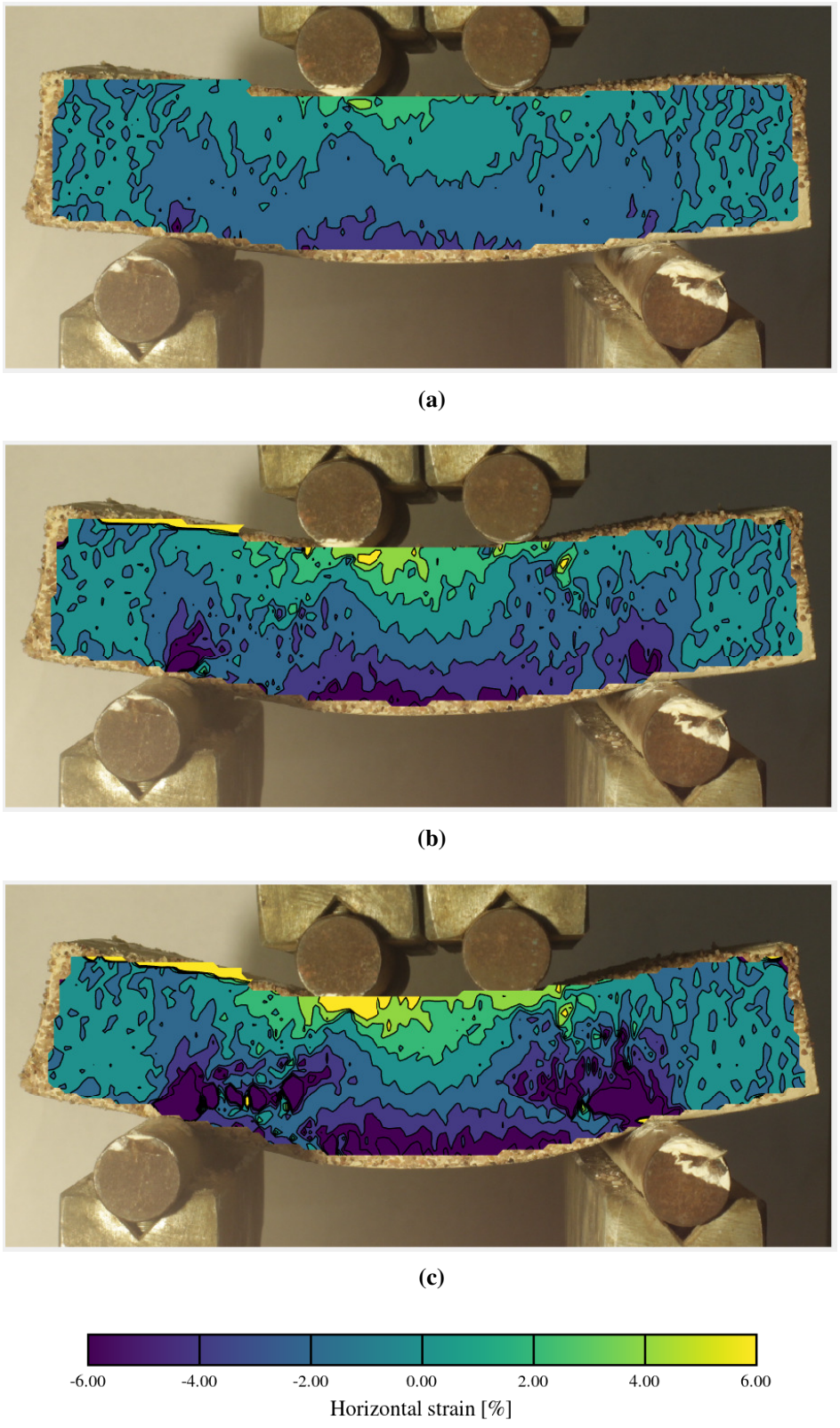

Figure 3.27: Total linear horizontal strain in Beam 12 for: a) linear behaviour b) the origin of micro-cracks and c) the origin of macro-cracks.

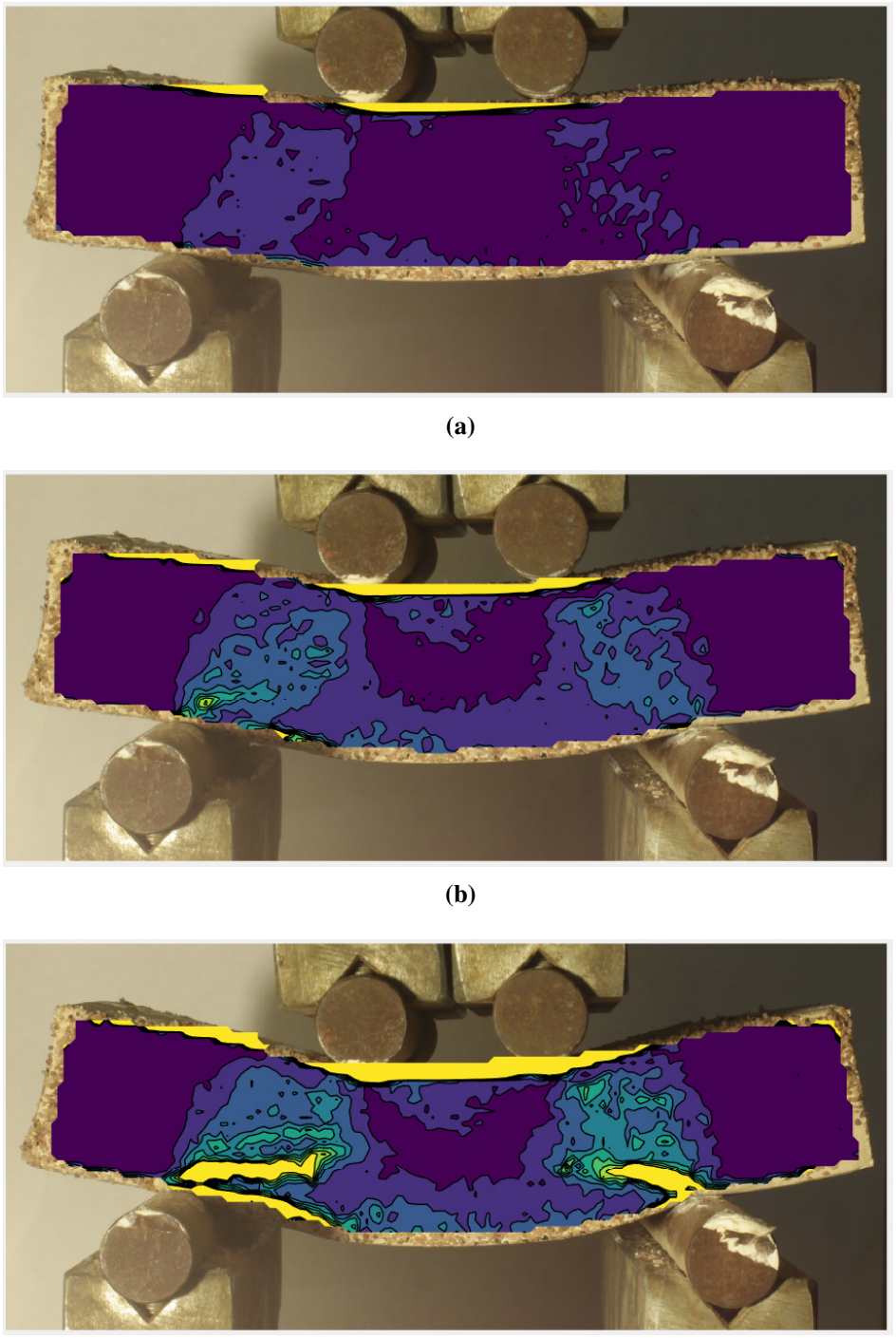

Figure 3.28: Total maximum shear strain in Beam 12 for: a) linear behaviour b) the origin of micro-cracks and c) the origin of macro-cracks.

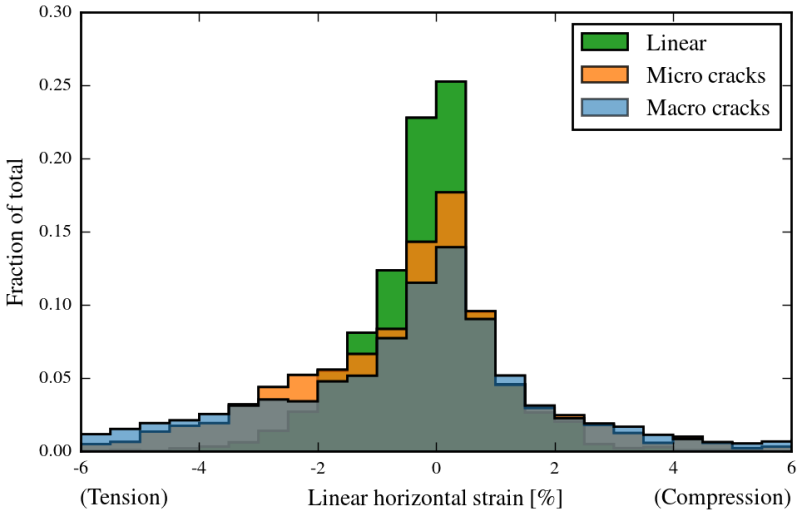

(a)

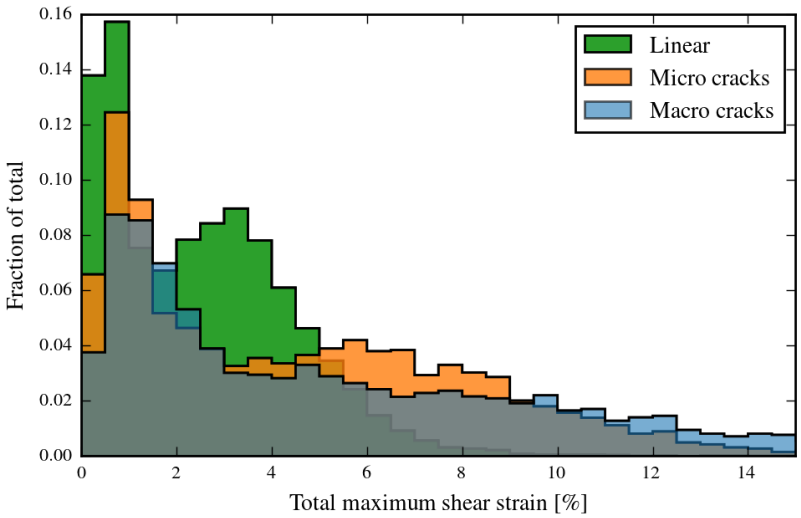

(b)

Figure 3.29: Distribution of strain in the beams for three points along the tensile stress-displacement curve: a) linear horizontal strain and b) shear strain.

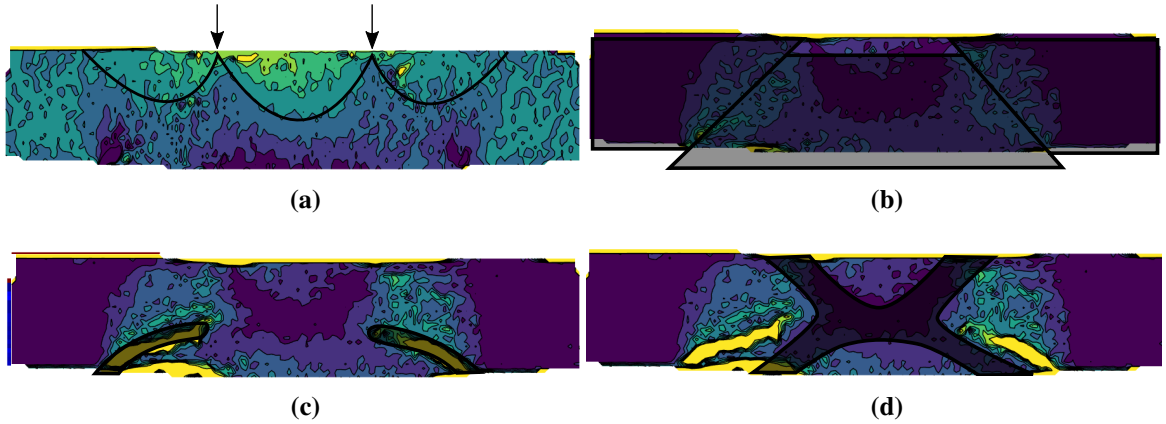

Figure 3.30: Progressive development of mechanisms identified in the bending beam tests: a) bearing failure (shear strain field), b) compression-shear (horizontal strain field), c) shear-tension (horizontal strain field) and d) zero strain zone (horizontal strain field).

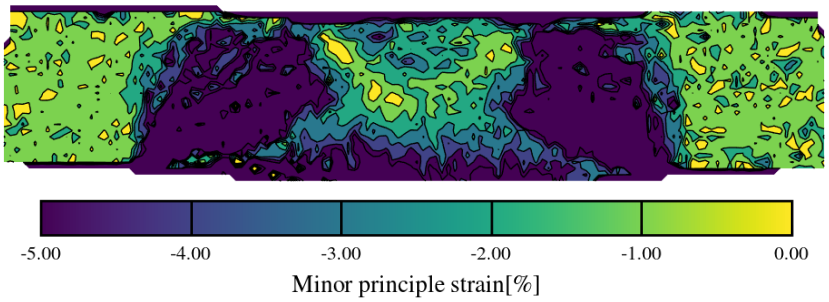

Figure 3.31: Minor principle strain in Beam 12 when macro-cracks first occurred (tensile strains are negative).

CHAPTER 4 FINITE ELEMENT ANALYSES

In Chapter 3 the fracture behaviour of unreinforced clay beams was investigated by means of a four point bending beam test. It was found that the fracture of clay is a three-stage process where firstly micro-cracks and secondly macro-cracks form. The occurrence of the cracks in the liner represent the serviceability limit state failure (SLS) discussed in Section 2.1.

To prevent and stunt the formation of these cracks, geogrid reinforcement was proposed. It was concluded in Chapter 2 that centrifuge modelling is a viable technique to study the behaviour of geogrid reinforced clay liners. However, as centrifuge modelling is a complex and time consuming process, numerical modelling was first conducted to obtain a better grasp of the problem. Finite element analyses (FEA) were done using the commercial software ABAQUS 6.13-3. Relying on the knowledge gained from the FEA, the centrifuge models in Chapter 5 were designed for maximum efficiency.

A paper entitled *Optimal geogrid reinforcement of clay liners* was presented by Marx & Jacobsz (2016b) at the First Southern African Geotechnical Conference in Rustenburg, South Africa. The paper was followed by *Geometric factors influencing the optimal position of geogrid reinforcement* by Marx & Jacobsz (2016a) at the 6th European Geosynthetics Congress in Ljubljana, Slovenia. The remainder of this chapter is based on the content of the two papers.

4.1 INTRODUCTION

Continued population growth places strain on current waste disposal facilities in South Africa. Limited air space suitable for landfilling, however, drives the need for alternative solutions to expand waste disposal capacity. One such solution is the vertical extension of current landfill sites (i.e. piggyback

landfills). This method entails building a new, fully lined, landfill on top of the existing waste. The old underlying general municipal waste, however, is prone to local and differential settlement (see for example El-Fadel & Khoury (2000)). Settlement of this waste will result in the clay liner bending, and eventually cracking, increasing its permeability and compromising its ability to perform as an effective barrier. Consequently, some form of tensile reinforcement is required in the clay.

In Chapter 2 of this document it was found that piggyback landfilling is viable a solution to the growing waste demands of South Africa. However, settlement of the old waste could compromise the integrity of the new liner. Geogrids can be used to reinforce the clay by disrupting the tensile strain fields that develop (Jones, 1985) and by providing support to the clay liner. Marx & Jacobsz (2016b) conducted a numerical study to investigate the optimal geogrid reinforcement positions in a simple clay liner, subject to differential settlement. The current chapter is an extension of that work, investigating the influence of various geometric factors on the optimal reinforcement strategy (ORS). The ORS is defined as the positions in the liner where reinforcement should be placed to minimise liner tensile strain, for a given reinforcement cost. Furthermore, the ORS also includes the proportion of total reinforcement cost to be expended at each of these positions to achieve the minimum tensile strain in the liner.

The objective was therefore to find the optimal position(s) within the liner at which to place the geogrid(s). This is done by adjusting the reinforcement stiffnesses and positions, to minimise the maximum tensile strain generated in the liner by a given imposed differential settlement profile, given a total cost of reinforcement. To summarise: the ORS entails the optimal position of geogrids, and stiffness of the geogrid placed at that position, given a maximum, total reinforcement cost.

To better understand the problem, the influence of a couple of key factors on the behaviour of the liner was investigated. These are: the overburden pressure applied, clay liner thickness, magnitude of central settlement, and the width and shape of the settlement trough developing in the underlying waste body. Each of these factors is a key consideration for piggyback landfill design:

1. The height of the landfill changes during the lifetime of the landfill (due to construction, but also consolidation of the waste). This, combined with the inherent variability in the unit weight of the waste (**Zekkos2005**; Kavazanjian, 2001), result in highly variable overburden pressure. For the remainder of the chapter the variation in height of the landfill will be represented by a change in overburden pressure.

2. The thickness of the landfill liner is usually prescribed by a national standard. However, when conducting model studies in a geotechnical centrifuge at high centripetal acceleration, the dimensions of the required model may result in it being quite fragile (a 12 mm thick model will represent a 600 mm thick prototype at 50G). Should the ORS prove to be insensitive to the liner thickness, models of more practical dimensions can be build for centrifuge modelling.
3. The width, shape, and magnitude of central settlement of a settlement trough occurring in a landfill depends on the occurrence of local voids and differential settlement. Both factors are difficult to measure in practice, highly variable in their nature, and not well understood.

The effect of differential settlement, rather than local settlement due to void formation, on the liner was investigated. Whilst local settlement might result in more severe deformation of the liner, this type of settlement is highly unlikely to occur in piggyback landfills to be constructed in South Africa. Considering that 1) primary settlement of the liner occurs in the first couple of months only (Section 2.2), and 2) the youngest landfills not constructed to the DWAF (1998) specifications will be 18 years old in 2016. It can be assumed that at any site viable for piggyback extension, current settlement will be mainly due to bio-degradation of the municipal waste and will therefore be more likely to be subject to differential settlement. Furthermore, during preparation of the surface of the old landfills for construction of the piggyback, any voids close to the surface will be collapsed, should they exist. Consequently, if a void is still able to form 18 years after deposition of the waste, it will be deep enough below the surface to induce differential settlement.

4.2 FINITE ELEMENT ANALYSES

To investigate the influence of the various factors identified on the ORS of the clay liner, a number of different finite element (FE) models were analysed. These plane strain problems were analysed in ABAQUS 6.13-3. The modelling approach was validated against the centrifuge models of Rajesh & Viswanadham (2011) and Rajesh & Viswanadham (2012b). The FE models of this study were equivalent to the prototype problems that the authors modelled in the centrifuge.

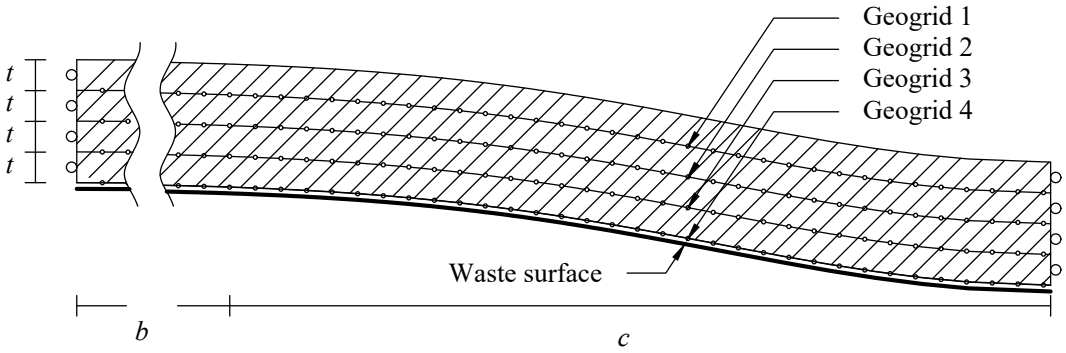

Figure 4.1: General geometry of FE models analysed.

4.2.1 General model

The key components of the model and the symbols representing them are presented in Figure 4.1. These are:

1. A clay liner of thickness $4t$ and half-width $b + c = 25$ m, where c is the half-width of the settlement trough. Between 4272 to 6768 continuum, plane strain, eight-node (CPE8) elements were used to model this liner. An isotropic linear elastic undrained Mohr-Coulomb plasticity model was used, i.e. an elastic-perfectly plastic model. Plé et al. (2012), Rajesh & Viswanadham (2012a) and Rajesh & Viswanadham (2015) all used an elasto-plastic Mohr-Coulomb model to model clay liners (see Section 2.5.3). Furthermore, Saada et al. (1994) found that, even during fracture, the behaviour of saturated clay was still dominated by plasticity. Consequently, the use of an elasto-plastic model is justified.

2. Four possible positions of geogrid reinforcement were considered. The South African standard for landfill design DWAF (1998) requires that the clay liner should be compacted in four distinct layers. The interfaces between these layers were identified as the possible reinforcement positions. Three-hundred-and-thirty-three to 423 linear elastic two-node truss (T2D2) elements were used to model the geogrids.

The interaction between the geogrid and the clay was modelled by merging coinciding geogrid and clay element nodes. Accordingly, the displacement at any of the merged nodes depended on both the clay element and the stiffer geogrid element. This models the reinforcing effect. The assumption holds while there is compatibility between the geogrid and the clay. Since the problem was modelled only up to the onset of fracture at the base or surface of the clay, this assumption is deemed reasonable (considering that the strain in a beam in bending increases from the neutral axis to the surface). Furthermore, Rajesh & Viswanadham (2015) found that

the response of their model was largely insensitive to the interface coefficient modelled between the geogrid and the clay. Koutsourais et al. (1991) found that for geogrids with large apertures the interactional properties were similar to that of the soil.

3. **The contact surface with the underlying waste body.** The upper surface of the waste body was set to displace according to a predefined settlement profile. This simulated the presence of a void below the liner causing differential settlement. The waste surface and the clay liner was modelled as separate parts and the contact was assumed to be frictionless as this is the most conservative modelling option. A frictional surface would confine the clay, inhibiting the clay elements from moving apart. Thus, lowering the tensile strain.

In terms of boundary conditions, displacement and rotation in the horizontal direction were prevented at the right hand side of the model, modelling symmetry. The same boundary condition was applied at the left hand side.

4.2.2 Validation model

The material models and reinforcement modelling approach discussed in the previous section were validated against the centrifuge models of Rajesh & Viswanadham (2011) and Rajesh & Viswanadham (2012b). A comparison with the numerical models of Rajesh & Viswanadham (2015) is also presented. These models represented a 1.2 m clay liner, 28 m long, with a settlement trough of 16 m width. The clay had a density of 1447 kg/m^3, a secant Young's Modulus of 2620 kPa, Poisson ratio of 0.3 and an undrained shear strength of 19 kPa. The clay liner was reinforced at the top quarter depth with a geogrid of stiffness 10 000 kN/m and Poisson ratio of 0.3. A 25 kPa overburden pressure was applied.

The same material properties and overburden pressure were applied for validation of the modelling approach of the current study. Assuming a density of 1500 kg/m^3 for the clay (equivalent to consolidation pressure of 630 kPa (Jessberger & Stone, 1991)), the tensile strength of the compacted clay ranges between 37.65 kPa (Thusyanthan et al., 2007) and 15 kPa (Tang et al., 2014). Modelling a tensile cut-off of this magnitude had only a minor effect on the strain behaviour while increasing the computational effort significantly. Accordingly, no tensile cut-off was modelled. This assumption, however, is only valid for imposed central settlements of limited extent (in this case < 1 m).

Rajesh & Viswanadham (2011) and Rajesh & Viswanadham (2012b) used a trapdoor to induce a 16 m wide settlement trough to the liner. It is assumed for this study that the deformed profile of the clay followed the Gaussian curve of Martos (1958) (see Equation 4.1). Accordingly, the simulated waste surface underlying the clay liner was displaced in the shape of this profile for validation. The parameter i (the distance from the centre to the point of inflection) is equal to a fifth of the trough width (New & O'Reilly, 1991) and was therefore set to 3.2 m (for a trough width of 16 m).

$$s = s_{max} \cdot e^{-\frac{x^2}{2i^2}} \tag{4.1}$$

The liner thickness was set to 1.2 m (i.e. $t = 0.3$ m). As with Rajesh & Viswanadham (2015) the geogrid was placed one quarter of the thickness (0.3 m) from the top of the liner. This reinforcement strategy was modelled with geogrids of stiffness 0 kN/m at Positions 2 to 4 (see Figure 4.1) and a stiffness of 10 000 kN/m at Position 1.

In landfills the typical length of the geogrid used will ensure sufficient lateral anchoring. However, in the centrifuge models of Rajesh & Viswanadham (2011) and Rajesh & Viswanadham (2012b) the model geogrids were not anchored at their edges. Slight separation of the model from the walls of the strong box could occur in the centrifuge. Accordingly, for the validation of the modelling approach, the horizontal restraint at the left edge of the general model (see Figure 4.1) was removed.

The maximum tensile and compressive strains predicted by the numerical validation model of this study at the surfaces of the clay liner, for different central settlements, are shown in Figure 4.2. Both the results of the reinforced and the unreinforced models are compared to the centrifuge models of Rajesh & Viswanadham (2011) and Rajesh & Viswanadham (2012b) and the numerical analysis of Rajesh & Viswanadham (2015). It was assumed that the strain results of the centrifuge models are presented as nominal (engineering) strain. Figure 4.2 indicate that the numerical model of the current study captures the trend of the physical model adequately.

4.2.3 Models analysed

A "standard" FE model was set up to be used as baseline for comparison in the subsequent sensitivity analyses. This model had a total width of 50 m (25 m modelled), a Gaussian settlement trough ($i = 3$, the distance from the centre of the settlement trough to the inflection point), total trough width of 15 m ($2c$ - Figure 4.1), maximum central settlement of 1 m, liner thickness ($4t$) of 1 m and an overburden

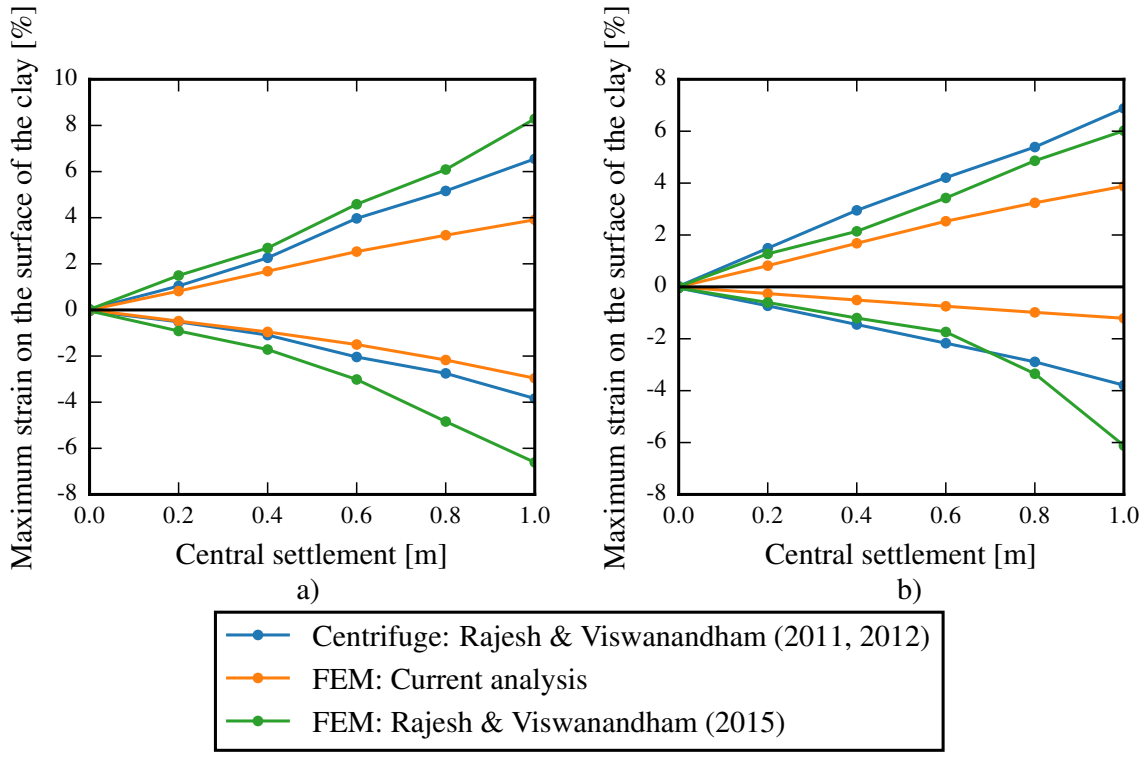

Figure 4.2: Validation of the FE model. Greatest nominal strain at the surface of: a) the unreinforced clay liner and b) the geosynthetic reinforced clay liner. Compressive strain is positive and tensile strain is negative.

pressure of 25 kPa (representing the landfill cover). The material models and properties of the standard model and all subsequent models were the same as those for the validation model.

To investigate the influence of the factors, identified earlier, on the behaviour of the clay liner, a number of variations of the standard model was analysed. A summary of these problems and their deviation from the standard model, are presented in Table 4.1. These analyses will be referred to as the sensitivity analyses.

4.3 PARETO FRONT GENERATION

To determine the optimum reinforcement strategy, objectives (criteria) to measure the performance of the designs against need to be established. Two such objectives were identified: 1) the total cost of reinforcement and 2) the maximum tensile strain occurring in the liner (assumed to be indicative of cracking and thus the permeability/performance of the liner). It was mentioned in Section 2.5.1

Table 4.1: Models optimised and their respective deviation from the standard model.

No.	Model name	Variation from standard model	No.	Model name	Variation from standard model
1.	0.5 m thick liner	Liner thickness of 0.5 m	5.	5 m trough	5 m wide settlement trough (c = 2.5 m)[i]
2.	1.5 m thick liner	Liner thickness of 1.5 m	6.	25 m trough	25 m wide settlement trough (c = 12.5 m)[i]
3.	0 kPa overburden	No overburden pressure	7.	Generalised bell	Settlement trough shaped as a generalised bell curve
4.	50 kPa overburden	50 kPa overburden pressure			

[i] c, the settlement trough width, is indicated in Figure 4.1.

that the tensile strain at which fracture initiates is independent from whether the liner is reinforced or not. Consequently, using the maximum tensile strain as criteria appears to be inadequate. However, geogrids were found to improve the performance of the liners by both increasing the stiffness of the system and by changing the stress distribution at the crack tip (Section 2.4). It is the effect of the first mechanism (increasing the stiffness) that the maximum strain criteria attempts to capture. As the stiffness of the system increases, the liner will settle less and the maximum tensile strain will decrease. For the purposes of this work the cost of reinforcement was assumed to be equivalent to the sum of the individual geogrid stiffnesses.

Both a lower cost and a lower maximum tensile strain would be indicative of a good design. However, these two objectives are in conflict - reducing the total amount of reinforcement (i.e. cost) increases the tensile strain and vice versa. Accordingly, one can isolate a number of designs where, for a given cost, no other design exists that results in a lower maximum tensile strain. This front of objective values that emerges is known as a Pareto Front (Arora, 2004). Given two objective functions (criteria), for any point on the Pareto front, reducing the one objective function will increase the other.

Numerous strategies exist to isolate these Pareto fronts. For the current project the DEAP (Distributed Evolutionary Algorithms in Python) software package (Fortin et al., 2012) was used to implement the NSGA-II algorithm (Deb et al., 2000), that was used to isolate the Pareto fronts. The NSGA-II algorithm was chosen for its ease of use (only one tuning parameter), as well as its efficiency (Konak et al., 2006).

The Pareto optimal front for the standard model is presented in Figure 4.3. The curves presented are all 30 point centered moving averages. As the cost of reinforcement was assumed to be equivalent to the stiffness of the geogrid, the horizontal axis displays tensile stiffness in lieu of cost. The maximum cost (stiffness) of reinforcement at any of the four reinforcement positions considered (indicated in Figure 4.1) was limited to 2.5 MN/m. This stiffness limit of 2.5 MN/m is at the upper range of commercially available geogrids.

The optimal reinforcement strategy for a given total reinforcement cost (stiffness) can be determined from Figure 4.3, as follows. Consider a total reinforcement cost of 2 MN/m as indicated in Figure 4.3a. For this reinforcement cost the maximum tensile strain in the liner can not be reduced below 2.7%, irrespective of how the total stiffness of 2 MN/m is distributed between the four reinforcement positions. The reinforcement strategy required to attain this strain of 2.7% is illustrated in Figure 4.3b. The reinforcement has to be distributed as follows: 31% of the total cost of the geogrids in Position 1 and 69% of the total cost in Position 4, i.e. a geogrid of stiffness 0.615 MN/m in Position 1 and a geogrid of stiffness 1.385 MN/m in Position 4. This allocation in cost (stiffness) is the optimal reinforcement strategy (ORS) defined earlier (Section 4.1). For the remainder of the chapter only the percentage of the total cost allocated to each position will be presented and not the actual stiffness.

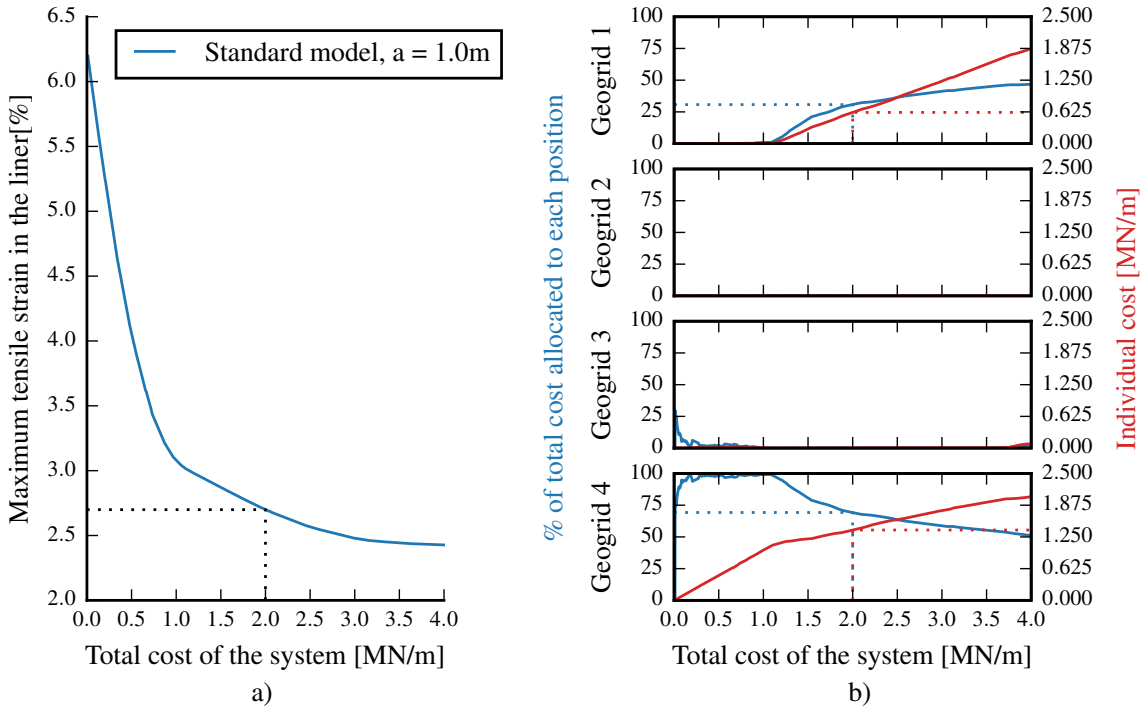

Figure 4.3: Pareto optimal front (a) and corresponding ORS (b) for the standard model.

4.4 SURROGATE SURFACE GENERATION

To determine the optimum reinforcement strategy for the each of the analyses listed in Table 4.1, numerous combinations of geogrid stiffnesses (designs) had to be analysed. Conducting a FE analysis for every possible design is impractical. Even conducting analyses only for the designs that the search algorithm evaluates is impractical. Consequently, the influence of only a number of designs on the maximum tensile strain was evaluated with a FE analysis. A surface was fitted to these results to allow for interpolation of the maximum strain at the remaining designs. For some physical phenomena, e.g. a 1D stress-strain relationship, the relationship between the variables can be defined as a simple mathematical relationship, e.g. $\sigma = E\varepsilon$. For other phenomena the relationship is too complex to be defined as a simple function. However, if a number of function values are known, an arbitrary curve, or surface (for multiple variables), can be fitted to the known data points to model the relationship. This allows for interpolation between data points. This arbitrary curve/surface usually has fitting parameters (for example the slope and intercept in the case of a straight line) that can be tuned to improve the fit of the function to the actual problem.

The current problem defines maximum tensile strain occurring in the liner as a function of the stiffness of the four geogrids. It is a complex problem, and thus no simple functional relationship exists. Accordingly, an arbitrary surface had to be fitted to the numerical data (results of the FE analysis for this problem) to define the relationship. The surface used was a radial basis function surface (RBF) with Gaussian base functions were (Forrester & Keane, 2009). The RBF consists of a series of bell-shaped (radial) functions that are summed to form the final surface.

Each RBF was generated from 900 different FE analyses. The geogrid stiffness allocation for each design was generated randomly. Using a uniform distribution to sample the designs could have resulted in some regions of the sampling space being under-represented. Accordingly, Latin Hypercube Sampling (LHS) was implemented (Ross, 2013). With LHS the sampling space is divided into n discrete segments. Subsequently, a uniform random sample is generated from each segment. Further manipulations are applied to ensure that, for a given design vector, all components originate from different segments. Accordingly, this method ensures that the entire sampling space is well represented.

The RBF surface fitted to the results of the FE analyses has a single tuning parameter, ε. This parameter

was adjusted to improve the fit of the RBF to the modelled data and thus lowered the prediction error. Ninety percent of the FE results were used to fit the RBF and the remaining 10% to calculate the prediction error, as suggested by Hastie et al. (2001). This process was repeated 10 times, each time using a different subset to calculate the prediction error. The ε-value was adjusted until the summed error was minimised. This ε-value was subsequently used to generate the RBF.

Similarly, the generalisation error made by the RBF (that is the error made predicting data other than the training set) can be calculated. For each problem 85% of the data was used to train the RBF while the prediction error was calculated for the remaining 15% of the data. For all problems considered the mean RMSE of the prediction error was 0.037% strain, while the standard deviation was 0.042% strain. Since all 900 designs (and not only 85%) were used to construct the RBFs used in the subsequent sections, it was assumed that the actual generalisation errors were even lower. It was found that the higher the prediction error of the RBF, the more difficult it was to generated a full set of Pareto optimum designs (see next section)

4.5 RESULTS AND DISCUSSION

The results of the sensitivity analyses are divided into two categories: those factors that did not have any distinct influence on the liner ORS (overburden pressure and clay liner thickness) and those that had (degree of central settlement, trough width and shape).

Compacted clay liners are generally heavily over-consolidated. Therefore, the liners will crack at fairly low strains (LaGatta et al., 1997). Consequently, it is assumed that the mass of clay will behave elastically prior to cracking. Accordingly, the strain distribution ($\varepsilon(x,y)$) in the liner prior to cracking can be approximated using elastic beam theory to facilitate understanding of the problem:

$$\varepsilon(x,y) = \frac{d^2 s}{dx^2} \cdot y \tag{4.2}$$

where s is the deflection at position x and y the distance from the neutral axis of the beam. The expression for strain above consists of two components: the curvature of the deformed beam and the distance from the neutral axis.

4.5.1 Variables with no influence on the optimum reinforcement strategy: overburden pressure and liner thickness

Clay is ductile and has little capacity to arch over voids. Consequently, as the waste settles, the clay will distort in the shape of the deformed waste surface, without spanning the void. Higher overburden pressure will not increase the distortion of the liner as the liner is already resting on the waste surface under self-weight. Thus, the general shape of the strain distribution will remain unchanged. Considering that the clay is heavily overconsolidated, the compression due to increased overburden pressure is slight. Thus, it is not expected that the overburden will have an influence on the optimum reinforcement strategy of the liner. The numerical results support these statements. In Figure 4.4, it can be seen that the optimum reinforcement strategy is the same for the three different overburden pressures considered.

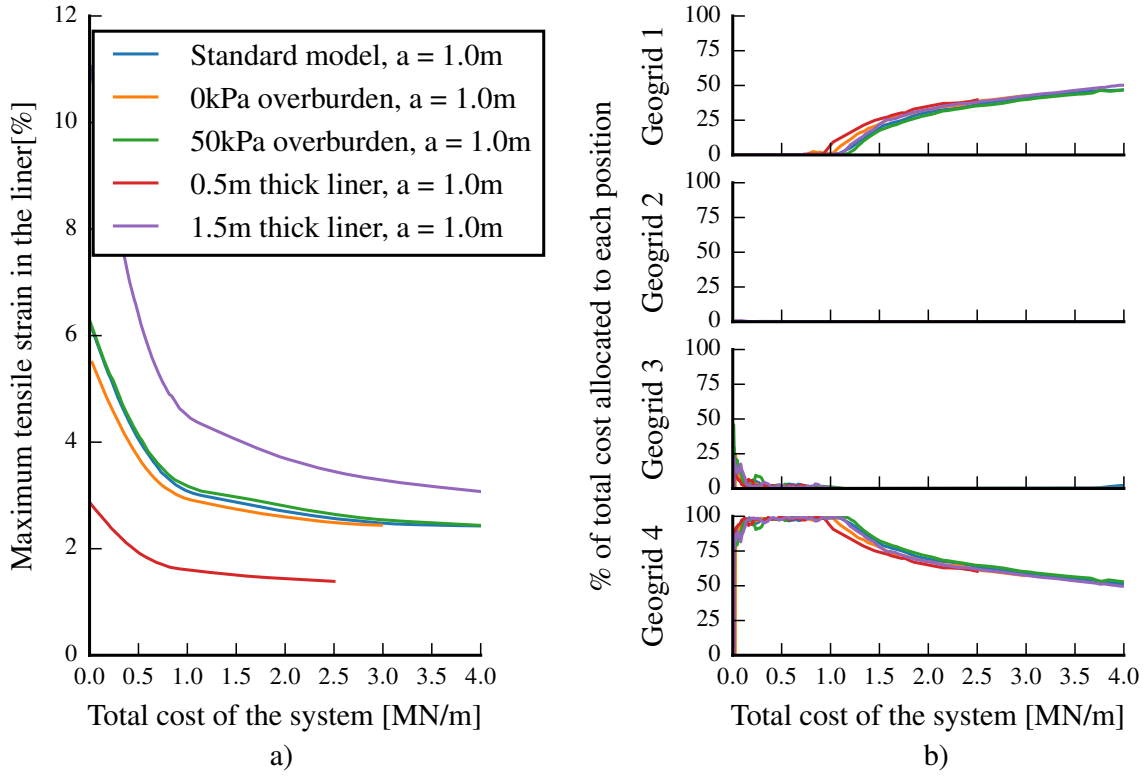

Figure 4.4: Pareto front (a) and corresponding ORS (b) of the standard model, models with varying overburden pressure and models with varying liner thickness.

The maximum strain in the liner, however, is influenced by the overburden pressure. This is due to the confining effect of the pressure that inhibits crack formation (Jessberger & Stone, 1991). Accordingly, the Pareto optimal front will translate upwards (i.e. higher strain) for lower overburden pressure

and downwards (i.e. lower strain) for higher overburden pressure (see Figure 4.4). The variation in overburden was, however, relatively small and did not have a significant effect on the Pareto front.

The strain at the surface of an elastic beam depends on the distance to the neutral axis (see Equation 4.2). As with a change in overburden, a change in thickness of the liner is assumed not to change the deflected shape, and by implication, also not affect the distribution of strain in the liner. Accordingly, the thickness of the clay liner does not have an influence on the reinforcement strategy. However, the strain at the outer extremities of the liner is proportional to the distance from the neutral axis (see Equation 4.2 and Viswanadham & Rajesh (2009)). Jessberger et al. (1989) found that the distortion required for tensile cracking was a function of liner thickness.

Accordingly, with increased liner thickness the maximum strain increases and the Pareto front will translate upward. In Figure 4.4 the Pareto front, as well as ORS is shown for clay liners of thickness 0.5 m, 1 m (standard liner) and 1.5 m. These results support the aforementioned reasoning.

4.5.2 Variables affecting the optimum reinforcement strategy: problem geometry

4.5.2.1 Central settlement

The strain distribution with depth in an elastic beam depends on the curvature of the beam at that position. Consequently, an increase in central settlement of the liner increases the deflected profile changes and the ORS will change accordingly. In Figure 4.5 the Pareto front and ORS for the standard liner for different degrees of central settlement (a) are presented.

As expected, the ORS differs for the varying central settlements. However, the optimal geogrid positions do not change (top quarter and bottom) as evident in Figure 4.5. Only the distribution of resources (summed stiffness) vary. As the central settlement (a) increases, more reinforcement is required at the top quarter of the liner. For the same total cost a liner that settled 1 m requires more reinforcement at the top quarter than one undergoing 0.4 m of settlement.

A possible interpretation for this behaviour is provided. Consider the two mechanisms of geogrid reinforcement: increasing the stiffness of the system and reducing the stress at the crack tip (Section 2.4). At low central settlement a significant reduction in tensile strain is achieved with the inclusion of reinforcement, as it increases the stiffness and shares the applied load between the clay and the geogrid. However, as the central settlement, and thus the curvature of the liner increases, a greater reduction in strain is achieved by reducing the tensile stress at the crack tip. Accordingly, the importance of reinforcing at top quarter depth increases due to the higher strain at the convex part of the trough.

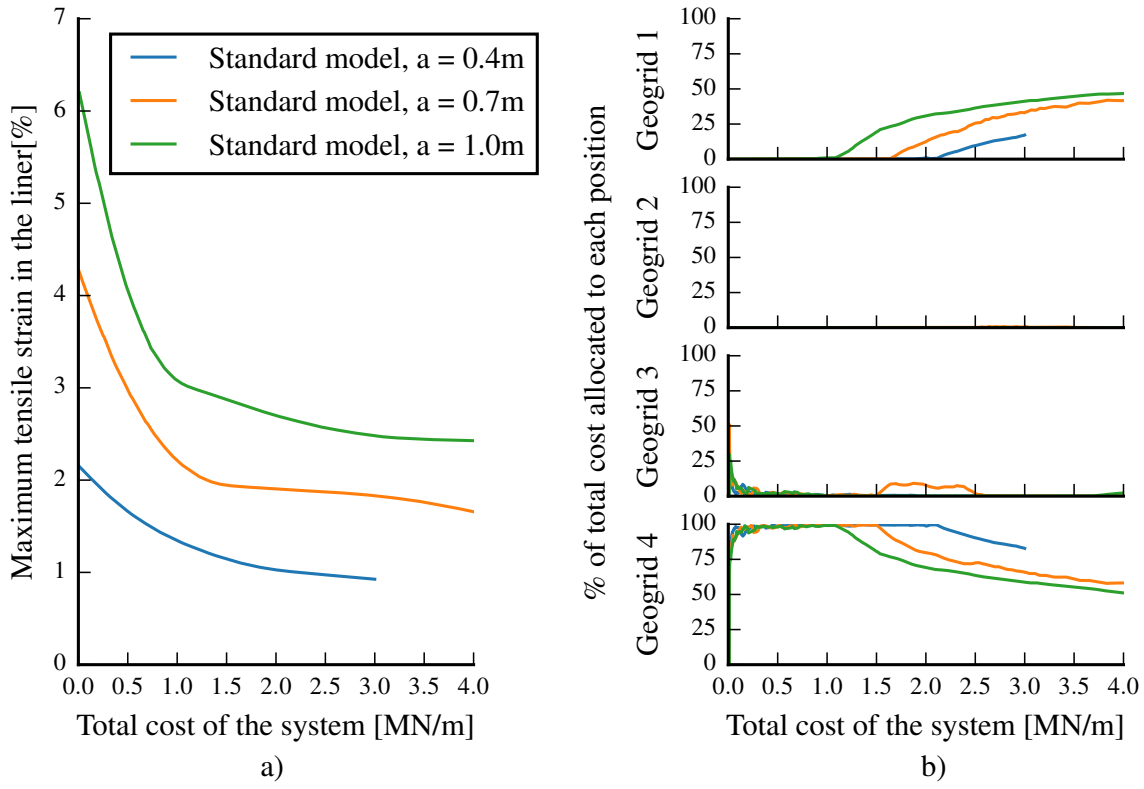

Figure 4.5: Pareto front (a) and corresponding ORS (b) for the standard model for varying degrees of central settlement.

4.5.2.2 Settlement trough width

Beams (or liners) displaced to the same curvature are assumed to be strained similarly, independent of the beam size (see Equation 4.2). The curvature, or distortion, is a function of the central settlement (a) and the settlement trough width ($2c$). LaGatta et al. (1997) defined this relationship as the distortion level (a/c, commonly defined as a/l). This relationship can be used to define the behaviour of distorted liners and allows for comparison.

The curvature, however, does not depend only on the ratio between the central settlement and trough half-width. Consider the expression for the curvature of the Gaussian curve (Equation 4.1) that was used to induced settlement, as defined in Equation 4.3.

$$\frac{d^2s}{dx^2} = \frac{2.5i \cdot S_{max}}{\sqrt{2\pi}i^3}\left(\frac{x^2}{i^2} - 1\right)e^{-\frac{x^2}{2i^2}} \tag{4.3}$$

Thus, the curvature is a function of the magnitude of central settlement and trough width, and not only the ratio thereof. Alternatively, Jessberger & Stone (1991) considered the distortion angle θ (see Figure 2.10 on p.19) as representative of liner deformation. However, similar to a/l, θ does not adequately capture the strain behaviour of the liner. Furthermore, Gabr & Hunter (1994) found that the tensile strain cannot be uniquely defined by the distortion level only. Both the overburden pressure (as discussed earlier) and the trough width should be considered. Accordingly, the distortion level alone might prove inadequate in describing the strain behaviour of clay liners.

In Figure 4.6 the Pareto front and corresponding ORS are presented for troughs of varying widths and the same a/l ratio of 0.093. Other distortion ratios was also investigated and found to behave similar. The Pareto fronts differ distinctly for the various trough widths. This suggests that the strain magnitude generated differs as a function of trough width, even though the distortion level is the same. For all ORSs, however, geogrids are required at the bottom of the liner and at the top quarter depth, specifically with the stronger geogrid at the bottom of the liner.

4.5.2.3 Trough shape

In the standard modelled the profile of the settled waste was modelled as a Gaussian curve. This shape is, however, only an assumption. The actual settlement trough may have a more random shape. To investigate the influence of trough shape on the ORS, the waste profile underlying the liner was also modelled to deform in the shape of a generalised bell curve (see Equation 4.4). The parameter m can be proven to be equal to the distance to the inflection point of the curve. Accordingly, m was set to be equal to 3, to have same inflection point as the standard model. The parameter n was set to 2 to model a steeper profile than the standard Gaussian curve (Figure 4.7). The resulting Pareto fronts and ORSs are compared to the standard curve in Figure 4.8, for a trough width of 15 m and various degrees of central

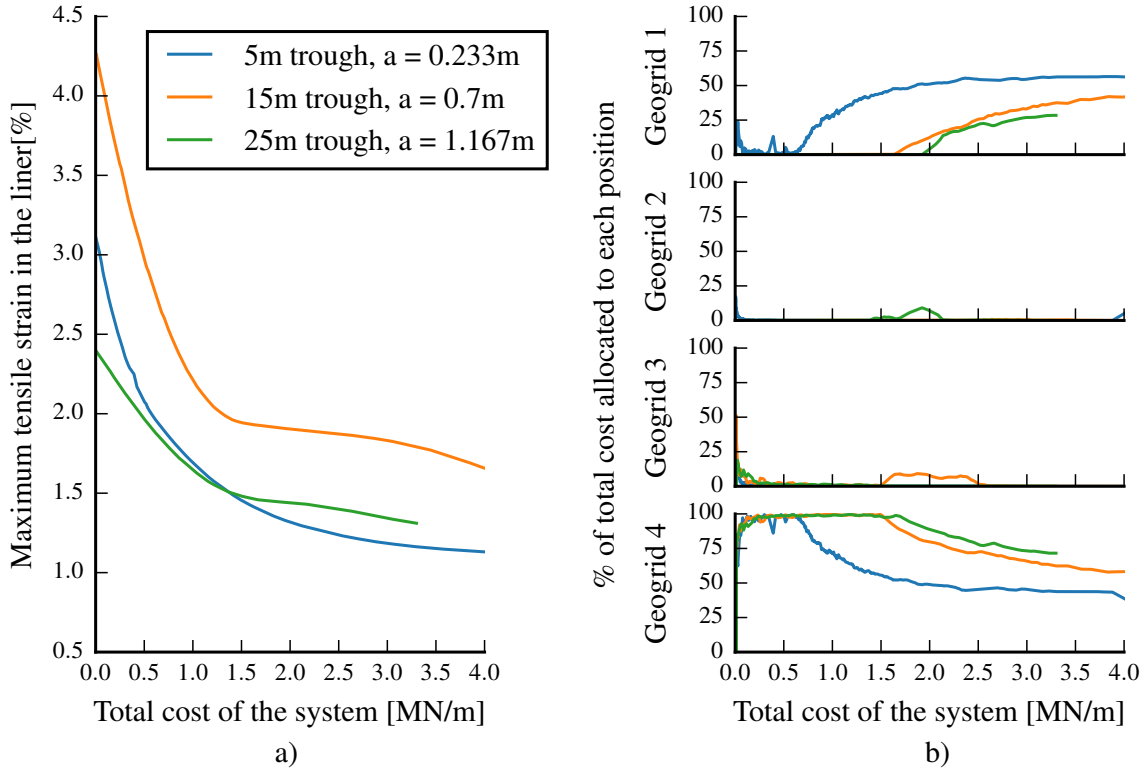

Figure 4.6: Pareto front (a) and ORS (b) for troughs of varying widths with $a/l = 0.09333$.

settlement. Although there is some noise in the ORS results, clear observations can be made.

$$s = S_{max} \cdot \frac{1}{1 + \left|\frac{x}{m}\right|^{2n}} \tag{4.4}$$

The ORS differed significantly for the two settlement troughs. Even though both ORSs comprises mainly of reinforcement only at the top quarter (Position 1) and bottom (Position 4), the relative importance differs. For example, reinforcing at the top (Position 1) rather than at the bottom is significantly more important for the generalised curve. Additionally, reinforcement at both positions is required for almost all costs. In contrast, for Gaussian settlement reinforcement is required at the top only after the stiffness in the first layer reaches the maximum (Figure 4.8).

Richards & Powrie (2011) found that the shape of the subsidence pattern had a significant influence on the hydraulic conductivity of a liner. Interestingly, they found that a liner subjected to a more jagged distortion profile resulted in poorer performance than a liner subjected to a smoother one. The steeper distortion corresponds to shearing of the liner and therefore a significant impairment in functionality. Likewise, the current analysis found that the generalised bell profile resulted in Pareto optimal fronts

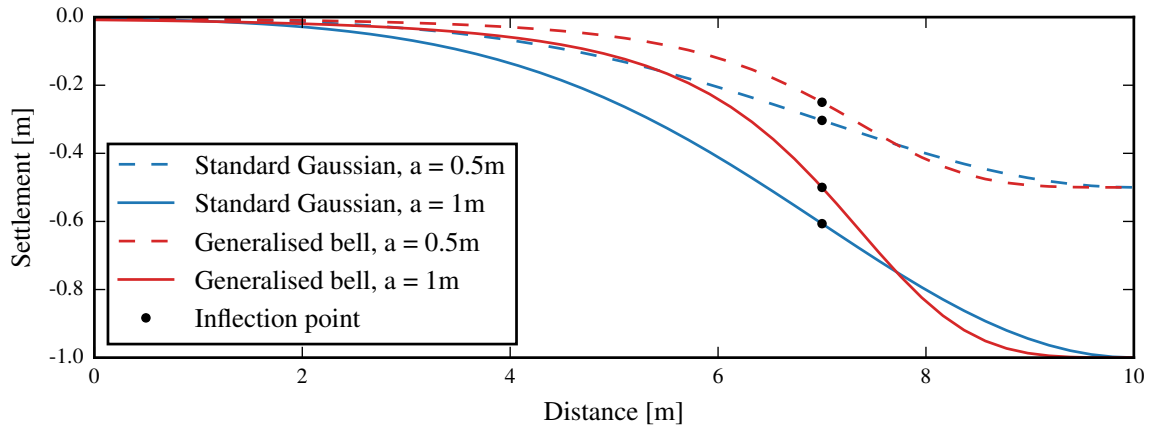

Figure 4.7: Shape of the settlement trough for the standard and generalised bell curves, for different central displacements.

of greater strain, compared to the equivalent Gaussian profiles, requiring greater expense in terms of reinforcement cost.

4.6 SUMMARY OF THE FINITE ELEMENT ANALYSES

The optimal reinforcement strategy for a clay liner subject to differential settlement was investigated. It was found that for the same imposed settlement profile neither the overburden pressure nor the liner thickness influenced the ORS. The reinforcement strategy for the standard problem (15 m Gaussian trough, 1 m thick liner and 25 kPa overburden pressure) primarily comprised of a geogrid at the bottom of the liner, with an additional geogrid at top quarter depth as more resource became available.

Trough width and shape, as well as central settlement, however, did have an influence on the ORS. For these parameters it was found that the addition of reinforcement at the top quarter of the liner is of importance (compared to the standard model). Furthermore, the ORS is highly sensitive to the shape of the settlement profile. For a steeper, generalised bell shaped settlement trough, reinforcement at the top quarter depth of the liner was of the greatest importance. For almost any cost the optimal reinforcement strategy entails a two-level approach.

A conservative design, that is insensitive to the factors considered, would consist of two-level geogrid reinforcement, both of the same stiffness. This is, however, only a preliminary recommendation and further work has to be conducted. Furthermore, it should be noted that the numerical results indicated

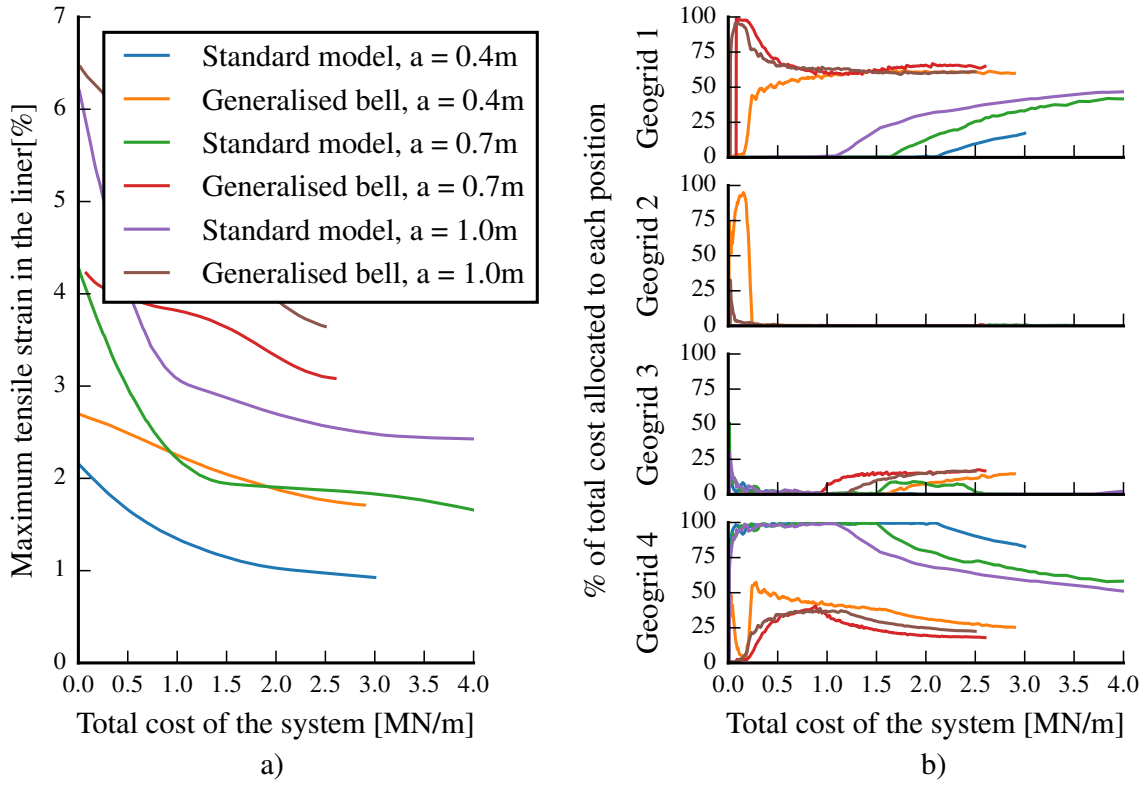

Figure 4.8: Pareto optimal front (a) and ORS (b) for both the standard and generalised bell curves, for a number of central settlements.

that these two reinforcement positions are at the top quarter and base of the liner. However, full bond was assumed between the geogrid and the clay at the base of the liner. As more conservative approach, is recommended that the lower reinforcement position should be placed at the bottom quarter of the liner to ensure sufficient bond exist.

Finite element analyses were used to investigate the behaviour of geogrid reinforced clay liners. It was found that other than the reinforcement position and stiffness (the variables for optimisation), the settlement trough also had a significant influence on the behaviour of the liner. Furthermore, liner thickness and overburden pressure did not influence the optimum reinforcement strategy, and thus had not to be investigated in the centrifuge modelling.

CHAPTER 5 CENTRIFUGE TESTS

In Chapter 3 bending beam tests were done to obtain a preliminary grasp of the behaviour of unreinforced clay liners when distorted. This was followed by numerical modelling of reinforced clay liners in Chapter 4. However, accurate efficient, numerical modelling of soil-geogrid interaction is still in is infancy. Only a number of authors modelled reinforced liners as the three-dimensional problem it truly is, e.g. Tran et al. (2013) and Hussein & Meguid (2016). The brittle tensile, plastic compressive, behaviour of the clay, the non-linear elastic geogrid and the soil-geogrid interaction complicates the numerical modelling.

As an alternative to numerical modelling, the behaviour of the geogrid reinforced soil can be investigated with physical modelling. However, full scale physical modelling is expensive and often impractical. These limitations of full scale modelling can be overcome, while retaining the benefits thereof, by building a scale model of the problem and testing it in a geotechnical centrifuge.

In the following section the principle of centrifuge modelling is discussed (Section 5.1). Thereafter, the series of centrifuge tests designed using the insights gained from Chapter 4 is discussed (Section 5.2). Finally, results of these tests are presented in Section 5.3.

5.1 CENTRIFUGE MODELLING PRINCIPLES

The stress state in a scale model differs considerably from the full scale problem (prototype model) it represents. As an example, a liner spanning a void and the scale model that is N times smaller is shown in Figure 5.1. The stress at the bottom of the actual liner (the prototype model) is $\sigma_p = \rho h g$. However, at the bottom of the model liner it is only $\sigma_m = \rho \frac{h}{N} g$. Thus, the stress differs with a factor

of $1/N$. However, should the (gravitational) acceleration acting vertically on the model be increased N-times, the stresses will be equivalent, $\sigma_m = \rho \frac{h}{N} \cdot Ng = \sigma_p$.

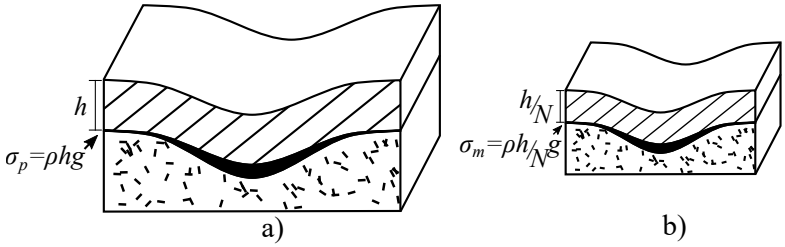

Figure 5.1: Prototype model of a clay liner spanning a void (a) and scale model N times smaller (b).

The vertical acceleration of the model (g) can be increased by subjecting it to centrifugal acceleration ($g = \omega^2 \cdot r$, where ω is the angular velocity and r the distance from the centre to the model). This principle is used in centrifugal modelling: by applying centrifugal acceleration to the scale model, its vertical acceleration is increased until the vertical stress in the model equals that in the prototype. Furthermore, undisturbed soils are unique in the regard that the horizontal stress is directly related to the vertical stress ($\sigma_h = \sigma_v \cdot K_0$). Thus, if the magnitude of the vertical stress in the scale model is increased to that in the prototype, the horizontal stress will follow suit.

When constructing a scaled-down model, a number of scaling laws are available to ensure that the behaviour of the scale model will accurately reflect that of the prototype. A summary of these laws can be found in Garnier et al. (2007). The most import of these laws is for dimensions - the dimensions of a scale model accelerated to Ng should be $1/N$ of that of the prototype.

The strength properties of the soil used in the scale model does not have to be scaled. The drained strength of soil is stress dependent ($\tau = c' + \sigma \tan \phi'$), while the undrained strength of clay is assumed to remain constant, independent of the problem size. Thus, the prototype soil can be used for the scale model and the strength behaviour will be correct. However, the scaling laws with regard to the localised shear bands and tension cracks observed in model clay liners in literature are unclear (Richards & Powrie, 2011). Furthermore, the influence of the size effect (Section 2.3.3) might result in a difference in fracture behaviour between a centrifuge test and a prototype liner.

The width of a localised shear band depends, amongst others, on particle size (see Scarpelli & Wood (1982) and Oda & Kazama (1998)). However, the centrifuge increases the stress exerted by a soil grain, but has no influence on its size whatsoever. Consequently, shear ruptures in the centrifuge might be of

the same actual width as those in the prototype. Consequently, the ratio between the thickness of the model and the shear band width will be significantly greater than in practice. Thus, the ultimate failure mechanism observed in the centrifuge might differ somewhat from that in the field. However, most of the studies on the relationship between shear bands and particle size were done on granular material. Furthermore, even should these findings hold for clay, clay particles are so fine that the shear band will still be significantly smaller than the thickness of the model. If a mean clay particle size of 16 μm (see Figure 3.1) and a prototype thickness of 0.6 m (DEA, 2013) modelled at 40g, are assumed, the ratio of model thickness to particle size is 937.5, an order of magnitude larger than the minimum ratio of 15 recommended by Taylor (1995).

5.2 CENTRIFUGE TEST DESIGN

The 150 *g*-ton centrifuge of the University of Pretoria was used for centrifuge modelling of geogrid reinforced clay liners subject to differential settlement. Details of the machine and data acquisition system can be found in Jacobsz et al. (2014). Since only a limited number of centrifuge models can practically be tested, these models should be designed to emphasize the relevant mechanisms that govern the problem.

One of the most significant decisions to make for a centrifuge model is the appropriate model scale and thus acceleration level. The centrifuge strongbox that was used in this study is 600 mm long (discussed in the next section). At an acceleration of 30*g* it would be equivalent to an 18 m long prototype liner. Thus, a sizeable segment of a landfill can be represented by the model. Consequently, a scale of 1:30 and an acceleration of 30*g* were selected. Furthermore, a model liner that is 30 mm thick (discussed later in the section) is equivalent to a 900 mm prototype liner. This thickness falls between the South African standard (600 mm, DEA (2013)) and liners used in other studies ($\approx$ 1200 mm, Table 2.6 on p.36).

For the numerical analyses in Chapter 4 the geogrid stiffness and position were identified as the two principal variables of the problem. The settlement trough geometry and magnitude of central settlement also had a significant influence on the optimal reinforcement strategy (ORS). Finally, liner thickness and overburden pressure were not found to influence the ORS.

No overburden stress was applied to the models as: a) it did not prove to influence the optimal reinforcement strategy (Chapter 4), b) this allowed for in-test measurement of crack propagation on the surface of the liner and, c) this would represent the most critical stage in a liner's life, as the addition of overburden will suppress tensile crack formation and induce (arguably) less critical shear ruptures in the liner (see Section 2.3.4: Jessberger & Stone (1991)).

Furthermore, as liner thickness did not influence the ORS, the models were cut to a manageable thickness of 30 mm (in model dimensions). A model liner of this thickness can easily be handled without being damaged during model preparation.

The shape and width of the settlement trough proved to have an influence on the ORS (Chapter 4). Nevertheless, it was not feasible to test models with both different reinforcement positions and different shaped settlement troughs. Varying the reinforcement positions was judged to have a more significant influence on the behaviour of the liner. Accordingly, the settlement trough shape and width were kept constant.

Viswanadham & Jessberger (2005) distorted the liners for 5 min at a time followed by 30 min of no settlement. During this 30 min the excess pore pressure generated in the liner was allowed to dissipate. Most of the other experiments discussed in Sections 2.3.4 & 2.5.1 distorted the liners at a constant rate without allowing any consolidation to occur. The first approach models primary or secondary consolidation of the waste below the liner, while the second models the sudden collapse of large objects (Section 2.2). However, continuous central settlement is assumed to shear the liner undrained (considering the low permeability of these liners). Consequently, this failure is more conservative (drained strength is in generally greater than undrained). Thus, for the present study the liners were distorted at a slow, constant rate.

A further key consideration was the rate of central settlement. For the first 5 mm of central settlement the piston was lowered at a rate of 1 mm/min. This allowed for the possibility to study arching in the sand at the small movements. For the remainder of the test, the platform settled at a rate of 3 mm/min to ensure that the behaviour remained undrained.

Similar to the settlement trough, the reinforcement position was identified as a key variable of the problem. The two most significant reinforcement positions identified from the results of the numerical

analyses (Chapter 4) - top quarter and bottom quarter depth (see Figure 4.1)- were selected for the centrifuge modelling. There could be concerns that embedding a geogrid inside a clay liner might compromise its hydraulic conductivity. However, consider Figure 5.2. The flow through of a system of two layers, with and without a void inbetween, can be calculated as:

Two adjacent soil layers (Figure 5.2a):	Two soil layers separated by a water filled void (Figure 5.2b):
$k_{eff_a} = \sum_i \frac{L_i}{L_i/k_i}$	$k_{eff_b} = \sum_i \frac{L_i}{L_i/k_i}$
$= \frac{L_1 + L_2}{L_1/k_1 + L_2/k_2}$	$= \frac{L_1 + L_2 + h_2}{L_1/k_1 + L_2/k_2 + h_2/\infty}$[i]
	$= \frac{L_1 + L_2 + h_2}{L_1/k_1 + L_2/k_2 + 0}$
$i_a = \frac{L_1 + L_2 + h_1 + h_2}{L_1 + L_2}$	$i_b = \frac{L_1 + L_2 + h_1 + h_2}{L_1 + L_2 + h_2}$
$\upsilon_a = ki \quad = \frac{L_1 + L_2 + h_1 + h_2}{L_1/k_1 + L_2/k_2}$	$\upsilon_b = ki \quad = \frac{L_1 + L_2 + h_1 + h_2}{L_1/k_1 + L_2/k_2}$

$$\upsilon_a = \upsilon_b$$

[i] Assuming the permeability of water to be infinite.

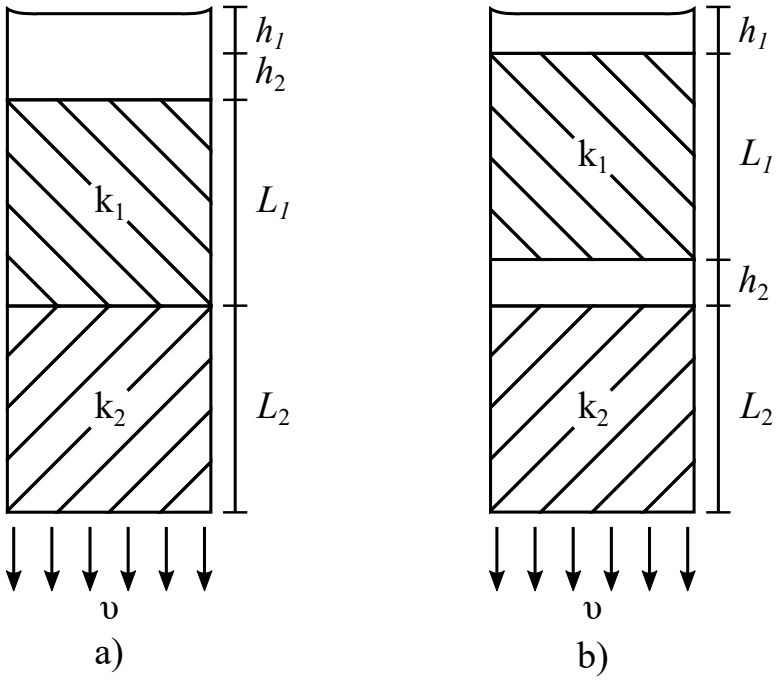

Figure 5.2: a) One dimensional flow through two heterogeneous layers, b) One dimensional flow through two heterogeneous layers separated by water.

Thus, the flow through a two-layer system, with or without a void in the centre, is the same. Accordingly, even should separation between the clay and and the embedded geogrid occur, the hydraulic conductivity of the liner will not be reduced for flow perpendicular to the liner.

The remaining key variable to consider is geogrid stiffness. It was not viable to vary both geogrid stiffness and reinforcement position in the centrifuge tests. As a number of authors had studied the effect of geogrid stiffness on liner performance before (Table 2.6, Section 2.5.1), the liner stiffness was kept constant. Only a single model geogrid was used.

To summarise, five centrifuge tests with four different reinforcement strategies were tested. These tests were:

1. Two tests of unreinforced model liners. These represented the baselines used to compare the reinforced tests against.
2. One model liner reinforced at the top quarter position. This reinforcement strategy was deemed to be optimal by Viswanadham (1996) and Rajesh & Viswanadham (2009).
3. One model liner reinforced at the bottom quarter position. This position represents the optimum for the numerical analyses of a liner subject to a Gaussian settlement trough. The position is also the intuitive reinforcement position for a geogrid bridging a void.
4. One model liner reinforced both at the top quarter and the bottom quarter positions: a double-reinforced liner. This was the optimum reinforcement strategy for the numerical analyses of a liner subject to a general settlement trough shape.

In the following subsections the components of the model (Section 5.2.1), the materials used (Section 5.2.2) and the construction technique used to form the model liner are discussed (Section 5.2.3). That is followed by a description of the measurement instrumentation used (Section 5.2.4) and finally the tests procedure adopted (Section 5.2.5).

5.2.1 Components of the model

The centrifuge models consisted of three basic parts: 1) a reinforced clay liner, 2) on top of a sacrificial sand layer and 3) overlaying a trapdoor used to induce differential settlement. A front view of the

model is presented in Figure 5.3. Key components are indicated and dimensions shown are actual dimensions. A photo of the strongbox before a test is shown in Figure 5.4.

In the previous section it was mentioned that a 30 mm thick clay liner was used. This liner was 600 mm long and 150 mm wide. A divider was placed in the back of the strongbox, leaving a 150 mm wide space behind the window. The reinforcement used for the clay is discussed in Section 5.2.2.2. A 100 mm thick sacrificial sand layer was placed below the clay. The purpose of this layer was to reshape the angular deflected profile directly above the trapdoor to a smooth deflected profile below the clay. A summary of the properties of the sand used is presented in Section 5.2.2.1.

The sand was placed on top of the trapdoor that was used to induce differential settlement to the clay. Previous authors predominantly used one of two different mechanisms to induce differential settlement (see Section 2.3.4). Either only a central platform moving downwards, resulting in a void with sharp ridges (Figure 5.5b), or a central platform moving downwards, supporting a trapdoor on either side (Figure 5.5a) was used. The sharp ridges induced below the clay by the first mechanism was judged not to be representative of the differential settlement that will occur in practice. Accordingly, the second mechanism that represents a settlement profile closer to the Gaussian curve used in Chapter 4 was used.

The settlement trough was modelled to be fairly wide, simulating a local void forming deep below the liner, or general differential settlement due to waste decomposition. This was done since a local void was judged unlikely to occur near the surface of the old waste dump in a piggy-back landfill. Any porous or weak spaces in the waste surface would be discovered and compacted during preparation of the surface for construction of the new piggy-back liner on top. Furthermore, the mechanism used to induced the settlement trough, as well as the shape of the trough, has been successfully used in literature (see Section 2.3.4 & 2.5.1). Other arguments for modelling differential settlement rather than void formation were presented in Section 4.1.

To induce the differential settlement, two 130 mm wide aluminium trapdoors were supported on a 130 mm wide central platform and hinged to 160 mm wide supports (Figure 5.3). This was equivalent to a 7.98 m wide void with 5.01 m support to either side at 30g. A Teflon sheet covered the aluminium trapdoors to prevent the sacrificial sand from clogging the hinges. The same type of Teflon sheet was placed on top of the central piston to reduce friction with the edges of the trapdoors.

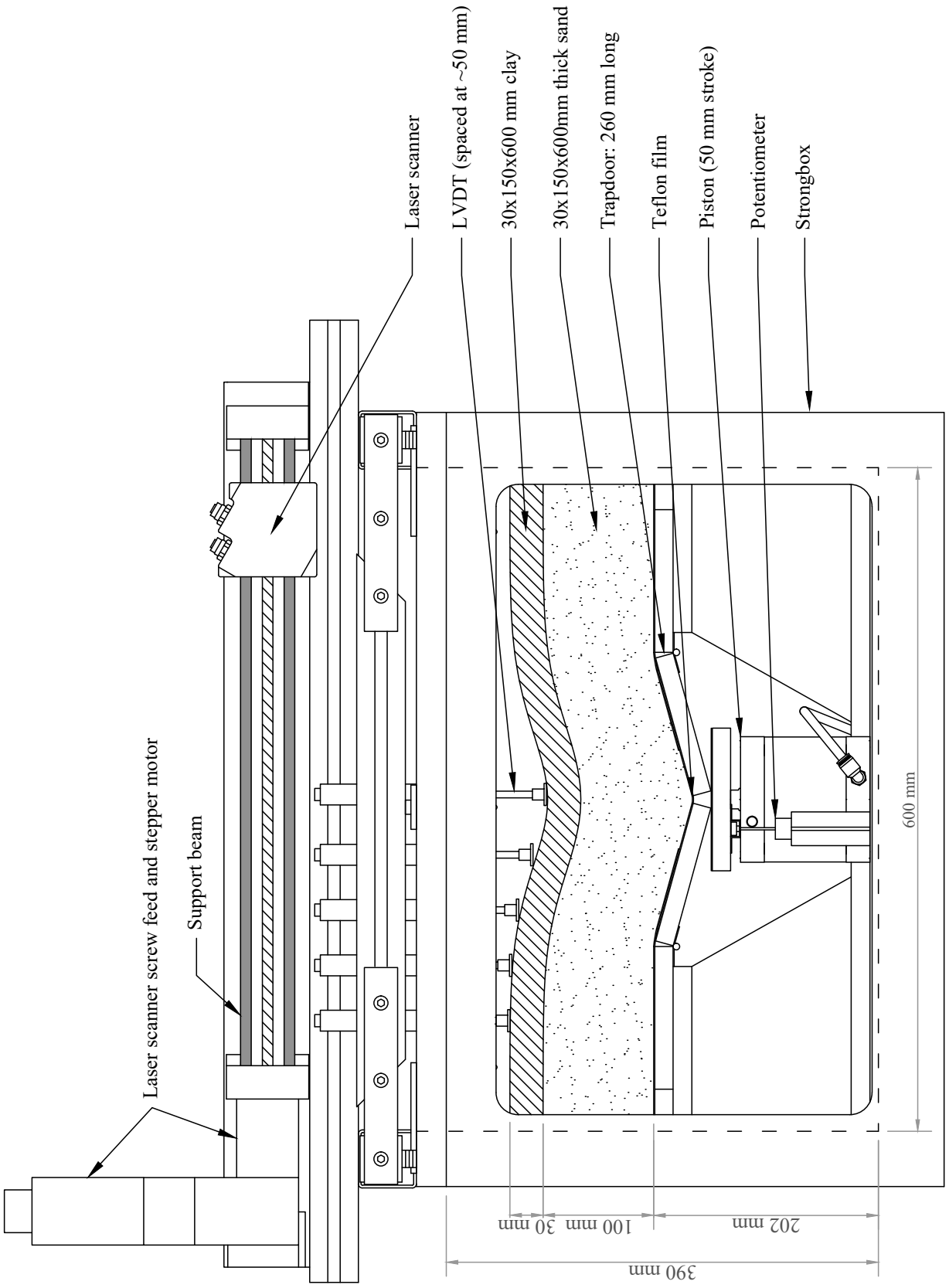

Figure 5.3: Drawing of the centrifuge model.

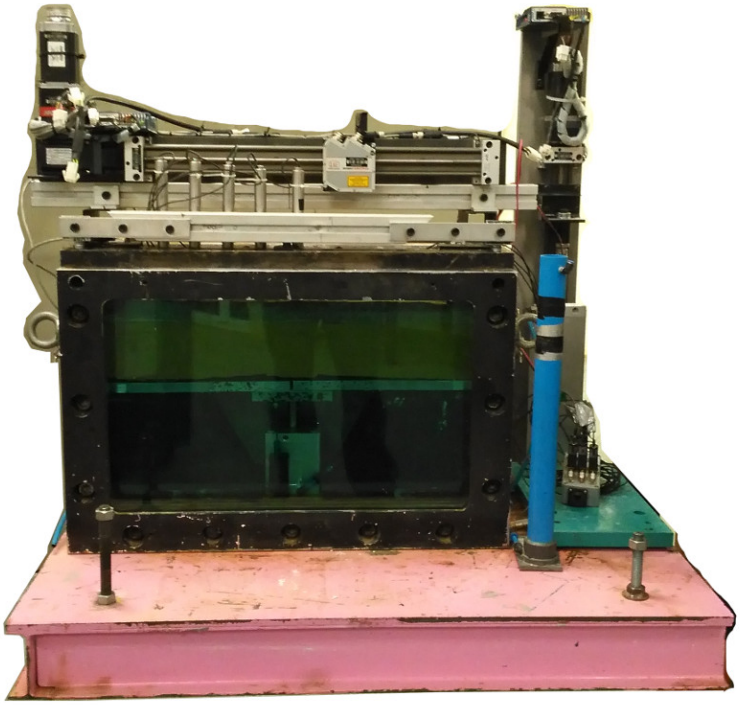

Figure 5.4: A photo of the model loaded in the strongbox before a test.

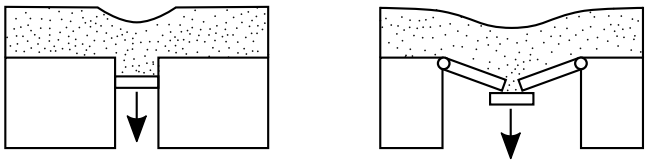

Figure 5.5: Typical mechanisms used to induce differential settlement to a model clay liner: a) central platform moving downwards and b) central platform with a trapdoor on either side.

The central platform was supported by a Festo ADN-80-50-I-P-A piston. The bottom compartment of the piston was filled with water. Once the test started, water was extracted from the bottom compartment (see Figure 5.6). This allowed the primary piston to settle under its own weight, lowering the trapdoors and inducing differential settlement. A maximum of 50 mm of central settlement, or 1.5 m at prototype scale, could be modelled. The water was extracted with a secondary piston connected to motorised linear actuator. A series of solenoid valves allowed for the secondary piston to be emptied into a standpipe once it reached capacity.

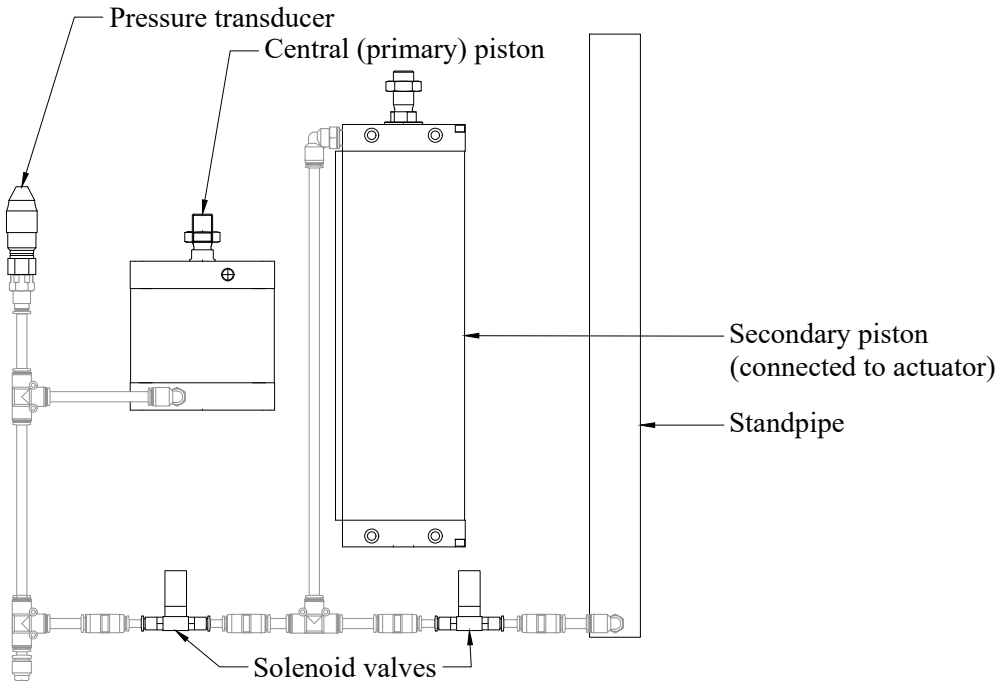

Figure 5.6: Layout of the hydraulic system used for the centrifuge test.

5.2.2 Materials used

In this subsection the sand, model geogrid reinforcement and clay used the centrifuge tests are discussed.

5.2.2.1 Sand properties

A comprehensive investigation into the properties of the sacrificial sand used was done by Archer (2014). The grading of the sand measured by both a sieve analysis and a Malvern Mastersizer 2000 particle size analyser (see Section 3.1.1) is shown in Figure 5.7. The specific gravity of the sand is 2.666, the minimum void ratio 0.60 and the maximum void ratio 0.92. Strength results from triaxial testing at three different relative densities are shown in Table 5.1.

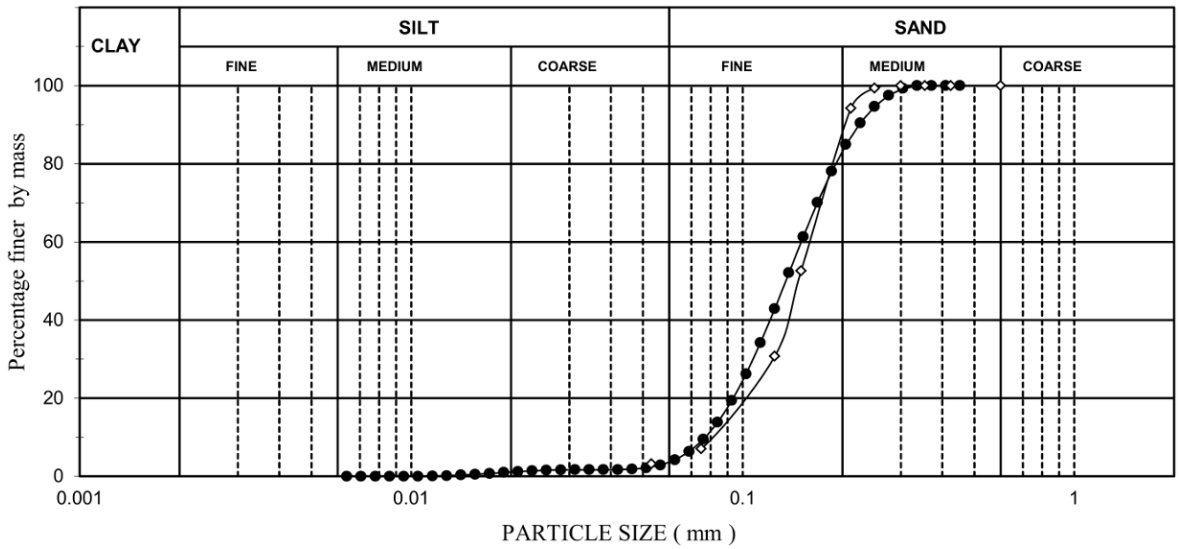

Figure 5.7: Grading analysis of the sand used for the sacrificial layer (from Archer (2014)).

Table 5.1: Results of the triaxial tests conducted on the sand used for the sacrificial layer by Archer (2014).

Relative density [%]	Friction angle (ϕ') [°]	c′ [kPa]
20%	32	0
50%	34	0
80%	39	0

5.2.2.2 Model geogrid reinforcement

The model geogrid used to reinforce the clay should replicate the behaviour of a prototype geogrid when under increased acceleration. Arguably, the four fundamental properties governing the behaviour of a geogrid are: stiffness, bond, strength and durability (Section 2.4).

The durability of the model geogrid is of little concern during centrifuge testing. Tests rarely last longer than a few hours. Consequently, there is no need to consider the long term behaviour of the model geogrid.

The tensile strain at failure of a clay liner (1-3%, Table 2.2) is significantly lower than the ultimate tensile strain of a geogrid (e.g. Shinoda & Bathurst (2004)). Thus, the strain behaviour of the model geogrid only has to be equivalent to the prototype up to the failure strain of the clay. Consequently,

when selecting a suitable model geogrid, the failure strain and strength are not relevant.

The remaining two fundamental geogrid properties, stiffness and bond, are of importance when choosing a model geogrid. The stiffness of a geogrid is defined in terms of the secant tensile modulus (J_{sec}, force per elongation). For the model geogrid to be equivalent to the prototyep at Ng, J_{sec} of the model geogrid should be $1/N^{th}$ of that of the prototype. A derivation of this scaling law is provided in Viswanadham & König (2004). The J_{sec} is a function of both the ultimate tensile strength (T_u) and the member spacing (N_t) of the geogrid. In turn, T_u depends on the area of each member, as well as its stiffness (E). Thus, by varying the member stiffness, member area, or member spacing of a geogrid, the (J_{sec}) is changed.

Ideally, a model geogrid will simply be constructed to $1/N^{th}$ the size of the prototype and from the same material. However, to manufacture a model geogrid of those dimensions is impractical (a 3 mm thick strand should be 0.1 mm thick at $30g$). Consequently, a geogrid with dimensions larger than $1/N^{th}$ of that of the prototype is usually used. As these dimensions change, the stiffness (J_{sec}) of the geogrid changes. Consequently, to construct a model geogrid of practical dimensions, while retaining the correct stiffness, a material different from that of the prototype might have to be used.

Stiffness, skin friction and aperture size influence the remaining fundamental geogrid property, i.e. bond. Of these three properties, the aperture size will be affected most if the model dimensions are not scaled by $1/N$. Furthermore, a reduction in aperture size will reduce the percentage open area of the model geogrid. The smaller area of clay-clay contact through the geogrid will result in a more severe artificial shear plane (Section 2.5) when compared to a prototype geogrid. The interface shear stress of the geogrid, however, depends on the normal stress and the interface friction angle, or skin friction ($\tau = \sigma_n \tan \phi_{inter}$). Since the normal stress increases with acceleration, the interface shear stress will follow suit, as long as the interface friction angle remains constant.

As summary of the scaling laws discussed, as well as other relevant laws derived by Viswanadham & König (2004), are summarised in Table 5.2. Ideally, all the properties of the model geogrid will be equivalent to that of the prototype at increased acceleration. However, at present it is not physically possible to construct such model geogrids and some model geogrid properties will be somewhat unrealistic for a prototype geogrid at increased acceleration.

Table 5.2: Scaling laws for using geogrids in the centrifuge Viswanadham & König (2004).

Property	$\frac{\text{Model}}{\text{Prototype}}$ at Ng
Strain [%]	1
Dimensions [i]	1/N
Percentage open area	$1/N^2$
Displacement	1/N
Stiffness	1/N
Pull-out force	$1/N^2$
Bond stress	1
Interface friction angle	1

[i] Length, width and thickness

A Huesker HaTe® 23.142 mesh was selected for the model geogrid (see Figure 5.8). The mesh is manufactured from polyethylene terephthalate (PET) plastic. Other basic properties of the geogrid is provided in Table 5.3. The unrealistic equivalent dimensions of this fine mesh at 30g gives some indication of the difficulty the centrifuge modeller has in finding a suitable model geogrid.

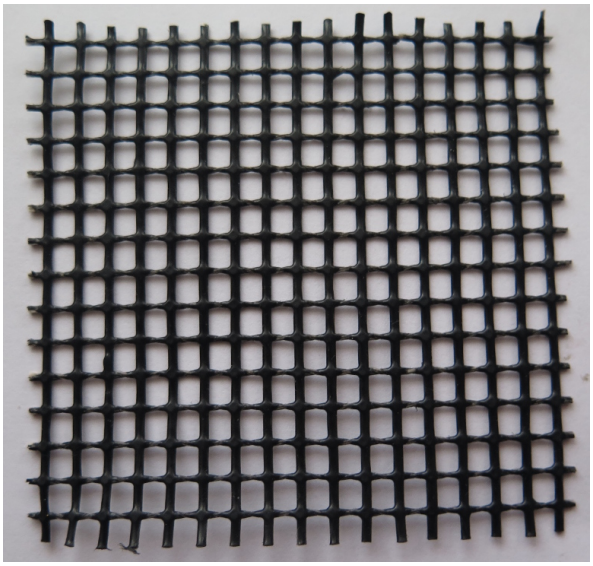

Figure 5.8: Photo of the HaTe® mesh used as a model geogrid.

The stiffness of the mesh was tested using the ASTM standard D6637-11 (2011) as a guideline. The Lloyds 5 kN press and load cell used for the bending beam tests (Section 3.2.1) was used. Two diamond coated pneumatic grips were used to clamp the mesh down as shown in Figure 5.10. The top grip was free to swivel in plane, while the bottom was held rigid.

Table 5.3: Properties of the HaTe® mesh used as model geogrid

Property[i]	Value	
	1*g*	30*g*
Unit mass[ii] [g/m^2]	160 (1.570)[iii]	160 (47.09)
Aperture size[ii] ($a_l = a_t$) [mm]	3 ± 0.5	90 ± 15
Open area [%]	64	64
Rib thickness [mm]		
Longitudinal[iv] (t_l)	0.29[vi]	8.7
Transverse[v] (t_t)	0.35	10.5
Rib width [mm]		
Longitudinal (b_l)	0.61	18.3
Transverse (b_t)	0.91	27.3

[i] For symbols see Figure 5.9. [ii] Testing done by the manufactorer according to EN ISO 10319 and EN ISO 12956.
[iii] Unit weight in round brackets. [N/m^2].
[iv] Also known as machine direction (MD).
[v] Also known as cross machine direction (CMD).
[vi] Values are the average of 10 measurements.

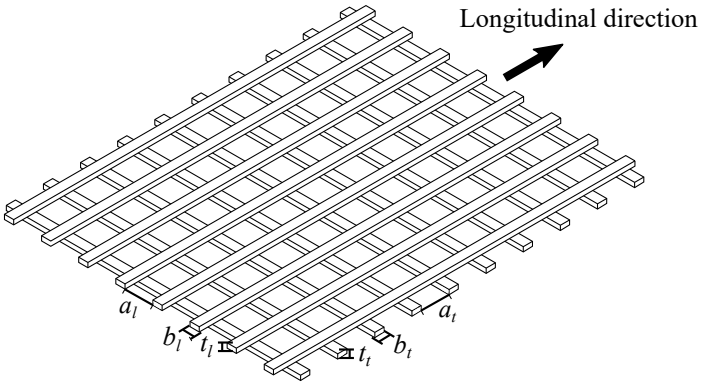

Figure 5.9: Common symbols used to define a geogrid's dimensions.

Each grip was large enough to clamp a sample of 8 x 8 apertures. The section of the sample that was free to strain comprised of 16 x 8 apertures for a total sample size of 32 x 8 apertures. D6637-11 (2011) prescribes that the sample should be 200 mm wide and 300 mm long, and that there should be at least two apertures and three ribs in the cross machine direction. The second requirement of the standard was conformed to. However, due to the size of the press a sample size of 200 x 300 mm could not be tested.

Figure 5.10: Tensile testing of the HaTe® mesh with a 5 kN Lloyds Tensile Tester.

The HaTe® mesh is fairly flexible and had some slack after it has been clamped in the press. A pre-tension load of 2.5 N was applied to the sample to remove the slack. This is within 1.25% of the ultimate tensile strength of the geogrid (Table 5.3) as D6637-11 prescribes. The sample was strained at a rate of 20 mm/min until the pre-tension load of 2.5 N was reached. After the pre-tension load was reached, the sample was tested at a rate of 6 mm/min. This strain rate, equivalent to ≈ 12.5%/min, is within the 10 ± 3%/min limit of the standard.

The pre-tension displacement was added to the initial gauge length to calculate the sample strain (D6637-11). Similarly, the pre-tension load of 2.5 N was subtracted from the measured load measured to determine the net load. The tensile load-strain behaviour of the mesh is presented for both the longitudinal and transverse directions in Figure 5.11a. The load-strain curve is initially steep, whereafter it becomes non-linear and flatter, typical for PET plastic (Dupaix & Boyce, 2005). These load-strain curves were used to calculate the secant tensile modulus of the mesh as shown in Figure 5.11b. The modulus value specified at a number of discrete point,s for both $1g$ and the equivalent $30g$ value, is shown in Table 5.4. The stiffness in the longitudinal direction is higher than in the transverse. This is probably because the fibres in the longitudinal direction are twisted around each other, increasing the

stiffness. In contrast, the fibres in the transverse direction are parallel to each other.

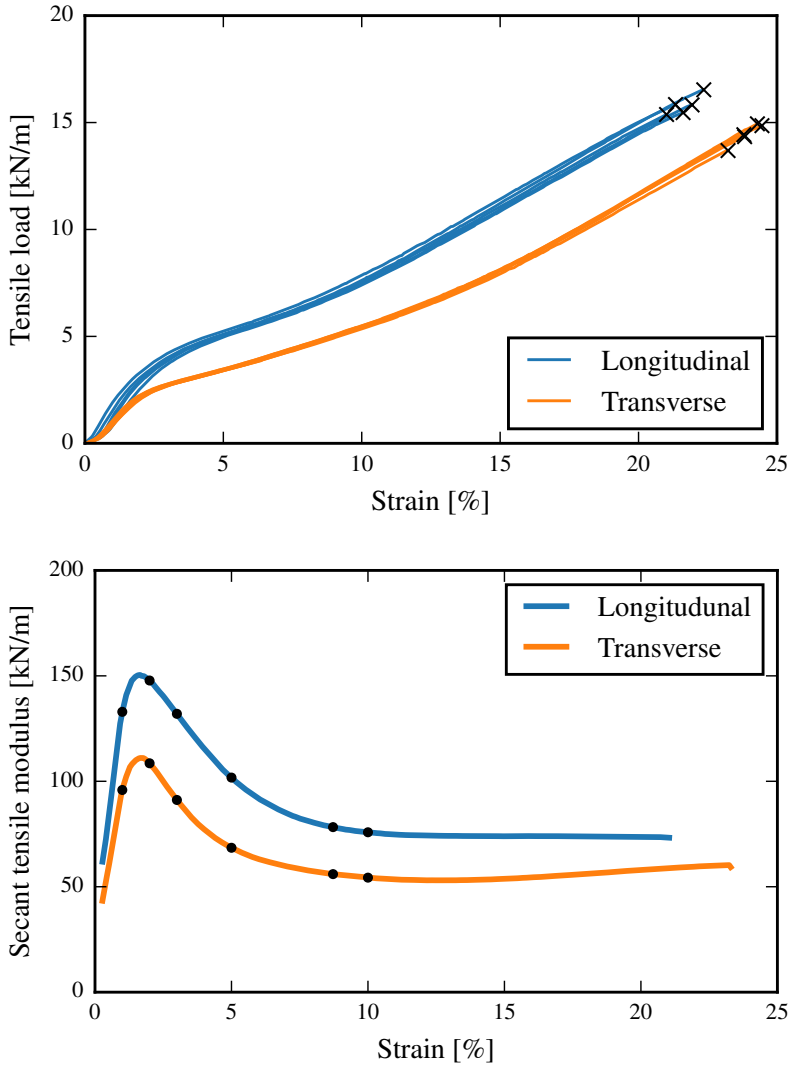

Figure 5.11: Tensile load-strain behaviour of the HaTe® mesh (a) and secant tensile modulus of the HaTe® mesh as a function of strain (b).

There was an initial increase in tensile modulus up to ≈ 1.7% strain. Thereafter, the tensile modulus decreased and eventually reached a plateau. The equivalent tensile modulus of the model geogrid at 30*g* (2876 kN/m at 1% strain) is fairly high for a geogrid. However, the use of this mesh as a model geogrid is still justifiable for the following three reasons: 1) geogrids with a higher tensile modules has been used in practice to span voids (e.g. 26 000 kN/m at 1.8% strain by (Alexview, 1997)), 2) the failure mechanism that occurs will still be representative of a PET geogrid and 3) previous centrifuge studies successfully used model geogrids of similar high tensile modulus (e.g Viswanadham & Jessberger (2005)).

Table 5.4: Secant tensile modulus of the HaTe® mesh at a number of strains.

Strain	J_{sec} [i] [kN/m]	
[%]	Transverse	Longitudinal
1	95.88 (2876)	132.9 (3988)
2	108.5 (3256)	147.8 (4434)
3	91.15 (2734)	132.0 (3960)
5	68.48 (2054)	101.8 (3053)
10	54.31 (1629)	75.83 (2275)

[i] Equivalent modulus at 30g shown in ().

Since the mesh is made of PET, the skin friction and related aspects of bond will be representative of a PET prototype geogrid. However, the percentage open area is low for geogrids. Furthermore, Shinoda & Bathurst (2004) found that under tensile loading a knitted PET geogrid undergoes limited lateral strain. Thus, this model geogrid will remain at the same width during testing, making it suitable for plane-strain testing in the centrifuge.

5.2.2.3 Clay properties

The same clay that was used for the bending beam tests (Chapter 3) was used for the construction of the model liners. The properties of the kaolin is discussed in detail in Section 3.1.

5.2.3 Model liner construction

It was mentioned in Chapter 3 that model clay liners consolidated to the required density behaved similar to compacted model liners. Consequently, the model clay liners used for the centrifuge tests were prepared by one dimensional consolidation to ensure repeatability. The mixing, consolidation, swell, cutting, reinforcement and placement of the model liners are discussed next. From mixing to swell, the steps followed were the same as for the bending beams tests in Section 3.2.2 and are repeated only briefly.

Mixing: The clay was mixed at a moisture content of 100% for a minimum of 10 min with a motorised mixer. For the first three tests (see Section 5.2) a vacuum was applied during the mixing. The final two slabs were mixed without any significant vacuum applied. However, similar undrained

shear strengths were measured as for the vacuum mixed slabs (compare the results of Figure 5.18 discussed later in this chapter). Consequently, the lack of vacuum applied to the final two tests should not have had a significant influence on the results. The slurry was poured into an oiled rectangular steel mould (710 mm x 155 mm), fitted with both top and bottom drainage.

Consolidation: The filled mould was placed in the consolidation press shown in Figure 3.8 (p.58). Thereafter, the clay was consolidated in stages up to 610 kPa. This consolidation pressure is equivalent to the 95% Proctor density of 1416 kg/m^3 and a void ratio of 0.88.

Swell: After the clay has fully consolidated at 610 kPa it was swelled in steps of approximately 100 kPa per hour back to 50 kPa. The clay remained at the final swell pressure of 50 kPa for a minimum of two hours to allow for the pore pressures to equilibrate.

Cutting: After the clay had swollen at 50 kPa for two hours it was removed from the consolidation press and prepared for the centrifuge. Firstly, the clay was demoulded and the surface trimmed using two wooden guides and a sharpened metal plate (Figure 3.11, p.61). These cuttings were used for moisture content samples. A further 55 mm was cut from either end of the 710 mm slab for a final model liner length of 600 mm. These pieces were wrapped in cling-film and stored for penetrometer testing to assess their consistency. Thereafter, a perforated plastic sheet glued to two wooden handles was placed on top of the clay. Both clay and plastic was turned over and the clay was trimmed at the bottom. Again the trimmings were used for moisture content cuttings. Finally, 5 mm was scraped from the length of the liner for a final width of 150 mm. One side of the model liner was lowered into washed sand grains to provide texture for PIV analysis. The remaining three exposed surfaces of the model liner were coated with petroleum jelly to prevent it from drying out during the centrifuge test.

Placement: During the time that the bottom of the liner was trimmed, the texture added and the petroleum jelly applied, significant suction developed between the surface of the clay and the plastic sheet. This suction was high enough that the clay could be lifted with the plastic sheet and placed in the centrifuge strongbox. After the model liner was placed in the strongbox, the plastic sheet was removed and a layer of petroleum jelly was applied to the surface of the model liner. The petroleum jelly was covered with fine sand to provide a better surface for the laser scanner.

Reinforcement: Some tests required that the HaTe® mesh should be embedded in the model liners for reinforcement. The mesh was used in the transverse direction for the centrifuge tests. Firstly, the aluminium anchors shown in Figure 5.12 were fixed to the mesh to prevent a pull-out failure from occurring . These anchors worked similar to the initial anchors used in pre-stressed concrete.

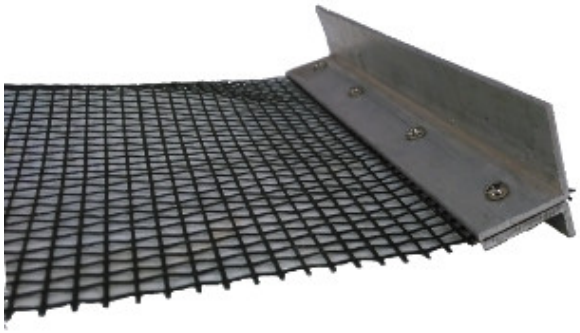

Figure 5.12: Aluminium anchors used to anchor the model geogrids.

To embed the geogrid in the model clay liners, a layer of clay was firstly consolidated to 400 kPa. After the consolidation and swell of the clay the mould was disassembled and the layer trimmed. Thereafter, the mesh was placed on top of this clay and the anchors pressed into in. Finally, the mould was reassembled, filled with slurry and the consolidation process was repeated, this time up to a final consolidation pressure of 610 kPa.

Some authors (Viswanadham & Jessberger, 2005) added markers to the ends of the geogrid ribs closest to the window. Tracking these markers during the test allowed for the calculation of the strain in the geogrid. However, these markers are quite large relative to the soil particles. Consequently, it was thought that the markers would distort the strains at the soil-geogrid interface at the strongbox window and no markers were used.

5.2.4 Measurement equipment

In this subsection the measurement equipment used are discussed. Firstly, the camera used for the DIC analyses is discussed, followed by some general measurement instrumentation used. Finally, the penetrometer testing used to measure the undrained shear strength of the liners is discussed.

5.2.4.1 Camera

The most critical piece of the instrumentation was a Canon 100D SLR camera fitted with a 40 mm fixed lens. This camera was used to continuously take photos of the liner as it deformed. These photos were subsequently used to measure the strain with Digital Image Correlation (DIC). DIC was discussed in detail in Section 3.2.3.1.

To determine whether there was any distortion of the photos by either the strongbox window or the camera, a photo was taken of a steel set square inside the strongbox. If the images were excessively distorted, a single calibration factor could not be used to convert image displacements from pixels to millimetres.

The photo of the steel set square is shown in Figure 5.13. The pixels between successive millimetre marks were counted. The number of pixels per millimetre ranged between 70 and 72 in the vertical direction with a standard deviation of 0.60, and ranged between 71 to 73 in the horizontal direction with a standard deviation of 0.62. Given the low standard deviations (less than a pixel), it was assumed that there was insignificant distortion of the images and a single calibration factor was therefore used. Consequently, the photos from the centrifuge analyses were calibrated by counting the number of pixels over a known length and scaling the remainder of the image by that ratio.

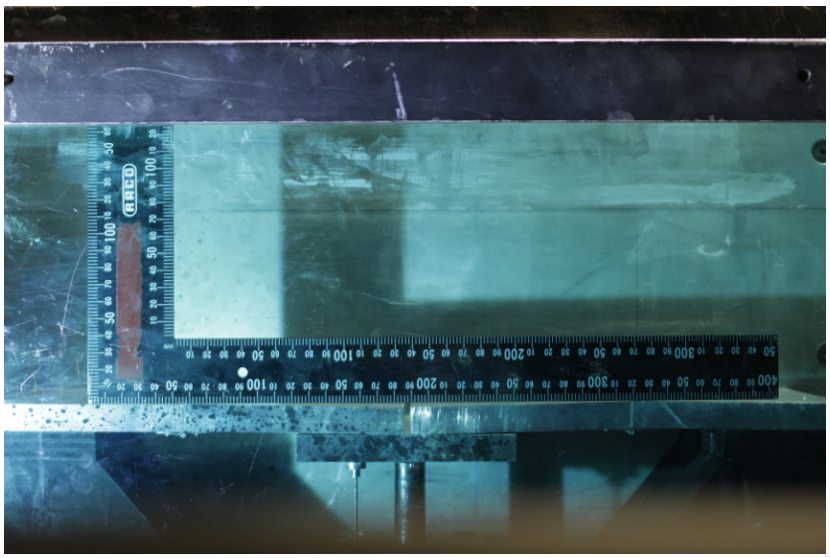

Figure 5.13: Photo of the steel set square used to determine whether the photos were distorted by either the camera or the strongbox window.

5.2.4.2 *General*

To complement the camera measurements a row of linear variable differential transformers (LVDT), spaced at ≈ 50 mm, were used to measure the shape of the settlement trough. The range of the LVDTs is only 30 mm, consequently, the instruments at the centre of the liner were out of range at the end of the test.Furthermore, potentiometer measured the settlement of the central piston while a pressure gauge monitored the pressure in the piston.

Finally, the surface of the clay liner was mapped in three dimensions with a Micro-Epsilon scanCONTROL 2900-100 laser scanner. Before the start and at the end of each test, a full scan of the surface was conducted. During the tests the settlement of the piston was stopped after every 5 mm and half of the surface of the clay was scanned.

5.2.4.3 *Penetrometer testing*

The undrained shear strengths of the model clay liners were measured with a miniature ball penetrometer. The penetrometer was manufactured from 5 mm ball bearing soldered to a hypodermic needle (see Figure 5.14). The free end of the needle was clamped to a Lloyds LC 50 N (014090) load cell on the Lloyds 5 kN press used for the testing of the HaTe® mesh. This load cell had a resolution of 0.0025 N and and measured within ±5% of the actual result. Equation 5.1 was used to convert the penetration force to undrained shear strength.

$$c_u = \frac{q}{N_b} = \frac{P_{ult}}{\pi r^2 N_b} \tag{5.1}$$

where c_u is the undrained shear strength, q the bearing resistance, P_{ult} the resisting force, r the radius of the penetrometer and N_b the bearing resistance factor.

A range of N_b factors found in literature is presented in Figure 5.15. For these tests a N_b factor of 13.5 was used. The tests were conducted at a penetration rate of 2 mm/s. In Appendix B the selection of the penetration rate and N_b, as well as the design of the test setup are discussed in more detail.

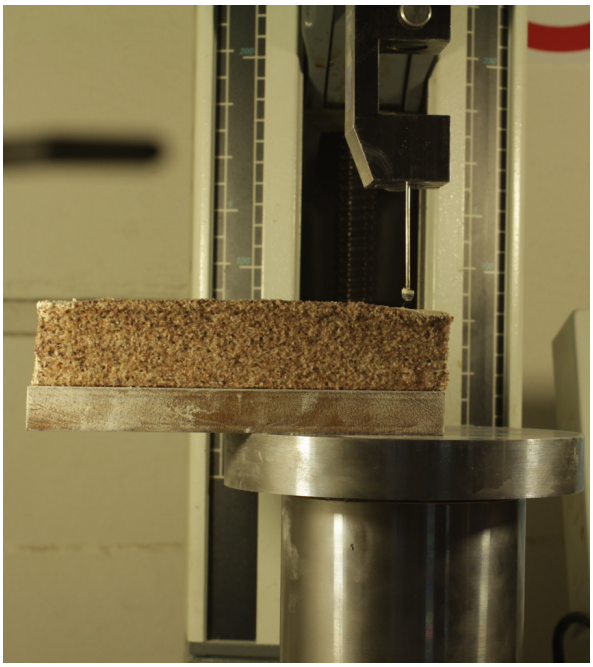

Figure 5.14: Miniature ball penetrometer test on textured clay.

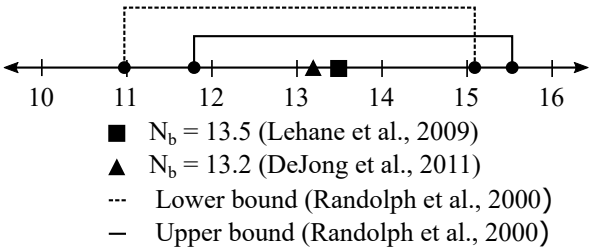

Figure 5.15: A comparison of N_b factors found in literature.

5.2.5 Test procedure

The procedure followed for each of the centrifuge tests is summarised in Table 5.5. Firstly, the model package was placed in the centrifuge. Thereafter, the acceleration was increased to 30g where the clay was allowed to consolidate. The LVDT measurements of the surface profile of the top-reinforced liner are shown in Figure 5.16 for the first 14.5 min of the first test. LVDT 1 is the left most instrument and LVDT 5 is at the centre. The two sharp drops in settlement is possibly due to slack in the hydraulic system. Furthermore, it appears that LVDT 2 got stuck after 5 minutes. After 15 min the liner was deemed to have consolidated sufficiently and there was no more slack in the hydraulic system. Further settlement was assumed to be due to creep. Settlement of the liner continued until the maximum possible settlement had been imposed. After the centrifuge test was completed, the

undrained shear strength profile of the liner was measured with the penetrometer from the blocks cut during preparation.

Table 5.5: General procedure for the centrifuge tests.

Step	Measurements conducted
1. Preparation and placement of the clay liner in the test package (Section 5.2.3).	- Moisture content samples taken. - Samples for penetrometer testing.
2. Loading of the test package onto the beam.	- 1g laser scan of the full surface. - 1g reference image.
3. Increased acceleration to 30g.	- LVDT measurements of surface profile.
4. Consolidation of the clay liner for 15 minutes.	- Full surface laser scan after consolidation. - Reference image before and after consolidation. - LVDT measurements of the surface profile.
5. Settlement of central piston at 1 mm/min for 5 mm.	- LVDT measurement of the surface profile. - Photos of the liner. - Potentiometer and pressure gauge measurements.
6. Laser scanning of the liner surface.	- Laser scanning of half of the liner surface.
7. Settlement of central piston at 3 mm/min for 5 mm, followed by a break for laser scanning of the surface. Repeated up to a total settlement of 50 mm.	- See steps 5 & 6.
8. Final laser scanning.	- Full scan of the surface of the liner.
9. Stop centrifuge.	- Post-test moisture content samples from the top of liner.
10. Penetrometer testing.	- Penetrometer tests on the samples collected in Step 1.

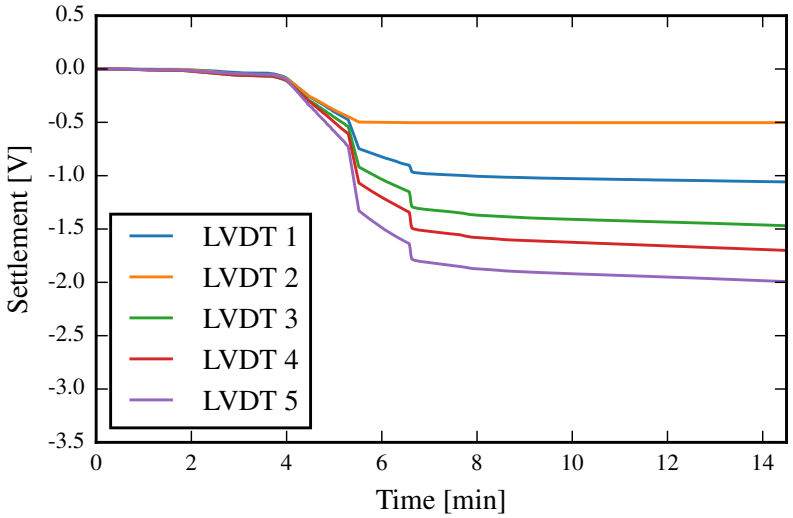

Figure 5.16: LVDT surface measurements for the first 14.5 minutes of the top-reinforced test.

5.3 RESULTS

In this section the results of the centrifuge modelling are discussed. Firstly, the undrained shear strength of the model liners as measured by the penetrometer tests are presented (Section 5.3.1). In Section 5.3.2 the cracks that were observed in the liners are discussed. These cracks were used to identify three magnitudes of central settlements at which the centrifuge tests were compared. Strain fields (Section 5.3.3) were calculated for the liners at these settlements and the liner's behaviour was compared. Finally, in Section 5.4 the effect of the experimental design on the results observed is discussed and some recommendations are made with regard to the optimal reinforcement of liners subject to differential settlement.

5.3.1 Moisture contents and shear strengths of the model liners.

Penetrometer tests were done on the two blocks of clay that were cut from the ends of each model liner after consolidation. Some additional consolidation did occur in the centrifuge. However, the consolidation stress in the centrifuge (16 kPa)[1] is significantly lower than the consolidation stress (610 kPa) during the preparation of the clay liners. Thus, the results of the penetrometer testing can be assumed to be representative of the liners in the centrifuge tests.

Nine to ten measurements were done along the length of the samples at an average spacing of 14 mm. Typical penetrometer results are shown in Figure 5.17. The penetrometer load-depth data for all the measurements of the second unreinforced liner are shown in Figure 5.17a. These results were conglomerated to find the average representative profile, as well the 95% confidence intervals shown in Figure 5.17b. The penetrometer samples were cut before the model liners were trimmed to the correct thickness. Consequently, the penetrometer results are over a depth greater than 30 mm.

The loads measured by the penetrometer were converted to undrained shear strength with Equation 5.1. The resulting profiles of shear strength with depth are shown in Figure 5.18. Consider the profile for the unreinforced liner in Figure 5.18a. As the penetrometer moves downwards, the measured resistance increases until the penetrometer is fully enveloped by the clay. From this depth onwards a constant undrained shear strength is measured and the theoretical relationship between c_u and q holds

[1] The stress at the base of a 30 mm thick clay liner with a unit weight of 17.75 kN/m^3 (from Section 3.3.1.1) accelerated to 30 g in the centrifuge is: $0.03 \times 17.75 \times 30 = 16$ kPa.

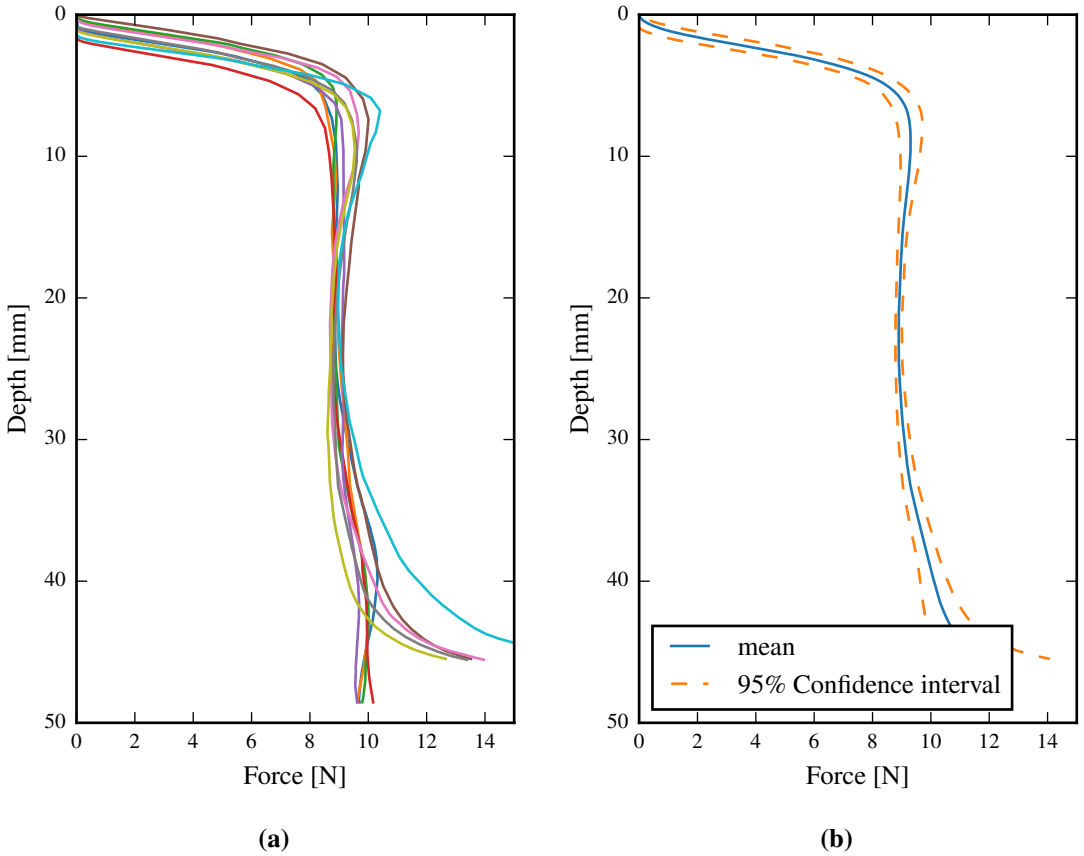

Figure 5.17: Typical penetrometer results: a) raw data and b) compiled data for the second unreinforced liner.

(Equation 5.1). Finally, as the penetrometer approaches the rigid base below the liner the additional confinement provided by the base results in an apparent increase in strength. When considering the constant segment of the curve only, the undrained shear strength of the unreinforced liner is 34.93 kPa.

The undrained shear strength of the bottom-reinforced liner increases distinctly at ≈30 mm (see Figure 5.18b). Similar behaviour can be observed for the remaining two tests. To understand why the undrained shear strength did not remain constant with depth one has to consider aspects of unsaturated soil mechanics.

The foundation of unsaturated soil mechanics is the soil water potential curve (SWPC), also known as the soil water retention curve (SWRC) or soil water characteristic curve (SWCC). This curve represents the relationship between the water retained in the soil for a given matric suction, or the matric suction

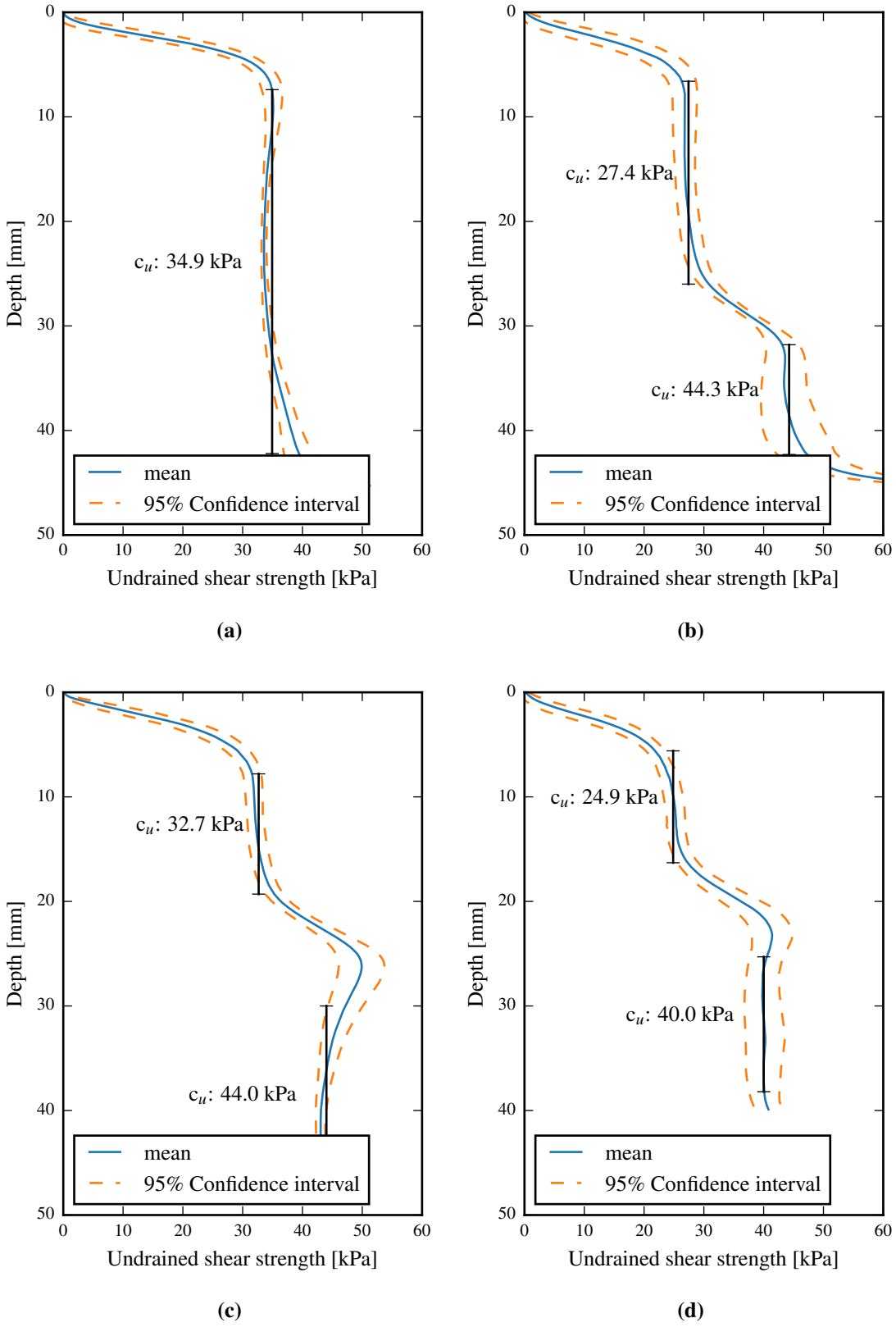

Figure 5.18: Undrained shear strength with depth of: a) the unreinforced liner, b) the bottom-reinforced liner, c) the top-reinforced liner and d) the double-reinforced liner.

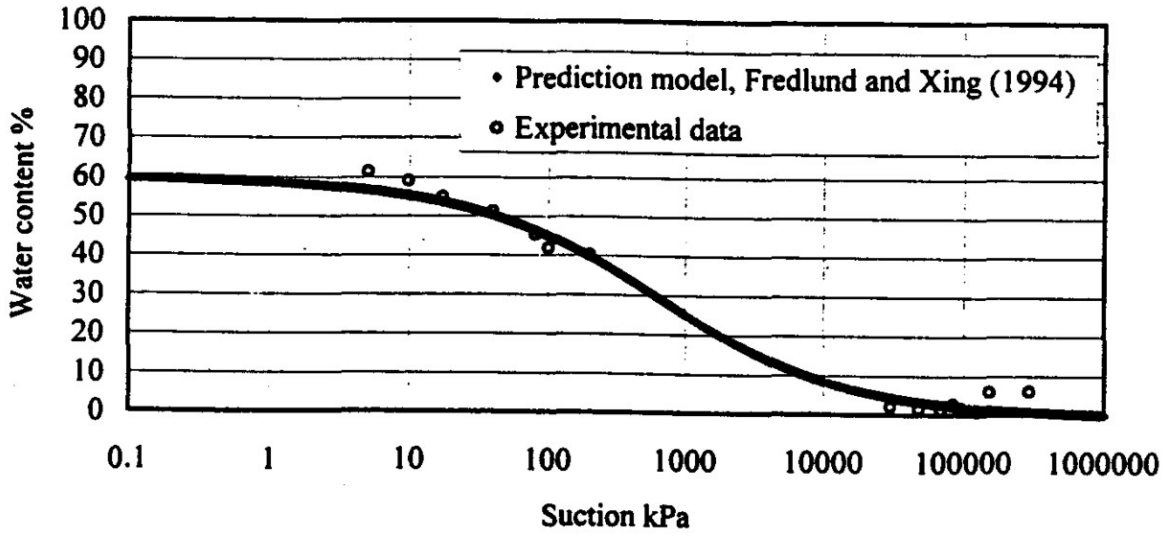

Figure 5.19: A SWPC for kaolin clay (Nishimura & Fredlund (2000)).

in the soil at a given moisture content (whether volumetric, gravimetric or degree of saturation) (Huat et al., 2012). The matric suction $(u_a - u_w)$ is the potential energy of the soil water due to capillary action and adsorption (Lu & Likos, 2004). When the matric suction is converted to pressure, it is negative (tensile).

A SWPC for kaolin clay is presented in Figure 5.19. The volumetric moisture content of the clay is shown as a function of the matric suction. Even when the clay is fully saturated (at ≈ 60% for the kaolin in Figure 5.19), a small change in moisture content will result in a change in matric suction.

A relationship between undrained shear strength of the clay (τ) and matric suction $(u_a - u_w)$ is presented in Equation 5.2. The SWPC model by van Genuchten (1980) is substituted into the model for undrained shear strength by Vanapalli et al. (1996).

$$\tau = c' + (\sigma_n - u_a)\tan\phi' + (u_a - u_w)\left(\tan\phi' \cdot \frac{1}{\left(1 + \left[\alpha(u_a - u_w)\right]^n\right)^{1-1/n}}\right) \tag{5.2}$$

where the material variables are: c' the intercept of the Mohr-Coulomb failure line, ϕ the friction angle, α and n fitting parameters for the SWPC; and the state variables are: u_a the pore air pressure and u_w the pore water pressure that are the components of the matric suction $(u_a - u_w)$, and σ_n the normal stress. For a soil drying under a constant normal stress Equation 5.2 can be simplified to:

$$\tau = f\left((u_a - u_w) \cdot g(u_a - u_w)\right) \tag{5.3}$$

Thus, a significant increase in suction due to a slight reduction in moisture content will result in a significant increase in shear strength. It is assumed that this behaviour resulted in the higher shear strength of the bottom layers of the model clay liners. The reinforced liners were prepared in two casts (as discussed in Section 5.2.3). For the second cast of each liner the mould was disassembled, the clay trimmed, the mesh added and the mould reassembled. During these ≈ 30 minutes the bottom part of the liner (that was cast first) dried out slightly. The moisture content at the top and at the bottom of the model liners is shown in Figure 5.20. A slight difference in moisture content between the top and bottom can observed. This slight change in moisture content induced a significant change in suction and thus the undrained shear strength increased at the base of the liners (seen in Figure 5.18b, c and d).

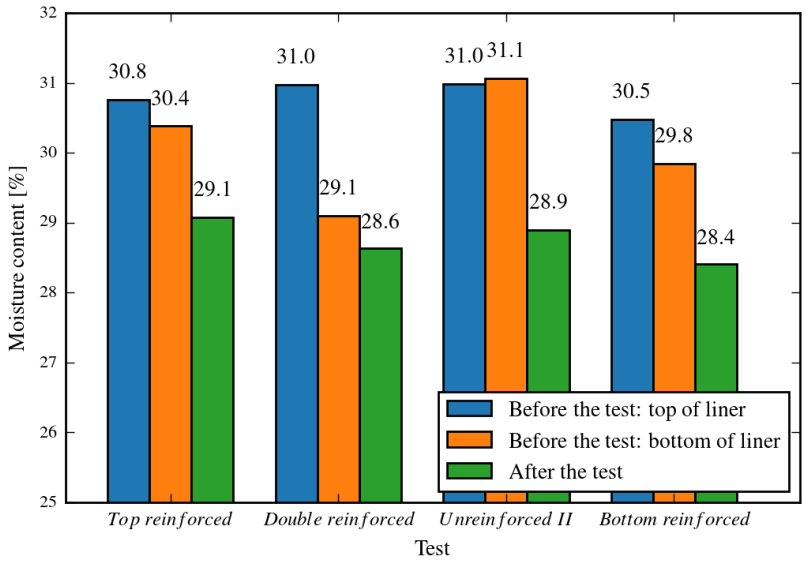

Figure 5.20: Moisture content at the top and bottom of the model liners.

The moisture contents of the liners after the centrifuge tests had been completed are also indicated in Figure 5.20. It appears that during the tests the moisture content of the liners decreased, most likely due to consolidation of the liner under the increased acceleration and some drying out.

5.3.2 Cracks observed in the model liners

Surface laser scans of the macro cracks that opened in the liners are shown in Figure 5.21. Photos of the cracks taken from the side are shown in Figure 5.22. The unreinforced liners simply cracked from the top through to the bottom at the two hogging zones. Similar behaviour was observed in the

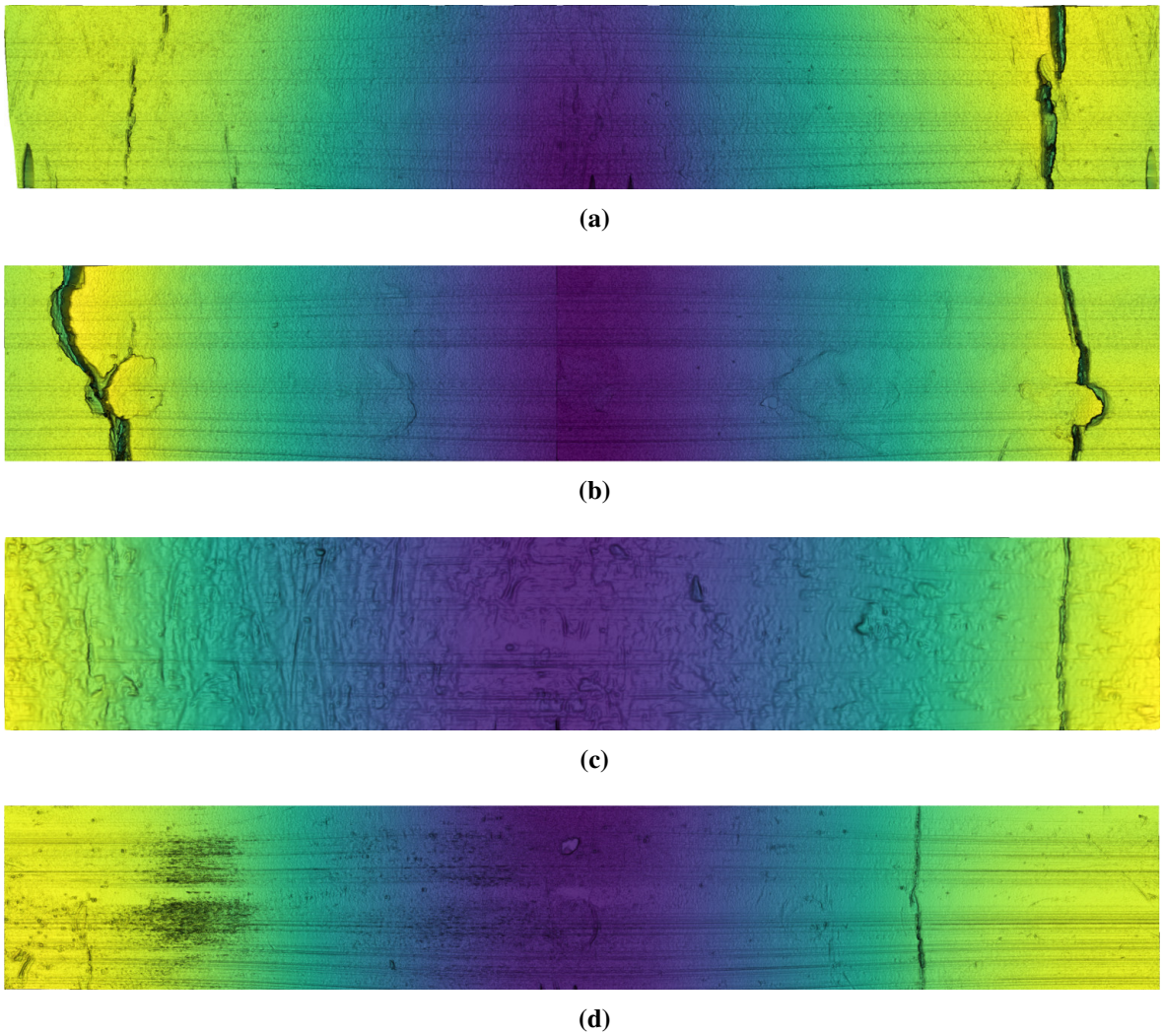

Figure 5.21: Laser scans of macro cracks on the liners surfaces: a) second unreinforced liner, b) bottom-reinforced liner, c) top-reinforced liner, d) double-reinforced liner.

bottom-reinforced liner, with the crack extending from the liner surface to the level of the geogrid. For both the double-reinforced and the top-reinforced liners, the crack terminated at the level of the top geogrid. After the centre displacement was subsequently increased, the cracks propagated through to the bottom. Similar cracks were reported by Jessberger & Stone (1991) for unreinforced tests and Viswanadham & König (2004) and Rajesh & Viswanadham (2009) for reinforced tests. From the photos of the cracks and the laser scans it is clear that the geogrid reinforcing has a beneficial effect on the fracture behaviour of liners subject to settlement. For the unreinforced and bottom reinforced liners the cracks are significantly more severe than for the top- and double-reinforced liners.

The photos shown in Figure 5.22 and others were used to visually identify the locations where macro

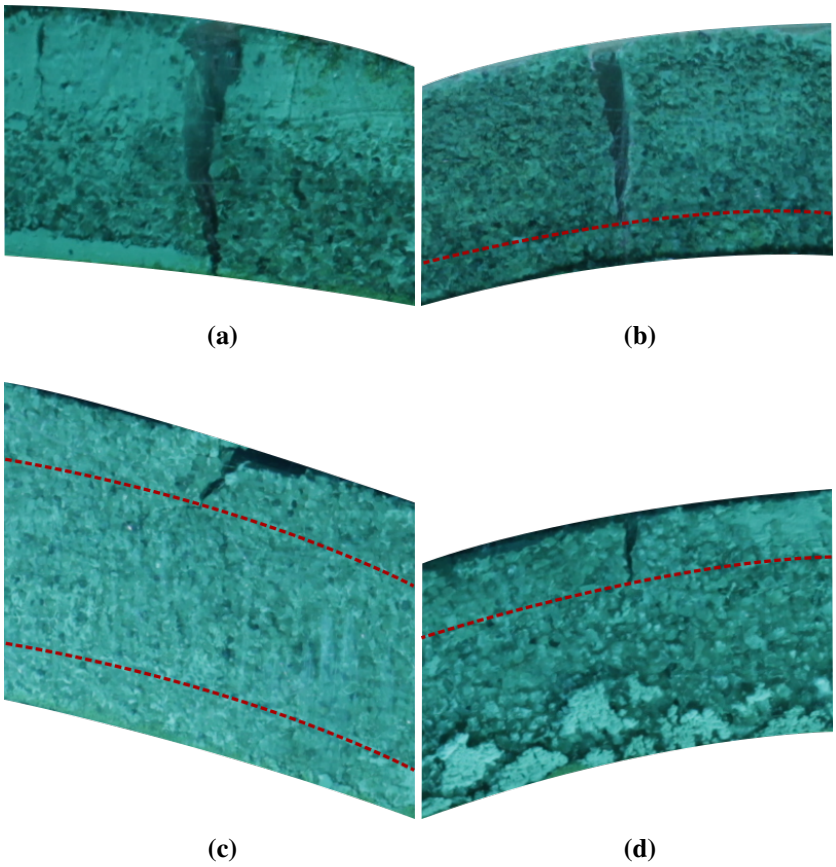

Figure 5.22: Cracks observed in a) the second unreinforced liner, b) the bottom reinforced liner, c) the double reinforced liner and d) the top reinforced liner. The position of the reinforcement is indicated with a red dashed line.

cracks originated in the liners. At each of these locations the linear horizontal strain at the surface of the liner was calculated. The same method and strain gauge length used for the bending beams tests (15.23 mm) was applied (Section 3.3.3.1). This strain is presented as a function of the central piston settlement in Figure 5.23. The settlement of the central piston was indicative of the magnitude of the depression below the liner. The displacements where the strain-displacement behaviour changed from linear to non-linear are indicated with a marker in the figure. As there were a limited number of data points (one for each digital image), the change from linear to non-linear was identified visually.

At an average central displacement of 4.06 mm the horizontal strain-displacement behaviour of the unreinforced liner deviated from linear. When considering the results of the bending beam tests in Chapter 3, this deviation from linear behaviour would correspond to the occurrence of micro-cracks. For the bottom-reinforced liner at two of three locations micro-cracks were assumed to occur at 7.88 mm central settlement. For the top-reinforced liner micro-cracks were assumed occur at 12.7 mm central

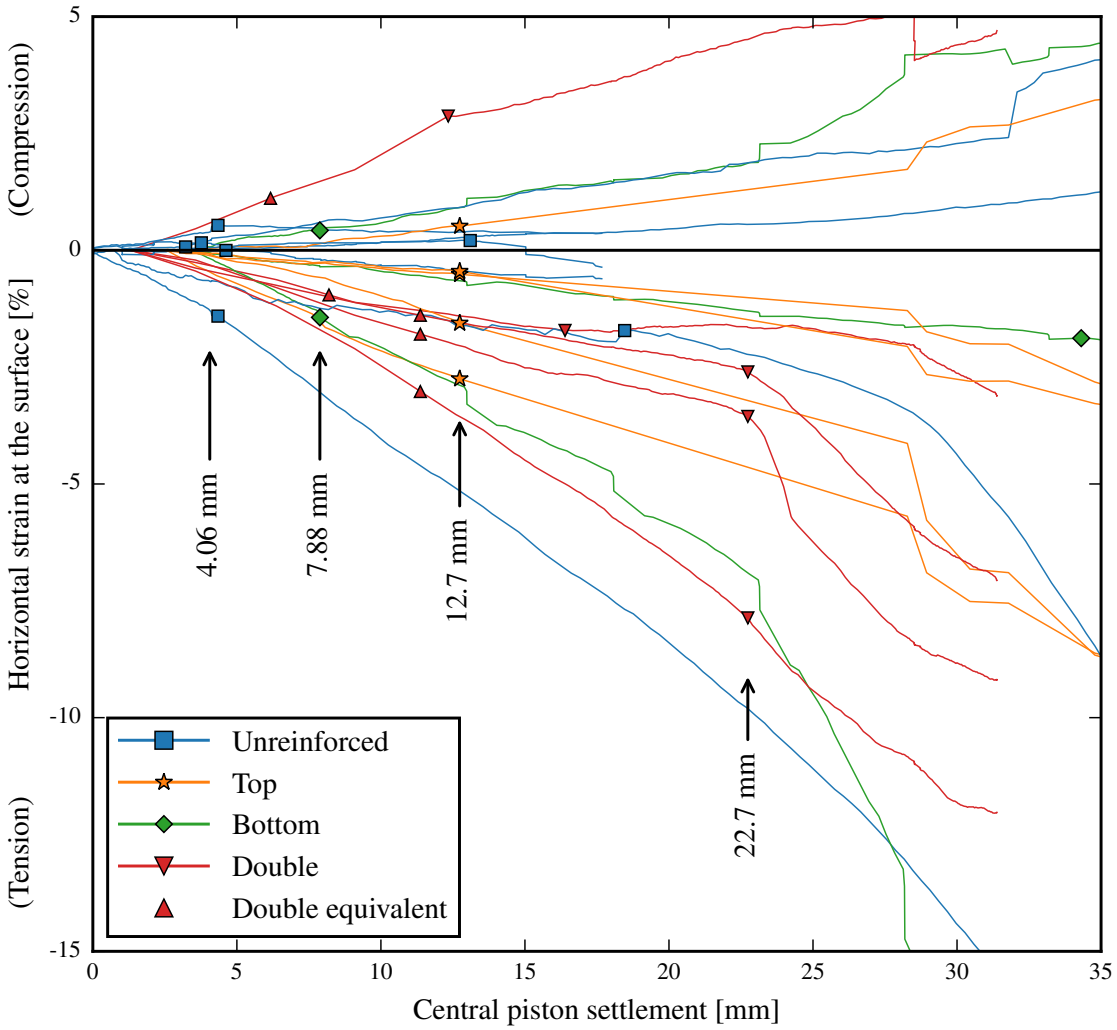

Figure 5.23: Strain-central piston settlement behaviour at the locations of the cracks. The origin of micro-cracks is indicated by a marker.

settlement and for the double-reinforced liner micro-cracks occurred at three locations for a settlement of 22.7 mm. These strain-displacement plots already show the benefit of geogrid reinforcement and the influence of reinforcement position. The unreinforced liner cracked under a smaller depression (central settlement) than the bottom-reinforced liner that, in turn, cracked at a smaller depression than the top- and double-reinforced liners. This implies that a greater void can form below the top- and double-reinforced liners before the integrity of the liners is compromised.

Two model geogrids were used to reinforce the double-reinforced liner. Thus, the total stiffness of the reinforcement for this liner is double that of the others. The obvious solution would have been to reduce the stiffness of the geogrids used for the centrifuge test of the double-reinforced liner by half. However,

this would have entailed sourcing another model geogrid with exactly the same dimensions and halve the stiffness, or reducing the stiffness of the HaTe® mesh used by half. Cutting every second strand of the HaTe® mesh, or a similar approach, would have had a significant influence on the interaction behaviour of the model geogrid. As seen in Section 2.4.1, the interaction between of geogrids and clay is a complex, non-linear problem. Thus, both sourcing another geogrid or reducing the stiffness of the model geogrid were impractical. Consequently, the HaTe® mesh was used at both reinforcement positions of the double-reinforced liner. To directly compare the results from a single reinforced test with a double reinforced test a suitable point of comparison had to be found.

Firstly, the behaviour of the double-reinforced system was assumed to be linear elastic until the onset of micro-cracks. Consequently, the results for a liner of one stiffness can be scaled linearly to find the behaviour equivalent to a system of a different stiffness (up to the occurrence of micro-cracks).

To compare the behaviour of a lower reinforcement stiffness liner system (Liner A) to that of a stiff liner system (Liner B), the point of comparison should be selected such that the stress in the stiffer liner (σ_B) should equal that in the less stiff liner (σ_A) :

$$\sigma_A = \sigma_B$$
$$\Rightarrow \frac{M_A \cdot y}{I_A} = \frac{M_B \cdot y}{I_B}$$

(In these tests the stress in the liners is predominantly due to bending.)

When the sand below the liner settles, support is removed below the liner. Consequently, the self-weight of the unsupported liner segment above the void induces a bending moment in the liner. It is shown in Appendix C that the relationship between the central settlement and moment in the centre of the liner is linear ($M = k \cdot \Delta$). Thus:

$$\frac{k \cdot \Delta_A \cdot y}{I_A} = \frac{k \cdot \Delta_B \cdot y}{I_B}$$
$$\Rightarrow \frac{\Delta_A}{\Delta_B} = \frac{I_A}{I_B} \tag{5.4}$$

The ratio Δ_A/Δ_B is proven to equal $1/2$ in Appendix C if the reinforcement stiffness of System B is double that of System A.

Consequently, during linear-elastic behaviour the stress distribution in the system of higher reinforcement stiffness (System B) will match that in the system of lower stiffness (System A), when the former is displaced by double the displacement of the lower stiffness system. Thus it is argued that for a given displacement of the top- or bottom-reinforced liners, the comparable behaviour of the double-reinforced liner will occur at double that central settlement.

The diamond markers in Figure 5.23 indicate the displacements where micro-cracks in the double-reinforced liner are assumed to have occurred, if its total stiffness was similar to that of the top- and bottom-reinforced liners. As with the similar cracking patterns observed in Figures 5.21 & 5.22, the assumed settlement required for micro-cracks formation is the same for the top-reinforced liner and the double reinforced liner at $3/5^{ths}$ of the locations. It would have been expected that the double-reinforced liner would crack at a larger central piston settlement (larger depression) than any of the other liners. However, the double reinforced liner had to be removed from the mould twice to place reinforcement. Consequently, it was drier than the other liners (Figure 5.20) and thus more brittle.

The three settlements stages where the behaviour of the unreinforced, bottom-reinforced and top-reinforced liners changed, i.e. (I) 4.06 mm, (II) 7.88 mm and (III) 12.7 mm, were selected as comparison points for subsequent analysis of the centrifuge tests. A summary of these settlement stages is presented in Table 5.6. For the remainder of the chapter the settlement stages will be referred to as Stage I, Stage II and Stage III.

Table 5.6: Critical settlement stages in the centrifuge tests for the comparison of the results.

Central settlement stage	Magnitude[i] [mm]	Significance
I	4.06	Occurrence of micro-cracks in the unreinforced liner.
II	7.88	Occurrence of micro-cracks in the bottom-reinforced liner.
III	12.7	Occurrence of micro-cracks in the top-reinforced (and double-reinforced) liner.

[i] The equivalent behaviour for the double reinforced liner would be at double this central piston settlement.

The approximate radii of curvature at the top of the liners where the micro-cracks opened are shown in Figure 5.24. The radii of curvature of the liners were calculated in a similar manner to the radii of

curvature for the bending beam tests (Section 3.3.2). For most of the tests the micro cracks formed at a comparable radius of curvature (and thus strain), confirming that the clay liners behaved consistently over all the tests.

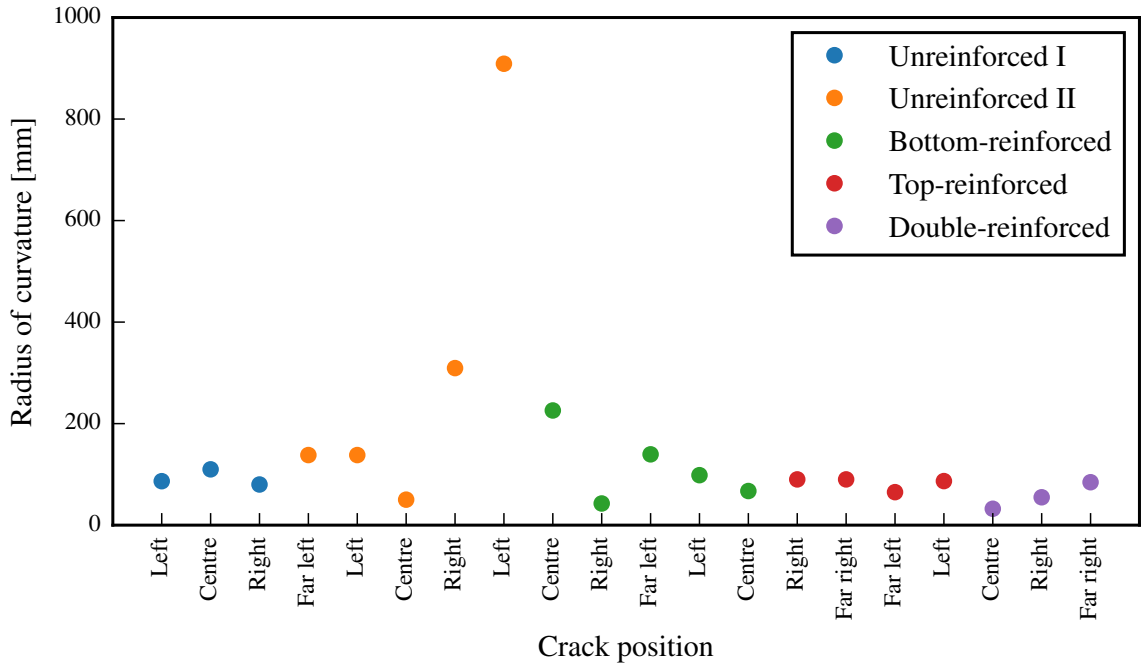

Figure 5.24: The radii of curvature where the micro-cracks originated at each location for the different tests.

5.3.3 Strain fields

The GeoPIV-RG DIC software (Stanier et al., 2015) was used to calculate strain fields across the depth of the model liners as they deformed. The analyses were highly sensitive to the size of the patches tracked. A series of large patches gave accurate displacements, however, the resulting strain field was quite coarse. Using a smaller patch size resulted in a higher resolution strain field at the cost of accuracy. Furthermore, large areas of the liner were unrepresented due wild vectors and patches with poor correlation that had to be removed. As a compromise between the high accuracy of large patches and high resolution of small patches, three sets of analyses were done for each centrifuge test: patches of 16 pixels diameter spaced at 16 pixels (≈ 2.26 mm), 24 pixel diameter pathces spaced at 24 pixels (≈ 3.91 mm) and 32 pixel diameter patches spaced at 32 pixels(≈ 4.52 mm).

The three sets of results were combined to form a final strain field for each test. Each of the three data sets was first interpolated over a regular gridded 16x16 pixel mesh. The biharmonic spline interpolation

procedure of MATLAB 2016b's `griddata` function was used. A weighted average of the three resulting meshes was calculated at each of the grid points to form the final strain field. Weights were assigned based on the expected error for each analyses. Both White et al. (2003) and Stanier et al. (2015) found that the error by the DIC analysis is proportional to the inverse of patch size. Accordingly, the weights were assigned as 1/(1/patch size), thus the patch size.

The process is illustrated in Figure 5.25. In Figure 5.25a the strain field calculated from a DIC analyses with 32 pixel diameter patches, interpolated over a regular gridded 16x16 mesh is shown. The stress concentration visible is the left hand crack in the second unreinforced liner (shown in Figure 5.22a) at Stage II. Similar strain fields are shown in Figure 5.25b & c for 24 and 16 pixel diameter patches. The high resolution but high number of random walking errors of the 16 pixel diameter analysis is clearly visible. Finally, the combined mesh that combines the accuracy of the coarse mesh with the resolution of the finer mesh is shown in Figure 5.25d.

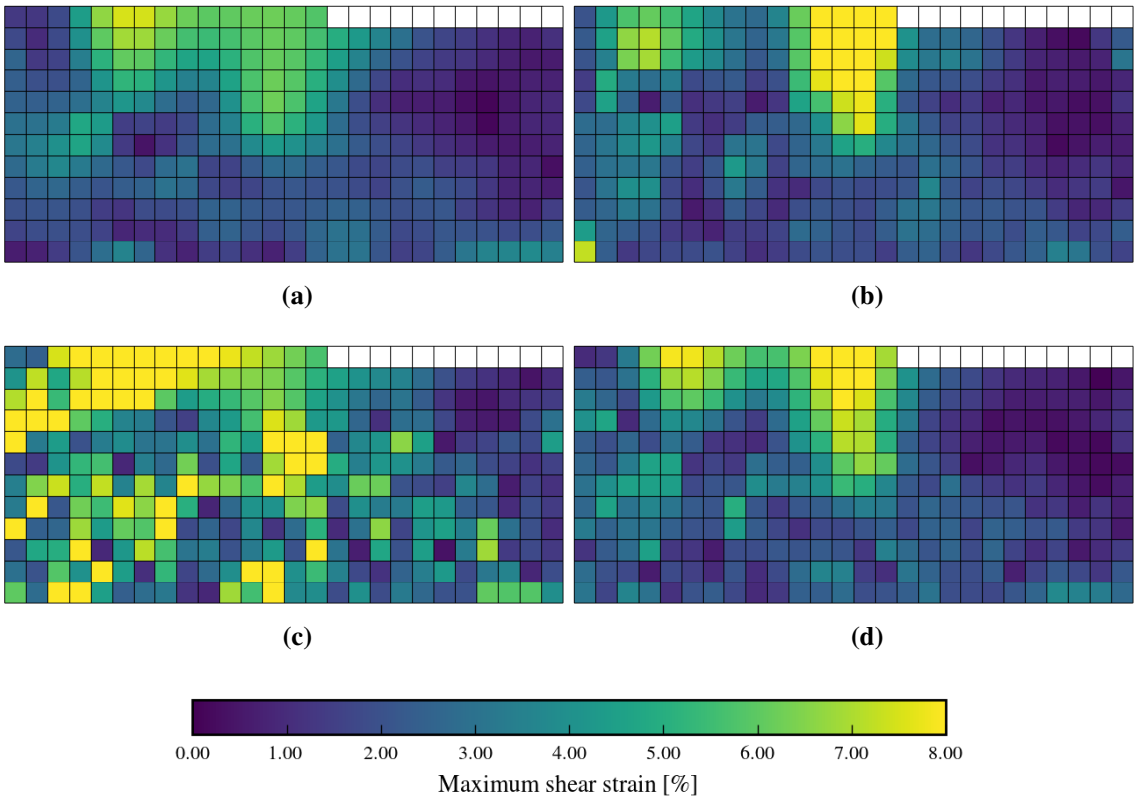

Figure 5.25: Combination of three sets of DIC strain fields of the left crack of the unreinforced liner into a single strain field. Figures a, b and c show the original data interpolated over a regular gridded 16x16 pixel mesh: a) 32 pixel diameter patches, b) 24 pixel diameter patches, c) 16 pixel diameter patches and d) the combined mesh.

5.3.3.1 *Scaling of the strain fields*

During model preparation and acceleration of the centrifuge tests there was some initial settlement of the liner due to slack in the hydraulic system. Consequently, the strain fields calculated from the DIC analyses cannot be assumed to represent the actual strain in the liner as it does not include the initial distortion of the liner. Thus, the strain fields for the various tests had to be scaled for it to be comparable. The horizontal strain fields for each test were scaled to fall in the range [-1;1] and the maximum shear strain fields in the range [0;1]. The stains were scaled by the minimum and maximum strain values during Stage III ($\varepsilon^* = (\varepsilon - \varepsilon_{min})/(\varepsilon_{max} - \varepsilon_{min})$), as these were assumed to be the extremes for the test. These minima and maxima were identified after outliers have been removed from the data. However, as the horizontal- and shear strain distributions were not normally distributed, the minimum (ε_{min}) and maximum strain (ε_{max}) values were identified by using techniques from the field of *Robust Statistics*. A detailed discussion on the identification of the outliers is presented in Appendix D.

To summarise, for a given test the maximum horizontal strain value in the test would equal one. The minimum horizontal strain would equal negative one. Similarly, the maximum shear strain in a test would equal 1.

5.3.3.2 *Resulting strain fields*

Shear and horizontal strain fields were generated for the second unreinforced liner and the three reinforced liners at each of the three stages identified in Figure 5.23, as summarised in Table 5.6. Only a number of these strain fields are shown in this chapter. The remainder of the strain fields can be found in Appendix E. For comparative purposes segments of the liners were isolated and the strain fields enlarged. The locations of these segments coincide with sections where significant cracks occurred and are indicated in Figure 5.26.

The first set of strain fields to be discussed are the shear strain fields in Figure 5.27 representing the left hand location indicated in Figure 5.26. As result of the scaling applied (Section 5.3.3.1), the strain intensities at a given stage should be comparable between tests. The strain concentrations in Figure 5.27 correspond to the shapes and locations of the macro-cracks identified in the photographs shown in Figure 5.22. At Stage III the strain concentrations in the unreinforced liner extended from

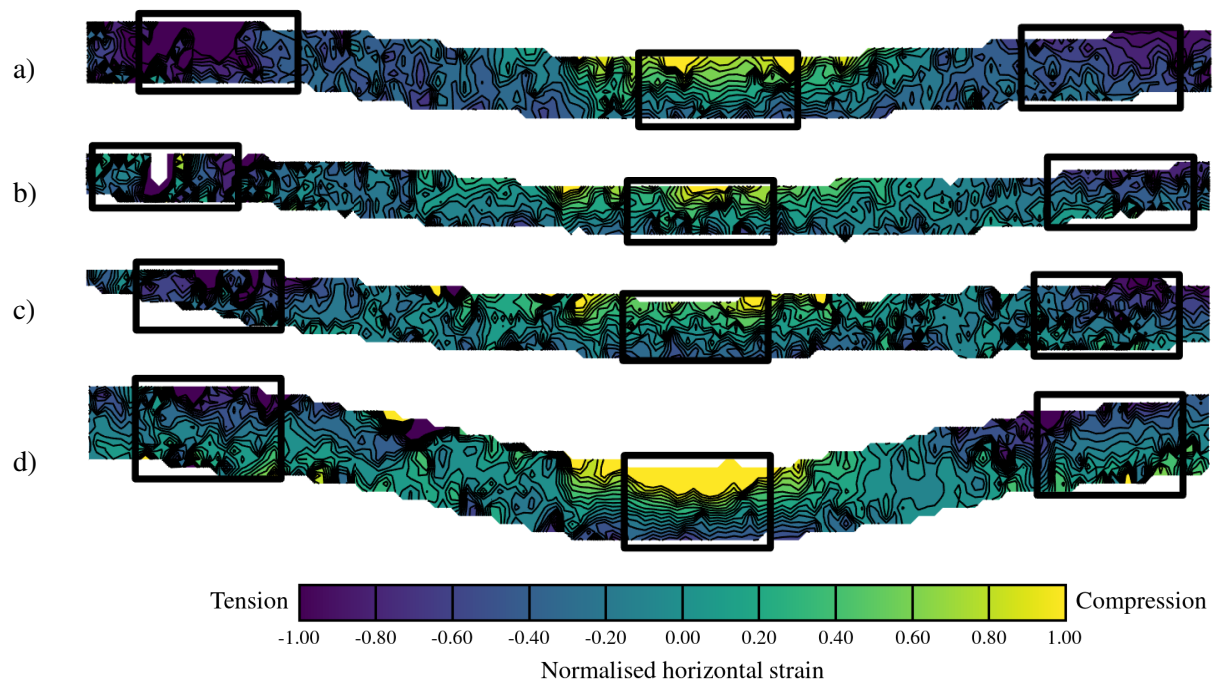

Figure 5.26: Normalised horizontal strain at Stage III (see Table 5.6) for: a) unreinforced, b) bottom-reinforced, c) top-reinforced, and d) double-reinforced liners.

the surface of the liner to its centre. The strain concentration for the bottom-reinforced liner extended from the liner surface to the base, while the strain concentrations of the top- and double-reinforced tests stopped at the level of the top geogrid.

The geogrid provided tensile resistance across the mouth of the cracks, reducing the stress and preventing it from opening up. Consequently, the strain concentrations stopped at the level of the top geogrid in the top- and double reinforced liners. In contrast, catastrophic crack growth occurred in the bottom-reinforced liner before the additional tensile resistance could be activated. Thus, in effect the liner behaved similar to an unreinforced liner. However, it was unexpected that strain concentration in the top reinforced liner was more severe than the unreinforced liner. This behaviour is most probably the result of imperfect sample preparation that created preferential paths for the macro-cracks. For central settlement greater than Stage III the strain concentrations and cracks at the right hand location of the top-reinforced liner were, as expected, less severe than the unreinforced liner.

There was an unexpected strain concentration at the base of the left hand section of the double-reinforced liner (Figure 5.27). However, when considering the right hand section (Figure E.3) this concentration is most probably an artefact of the DIC analysis (possibly a wild vector).

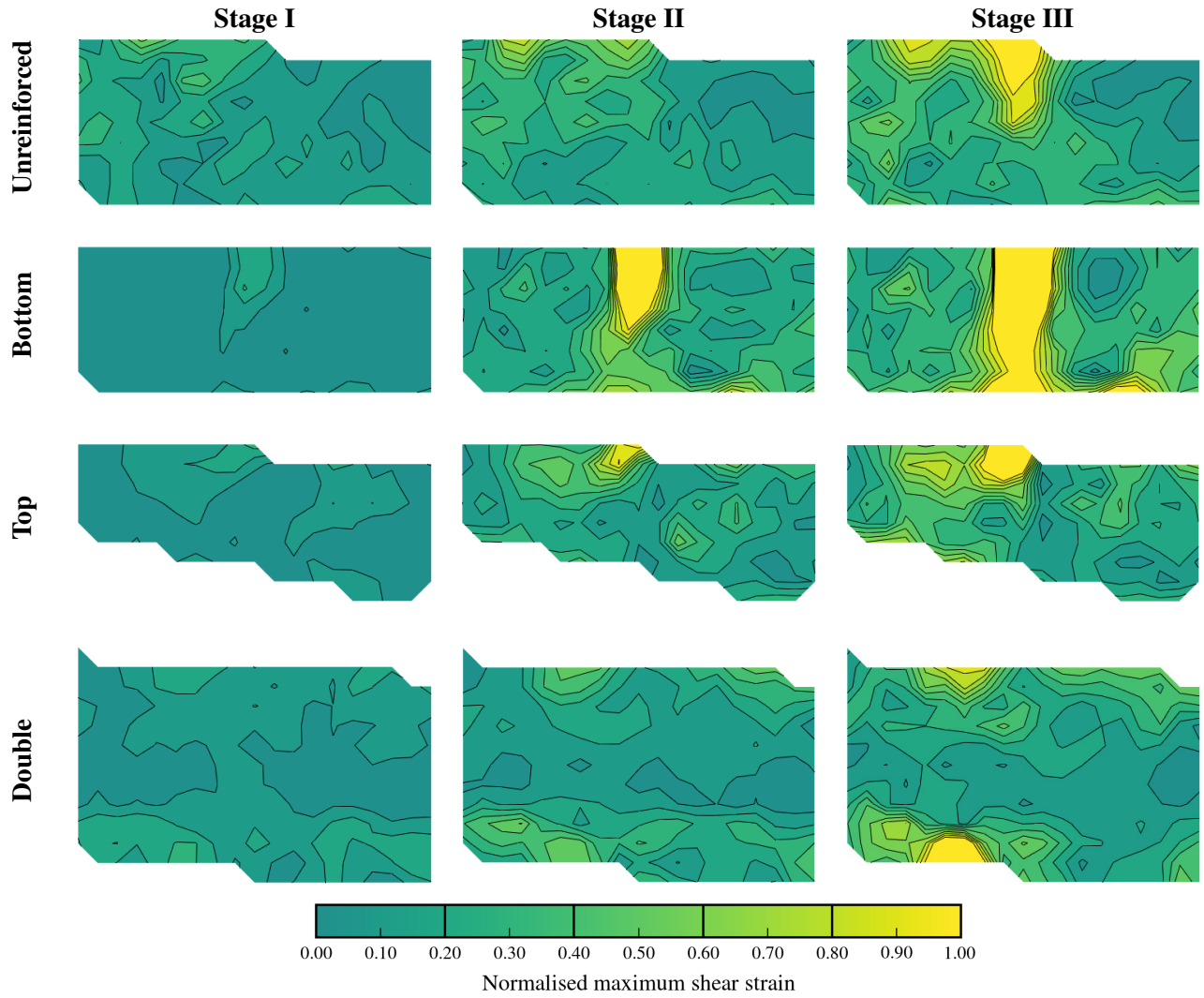

Figure 5.27: Comparison of normalised maximum shear strain at the location of the left hand crack (see Figure 5.26) for all the tests, at the three different stages.

Horizontal strain fields at the centre of the liners are shown in Figure 5.28. It appears that, for all the liners, a larger area at the centre of the liner was at, or above, the maximum compressive strain (1) rather than in tension (-1). The friction at the base of the liners, due to the sacrificial sand underneath, prevented the cracks from opening up and limited the tensile strain. Concurrently, the clay yielded in compression at the surface, resulting in large plastic strains. The nett effect was the imbalanced strain distribution observed in Figure 5.28.

In the case of the unreinforced liner, the friction due to the underlying sand was so significant that the centre of the liner failed in compression before it could crack. Slip planes are clearly visible in the laser scan of the centre shown in Figure 5.29. Thus, the underlying sacrificial sand layer had a

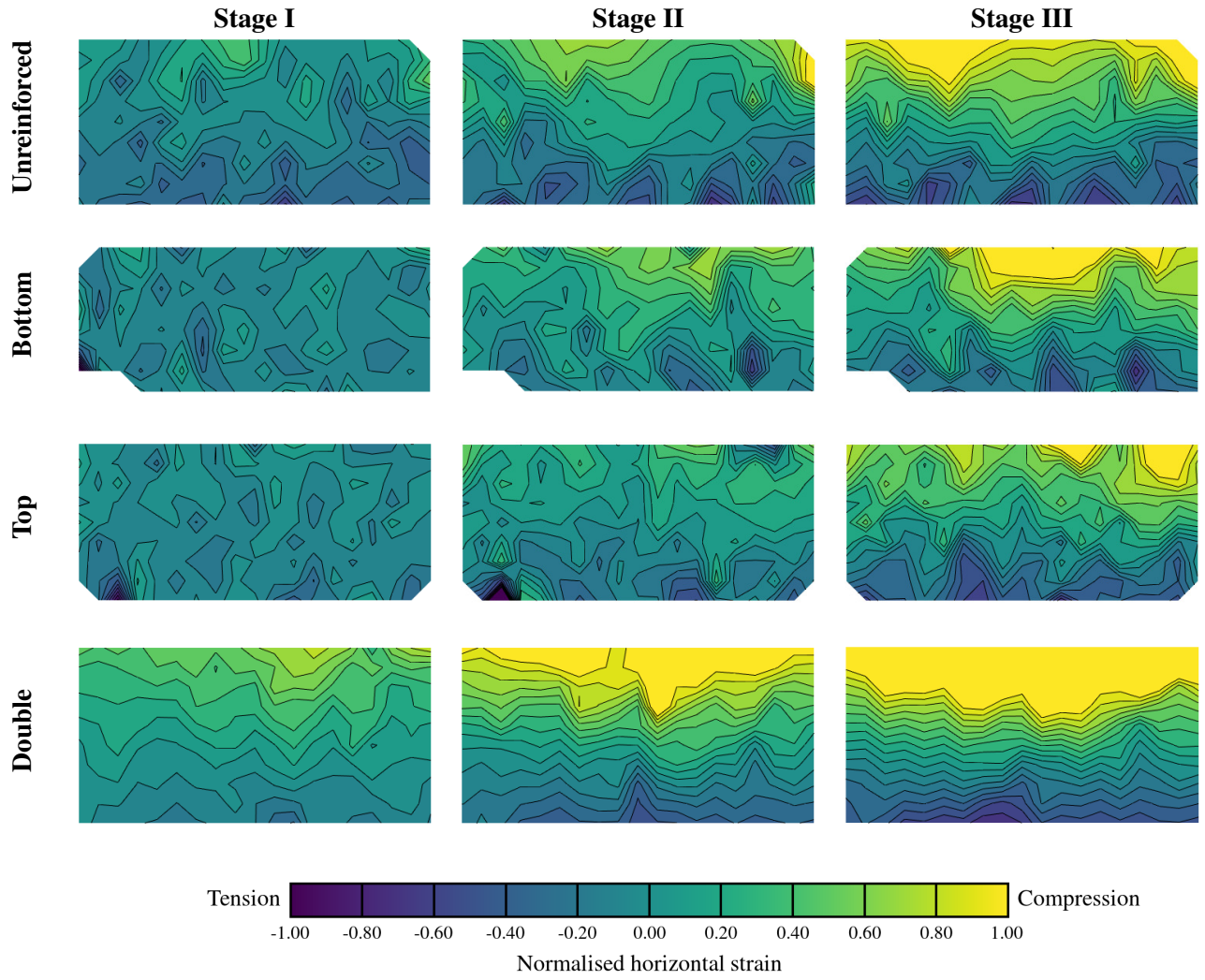

Figure 5.28: Comparison of normalised horizontal strain at the centre (see Figure 5.26) for all the tests, at the three different stages.

significant influence on the performance of the liners.

From Figure 5.28 it is clear that a significantly larger area at the centre of the double-reinforced liner is at a high compressive strain than for the other liners. A possible explanation is that at Stage III macro cracks still had not opened in the liner. Consequently, significant energy could have been present in the liner and that resulted in the high compressive strains.

To summarise: from the strain fields two observations could be made with regard to the behaviour of the liners: 1) the reinforcement position had a significant influence on the strain concentrations present in the liners and 2) the friction due to the sand below the liners had a significant influence on

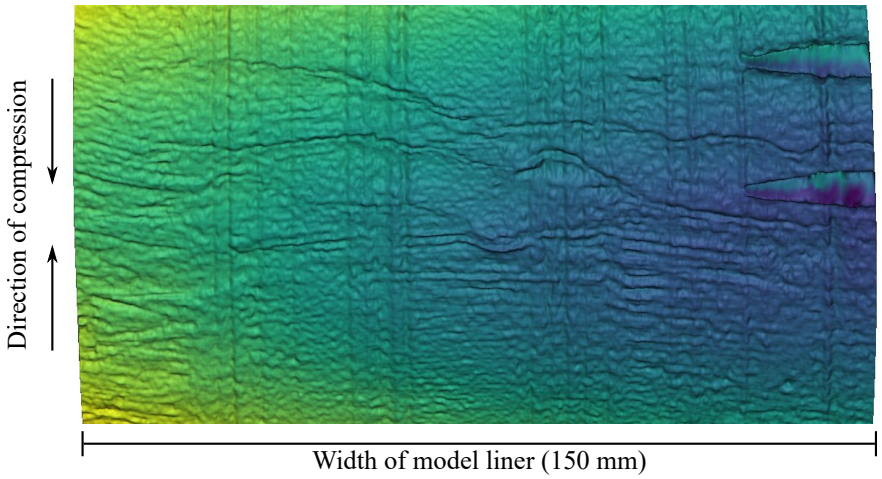

Figure 5.29: Compression failure at the centre of the second unreinforced liner.

the behaviour of the liners.

5.3.3.3 Strain distributions

Similar to the bending beam tests in Chapter 3, additional insight into the behaviour of the model liners under settlement could be gained from histograms of the strain fields. These histograms show the fraction of the liner at a given (normalised) strain. In Figure 5.30 the histograms for both shear and horizontal strain across the liners as a whole are shown. Histograms for the left and right sections of the liners showed similar behaviour to those for the beam as a whole and can be found in Appendix F. Histograms for the centre of the liners only (see Figure 5.26) are presented in Figure 5.31.

Consider the histograms of shear strain over the full liners in Figure 5.30a-c. During Stages I, II & III the shear strain distributions were similar for the unreinforced, top-reinforced and bottom-reinforced liners. However, the distribution for the double reinforced liner has a lower peak than the others, indicating that a greater portion of the liner is strained. Thus, the geogrid is effective in distributing the applied load across the all of the clay, i.e. there is full compatibility between the geogrid and the clay even after a significant void has formed. Better compatibility implies that no separation between the geogrid and clay has occurred. Furthermore, a uniform shear strain distribution implies less strain concentrations, i.e. cracking, in the clay. Thus, with better compatibility and less cracks the permeability of the double reinforced liner will be lower than the other liners for a significant void.

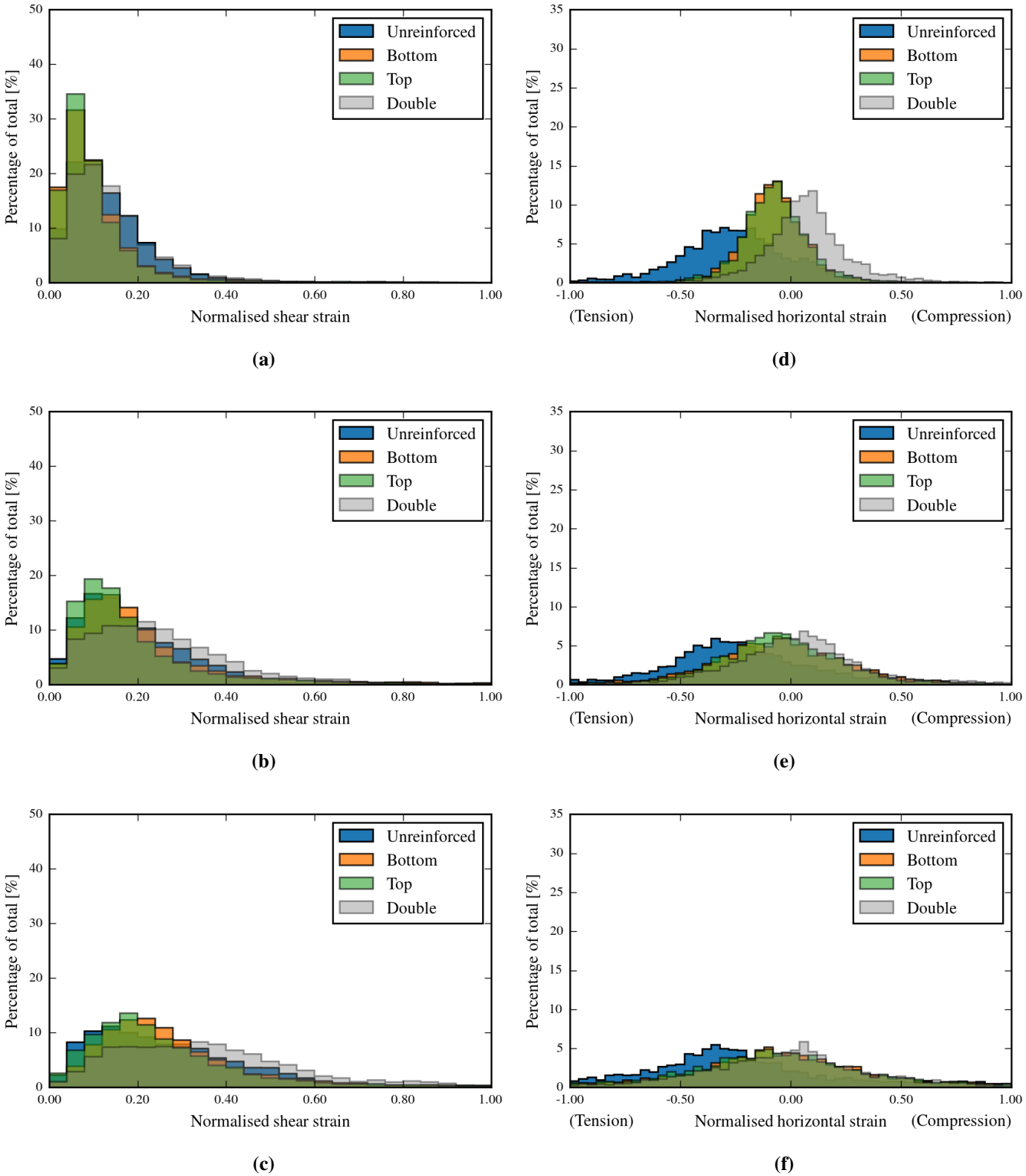

Figure 5.30: Histograms of the shear (a-c) and horizontal (d-e) strain distribution in the full liners. Stage I: a & d, Stage II: b & e and Stage III: c & f.

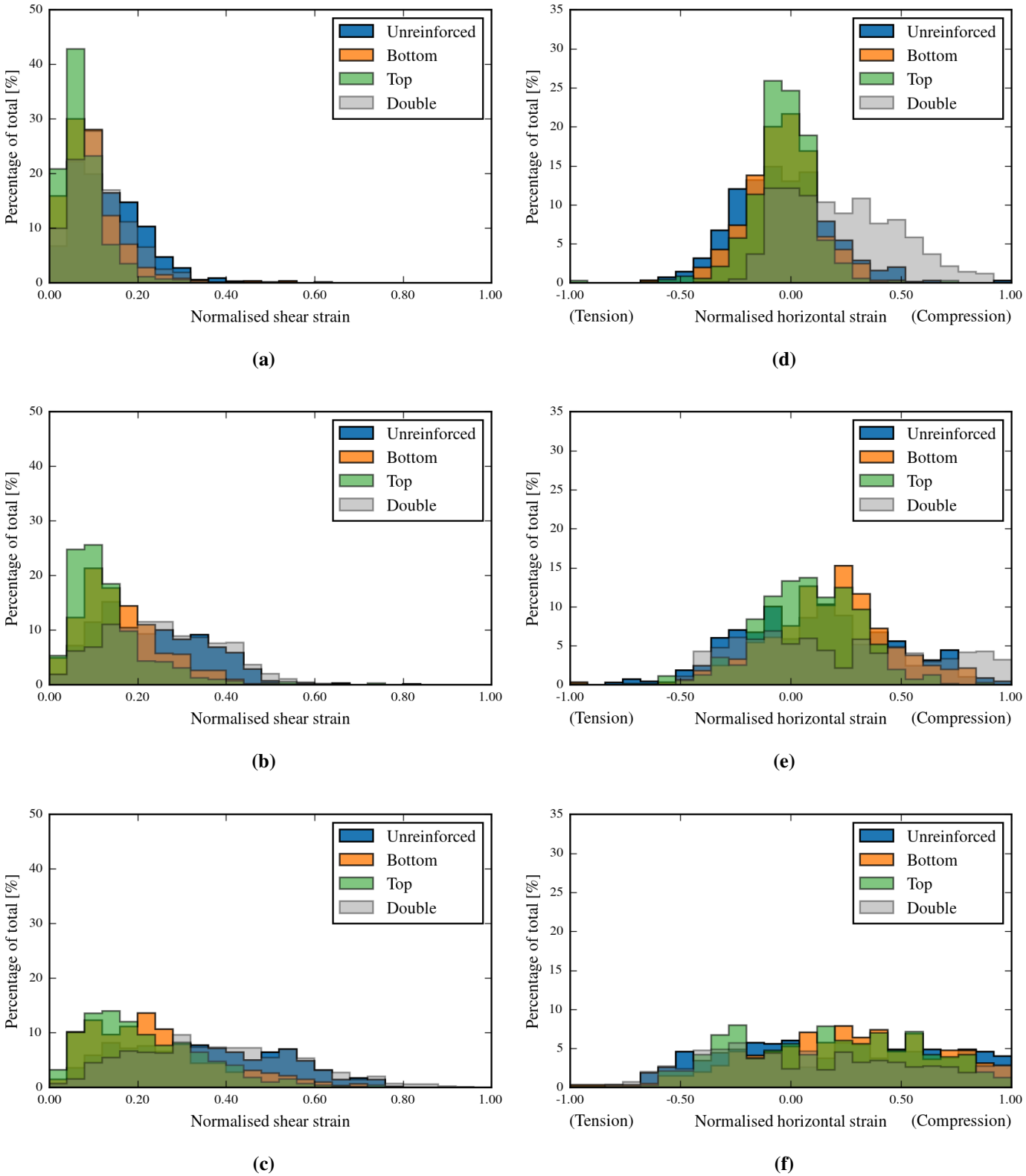

Figure 5.31: Histograms of the shear (a-c) and horizontal (d-e) strain distribution at the centre of the liners. Stage I: a & d, Stage II: b & e and Stage III: c & f.

In Figure 5.30d the horizontal strain distributions for the bottom- and top-reinforced liners are symmetric around zero at Stage I. The horizontal strain distributions for the unreinforced liner is centred below zero. This indicates that, as expected, significant tensile strains were present in the unreinforced liner as micro-cracks had already started to occur at Stage I (Table 5.6). Once micro-cracks were fully established in the bottom-reinforced liner at Stage II (Figure 5.30e) and in the top-reinforced liners at Stage III (Figure 5.30f), the centres of the distributions also shifted below zero. The distribution of the double-reinforced liner is centred around zero in Stages I, II & III, indicating that the tensile and shear stresses in the clay are in balance and that catastrophic crack growth has yet to occur.

The shear strain histograms for the centre of the liners (Figure 5.31) are similar to those for the full liners (Figure 5.30). However, the horizontal strain distributions are almost uniformly distributed from -1 to 1 during Stage III (Figure 5.31f). The distributions for the bottom- and top-reinforced tests do tend to compression while that of the double-reinforced test is slightly double peaked.

Should the horizontal strain in the clay liner change linearly with depth (thickness) and be constant along a length, the horizontal strain distribution will be uniform over that length (see Figure 2.10, p.19 for *depth* and *length*). In liners bending, the horizontal strain is constant at the centre only along a very narrow length. Consequently, the strain distribution tends towards normal for most of the histograms presented (Figures 3.29, 5.30d-f). However, at the centre of the model liners, the radius of curvature of the settlement trough is greater than at the centre of the bending beam tests. Consequently, the strain was constant over a much longer length. As more of the liner was deformed, this length over which the strain was uniform further increased. Thus, the horizontal strain distributions were uniform at Stage III (Figure 5.31f).

5.4 DISCUSSION

5.4.1 Effect of experimental design aspects on the outcome of the tests

Before the behaviour of a full-scale problem can be predicted from the centrifuge tests, the modelling decisions that might have influenced the results have to be considered. A number of questions might arise regarding the results presented in the preceding sections.

The first question that arises is why the bottom-reinforced liner performed as poorly as the unreinforced liner? A geogrid improves the clay liner by: 1) providing tensile resistance that inhibits crack growth and 2) increasing the stiffness of the system and thus reducing the settlement and curvature of the liner (that, in turn, reduces the strains).

In a bottom-reinforced liner the tensile resistance is irrelevant for a crack that originated at the surface of the liner. By the time the crack reached the level of the geogrid the integrity of the liner had already been compromised. Thus, the only way for the geogrid at the bottom quarter to improve the performance of the liner would be to increase the stiffness of the system. This increase in stiffness can only occur once the geogrid had strained sufficiently to become load bearing. For the centrifuge experiments conducted, the radius of curvature at the base of the settlement trough was relatively large. Consequently, by the time sufficient settlement had occurred for the geogrid to strain, the clay had already cracked at the hogging zones.

The second question refers to why the performance of the top-reinforced liner was relatively similar to that of the double-reinforced liner. The answer again lies in the two mechanisms of improvement provided by the geogrid: tensile resistance and stiffness. The clay liners rested on top of a sacrificial layer of sand. This sand provided frictional resistance across the base of the liner. Consequently, the opening up of macro-cracks were inhibited at the liner's base. In this regard the sand acted to some extent in the same manner as a geogrid placed at the base of the liner. It restrained movement and reduced the stress at the crack tips. Consequently, the top-reinforced liner performed similar to the double-reinforced liner. Only once significant central settlement had occurred did the double-reinforced liner begin to span the void (as did the bottom-reinforced liner). From this point onwards the behaviour of the double-reinforced liner was more favourable than that of the top-reinforced liner. This frictional effect by the underlying sand was also observed by Viswanadham & Jessberger (2005).

To summarise: two aspects of the experimental design had an influence on the liner behaviour observed, i.e. the shape of the imposed settlement trough (similar to the numerical results in Chapter 3), and the friction from the underlying sand.

5.4.2 Optimal reinforcement recommendations based on the centrifuge test results

From the preceding discussion it is clear that determining the optimal reinforcement position for the liners is not as simple as taking the results of the centrifuge modelling at face value. For a prototype problem similar to the centrifuge models, e.g. a capping layer, top reinforcement would be optimal. Under the conditions tested top-reinforced liners performed similar to double-reinforced liners, while bottom reinforcement was showed to be ineffective. The bottom reinforcing was ineffective due to the shape of the settlement trough (approximately a Gaussian curve, see Figure 4.7) that had a greater radius of curvature in tension than in compression. Consequently, the reinforcement at the top reduced the tensile strain at the crack tip, stemming crack propagation. Furthermore, some initial displacement was required before the geogrid strained sufficiently to become load bearing, increase the stiffness of the system and reduce the distortion. In contrast, the geogrids modelled in the numerical analyses (Chapter 4) were load bearing once settlement started and thus immediately reduced the distortion. Consequently, in the numerical analyses bottom reinforcement was shown to be optimal for a Gaussian shaped settlement trough. Thus, the difference in behaviour between the centrifuge tests and numerical analyses, when only a single geogrid is used for reinforcement, is due to the different mechanisms of geogrid reinforcement that was mobilised.

Should the problem vary from that modelled in the centrifuge analyses, the optimal reinforcement solution will likely change. The addition of sand as overburden could have improved the performance of the bottom-reinforced liner, perhaps suppressing crack growth until the geogrids had strained sufficiently to become load bearing. A change in the imposed settlement trough shape would have had a similar effect as observed in the numerical modelling (Section 4.5.2.3), i.e. double reinforcement would have been the only viable solution.

The following recommendations are presented:

1. If collapse is expected to occur deep below the base of the liner, e.g. where significant surface preparation took place before construction, little settlement will occur directly under the liner. The settlement trough will most probably be in the shape of a wide Gaussian curve. In this case, i.e. capping layers, top reinforcement of the liner would be optimal (as recommended by previous authors (Viswanadham, 1996; Rajesh & Viswanadham, 2009)).

2. If significant collapse is expected directly below the liner, and the ensuing sinkhole is expected to propagate through the liner and overlying waste, bottom-reinforced is recommended to prevent such propagation. It should be noted that, depending on the void size, even with the bottom reinforcement in place the liner will still crack through. The geogrid will simply support the overlying material and prevent it from collapsing into the cavity.
3. Should collapse be expected directly below the liner, and it is required that the integrity of the liner should remain intact, double reinforcement is recommended. That is, the geogrid reinforcement available should be split between the top and bottom quarters of the liner. Van Eekelen & Bezuijen (2014) showed that an embankment basal reinforced with two geogrids of stiffness M each, performed the same as an embankment basal reinforced with single geogrid of stiffness 2M. Accordingly, by splitting the geogrid reinforcement in two, the same load bearing capacity as for a single stiff geogrid will be retained. Furthermore, tensile resistance will be provided at all three regions where high tensile strain is expected, suppressing crack growth.

CHAPTER 6 CONCLUSIONS AND RECOMMENDATIONS

In the following sections conclusions made from the bending beam tests, numerical results and centrifuge tests are summarised. Furthermore, some recommendation for further work is also presented.

6.1 CONCLUSIONS FROM THE STUDY

The use of the piggyback landfilling technique has become a viable alternative to new landfills as the airspace available for landfills in South Africa decreases. However, in these piggyback landfills, settlement of the underlying waste could result in cracking of the clay liner of the new landfill. This cracking increases the permeability of the clay liner and thus compromises its ability to perform as an effective barrier. Geogrids have been used successfully in the clay liners to mitigate the effects of the waste settlement. However, limited research has been done on the optimal placement of these geogrids.

This study investigated the optimal placement of geogrid reinforcement in clay liners subject to differential settlement. Firstly, the fracture behaviour of unreinforced clay liners was investigated by means of four point bending tests on clay beams (Chapter 3). It was found that the load-displacement behaviour of the beams was linear until micro-cracks formed. Once the micro-cracks formed, the tensile strain at the base of the liner increased significantly and deviated from linear. When the micro-cracks were present, the behaviour became non-linear up to the peak load where macro-cracks opened.

After the behaviour of unreinforced clay beams was studied, finite element analyses were used to investigate the behaviour of reinforced liners subject to differential settlement (Chapter 4). The effects of liner thickness, overburden pressure, trough width, trough shape and imposed central settlement on

the optimal reinforcement strategy (ORS) were investigated. The ORS describes the optimal position for geogrid reinforcement in a liner, and the stiffness to be applied at that position, given a maximum reinforcement cost.

To determine the ORS the effect of numerous combinations of geogrid stiffnesses and reinforcement positions (designs) were analysed. Conducting a FE analysis for every possible design is impractical. Consequently, a RBF surrogate surface was used to interpolate the behaviour of the reinforced liners based on the results of a limited number of FE analyses. It was found that only trough width, trough shape and central settlement influenced the optimal reinforcement strategy. The results suggested reinforcement at the bottom quarter of the liner for a Gaussian shaped settlement trough. For a more general settlement trough the results suggested equal reinforcement of the liner at both the bottom and the top quarter depths .

Finally, centrifuge tests of reinforced model clay liners subject to differential settlement were conducted (Chapter 5). The position of geogrid reinforcement in the liners was varied between the tests. Two unreinforced liners, a bottom reinforced liner, a top reinforced liner and a double reinforced liner were modelled. For these centrifuge models with a wide settlement trough the bottom reinforced liner cracked from the top through to the bottom, similar to the unreinforced liner. However, the liner reinforced at the top was as effective as double reinforcement. For these two liners the cracks stopped at the depth of the top geogrid.

By considering the results of both the numerical analyses and centrifuge tests it can be concluded that the position of optimal reinforcement depends on the specific problem. Furthermore, the following conclusions can be made with regard to the optimal placement of geogrid reinforcement in clay liners subject to differential settlement: for liners where collapse is expected deep below the base of the liner (i.e. a capping liner), top reinforcement is effective. However, if the type of distortion that will be imposed on the liner is unknown, the optimal reinforcement strategy will be to divide the available reinforcement equally between the top quarter and bottom quarter depths of the liner[1]. The double reinforcement strategy is the most conservative and was also found optimal in the numerical results for a settlement trough in the shape of a generalised bell curve.

[1] Given that the available reinforcement positions are at the surface, top quarter, middle, bottom quarter and base of the liner.

6.2 RECOMMENDATIONS FOR FURTHER WORK

The following recommendations are presented for further numerical modelling of geogrid reinforced clay liners:

1. In a number of other soil reinforcement applications the optimal reinforcement position was found to be at third depths in the soil (Kuo & Hsu, 2003; Palmeira & Viana, 2003). Thus, it is recommended that these additional reinforcement positions should be investigated for clay liners.
2. The geogrid cost model used for the optimisation assumed a linear relationship between geogrid stiffness and cost. It is recommended that the effect of alternative cost models on the ORS be investigated.
3. The material models used in the numerical modelling of this study can be improved. A non-linear elastic model for the geogrid, and a fracture model for the clay liner are recommended.
4. To investigate the post-fracture behaviour of the reinforced liners, the modelling of the geogrid-clay interaction should be improved.
5. Finally, it is recommended that the waste body overlying the liner should be modelled explicitly, rather than assuming it to be equivalent to a uniform stress applied along the surface of the liner. Consequently, arching mechanisms in the waste that might influence the behaviour of the model liners will be considered.

For further physical modelling the following recommendations are made:

1. It has been show numerous times in the field of fracture mechanics that the size of a specimen influences its fracture behaviour. Consequently, it is recommended that for future flexural tests of clay beams, a number of different sample sizes should be tested. Furthermore, the effect of sample size on the fracture behaviour of centrifuge models should also be investigated.
2. Care should be taken when embedding reinforcement in the model clay liners. Even if the liner dries out only slightly, the undrained shear strength of the clay could change significantly.
3. During the centrifuge tests the matric suction in the model liners can be measured to monitor whether the behaviour remains undrained.
4. It will be beneficial to mitigate the effect of the friction provided by the underlying sand in the centrifuge tests. Sand overburden can be placed on top of the model liners to provide the same frictional reinforcement effect to the surface of the liners.

REFERENCES

Abu-Farsakh, M., Coronel, J. & Tao, M. 2007. Effect of Soil Moisture Content and Dry Density on Cohesive Soil-Geosynthetic Interactions Using Large Direct Shear Tests. *Journal of Materials in Civil Engineering* ,Vol. 19, No. 7, pp. 540–549.

Ajaz, A. & Parry, R. 1975. Stress-strain behaviour two compacted clays in tension and compression. *Géotechnique* ,Vol. 25, No. 3, pp. 495–512.

Alexview, D. 1997. Bridging a sink-hole by high-strength high-modulus geogrids. *Proceedings of Geosynthetics '97*. California.

Alfaro, M., Miura, N. & Bergado, D. 1995. Soil-Geogrid Reinforcement Interaction by Pullout and Direct Shear Tests. *Geotechnical Testing Journal* ,Vol. 18, No. 2, pp. 157–167.

Archer, A. 2014. *Using small-strain stiffness to predict the settlement of shallow foundations on sand*. MEng dissertation. University of Pretoria.

Arora, J. 2004. *Introduction to Optimum Design*. Academic Press, p. 672.

Badu-Tweneboah, K., Metha, H., Goldshmid, T. & Tyner, W. 2009. Design of a Geosynthetic Containment System for the Vertical Expansion of a Previously Closed, Unlined Solid Waste Landfill. *Proceedings of the GIGSA GeoAfrica 2009 Conference*, No. September, pp. 1–10.

Benson, C., Zhai, H. & Wang, X. 1994. Estimating hydraulic conductivity of compacted clay liners. *Journal of Geotechnical Engineering* ,Vol. 120, No. 2, pp. 366–387.

Benson, C., Daniel, D. & Boutwell, G. 1999. Field performance of compacted clay liners. *Journal of Geotechnical and Geoenvironmental Engineering* ,Vol. 125, No. 5, pp. 390–403.

Bergado, D., Chai, J., Abiera, H., Alfaro, M. & Balasubramaniam, A. 1993. Interaction between cohesive-frictional soil and various grid reinforcements. *Geotextiles and Geomembranes* ,Vol. 12, No. 4, pp. 327–349.

Brys, G., Hubert, M. & Struyf, A. 2004. A robust measure of skewness. *Journal of Computational and Graphical Statistics* ,Vol. 13, No. 4, pp. 996–1017.

BS5930:1999. 1999. *Code of practice for site investigations*. Tech. rep. British Standard Institution, London.

Burland, J. 1990. On the compressibility and shear strength of natural clays. *Géotechnique* ,Vol. 40, No. 3, pp. 329–378.

Carroll, R. & Chouery-Curtis, V. 1991. Geogrid reinforcement in landfill closures. *Geotextiles and Geomembranes* ,Vol. 10, No. 5-6, pp. 471–486.

Casagrande, A. 1932. Research on the Atterberg limits of soils. *Public Roads* ,Vol. 13, No. 8, pp. 121–136.

Case, J. & Chilver, A. 1971. *Strength of materials and structures*. 2nd Ed. Edward Arnold, p. 183.

Chang, J., Hannon, J. & Forsyth, R. 1977. Pull resistance and interaction of earthwork reinforcement and soil. *Transportation Research Record*, No. 640, pp. 1–7.

Charles, J. 1991. The causes, magnitude and control of ground movements in fills. *Proceedings of the 4th International Conference on Ground Movements and Structures, invited review paper, Cardiff, Pentech Press, London*, pp. 3–29.

Chen, Y., Gao, D. & Zhu, B. 2009. Controlling strain in geosynthetic liner systems used in vertically expanded landfills. *Joumal of Rock Mechanics and Geotechnical Engineering* ,Vol. 1, No. 1, pp. 48–55.

Clayton, C., Matthews, M. & Simons, N. 2016. *Site Investigation*. 2nd Ed. Pp. 6–3.

D653-14, A. 2014. *Standard Terminology Relating to Soil, Rock, and Contained Fluids*. Tech. rep. ASTM International.

D6637-11, A. 2011. *Standard Test Method for Determining Tensile Properties of Geogrids by the Single or Multi-Rib Tensile Method*. Tech. rep. ASTM International.

Deb, K., Agrawal, S., Pratap, A. & Meyarivan, T. 2000. A fast elitist non-dominated sorting genetic algorithm for multi-objective optimization: NSGA-II. *NSGA-II. In: Proceedings of sixth international conference on parallel problem solving from nature, 18-20 September, 2000*. Paris, France: Springer, 2000, pp. 849–858.

DeJong, J., Yafrate, N. & Degroot, D. 2011. Evaluation of Undrained Shear Strength Using Full-Flow Penetrometers. *Journal of Geotechnical and Geoenvironmental Engineering* ,Vol. 137, No. 1, pp. 14–26.

Department of Environmental Affairs (DEA). 2013. *National Environmental Management: Waste Act, 2008 (Act No 59 of 2008)*. Tech. rep. Government Gazette: No. 36784:R.636 23 Aug.

Department of Water Affairs and Forestry (DWAF). 1998. *Waste management series, second edition: Minimum Requirements for Waste Disposal by Landfill*. Tech. rep.

Dias, A. 2003. *Numerical Analyses of Soil-Geosynthetic Interaction in Pull-out Tests*. M.Sc. thesis. University of Brasilia, Brasilia, Brazil (in Portegeuse), p. 115.

Dupaix, R. & Boyce, M. 2005. Finite strain behavior of poly(ethylene terephthalate) (PET) and poly(ethylene terephthalate)-glycol (PETG). *Polymer* ,Vol. 46, No. 13, pp. 4827–4838.

Dyer, M. 1985. *Observation of the Stress Distribution in Crushed Glass with Applications to Soil Reinforcement*. PhD thesis. University of Oxford.

Edelmann, L., Katzenbach, R., Amann, P. & Weiss, J. 1996. Large-scale deformation tests on soil layers for landfills. *Proceedings of the 2nd International Congress on Environmental Geotechnics*. Osaka, Japan, pp. 205–209.

Edgers, L., Noble, J. & William, E. 1992. A biologic model for long term settlement in landfills. *Proceedings of the Mediterranean Conference on Environmental Geotechnology*. Ed. by M. Usmen & Y. Acar. Cesme, Turkey: Balkema, Rotterdam, pp. 177–184.

El-Fadel, M. & Khoury, R. 2000. Modeling settlement in MSW landfills: a critical review. *Critical Reviews in Environmental Science and Technology* ,Vol. 30, No. 3, pp. 327–361.

Fang, H.-Y. 1994. Cracking and fracture behaviour of soil. *Fracture mechanics applied to Geotechnical Engineering*. Ed. by L. Vallejo & R. Liang. Atlanta, Georgia, pp. 102–117.

Forrester, A. & Keane, A. 2009. Recent advances in surrogate-based optimization. *Progress in Aerospace Sciences* ,Vol. 45, No. 1, pp. 50–79.

Fortin, F.-A., De Rainville, F.-M., Gardner, M.-A., Parizeau, M. & Gagné, C. 2012. DEAP : Evolutionary Algorithms Made Easy. *Journal of Machine Learning Research* ,Vol. 13, pp. 2171–2175.

Fredlund, D., Houston, S., Nguyen, Q. & Fredlund, M. 2010. Moisture Movement Through Cracked Clay Soil Profiles. *Geotechnical and Geological Engineering* ,Vol. 28, No. 6, pp. 865–888.

Gabr, M. & Hunter, T. 1994. Stress-strain analysis of geogrid-supported liners over subsurface cavities. *Geotechnical and Geological Engineering* ,Vol. 12, pp. 65–86.

Garnier, J., Gaudin, C., Springman, S., Culligan, P., Goodings, D., König, D., Kutter, B., Phillips, R., Randolph, M. & Thorel, L. 2007. Catalogue of Scaling Laws and Similitude Questions in Geotechnical Centrifuge Modelling. *International Journal of Physical Modelling in Geotechnics* ,Vol. 7, No. 3, pp. 1–1–23–23.

Gere, J. & Timoshenka, S. 1991. *Mechanics of Materials*. 3rd Ed. Nelson Thornes, Cheltenham, UK.

Giroud, J.-P. 1981. Designing with geotextiles. *Matériaux et Constructions* ,Vol. 14, No. 82, pp. 257–272.

Giroud, J.-P., Bonaparte, R., Beech, J. & Gross, B. 1990. Design of soil layer-geosynthetic systems overlying voids. *Geotextiles and Geomembranes* ,Vol. 9, No. 1, pp. 11–50.

Gourc, J., Camp, S., Viswanadham, B. & Rajesh, S. 2010. Deformation behavior of clay cap barriers of hazardous waste containment systems : Full-scale and centrifuge tests. *Geotextiles and Geomembranes* ,Vol. 28, No. 3, pp. 281–291.

Griffith, A. A. 1920. The Phenomena of Rupture and Flow in Solids. *Philosophical Transactions of the Royal Society A: Mathematical, Physical and Engineering Sciences* ,Vol. 221, No. 582-593, pp. 163–198.

Hallett, P. D. & Newson, T. a. 2001. A simple fracture mechanics approach for assessing ductile crack growth in soil. *Soil Science Society of America Journal* ,Vol. 65, p. 1083.

Hastie, T., Tibshirani, R. & Friedman, J. 2001. *The elements of statistical learning*. New York: Springer.

Hibbeler, R. 2011. *Mechanics of materials*. 8th Ed. Prentice Hall, pp. 312–314.

Hoornweg, D. & Bhada-Tata, P. 2012. What a waste: A global review of solid waste management. *Urban development series knowledge papers* ,Vol. 15, pp. 1–98.

Huat, B., Toll, D. & Prasad, A. 2012. *Handbook of tropical residual soils engineering*. CRC Press/Balkema, pp. 129–131.

Hubert, M. & Vandervieren, E. 2008. An adjusted boxplot for skewed distributions. *Computational Statistics and Data Analysis* ,Vol. 52, No. 12, pp. 5186–5201.

Hussein, M. & Meguid, M. 2016. A three-dimensional finite element approach for modeling biaxial geogrid with application to geogrid-reinforced soils. *Geotextiles and Geomembranes* ,Vol. 44, No. 3, pp. 295–307.

IGS. 2009. *Recommended Descriptions of Geosynthetics Functions , Geosynthetics Terminology , Mathematical and Graphical Symbols*. Tech. rep. IGS Secretariat, pp. 1–31.

Jacobsz, S., Kearsley, E. & Kock, J. 2014. The geotechnical centrifuge facility at the University of Pretoria. *Proceedings of the 8th International Conference on Physical Modelling in Geotechnics 2014*. Perth, Australia: CRC Press.

Jessberger, H. & Klos, U. 1992. Geotechnical aspects of design and construction of waste containment facilities. *Proceedings of the Mediterranean Conference on Environmental Geotechnology1*. Ed. by M. Usmes & Y. Acar. Cesme, Turkey: Balkema, Rotterdam, pp. 125–136.

Jessberger, H. & Stone, K. 1991. Subsidence effects on clay barriers. *Géotechnique* ,Vol. 41, No. 2, pp. 185–194.

Jessberger, H., Giittler, U. & Stone, K. 1989. Centrifuge modelling of subsidence effects on clay barriers. *Proceedings of the 2nd International Landfill Symposium, Sardinia*.

Jewell, R., Milligan, G., Sarsby, R. & Dubois, D. 1984. Interaction between soil and geogrids. *Symposium on Polymer Grid Reinforcement in Civil Engi-neering*. ICE, London.

Jones, C. 1985. *Earth Reinforcement and Soil Structures*. Butterworth and Co. Ltd.

Jones, D. & Dixon, N. 2005. Landfill lining stability and integrity: The role of waste settlement. *Geotextiles and Geomembranes* ,Vol. 23, No. 1, pp. 27–53.

Karihaloo, B. 1995. *Fracture mechanics & structural concrete*. Longman Scientific & Technical.

Kavazanjian, E. 2001. Mechanical Properties of Municipal Solid Waste. *Proc. Sardinia - 8th International Waste Management and Landfill Symposium, Cagliari, Italy*. Ed. by T. Christensen, R. Cossu & R. Stegmann. Vol. 3, pp. 415–424.

Kavazanjian, E., Matasovic, N., Bonaparte, R. & Schmertmann, G. 1995. Evaluation of MSW properties for seismic analysis. *Proceedings of the Specialty Conference on Geotechnical Practice in Waste Disposal*, pp. 1126–1141.

Kim, T.-H. & Hwang, C. 2003. Modeling of tensile strength on moist granular earth material at low water content. *Engineering Geology* ,Vol. 69, No. 3-4, pp. 233–244.

Kim, T.-H. & Sture, S. 2008. Capillary-induced tensile strength in unsaturated sands. *Canadian Geotechnical Journal* ,Vol. 45, No. 5, pp. 726–737.

Knappett, J. & Craig, R. 2012. *Craig's Soil Mechanics*. 8th Ed. Spon Press, New York.

Konak, A., Coit, D. & Smith, A. 2006. Multi-objective optimization using genetic algorithms: A tutorial. *Reliability Engineering and System Safety* ,Vol. 91, No. 9, pp. 992–1007.

Kong, F. & Evans, R. 1987. *Reinforced and prestressed concrete*. 3rd Ed. Van Nostrand Reinhold (UK) Co. Ltd, pp. 200–201.

Koutsourais, M., Sprague, C. & Pucetas, R. 1991. Interfacial friction study of cap and liner components for landfill design. *Geotextiles and Geomembranes* ,Vol. 10, No. 5-6, pp. 531–548.

Kuo, C. & Hsu, T. 2003. Traffic induced reflective cracking on pavements with geogrid-reinforced asphalt concrete overlay. *Proceedings of the 82th Annual Meeting at the Transportation Research Board.*

LaGatta, M., Boardman, B., Cooley, B. & Daniel, D. 1997. Geosynthetic clay liners subjected to differential settlement. *Journal of Geotechnical and Geoenvironmental Engineering* ,Vol. 123, No. 5, pp. 402–410.

Lee, K., Cassidy, M. & Randolph, M. 2012. Use of epoxy in developing miniature ball penetrometers. *International Journal of Physical Modelling in Geotechnics* ,Vol. 12, No. 3, pp. 119–128.

Lehane, B., O'Loughlin, C., Gaudin, C. & Randolph, M. 2009. Rate effects on penetrometer resistance in kaolin. *Géotechnique* ,Vol. 59, No. 1, pp. 41–52.

Leonards, G. & Ramiah, B. 1959. *Time effects in the consolidation of clay*. Philadelphia: ASTM, pp. 116–130.

Leung, C. & Law, J. 1994. Piggy-back landfill expansions. *Solid Waste Association of North America (SWANA) Virginia Conference*.

Liang, R., Lommler, F., Lee, S. & Meyers, B. 1994. Case studies: Clay cover cracking analysis using FEM techniques. *Fracture mechanics applied to Geotechnical Engineering*. Ed. by L. Vallejo & R. Liang. Atlanta, Georgia, pp. 86–101.

Ling, H., Leshchinsky, D., Mohri, Y. & Kawabata, T. 1998. Estimation of Municipal Solid Waste Landfill Settlement. *Journal of the Geotechnical and Geoenvironmental Engineering* ,Vol. 124, No. 1, pp. 21–28.

Lu, N. & Likos, W. 2004. *Unsaturated soil mechanics*. John Wiley & Sons, p. 34.

Martos, F. 1958. Concerning an approximate equation of subsidence trough and its time factors. *International Strata Control Congress*. Leipzig, pp. 191–205.

Marx, D. & Jacobsz, S. 2016a. Geometric factors influencing the optimal position of geogrid reinforcement. *Proceedings of the 6th European Geosynthetics Congress*. Ljubljana, Slovenia, pp. 1455 –1466.

Marx, D. & Jacobsz, S. 2016b. Optimal geogrid reinforcement of clay liners. *Proceedings of the First Southern African Geotechnical Conference*. Ed. by S. Jacobsz. CRC Press.

McDougall, J. & Pyrah, I. 2001. Settlement in the landfilled waste: Extending the geotechnical approach. *Proceedings Sardinia 2001 - Eighth International Waste Management and Landfill Symposium*. Ed. by T. Christensen, R. Cossu & R. Stegmann. Vol. III. Cagliari, Sardinia, Italy, pp. 481–490.

Mesri, G. & Abel-Ghaffar, M. 1993. Cohesive Intercept in Effective Stress-Stability Analysis. *Journal of Geotechnical Engineering* ,Vol. 119, No. 8, pp. 1229–1249.

Mishra, D., Qian, Y., Kazmee, H. & Tutumluer, E. 2014. Investigation of Geogrid-Reinforced Railroad Ballast Behavior Using Large-Scale Triaxial Testing and Discrete Element Modeling. *Transportation Research Record: Journal of the Transportation Research Board*, No. 2462, pp 98–108.

Mitchell, J. & Soga, K. 2005. *Fundamentals of Soil Behavior*. 3rd Ed. John Wiley & Sons, pp. 176–177.

New, B. & O'Reilly, M. 1991. Tunnelling induced ground movements; predicting their magnitude and effects. *Proceedings of the 4th International Conference on Ground Movements and Structures, invited review paper, Cardiff, Pentech Press, London*, pp. 671–697.

Nishimura, T. & Fredlund, D. 2000. Unconfined Compressive Strength of a Silty Soil and Kaolin below the Residual State. *GeoDenver Conference*. Denver, Colorado.

Oda, M. & Kazama, H. 1998. Microstructure of shear bands and its relation to the mechanisms of dilatancy and failure of dense granular soils. *Géotechnique* ,Vol. 48, No. 4, pp. 465–481.

Palmeira, E. 2009. Soil-geosynthetic interaction: Modelling and analysis. *Geotextiles and Geomembranes* ,Vol. 27, No. 5, pp. 368–390.

Palmeira, E. & Milligan, G. 1989. Scale and other factors affecting the results of pull-out tests of grids buried in sand. *Geotechnique* ,Vol. 39, No. 3, pp. 511–524.

Palmeira, E. & Viana, H. 2003. Effectiveness of geogrids as inclusions in cover soils of slopes of waste disposal areas. *Geotextiles and Geomembranes* ,Vol. 21, No. 5, pp. 317–337.

Plaxis. 2002. *User's Manual*.

Plé, O., Manicacci, A., Gourc, J. & Camp, S. 2012. Flexural behaviour of a clay layer: experimental and numerical study. *Canadian Geotechnical Journal* ,Vol. 49, No. 4, pp. 485–493.

Rajesh, S. & Viswanadham, B. 2009. Evaluation of geogrid as a reinforcement layer in clay based engineered barriers. *Applied Clay Science* ,Vol. 46, No. 2, pp. 153–165.

Rajesh, S. & Viswanadham, B. 2011. Hydro-mechanical behavior of geogrid reinforced soil barriers of landfill cover systems. *Geotextiles and Geomembranes* ,Vol. 29, No. 1, pp. 51–64.

Rajesh, S. & Viswanadham, B. 2012a. Centrifuge and numerical study on the behavior of clay-based landfill covers subjected to differential settlements. *Journal of Hazardous, Toxic and Radioactive Waste* ,Vol. 16, No. 4, pp. 284–297.

Rajesh, S. & Viswanadham, B. 2012b. Centrifuge Modeling and Instrumentation of Geogrid-Reinforced Soil Barriers of Landfill Covers. *Journal of Geotechnical and Geoenvironmental Engineering* ,Vol. 138, No. 1, pp. 26–37.

Rajesh, S. & Viswanadham, B. 2015. Numerical Simulation of Geogrid-Reinforced Soil Barriers Subjected to Differential Settlements. *International Journal of Geomechanics* ,Vol. 15, No. 4, pp. 1–15.

Randolph, M. 2004. Characterisation of soft sediments for offshore applications. *2nd International Conference on Geotechnical and Geophysical Site Characterisation*. Vol. 1. Porto, pp. 209–232.

Randolph, M. 2016. Personal communication.

Randolph, M., Hu, Y. & Martin, C. 2000. Limiting resistance of a spherical penetrometer in cohesive material. *Géotechnique* ,Vol. 50, No. 5, pp. 573–582.

Richards, D. & Powrie, W. 2011. Physical modelling of in-ground waste repository capping systems. *Waste and Resource Management* ,Vol. 164, No. WR1, pp. 53–65.

Richardson, G. & Allen Marr, W. 1996. *Geotechnical considerations for the design of piggy backed lined landfills*. San Diego.

Robinson, R. & Allam, M. 1998. Effect of clay mineralogy on coefficient of consolidation. *Clays and Clay Minerals* ,Vol. 46, No. 5, pp. 596–600.

Rogowski, A. 1964. *Strength of soil aggregates*. PhD thesis, pp. 203–211.

Ross, S. 2013. *Simulation*. 5th Ed. Elsevier Ltd, pp. 244–245.

Rousseeuw, P. & Hubert, M. 2011. Robust statistics for outlier detection. *Wiley Interdisciplinary Reviews: Data Mining and Knowledge Discovery* ,Vol. 1, No. 1, pp. 73–79.

Roylance, D. 2001. *Introduction to Fracture Mechanics*. Tech. rep. Cambridge, MA 02139: Massachusetts Institute of Technology.

Rust, M. 2003. *The mechanics of continuous flight augers in clay*. PhD thesis. University of Southampton, pp. 69,93.

Saada, A., Liang, L. & Bianchini, G. 1994. Fracture mechanics and plasticity in saturated clay. *Fracture mechanics applied to Geotechnical Engineering*. Ed. by L. Vallejo & R. Liang. Atlanta, Georgia.

Scarpelli, G. & Wood, D. 1982. Experimental observations of shear patterns in direct shear tests. *Deformation and Failure of Granular Materials: International Union of Theoretical and Applied Mechanics symposium on deformation and failure of granular materials*. Ed. by P. Vermeer & H. Luger. January 1982. Balkema, Rotterdam, pp. 473–484.

Schofield, A. & Wroth, P. 1968. *Critical State Soil Mechanics*. McGraw-Hill, London.

Shinoda, M. & Bathurst, R. 2004. Lateral and axial deformation of PP, HDPE and PET geogrids under tensile load. *Geotextiles and Geomembranes* ,Vol. 22, No. 4, pp. 205–222.

Stanier, S., Blaber, J, Take, W. A. & White, D. 2015. Improved image-based deformation measurement for geotechnical applications. *Canadian Geotechnical Journal* ,Vol. 13, No. October 2015, pp. 1–35.

Stuart, J. 1962. Interference between foundations, with special reference to surface footings in sand. *Geotechnique* ,Vol. 12, No. 1, pp. 15–22.

Stulgis, R., Soydemir, C., Telgener, R. & Hewitt, R. 1996. Use of geosynthetics in 'piggyback landfills': a case study. *Geotextiles and Geomembranes* ,Vol. 14, No. 7-8, pp. 341–364.

Surarak, C., Likitlersuang, S., Wanatowski, D., Balasubramaniam, A., Oh, E. & Guan, H. 2012. Stiffness and strength parameters for hardening soil model of soft and stiff Bangkok clays. *Soils and Foundations* ,Vol. 52, No. 4, pp. 682–697.

Tang, C.-S, Pei, X.-J, Wang, D.-Y, Shi, B. & Li, J. 2014. Tensile Strength of Compacted Clayey Soil. *Journal of Geotechnical and Geoenvironmental Engineering* ,Vol. 141, No. 4.

Taylor, R., ed. 1995. *Geotechnical centrifuge technology*. Blackie Academic & Professional.

Teixeira, S. 2003. A Study on Soil-Geogrid Interaction in Pull-out Tests and Its Application to the Analysis and Design of Reinforced Structures, p. 214.

Thusyanthan, N. 2005. *Behaviour of landfill systems under monotonic and earthquake loading*. PhD. University of Cambridge.

Thusyanthan, N., Madabhushi, S. & Singh, S. 2007. Tension in geomembranes on landfill slopes under static and earthquake loading-Centrifuge study. *Geotextiles and Geomembranes* ,Vol. 25, No. 2, pp. 78–95.

Tran, V., Meguid, M. & Chouinard, L. 2013. A finite-discrete element framework for the 3D modeling of geogrid-soil interaction under pullout loading conditions. *Geotextiles and Geomembranes* ,Vol. 37, pp. 1–9.

Turner, C. & Kolednie, O. 1994. A micro and macro approach to the energy dissipation rate model of stable ductile crack growth. *Fatigue & Fracture of Engineering Materials & Structures* ,Vol. 17, No. 9, pp. 1089–1107.

Turner, C. & Kolednik, O. 1994. Application of energy dissapation arguments to stable crack growth. *Fatigue & Fracture of Engineering Materials & Structures* ,Vol. 17, No. 10, pp. 1109–1127.

Vallejo, L. 1994. Application of Fracture Mechanics to Soils: An Overview. *Fracture mechanics applied to Geotechnical Engineering*. Ed. by L. Vallejo & R. Liang. Atlanta, Georgia, pp. 1–21.

Van Genuchten, M. 1980. A Closed-form Equation for Predicting the Hydraulic Conductivity of Unsaturated Soils. *Soil Science Society of America Journal* ,Vol. 44, No. 5, p. 892.

Van Eekelen, S. & Bezuijen, A. 2014. Is 1+1=2? Results of 3D model experiments on piled embankments. *10th International Conference on Geosynthetics*. Berlin.

Vanapalli, S., Fredlund, D., Pufahl, D. & Clifton, A. 1996. Model for the prediction of shear strength with respect to soil suction. *Canadian Geotechnical Journal* ,Vol. 33, No. 3, p. 2.

Verboven, S. & Hubert, M. 2010. MATLAB library LIBRA. *Wiley Interdisciplinary Reviews: Computational Statistics* ,Vol. 2, No. 4, pp. 509–515.

Viswanadham, B. 1996. *Geosynthetic reinforced mineral sealing layers of landfills*. Phd. Bochum, Germany: Ruhr University.

Viswanadham, B. & Jessberger, H. 2005. Centrifuge Modeling of Geosynthetic Reinforced Clay Liners of Landfills. *Journal of Geotechnical and Geoenvironmental Engineering* ,Vol. 131, No. 5, pp. 564–574.

Viswanadham, B. & König, D. 2004. Studies on scaling and instrumentation of a geogrid. *Geotextiles and Geomembranes* ,Vol. 22, No. 5, pp. 307–328.

Viswanadham, B. & Mahesh, K. 2002. Modeling deformation behaviour of clay liners in a small centrifuge. *Canadian Geotechnical Journal* ,Vol. 39, No. 6, pp. 1406–1418.

Viswanadham, B. & Muthukumaran, A. 2007. Influence of geogrid layer on the integrity of compacted clay liners of landfills. *Soils and Foundations* ,Vol. 47, No. 3, pp. 517–532.

Viswanadham, B. & Rajesh, S. 2009. Centrifuge model tests on clay based engineered barriers subjected to differential settlements. *Applied Clay Science* ,Vol. 42, No. 3-4, pp. 460–472.

White, D., Take, W. & Bolton, M. 2003. Soil deformation measurement using particle image velocimetry (PIV) and photogrammetry. *Geothechnique* ,Vol. 53, No. 7, pp. 619–631.

APPENDIX A CONSTRUCTS USED TO CALCULATE THE C_V VALUES FROM THE OEDOMETER RESULTS

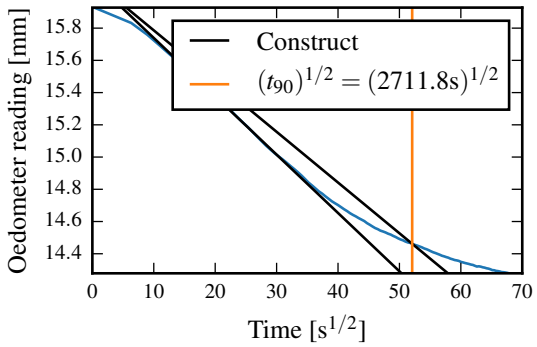

(a) σ = 103.5 kPa

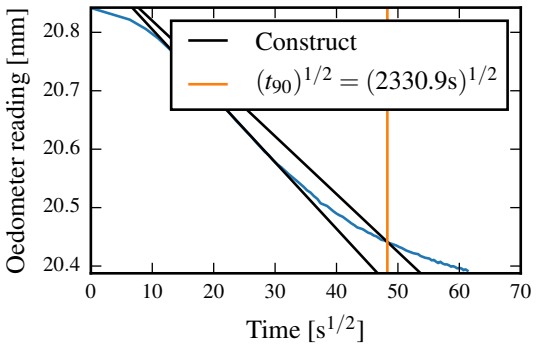

(b) σ = 208.0 kPa

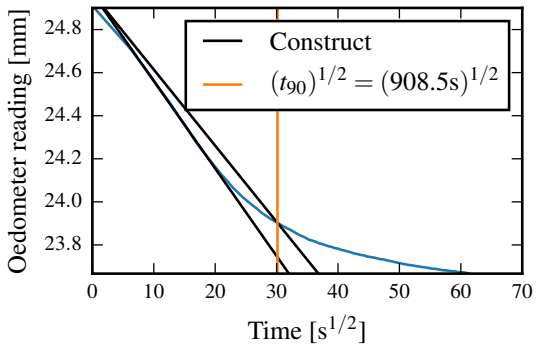

(c) σ = 416.8 kPa

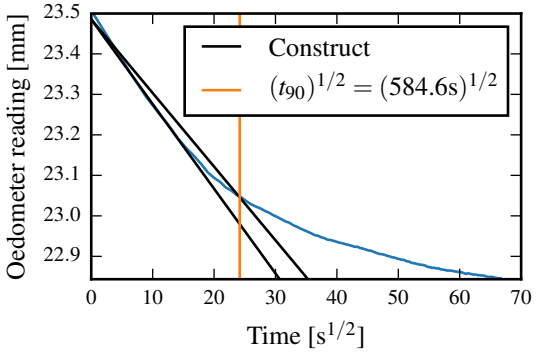

(d) σ = 625.9 kPa

Figure A.1: Constructs used to calculate t_{90} using Taylor's method for Oedometer 2.

Table A.1: Values used to calculate the coefficients of consolidation for oedometer test 2.

Stress [kPa]	t_{90} [s]	d [mm]	c_v [m^2/y]
103.5	2711.8	16.35	2.64
208.1	2330.9	15.41	2.73
416.8	908.5	14.55	6.24
625.9	584.6	13.85	8.78

APPENDIX B DETAILS OF THE PENETROMETER TESTING

During the centrifuge tests the model liners deform undrained. By pushing a penetrometer into the clay the undrained shear strength with depth can be calculated. The force required to push the penetrometer can be converted to undrained shear strength from known plasticity solutions for the flow of the clay around the penetrometer. One commonly known penetrometer is the cone penetrometer test (CPT).

A newer type of penetrometer that was developed is the family of full flow penetrometers (ball and T-bar penetrometers). These penetrometers has a number of advantages over the CPT (DeJong et al., 2011). Probably the most significant of these advantages is that the soil flows around the ball (or t-bar), rather than being displaced (as in the case of a CPT). This allows for the derivation of upper and lower bound plasticity solutions of the problem closer to the true solution. These plasticity solutions are used to convert the penetration force to undrained shear strength of the clay.

A miniature ball penetrometer has been successfully used by Lee et al. (2012) in a centrifuge, in flight. The penetrometer was made of epoxy resin with a strain gauge embedded inside the rod. For the current research either in-flight penetrometer testing or in-flight laser scanning of the surface could be conducted. In-flight laser scanning was judged to be more beneficial and more practical with the equipment available. Consequently, the penetrometers tests were done on clay cut from the sides of the model liner during preparation (Section 5.2.3).

For this study a miniature ball penetrometer was used to measure the undrained shear strength of the model clay liners. A ball penetrometer, rather than a T-bar, was used as it has a slightly smaller footprint and thus disturbed less of the sample. To construct the penetrometer, a 5 mm ball bearing was

soldered onto a 1.58 mm hypodermic needle (see Figure 5.14). The ratio of the projected area of the ball to that of the rod is 10.0 : 1. This is greater than the minimum of 5 : 1 required for a variability of less than 10% in the results measured (DeJong et al., 2011). The free end of the needle was clamped to a Lloyds LC 50 N (014090) load cell on the Lloyds 5 kN press used for the testing of the HaTe® mesh. This load cell had a resolution of 0.0025 N and and measured within ±5% of the actual result.

There are a number of problems associated with measuring the applied load at the end of the hypodermic needle and not at the ball itself. Firstly, bending of the shaft might skew the load measurements. However, the short stainless steel needle is quite stiff and the effect of bending was ignored. Secondly, should shaft friction have occurred on the needle it would have been recorded by the load cell together with the penetration resistance . The model liner is, however, only 6 ball diameters thick. Furthermore, no clay was observed on the shaft of the penetrometer. Thus, the clay did not swell back and envelop the penetrometer for this thin layer. Consequently, the probability that shaft friction was measured by the load cell was deemed negligible.

The theoretical relationship between the undrained shear strength of the clay and the load measured is:

$$c_u = \frac{q}{N_b} = \frac{P_{ult}}{\pi r^2 N_b} \tag{B.1}$$

where c_u is the undrained shear strength, q the bearing resistance, P_{ult} the resisting force, r the radius of the penetrometer and N_b the bearing resistance factor.

Randolph et al. (2000) developed theoretical upper and lower bounds for N_b based on plasticity solutions of the penetrometer in clay. These solutions were developed for both the Tresca and the Von Mises yield criteria for a perfectly smooth and a fully rough ball. DeJong et al. (2011) developed a relationship between the sensitivity (S_t) of the clay and N_b:

$$N_b = 13.2 - \frac{7.5}{1 + \left(\frac{S_t}{10}\right)^{-3}} \tag{B.2}$$

where S_t is the sensitivity of the soil, defined as c_u/c_{ur}, c_u is the undrained shear strength and c_{ur} the remoulded undrained shear strength. Finally Lee et al. (2012) back calculated a N_b of 13.5 for their miniature epoxy ball penetrometer from T-bar penetrometer results. The bounds for N_b, the value calculated by Lee et al. (2012), as well as the N_b calculated from Equation B.2 is shown in Figure 5.15. Consequently, a N_b factor of 13.5 was used for the current study.

The presence of the needle (rod) results in a smaller area above the ball in contact with the clay than below. Consequently, a correction factor for overburden pressure (σ_{v0}) can be applied to the penetration resistance. However, the difference in area is small enough to ignore this correction factor (Randolph, 2004). Furthermore, for these model liners $q \approx 472.5$ kPa and $\sigma_{v0} \approx 0.6$ kPa at the bottom of the liner (assuming $w = 31\% \Rightarrow \gamma_b = 18.75$ kN/m^3, see Section 3.3.1.1). Thus, the effect of overburden stress is negligible.

The penetration resistance measured is influenced by the rate at which the test is conducted. Lehane et al. (2009) studied this rate effect for both a T-bar and a ball penetrometer for a range of penetration velocities (0.003 mm/s to 100 mm/s). The typical shape of the relationship between penetration resistance normalised by overburden pressure (q/σ'_v), and normalised penetration velocity (V) is illustrated in Figure B.1.

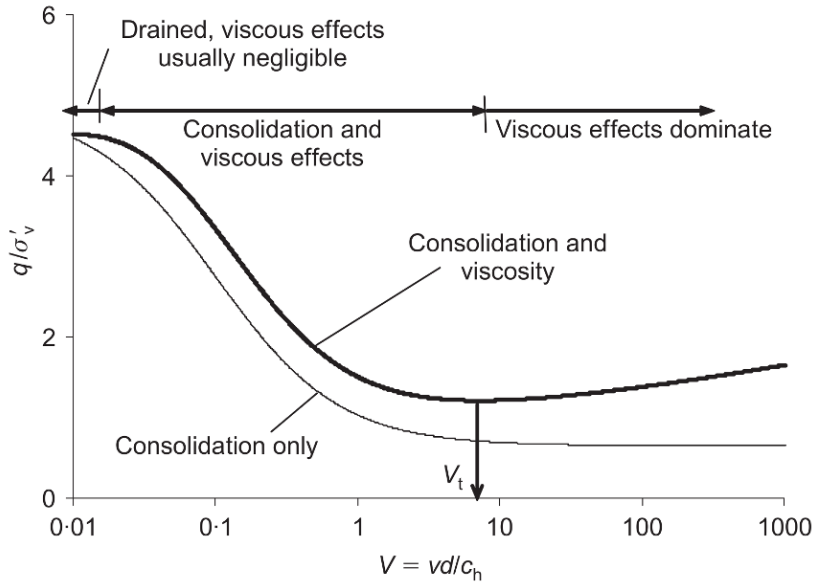

Figure B.1: The influence of penetration velocity (V) on penetration resistance (q) (Lehane et al., 2009).

At low penetration velocities the pore pressure generated can dissipate (consolidation occurs) and thus the clay behaves drained. Consequently, a resistance higher than the undrained shear strength is measured. As the penetration velocity decreases, the dissipation rate and thus the penetration resistance follow suit and the behaviour approaches undrained. However, when the penetration rate increases too much, the viscosity of the soil starts to noticeably resist the movement of the ball. In between these extremes lies an optimum where the measured resistance is a minimum. This minimum is assumed to represent the undrained shear strength of the clay. The influence of viscosity on penetration resistance

is significantly less than that of consolidation. Furthermore, it appears that the minimum velocity only has to be accurate within an order of magnitude.

The standard field testing velocity of a ball penetrometer with diameter d is $v/d = 0.175$ m^2/s (Lehane et al., 2009). Thus, for a 5 mm ball penetrometer $v = 0.88$ m/s. For the tests conducted by Lee et al. (2012) with a miniature ball penetrometer a penetration velocity of 1.53 m/s was used. Randolph (2016) suggested a normalised velocity (V) of 30 or greater. Thus, for the kaolin used in the present study:

$$V = \frac{vd}{c_v} \geq 30, \qquad (d = 5 \text{ mm}, c_v = 8.77 \text{ m}^2\text{/y (see Section 3.1.2)})$$

$$\Rightarrow v \geq 1.669 \text{ mm/s}$$

Consequently, to test at a conservative velocity at which no undrained effects will occur, a testing velocity of 2 mm/s was adopted.

APPENDIX C ADDITIONAL CALCULATIONS TO INTERPRET THE RESULTS OF THE DOUBLE REINFORCED LINER

C.1 RELATIONSHIP BETWEEN THE MOMENT IN THE LINERS AND CENTRAL SETTLEMENT.

The bending moment in a beam can be related to its deflection with the Bernoulli-Euler equation:

$$M(x,y) = \frac{d^2y}{dx^2}EI$$

If a clay liner spans a void of width l, the deflected shape can be approximated by a beam of length l, fixed at both ends, subject to a distributed load W equal to the self-weight of the beam:

$$y(x,l) = \frac{Wl}{24EI}(\delta^2 - 2\delta^3 + \delta^4), \qquad \delta = x/l$$

Consequently:

$$M(x,l) = \frac{W}{12}\cdot\left(l + 6x^2\cdot\frac{1}{l} - 6x\right)$$

If a Gaussian shaped settlement trough is induced, similar to the surface depression caused by a tunnel (New & O'Reilly, 1991), then the width of the void below the liner (l) is:

$$l \approx 5i, \text{ and } k^*\cdot z$$

Where k^* is an empirical factor related to the soil type and z can be thought to be equivalent to the depth of the settlement trough, Δ. Thus:

$$l = 5k^*\cdot\Delta$$

And:

$$M(x,l) = \frac{W}{12} \cdot \left(5k^* \cdot \Delta + 6x^2 \cdot \frac{1}{5k^* \cdot \Delta} - 6x \right)$$

Consequently, at the centre of the liner $(x = 0)$:

$$M \approx k \cdot \Delta$$

C.2 CALCULATION OF THE RATIO IN MOMENT OF INERTIA OF TWO REINFORCED LINERS

In Equation 5.4 it was shown that for $\sigma_A = \sigma_B$ the following ratio should hold:

$$\frac{\Delta_A}{\Delta_B} = \frac{I_A}{I_B}$$

where σ_A is the stress in a reinforced liner system, σ_B the stress in another reinforced liner system of double the stiffness of the first, I_A the moment of inertia of the first liner system, and I_B the moment of inertia of the second liner system.

To calculate the moment of inertia of a geogrid reinforced liner the *transformed section method* can be used (Hibbeler, 2011). In this method the ratio of the geogrid stiffness to clay stiffness ($n = E_G/E_C$) is used to transform the width of the geogrid to an equivalent clay width ($b_t = b \cdot n$). This new section is used to calculate the moment of inertia. In Figure C.1 a reinforced liner as well as two transformed sections is shown. The first transformed section (Liner A) is for a geogrid reinforcement of stiffness E_G and the second (Liner B) for a geogrid reinforcement of stiffness $2E_G$.

If $I_{C_{xx}}$ is the moment of inertia of the clay around the neutral axis of the beam, and $I_{GA_{xx}}$ the moment of inertia of one of the geogrids in Liner A around the neutral axis of Liner A, then the moment of inertia of Liner A around the neutral axis is $I_{A_{xx}} = I_{C_{xx}} + 2I_{GA_{xx}}$.

Furthermore, since $n_B = 2n_A$ it implies that $b_B = 2b_A$, thus $I_{GB_{xx}} = 2I_{GA_{xx}}$. Consequently, the moment of inertia of Liner B is $I_{B_{xx}} = I_{C_{xx}} + 2I_{GB_{xx}} = I_{C_{xx}} + 4I_{GA_{xx}}$.

Accordingly, the ratio of moment of inertias can be calculated as:

$$\frac{I_A}{I_B} = \frac{I_{C_{xx}} + 2I_{GA_{xx}}}{I_{C_{xx}} + 4I_{GA_{xx}}}$$

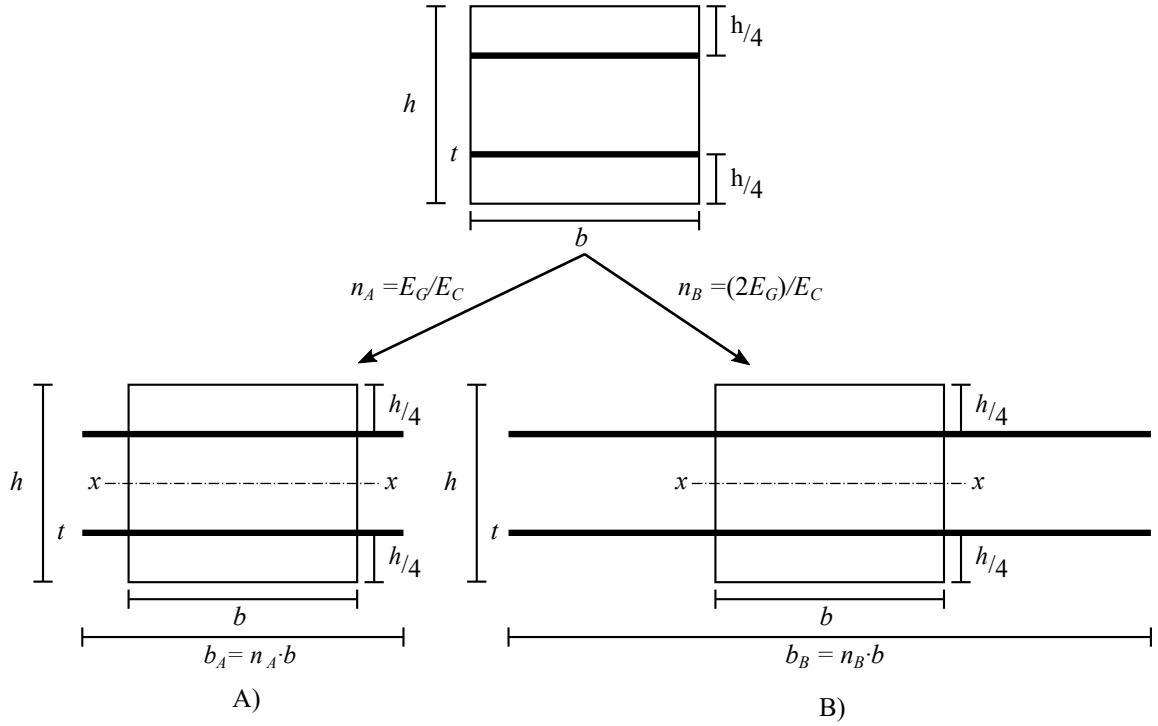

Figure C.1: Transformed section of reinforced clay liner a) geogrid stiffness of E_G and b) geogrid stiffness of $2E_G$.

However, the stiffness of the geogrid (E_G) is several orders of magnitude greater than that of the clay (E_C). Thus, the moment of inertia of the clay ($I_{C_{xx}}$) is several orders of magnitude smaller than that of the geogrid ($I_{GA_{xx}}$). Consequently:

$$\frac{\Delta_A}{\Delta_B} = \frac{I_A}{I_B} \approx \frac{2I_{GA_{xx}}}{4I_{GA_{xx}}} = \frac{1}{2}$$

APPENDIX D SCALING THE STRAIN FIELDS

Scaling by the actual minimum and maximum strain values could be problematic due to the large number of outlier strain values that were expected. The presence of wild vectors, the possibility of high aspect ratio triangular elements in the strain calculations and the extreme strains that were present after macro-cracks opened all contributed to the large expected number of outliers. As such, using the actual minimum and maximum values of the data set skewed the scaling.

Accordingly, the outliers were first removed from the data set before the minima and maxima were used for scaling. Traditional methods of outlier detection such, as the three-sigma method, can suffer from masking and swamping (Rousseeuw & Hubert, 2011). Masking implies that the weight of the outliers are so significant that the detection method itself is biased by the outliers. When good data points are incorrectly identified as outliers, it is known as swamping. The field of Robust Statistics attempts to address both these issues (Rousseeuw & Hubert, 2011).

In robust statistics the median (Q_2) of a data set is used as a measure of the centre, as the mean is easily skewed by outliers (masking). The outliers can be isolated with a simple box-and-whiskers plot. The limits for the outliers are shown in Figure D.1: a) one and a half (1.5) times the inter-quartile range (IQR) below the first quartile (Q_1) and b) 1.5IQR above the third quartile (Q_3).

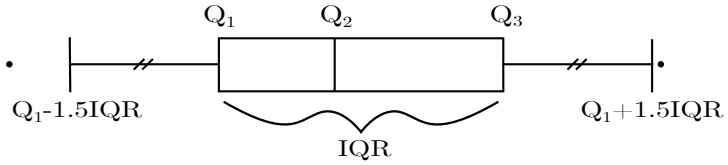

Figure D.1: Outlier detection with a box-and-whiskers diagram.

The problem with the box-and-whiskers approach is that it assumes that the data set is symmetrical. The distance from the bottom limit to Q_1 is the same as the distance from Q_3 to the top limit. However,

the strain fields for the centrifuge tests were not necessarily symmetrical. For example, the maximum shear strain data ranged from 0 to 1. Consequently, an approach that incorporated the skewness of the data in the outlier detection was used.

Hubert & Vandervieren (2008) identified the *medcouple* of Brys et al. (2004) as a suitable measure of the skewness of the data. The medcouple is defined as:

$$\mathrm{MC}(F) = \underset{x_1 < Q_2 < x_2}{\mathrm{med}}\ h(x_1, x_2) \tag{D.1}$$

and:

$$h(x_i, x_j) = \frac{(x_j - Q_2) - (Q_2 - x_i)}{x_j - x_i} \tag{D.2}$$

where x_1 is all the values of F smaller than the mean (Q_2) of F, x_2 is all the values larger than the mean and h is known as the so-called kernel function.

Thus, medcouple is the median of h evaluated for all the possible combinations of the values in x_1 and x_2. For this study the medcouple was calculated using the MATLAB implementation of the LIBRIA package (Verboven & Hubert, 2010).

A medcouple smaller than zero implies that the distribution is skewed to the left and a medcouple larger than zero implies that the distribution is skewed to the right. The relative magnitude indicates the degree of skewness.

To incorporate the medcouple into the limits from the box-and-whiskers plot, Hubert & Vandervieren (2008) suggested the use of an exponential function. For a medcouple larger than zero, the outliers would be the data outside the interval:

$$[Q_1 - 1.5e^{-4\mathrm{MC}} \cdot \mathrm{IQR}\ ;\ Q_3 + 1.5e^{3\mathrm{MC}} \cdot \mathrm{IQR}], \qquad \mathrm{MC} \geq 0 \tag{D.3}$$

where Q_1 is the first quartile, Q_3 the second quartile, IQR the interquartile range ($Q_3 - Q_1$) and MC the medcouple. For a medcouple smaller than zero:

$$[Q_1 - 1.5e^{-3\mathrm{MC}} \cdot \mathrm{IQR}\ ;\ Q_3 + 1.5e^{4\mathrm{MC}} \cdot \mathrm{IQR}], \qquad \mathrm{MC} < 0 \tag{D.4}$$

The exponential constants of 3 and 4 were selected by Hubert & Vandervieren (2008) after considering 12 605 distributions of five different families.

For each centrifuge test the minimum and maximum of all the strain data were calculated with either Equation D.3 or Equation D.4. The horizontal strain data was scaled between -1 and 1 with these minimum and maximum and the shear strain data between 0 and 1. Consequently, the maximum horizontal strain and maximum shear strain over all three stages was equal to one, while the minimum horizontal strain was equal to negative one.

APPENDIX E ADDITIONAL STRAIN FIELDS FOR THE CENTRIFUGE TESTS

SHEAR

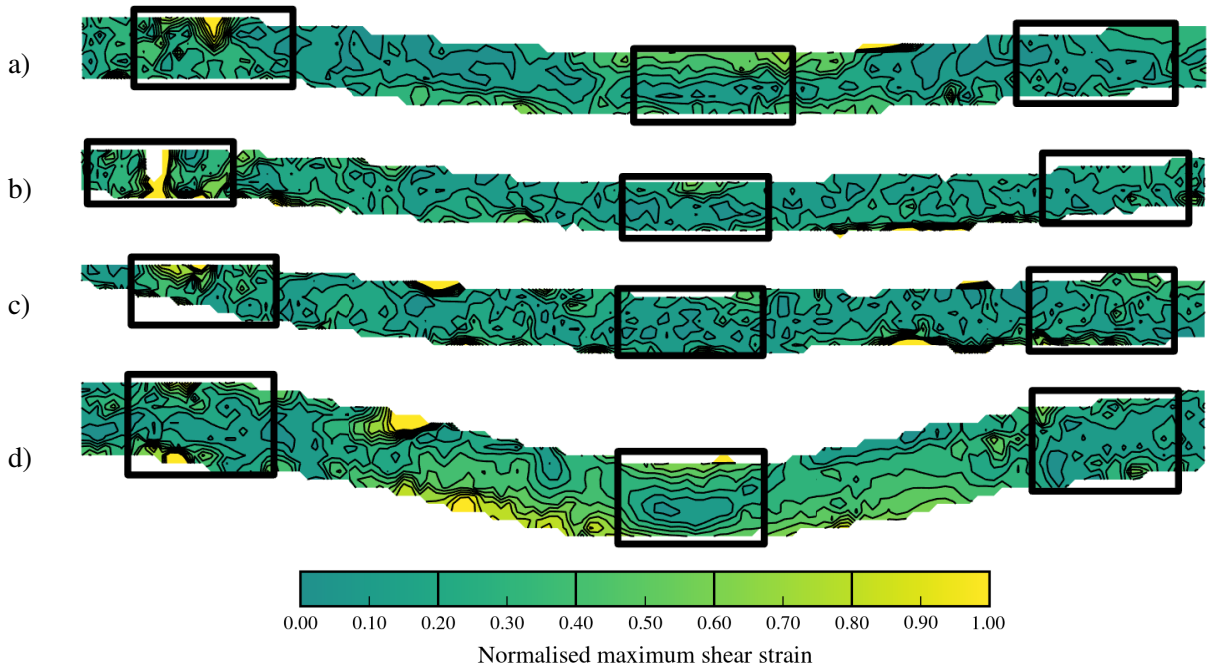

Figure E.1: Normalised maximum shear strain at Stage III (see Table 5.6) for a) unreinforced, b) bottom-reinforced, c) top-reinforced, and d) double-reinforced liners.

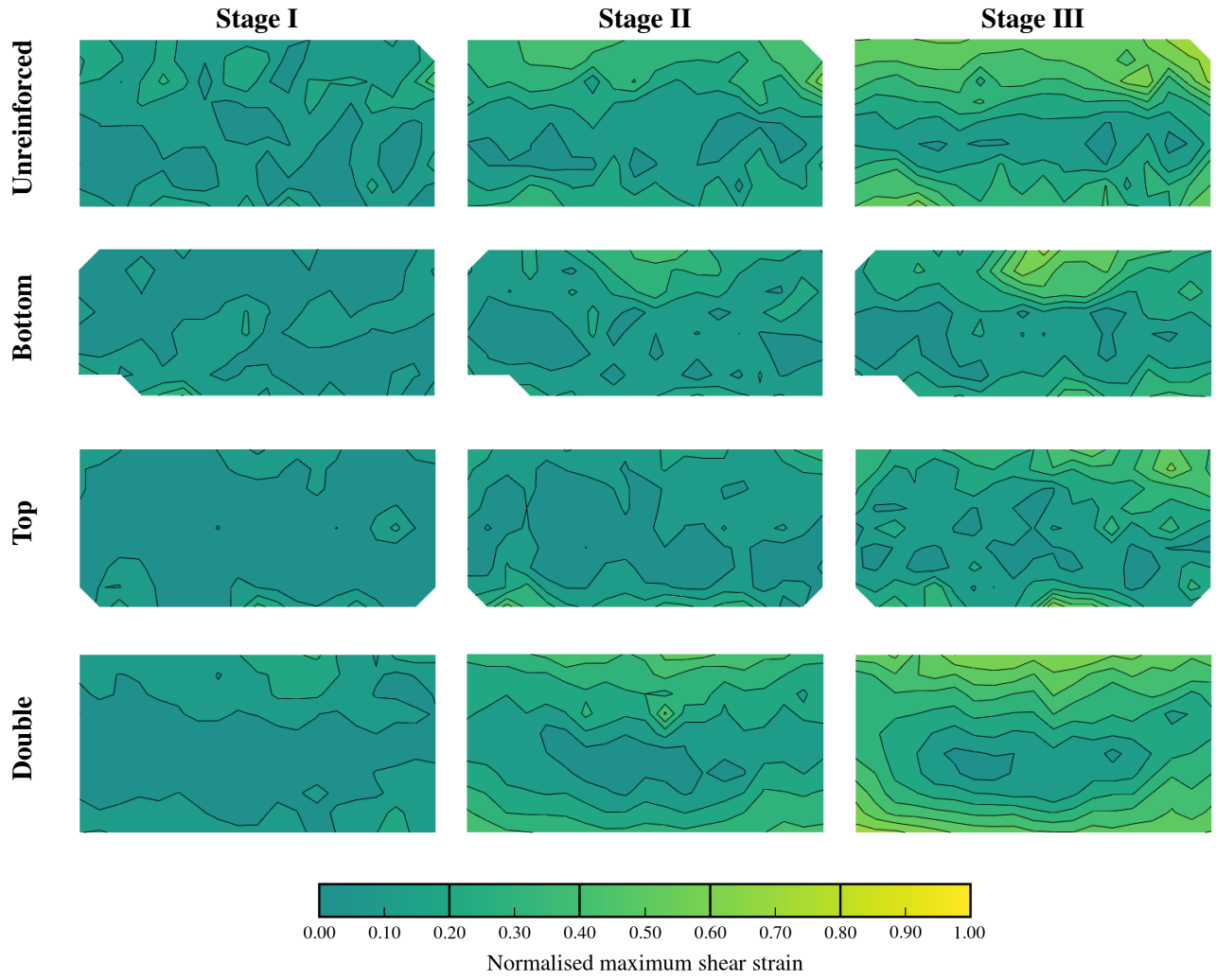

Figure E.2: Comparison of normalised maximum shear strain at the centre (see Figure 5.26) for all the tests, at the three different stages.

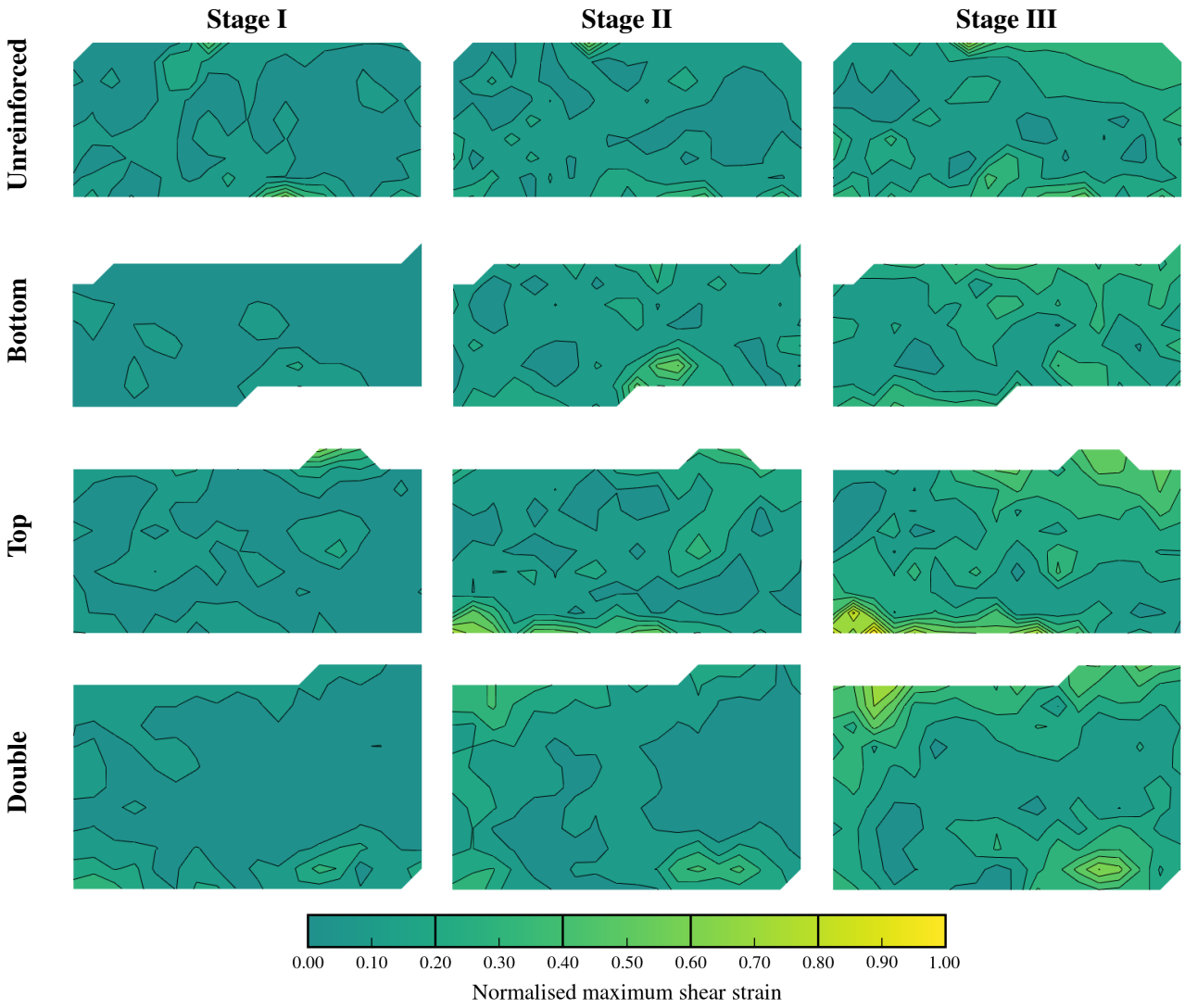

Figure E.3: Comparison of normalised maximum shear strain at the location of the right hand crack (see Figure 5.26) for all the tests, at the three different stages.

HORIZONTAL STRAIN

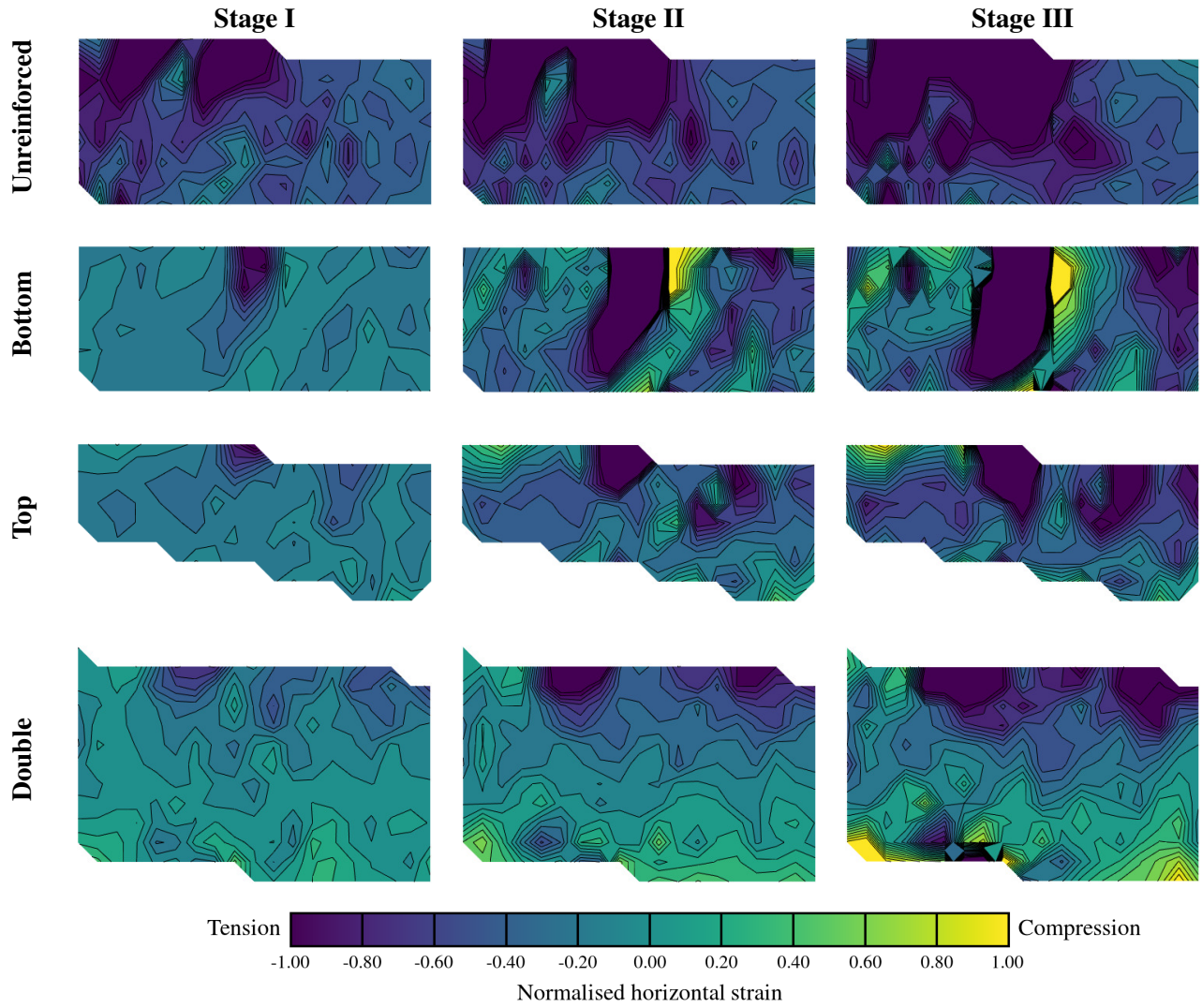

Figure E.4: Comparison of normalised horizontal strain at the location of the left hand crack (see Figure 5.26) for all the tests, at the three different stages.

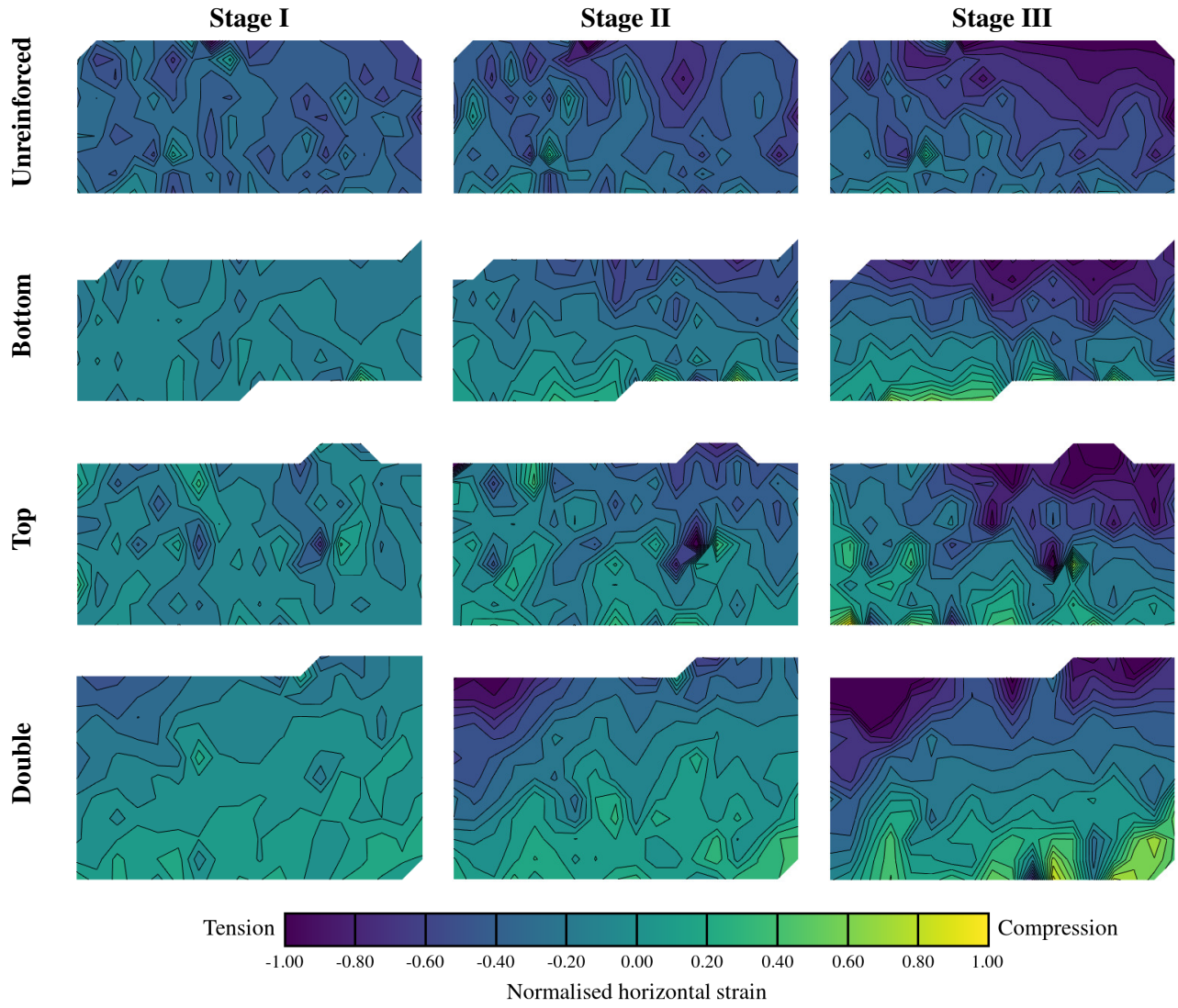

Figure E.5: Comparison of normalised horizontal strain at the location of the right hand crack (see Figure 5.26) for all the tests, at the three different stages.

APPENDIX F ADDITIONAL HISTOGRAMS OF STRAIN DISTRIBUTION FOR THE CENTRIFUGE TESTS

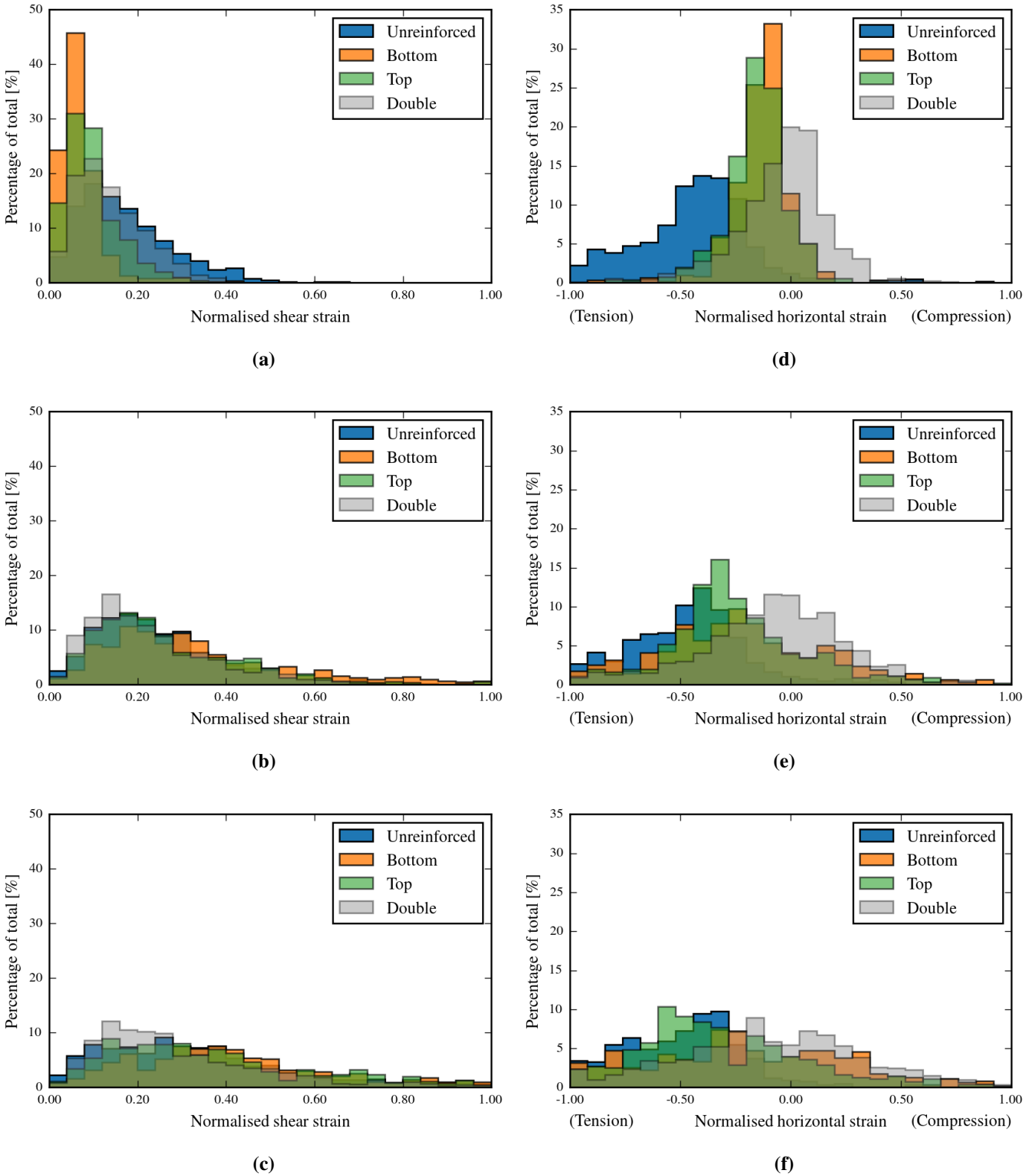

Figure F.1: Histograms of the shear (a-c) and horizontal (d-e) strain distribution at the left fractures. Stage I: a & d, Stage II: b & e and Stage III: c & f.

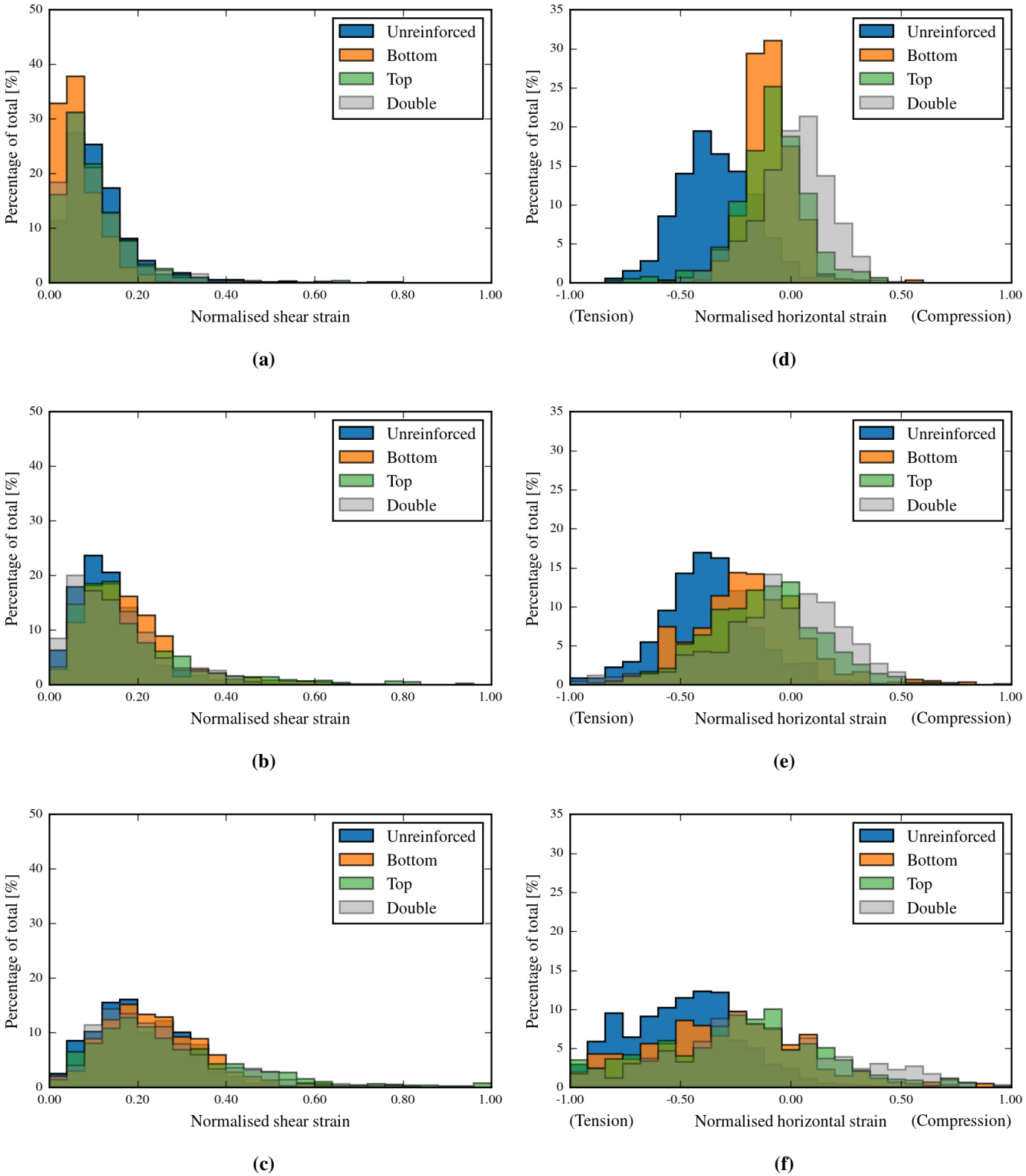

Figure F.2: Histograms of the shear and horizontal strain distribution at the right fractures Stage I: a & d, Stage II: b & e and Stage III: c & f.